University of Southern Queensland

Novel Fibre Composite Civil Engineering Sandwich Structures: Behaviour, Analysis, and Optimum Design

A Dissertation submitted by

Ziad Khalaf Awad

B.sc. Eng., M.sc. Eng.

Supervised by

Assoc. Prof. Thiru Aravinthan

Dr. Yan Zhuge

For the award of

DOCTOR OF PHILOSOPHY

2012

Abstract

Fibre reinforced polymer (FRP) composite sandwich structures are increasingly used in the construction of civil engineering applications because of their outstanding strength and light weight properties. However, the use of FRP products has some design difficulties as a result of the composition of the fibre and matrix. The design variables usually are fibre and matrix properties, fibre direction, laminate composition, and core thickness. The combination of the design variables leads to a complex design problem, and the optimisation of fibre composite sandwich structures is rarely straightforward. This is due to the complicated behaviour, and the multiple design variables and objectives required to be considered. This research deals with the presentation of a glass fibre reinforced polymer (GFRP) sandwich structure analysis and design. Based on the literature review, a design optimisation methodology was proposed for the FRP composite structures. The methodology contains three parts; experimental investigation, Finite Element Analysis (FEA) with modelling verification, and design optimisation of the GFRP sandwich structures.

Several experimental static and free vibration tests were made on the GFRP sandwich beams and slabs. The experimental investigation provided good information about understanding the behaviour of the GFRP sandwich structures. A user subroutine UMAT was written to model the GFRP sandwich skins in three dimensions (3D) FEA. The FEA model was verified with the structural experimental behaviour in static and free vibration tests. The FEA analysis helped in-depth understanding of the GFRP sandwich structure behaviour, and provided an acceptable model for design optimisation.

The design optimisation considered the Adaptive Range Multi-Objective Genetic Algorithm (ARMOGA) as an optimisation method. ARMOGA has robustness, ability in dealing with both continuous and discrete variables, and it has excellent searching for a global optimum. A design optimisation was done with the multi-objective cost and mass minimisation. The design optimisation was done on GFRP slab designs in one-way and two-way spaning. In addition, the optimisation of the single and glue laminated GFRP sandwich beam was also investigated.

Single and glue laminated GFRP sandwich beams behaviour was investigated. Static four point tests were conducted for the beam investigation. The investigation showed that shear span to depth ratio (a/d) is the main factor controlling the behaviour of the GFRP sandwich beam under combined shear and moment. Single sandwich beams showed higher shear and bending strength than glue laminated beams. The static experimental results indicated that there are three types of failure that can be seen in the GFRP sandwich beam; core crushing, core shear, and top skin compression failure. The GFRP sandwich beam did not show debonding as a failure mode because the skin-core interaction strength is close to the tensile and shear strengths of the core. The prediction shear equation showed acceptable results for beams with an a/d less than 2, and the bending equation showed good results for the beams of a/d greater than 4.5.

One-way and two-way GFRP sandwich slabs were tested under static point load. GFRP sandwich slab tests showed that the core to skin ratio and the total slab thickness have a big effect on the GFRP sandwich slab load capacity. Slabs with 18 mm thickness and with a 3 mm skin thickness showed double load capacity compared to 15 mm slab thickness with a 1.8 mm skin thickness. In addition, the support system has an effect on the slab behaviour and it represents an important aspect in the design. The two-way supported slab has approximately double loading capacity compared to the one-way supported slab. Square slabs with $\pm 45^{o}$ fibre orientation have a lower deformation and higher stiffness than $0^{o}/90^{o}$ orientation two-way square slabs. The effect of screw boundary restraint has a small influence on the behaviour of GFRP sandwich slabs. The effect of the slab width to length ratio is small at service load levels while it has more impact on the ultimate failure load level. The ultimate failure load decreases as the slab width to length ratio is increasing.

One-way and two-way slabs were tested for free vibration behaviour in single and continuous support systems. The free vibration tests showed that the span length of the slab had an impact on the natural frequency with an increase in span length reducing the natural frequency of the slab. Two-way slabs have a higher natural frequency than one-way slabs. Three boundary restraint types were investigated. Screw restraint slabs have a higher frequency than the simple restraint slabs.

Moreover, glue restraints have a larger frequency than screw restraint slabs. The $0^o/90^o$ and $\pm45^o$ skin fibre orientations were also studied. GFRP one-way sandwich slabs with $\pm45^o$ fibre orientation had a lower frequency than slabs with $0^o/90^o$ fibre orientation, while, the GFRP two-way sandwich slab with $\pm45^o$ fibre orientation had a higher frequency than slabs with $0^o/90^o$ fibre orientation.

Non-linear FEA revealed that the material models for the skin and phenolic core give an acceptable behaviour. The comparison of the FEA results was done with different experimental tests for the slabs and beams. The FEA model using the CRUSHABLE FOAM model and Hashin model gave a good prediction for the GFRP sandwich structure's behaviour. The core part did not reach the hardening behaviour when the structure failed due to core shear and top skin compression. The same FEA model was used to predict the free vibration of the GFRP sandwich slabs. The FEA model developed in this work provided a good prediction of the free vibration behaviour of GFRP sandwich beams and slabs. This model can be used for design optimisation with confidence.

Multi-objective optimisation revealed that slab thickness is affected by the slab span. The required slab skin thickness and core thickness have an approximately linear relationship with the slab span length. The slab and beam designs are controlled by mid-span deflection limits. The strength constraints showed no contribution to the design optimisation. The design showed that the optimum core to skin thickness ratio of the beam is 11.0. The glue laminated beam optimisation indicated that the single sandwich beam has an optimum depth design less than the glue laminated beam. The depth of the glue laminated beam increases with the increase of sandwich layers.

From this study, it was concluded that experimental investigations gave a better understanding of the behaviour of novel GFRP sandwich structure. In addition, the FEA modelling added more knowledge to understanding the behaviour of such structures. The optimisation design presented the design variables of the GFRP sandwich beams and slabs.

Certification of Dissertation

I certify that the ideas, experimental work, results, analysis, and conclusions reported in this dissertation are entirely my own effort, except where otherwise acknowledge. I also certify that the work is original and has not been previously submitted for any award, except where otherwise acknowledged.

……………………………………. / /2012

Signature of Candidature Date

Ziad Khalaf Awad

ENDORSEMENT

……………………………………. / /2012

Signature of Supervisor/s

Date

……………………………………. / /2012

Signature of Supervisor/s

Date

Acknowledgements

My thanks and appreciations go to Assoc. Prof. Thiru Aravinthan, my principal supervisor, for his guidance, encouragement, persistence, patience and expert advice. Interaction with him has inspired my love of research and has allowed me to seek new and exciting challenges. I will always remember the time we spent on research and publications. I wish to express my sincere gratitude to my associated supervisor Dr. Yan Zhuge and my external adviser Dr. Luis Felipe Gonzalez Toro from Queensland University of Technology (QUT), for guiding this project and making me realize the importance of perfection and quality. In addition, my great thanks for Prof. Frank Bullen for his expert advice and valuable input to my research.

I also would like to thank Assoc. Prof. Talal Yusaf for his support. My thanks also go to Assoc. Prof. Karu Karunasena for his support at initial stage of the research. Thanks are also in order to Dr. Allan Manalo, Dr. Jayantha Epaarachchi, Dr. Belal Yusaf, Wayne Crowell, Mohan Trada, my colleagues, and all the technicians in the USQ labs and offices. I would also like to acknowledge the support of the Faculty of Engineering and Surveying and the Center of Excellence in Engineering Fibre Composites. Also, I thank FoES Associated Dean (Research) Assoc. Prof. Armando Apan and his assistant Juanita Ryan for their support. My acknowledgment to my sponsor Iraqi Government, and special thanks to the Iraqi Cultural Attaché office (Canberra) for all the supports during the period of the study. Finally, my thanks go to Ernest Dunwoody, who helps me in editing the thesis.

My admiration and respect go to my father and mother for their help and prayers. Many thanks go to my brothers and relatives for their help. Finally, my thanks go to my wife and my beautiful son Tareq for their endless love and continuous encouragement during this endeavour.

Associated publications[1]

Journals

Awad, ZK, Aravinthan, T, Zhuge, Y & Gonzalez, F 2012, 'A review of optimization techniques used in the design of fibre composite structures for civil engineering applications', *Materials & Design*, vol. 33, no. 1, pp. 534-44.

Awad, ZK, Aravinthan, T, & Manalo, A 2012, 'Geometry effect on the behaviour of single and glue-laminated GFRP composite sandwich beams loaded in four-point bending ', *Materials & Design*, vol. 39, pp. 93-103.

Awad, ZK, Gonzalez, F & Aravinthan, T 2010, 'Advanced robust design optimization of FRP sandwich floor panels', *IOP Conference Series: Materials Science and Engineering*, vol. 10, no. 1, pp. 1-9.

Awad, ZK, Aravinthan, T, & Zhuge, Y 2012, 'Experimental and numerical analysis of an innovative GFRP sandwich floor panel under point load ', *Engineering Structures,* vol. 41, pp. 126-35.

Awad ZK, Aravinthan, T, & Zhuge, Y, 'Investigation of the free vibration behaviour of an innovative GFRP sandwich floor panel ', *Construction & Building Materials,* (under review).

Refereed conference proceedings

Awad, ZK, Aravinthan, T & Zhuge, Y 2009, 'Finite element analysis of fibre composite sandwich panel', paper presented to Southern Engineering Conference: Infrastructure Investment for a New Economy, Springfield, Queensland, Australia.

Awad, ZK, Aravinthan, T & Zhuge, Y 2010, 'Cost optimum design of structural fibre composite sandwich panel for flooring applications', paper presented to 5th International Conference on FRP Composites in Civil Engineering (CICE 2010), Beijing, China.

Awad, ZK, Aravinthan, T, Zhuge, Y & Gonzalez, F 2010, 'Multi-objective design optimization of an innovative fibre composite sandwich panel for civil engineering applications', paper presented to 21st Australasian Conference on the Mechanics of Structures and Materials: Incorporating Sustainable Practice in Mechanics of Structures and Materials (ACMSM21), Melbourne.

Awad, ZK, Aravinthan, T, Zhuge, Y & Gonzalez, F 2010, 'Investigation of frequency characteristics of GFRP/phenolic sandwich beams', paper presented to Southern Region Engineering Conference (SREC2010), Toowoomba, QLD 4350, Australia.

Awad, ZK, Aravinthan, T, Zhuge, Y & Gonzalez, F 2012, 'Multi-objective design optimization of GFRP sandwich Beam', Abstract submitted to ACMSM22 conference, Sydney.

---

[1] Some of the above publications are available through USQ - *ePrint*: (http://eprints.usq.edu.au/view/people/Awad=3AZiad_K=2E=3A=3A.html).

Table of Content

Chapter 8 Summary and conclusions

Appendix A FRP composite materials mechanical properties

Appendix B Free vibration behaviour of GFRP sandwich beams

Appendix C Source code: UMAT subroutine

Appendix D Design of slab- beam structure

List of Figures

Chapter 1 Introduction

Chapter 2 Design of FRP composite civil engineering structures: a review

Chapter 3 Behaviour of single and glue laminated GFRP sandwich beams

Chapter 4 Behaviour of GFRP sandwich slabs

Chapter 5 Free vibration behaviour of GFRP sandwich slabs

Chapter 6 FE simulation and modelling verifications

Chapter 7 Optimum design of GFRP sandwich slabs and beams

Appendix A FRP composite materials mechanical properties

Appendix B Free vibration behaviour of GFRP sandwich beams

Appendix D Design of slab- beam structure

List of Tables

Chapter 2 Design of FRP composite civil engineering structures: a review

Chapter 3 Behaviour of single and glue laminated GFRP sandwich beams

Chapter 4 Behaviour of GFRP sandwich slabs

Chapter 5 Free vibration behaviour of GFRP sandwich slabs

Chapter 6 FE simulation and modelling verifications

Chapter 7 Optimum design of GFRP sandwich slabs and beams

Appendix A FRP composite materials mechanical properties

Appendix B Free vibration behaviour of GFRP sandwich beams

Appendix D Design of slab- beam structure

Notations

A	Area
a	Shear span
a_n	Boundary conditions parameters
$\dot{a}$	Momentum
b	Width
$\bar{b}$	Strength of attraction coefficient
c	Core thickness
C	Cost
c_1	Aspect ratio constant
$\bar{c},\ \bar{d}$	Particle position factor
C_{ij}	Stiffness coefficient
D	Rigidity
d	Depth
d_c	Distance from the centre of the core to the neutral axis
d_f, d_m, *and* d_s	Damage factors for the composite
d_s	Distance from the centre of the skin to the neutral axis
E	Elastic modulus
E_a	Apparent stiffness modulus
E_{core}	Core elastic modulus
E_l	Longitudinal elastic modulus
EI	Equivalent bending stiffness
E_{skin}	Skin elastic modulus
E_t	Transverse elastic modulus
f	Frequency (hz)
f_{avg}	Average fitness value
F_f^c	Fibre failure index in compression
F_f^t	Fibre failure index in tension
F_l^c	Inter-laminar compression failure
F_l^t	Inter-laminar tension failure
F_m^c	Matrix failure index in compression
F_m^t	Matrix failure index in tension
$F.S$	Factor of safety
F^s	Shear flexibility
f_v	Fitness value
$\bar{f}(H)$	Fitness value number
G	Shear modulus
G_f	Fibre shear modulus
G_m	Matrix shear modulus
$g_1, g_2, \ldots, g_n$	Constraints
g	Lagrange multiplayer
h	Layer thickness
H	Flexibility matrix
I	Moment of inertia
i	Iteration number
j	Number of design constraints
K	Stiffness
k	Increment number

$\bar{k}$	Number of the objective functions
L	Span length
l	Load span
L_x	Longitudinal span length
L_y	Transverse span length
$\bar{L}$	Total length of the string
m	Schema number
M	Mass
M_b	Bending moment
M_f	Fibre mass Fraction
M_m	Matrix mass Fraction
$\bar{M}$	Damage operator
N	Number of sandwich layers
n	Constraints number
$O(H)$	Order of Schema
P	Point load
$\bar{P}$	Probability
P_G	Shear capacity of glue laminated beam
P_{s1}, P_{s2} and P_{s3}	Shear load capacity
p_c and p_m	Probabilities of crossover and mutation respectively
Q	Transverse force
q	Randomly generated number
q_o	Constant parameter
Q_t	First moment of area
r	Core to thickness ratio
R	Scalar damage variable
$\dot{R}$	Optimum solution
$\bar{R}$	Slab dimensions aspect ratio
R_E	Exterior radius of normalised tolerance
t	Skin thickness
t_f	Fibre thickness
t_m	Matrix thickness
T	Rotation matrix
$\bar{t}$	The generation number
ult	Subscript means ultimate
v	Velocity
V	Shear force
V_f	Fibre volume fraction
V_m	Mass volume fraction
W	Distributed load
$\bar{W}$	Feasible solution
$\bar{w}$	Circular frequency (rad/s)
x	Variable
$\bar{x}$	Particle position
x^s	Position of slave surface
x^m	Position of master surface
x, y, z	Global coordinates
X^T and X^c	Fibre strength in tension and compression
Y^T and Y^c	Matrix strength in tension and compression
z	Distance from neutral axis

Z^T and Z^c	Normal strength of the composite layers
α_r and fl_i	Control parameters
$\bar{\beta}$	Parameter
μ_i	The normal distribution
σ_i	Standard deviation
$\tilde{\tau}$	The pheromone
β_i	Safety - index
δ	Deflection
$\delta(H)$	length of Schema H
ε	Strain
ζ	Error
η	Robust index
θ	Fibre orientation
λ	Lagrange multiplier
ξ	Damping ratio
ρ	Density
σ	Stress
σ_f	Skin stress
σ_{ult}	Ultimate strength
τ	Shear stress
υ	Poisson's ratio
υ_f	Fibre Poisson's ratio
υ_m	Matrix Poisson's ratio
ψ	Real response
ϕ	Rotation

Chapter 1

Introduction

1.1 General

There is a growing concern with the worldwide deterioration of traditional materials such as concrete, steel, and timber. Recently, attention has shifted to the use of fibre reinforced polymers (FRP) as alternative materials. Their light weight and high strength to weight ratio can produce a lighter structure with an increase the live load capacity. Furthermore, the resistance of FRP materials to corrosion means that they can be used to replace steel and reinforced concrete in situations when they would be exposed to corrosion. Generally, traditional materials like concrete, steel, and timber are cheaper than the FRP materials. Although there are overall benefits of using FRP materials, they are not commonly used in the civil engineering applications because of their higher initial cost than traditional materials. Furthermore, new FRP composite materials are being developed using different types of components. For these reasons, it is desirable to investigate and understand the existing FRP composites behaviour when it is used in civil engineering applications. This is compounded by the lack of standard design codes and specifications to guide their use in civil engineering applications.

The FRP composites are different from traditional materials. FRP materials are normally anisotropic. This makes their analysis more difficult. The properties of the FRP composites are based on their component elements (fibre and matrix) and the configuration of the fibre within the matrix (Kutz 2006). FRP composites have been used in different structural applications such as bridges, beams, slabs, sleepers, and walkways as shown in Figure 1.1. The design of existing FRP composite structures is based on the experimental evaluation, designer experience, and information adopted from design guides developed for other structural materials.

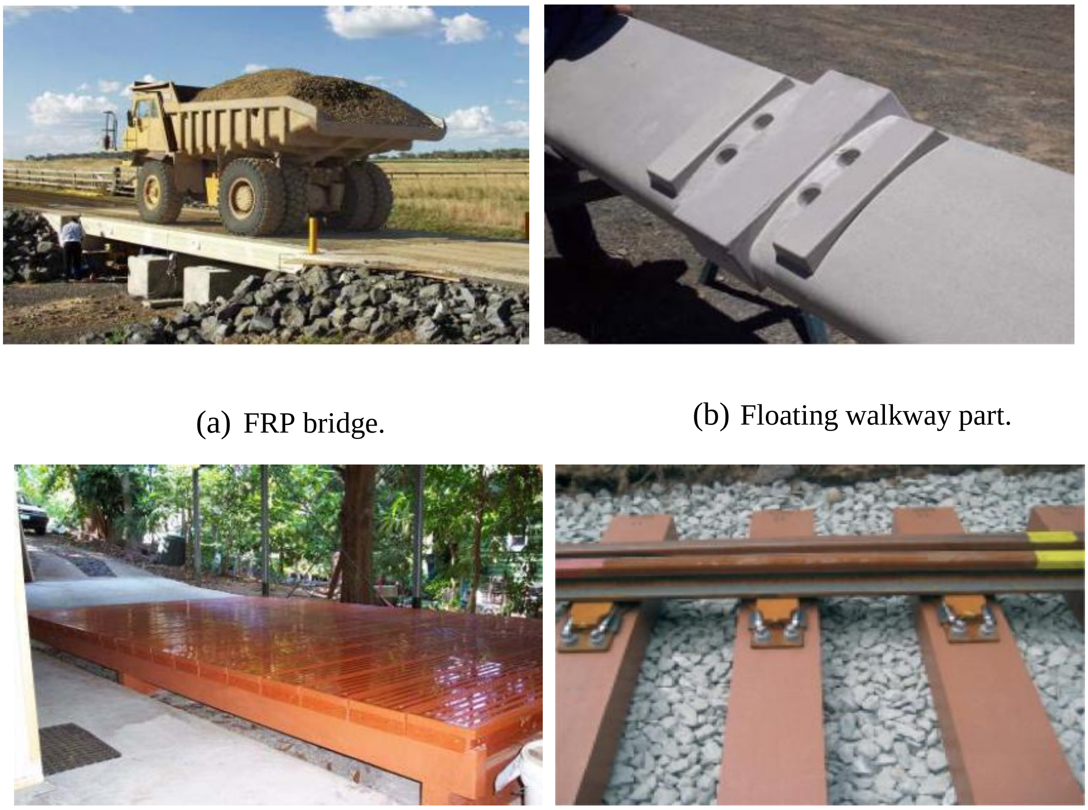

(a) FRP bridge.

(b) Floating walkway part.

(c) Pedestrian bridge deck.

(d) Railway sleeper.

Figure 1.1 FRP civil structural applications.

1.2 Background

In structural applications, FRP is usually stacked in a number of layers with each layer having a combination of fibre and matrix material. The fibres can be uniformly oriented in typically two or more directions, or they may be oriented randomly. The optimum use of the FRP composite material is obtained when the fibre is oriented in a specific direction to obtain highest strength and stiffness values in the loading direction and lower strength and stiffness values in other directions. Sandwich structures are used in civil engineering applications due to their high stiffness to weight ratio. The sandwich structure is made of three parts; a top skin, bottom skin, and the core. The analysis of sandwich structures is different from the multi-layered FRP structure. The analysis method should consider different models for the core, skins, and the interaction between them. Furthermore, the design of sandwich structure has to save the materials in the skin parts and in the core part as well. To obtain an optimal design the designer has to select where to put material and which materials to use in both the core and in individual skin layers.

Achieving the optimum use of materials needs a powerful and reliable numerical design tools to satisfy the FRP design parameters. This includes the use of complex geometric forms, multiple layers, and different materials. Investigators have spent a lot of attention in developing FRP design tools using different experimental tests, optimisation methods and analysis methods. The following sections of this chapter introduce the different FRP composite elements and the design of FRP structure.

1.2.1 FRP composite elements

Composite materials have different properties, and this allows different configurations to be made to meet different needs (Hassani & Hinton 1999). Glass fibre reinforced polymer (GFRP) is well known today in commercial markets and represents the most versatile industrial material. It has benefits of high-tensile strength, fire resistance, chemical resistance, hardness, moisture resistance (Frederick et al. 2001; Knox 1982), and relatively low cost compared to other composite products (Lavoie 1997).

However, it also has some disadvantages compared to traditional materials. These include its relatively low modulus of elasticity and its high cost. Different forms of GFRP composites are used for specific civil engineering applications such as; pultrusion, plates, and sandwich panel, as shown in Figure 1.2.

The pultruded elements are manufactured with different cross section shapes and dimensions as shown in Figure 1.2(a) (Jiang et al. 2012). The plate and sandwich elements are shown in Figure 1.2(b). The FRP plate is made of multi-layers of material stacked together horizontally with different fibre orientations. The GFRP sandwich panel is made from three parts; top GFRP skin, bottom GFRP skin and core as shown in Figure 1.2(b). The core material can be made in different forms of solid and voided core. Recently, a novel GFRP sandwich panel has been used for different structural applications such as slabs, bridge deck, beams, girders, and railway sleepers (Manalo et al. 2010a). This novel GFRP sandwich panel demonstrated the flexibility of using a single panel in different applications by adhesively bonding several panels together.

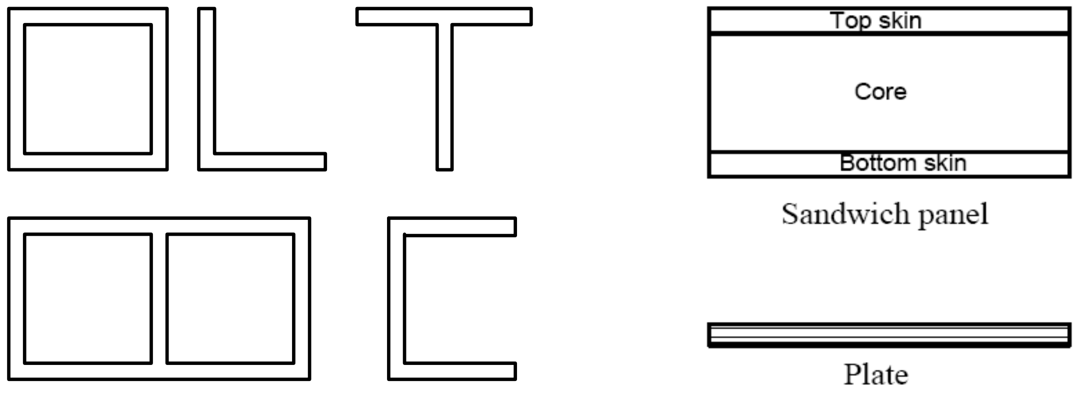

(a) Pultruded sections. (b) Panel and plate.

Figure 1.2 FRP composite elements.

1.2.2 FRP structure design optimisation

Composite materials have been developed to be used in numerous civil engineering applications during the last two decades. The laboratory tests were developed to identify design parameters and to document the behaviour of the FRP structures (Hadcock 1982). Experimental investigation and analysis were also conducted on FRP composite structures to understand their behaviour. This provided reliable information for the designers. Designing FRP composites structure requires considering serviceability requirements, design strength criteria, high temperature effects, water effects, durability and manufacturing complexity. There are no standard codes that specify or cover the full range of sections of composite members, including available sections properties and allowable strength (Cripps 2002). Most of the available FRP composite structure designs are conservative due to the limitation in the design standards and full understanding of the FRP materials behaviour. The existing FRP composite structure designs depend on different specifications. These specifications mainly rely on a combination of understanding the behaviour of FRP structures, experimental results, and the recommendations of the available codes and design guides (Quinn 1999).

However, developing an optimum design method of FRP composite structure is very important for more efficient use of materials which can minimise their cost (Hollaway & Head 1999). Miravete (1996) says, "*Optimisation of composite materials is a recent issue, because both optimisation techniques and composite* *structures have been developed during the last few decades and therefore, the conjunction of them is more recent*".

Finite Element Analysis (FEA) method and optimisation methods were used in the design of FRP composite structures (Miravete 1996). The FEA method is able to deal with the complicated characteristics of the FRP materials such as their geometry, material behaviour, and multi-layer structure. Verification of the FE modelling with the experimental behaviour is strongly recommended before it is used in design. Design optimisation is required for FRP civil engineering structures to achieve cost savings, mass minimization, maximizing bending stiffness, and to enhance the structure against dynamic loading. Optimisation techniques can be used to find the ideal values of the design variables, find the relationships between both variables and constraints, and to design the structure to meet multiple objectives. Additionally, consideration of the effect of free vibration in the design is very important to avoid any structural resonance such as in building floors, stadiums, and bridges.

1.3 Novel GFRP sandwich panel

A novel fibre composite sandwich panel with GFRP skins and a solid modified phenolic core was developed by an Australian manufacturer (Manalo et al. 2010d; Van-Erp 2010). The core density of the panel is 950 kg/m^3 higher than usual. The overall density of the novel GFRP sandwich panel is 1100 kg/m^3. This sandwich panel offers many benefits compared to conventional sandwich panels including a high strength to weight ratio, good thermal insulation, moisture resistance, and termite resistance. The new panel composition is contains approximately 15 kg of polymer per square meter, and 65 % of this polymer is plant based (Van-Erp 2010). It has a carbon foot print similar to timber. Furthermore, this panel offers the ability to cut, drilled, glued, and shaped on site. These features give this type of composite panel a wide range of applications in Australia for use as; slabs, glue laminated beams, bridge decks and girders, and railway sleepers. A typical panel is shown in Figure 1.3.

Some core materials such as balsa wood and light weight foam are soft, and may be crushed under a compression load. Others such as honeycomb and trussedcore structures have a high compressive strength but low capacity to hold mechanical connections. The novel GFRP sandwich panel has a high core density which provides good resistance to compression forces. Several studies were done to investigate the mechanical properties of this GFRP sandwich panels. The flexural and shear behaviour of the single and glue laminated sandwich beams have been investigated by Manalo et al. (2010b; 2010c; 2010d). A preliminary study on the behaviour a slab under point load and distributed load was done by Islam and Aravinthan (2010). These investigations found that the product is suitable for structural applications. They recommended that the static and dynamic behaviour of the novel GFRP sandwich panel needed more investigation. In addition, the design of the novel GFRP sandwich panel as a new structural element needs more investigations. A sample of this panel in use a floor panel and bridge deck applications is shown in Figure 1.4.

Figure 1.3 Novel GFRP sandwich panel.

(a) Floor panel.

(b) Bridge deck using glue-laminated panels.

Figure 1.4 Structural applications of the GFRP sandwich panel.

1.4 Objectives

Past research focused on the optimum design of FRP structural elements for use in civil, mechanical, and aeronautical applications. Exploring the design of the novel GFRP composite sandwich beams and slabs is essential to provide information for the engineers. The focus of this study is to investigate the behaviour of the innovative sandwich structures, build a FEA model, and find the optimum design for the GFRP sandwich slabs and beams in civil engineering applications. Studying the optimum design of the civil engineering structures mainly considers several parameters such as loads, spans, strength, and deflection limit for serviceability.

The main objectives of the study as follows:

(a) Understanding the static behaviour of the GFRP single sandwich beam, glue laminated sandwich beam, and slabs.
(b) Investigate the free vibration behaviour of the GFRP sandwich beams and slabs.
(c) Develop a non-linear 3D FEA model with an appoperiate subroutine for the GFRP sandwich structure simulation.
(d) Multi-objectve design optimisation for the GFRP sandwich slabs and beams with cost and mass minmisation.

1.5 Scope of the thesis

The current research focuses on the novel GFRP composite sandwich panel as a new product in civil engineering structural beam and slabs applications. This work considers the following aspects:

- Review of the design optimisation techniques used in the design of FRP composite civil engineering structures.
- Finding the GFRP skin and core material mechanical properties.
- Testing and evaluating of the static load behaviour of GFRP sandwich beams and slabs under point load.
- Testing and evaluating of the free vibration behaviour of the GFRP sandwich slabs.

- Compare the FE simulation with the experimental tests for the beams and slabs in both static and free vibration behaviours.
- Optimise the GFRP sandwich beams and slabs under the variation of span and load.

The scope of the thesis was developed to achieve the design methodology for the novel GFEP sandwich structures. Nevertheless, the accompanying intellectual patent of this GFRP sandwich panel would not allow the author to consider the microstructure and materials optimisation of this product. In addition, due to thesis limitation the following issues are beyond the scope of the study:

- Experimental investigation of the combined slab-beam structure.
- Investigate the long term behaviour of the GFRP sandwich structures.
- Impact and fatigue effects on the GFRP sandwich structures.

1.6 Thesis outline

The study is focused on understanding the behaviour of the novel GFRP sandwich structure, numerical modelling and simulation, and optimising the design of potential GFRP sandwich structures. The thesis is divided into 8 chapters as follows:

- Chapter 1 is the introduction and it gives a brief outline of the background to FRP, novel sandwich panel, and a structure of the dissertation.
- Chapter 2 reviews the existing studies on the optimum design of GFRP civil engineering structures such as; beams, slabs, and bridge decks. In addition, the review of literature explores the design of the existing FRP composite structures and how they were designed using different methods.
- Chapter 3 covers the experimental investigation of the single and glue laminated GFRP sandwich beams in four point bending test. The GFRP sandwich beam geometry variations were considered in the experimental analysis.
- Chapter 4 deals with the experimental investigation of the GFRP sandwich slabs under static loading. The variations considered in the experimental analysis are slab geometry, support types, and boundary restraints.

- Chapter 5 concerns with the experimental investigation of the GFRP sandwich slabs in free vibration. The variations considered in the experimental analysis are geometry, support types, and boundary restraints.
- Chapter 6 presents the finite element modelling and simulation of the GFRP sandwich beams and slabs under static and free vibration behaviour.
- Chapter 7 covers the design criteria of the GFRP slabs and the optimum design under uniformly distributed and point loads. In addition, the design of the single and glue laminated GFRP sandwich beam under the transverse load from the slabs was presented.
- Chapter 8 summarising the main findings of the thesis and makes recommendations for future work.

1.7 Summary

Many countries have used the FRP structures instead of conventional concrete, steel and timber structures. The traditional structures showed degradation under the effects of cyclic load and environment action. Many applications use the glass fibre due to the low cost. Recent development of the novel GFRP sandwich panel showed that it has acceptable mechanical properties to be used in several structural applications. Understanding the behaviour and numerical simulation of this product in order to optimise the design is the key motivation of this research.

Chapter 2

Design of FRP composite civil engineering structures: a review

2.1 Introduction

In the last 70 years since the Second World War, fibre reinforced polymers (FRP) have been used in many structural applications due to their excellent strength and weight characteristics and because they can be used in applications with complex shapes (Iyer & Sen 1991). These composite materials can be classified into two groups. First is filled material, which is any material whose properties are improved by adding fillers. The second type is reinforced composite material, which has long high strength fibres bound by resin (Vasiliev & Morozov 2001). The FRP composite material typically contains fibre mixed with some resin. Commonly used types of fibre are glass, carbon and aramid. Types of resin include epoxy, polyester, vinylester, and Phenolic resins (Bank 2006). They have many benefits such as weight saving (high strength to weight ratio), able to add to the old structures in the form of strengthening and repairing, low maintenance requirements, resistance to environment effects, and an ability to be formed into complex shapes. All these advantages encourage engineers to use these materials in numerous structural forms. (Cripps 2002).

Two parameters are used to measure the relative advantages of composite materials. The specific modulus represents the ratio of the elastic modulus (E) to the density (ρ). The specific strength represents the ratio of ultimate strength (σ_{ult}) to the material density (Kaw 1997).

$$\text{Specific modulus}= \frac{E}{\rho} \qquad 2.1$$

$$\text{Specific strength}= \frac{\sigma_{ult}}{\rho} \qquad 2.2$$

Specifications of different materials are shown in Figure 2.1 (Gay et al. 2003). FRP materials have been used increasingly in the last two decades in civil engineering applications to construct large-scale fibre composite structures such as traffic and pedestrian bridges. Pedestrian bridges in rural areas are perhaps the best known application of the fibre composites, but there are limited design guidelines for these applications. Designers are likely to combine between the specification for pedestrian bridge crossings and specifications for highway bridge (Abro et al. 2007; Nayomon & Nobuhiko 2003). Most of the available fibre composite design structures depend on the coupon level experimental tests. The results from this test are adopted in the Finite Element Analysis (FEA) model to get the analysis results used for designing the real structure (Spearing et al. 1998). Manual prediction of the design variables during re-analysis is unlikely to produce an optimum design. The efficiency of the re-analysis process depends on the experience of the designers.

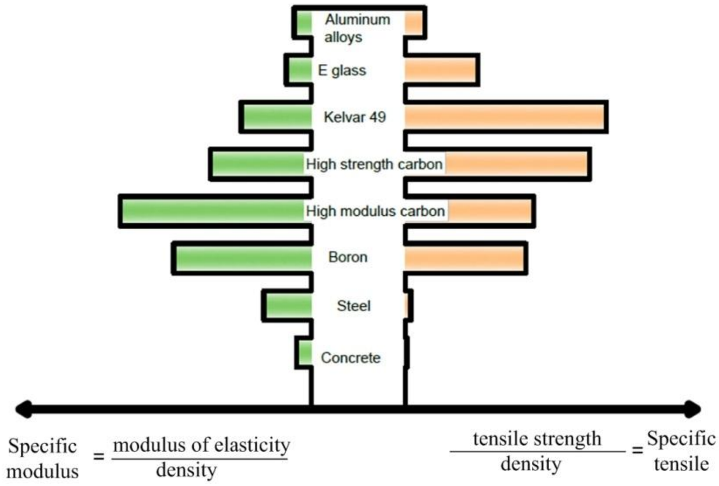

Figure 2.1 Material specific characteristics (Adopted from Gay et al. (2003)).

The Centre of Excellence in Engineered Fibre Composites (CEEFC) at the University of Southern Queensland (USQ) participated in the research, development and installation of the first fibre composite bridge in Australia in 2002 (Van-Erp et al. 2006). Earlier Structure and Materials Research Laboratory at Virginia Polytechnic Institute and State University developed a fibre composite bridge design in 1997 (Neely et al. 2004). This new bridge was installed across the Tom's Creek instead of timber bridge. The Tom's Creek composite bridge was designed according to the EXTREN DWB design guide (Lesko & Cousins 2003). Also in 1997, Potntresina pedestrian bridge was built in Switzerland. The bridge was designed to carry a load of 500 kg/m^2 (Keller et al. 2007). Additionally, fibre composites have also been used to construct railway sleepers (Namura et al. 2005), floating walk-ways and piles (Van-Erp et al. 2006). Generally, the composite beam and slab elements support other brittle parts of the structure such as walls and finishing. Therefore, the allowable deflection limit under the service load is an important consideration in the design. The EUROCOMP design code recommends a deflection limit for the fibre composite structure under the serviceability conditions which is between span/150 to span/400 (Clarke 1996).

In the USA, attention has been focused on the use of fibre composites for non-corrosive and light weight bridge decking systems. Over 117 bridges have been built or rehabilitated up till 2008 using fibre composites (O'Connor 2008). In the absence of the beneficial design standards for fibre composite structures in civil engineering applications, the optimisation methods and Finite Element Analysis (FEA) represent the best way of getting an acceptable structural design solution. This chapter reviews the importance of the optimisation techniques and their application to the design of fibre composite structures of civil engineering purposes.

2.2 Challenges in the design of fibre composite structures

Many researchers have accepted that the traditional materials such as wood, steel and concrete are vulnerable to corrosion. New construction techniques have been trialled using FRP materials as alternatives to the traditional steel, concrete, and wood materials (Daly & Duckett 2002). In addition, their use has been increasing for the repairing, strengthening and replacement of old structures. Evaluation of fibre composite use in civil engineering applications is important to justify whether or not this material is reliable enough to be used in construction. Steel is a homogenous material with a constant stiffness in all directions. FRP composite material has a different stiffness in different directions. This means that a fibre composite member designed for tension, without an enough transverse reinforcement, cannot be loaded with torsion forces (Loughlan & Ahmed 2008). Fibre composites are generally anisotropic, brittle, have a low modulus and are highly dependent on the properties of its components matrix and fibre. The design of fibre composite structures is not only a shape or geometry design; the material itself should be included in the design process (Kim et al. 2011). Any design method for fibre composite structures should consider the fibre plies design level and the overall geometry level of the structure. Optimisation methods offer the advantage of solving the geometry and materials design issues simultaneously.

2.3 Experimental investigation of fibre composite structures

The experimental investigation is regarded as an important assessment for the design of composite structures. This section presents the available experimental studies in the civil engineering application of fibre composite beams and decks.

2.3.1 Fibre composite beam

Fibre composite girders have been used by civil engineers to replace traditional wood girder in old bridges. There are about 27,000 timber bridges in Australia. Most of them are 50 years old and have degraded due to age and environmental conditions (Crews et al. 2004). The Queensland Department of Transport and Main Roads recommended the replacement of these degraded bridge girders by new girders with the same stiffness. There are a few design requirements by the Queensland Department of Transport and Main Roads related to the stiffness of the new girder. The CEEFC has participated in the development of a new hybrid composite girder. The novel GFRP sandwich panel was used in the development of the hybrid girder. The cross sections and dimensions of the girder beam are shown in Figure 2.2(a) (Aravinthan 2009).

The design of fibre composite beams can have different configurations, either in the form of one pultruded section or in the form of a combination of different pultruded sections. Wagners CFT Company of Toowoomba/Queensland developed a glass fibre composite (GFRP) I-beam girder for the replacement of wood bridge girder. The fibre composite I-beam section is made from square pultrusion, plates and pultruded angles as shown in Figure 2.2(b). The experimental test showed that the failure moment is 20% higher than the required moment, but the stiffness is 7% less than the required (Kemp 2008). Those two different beams to be developed in stages of the design process based on the full scale experimental tests. These types of fibre composite girders require substantial research and development to satisfy the design requirement for environmental impact, long-term durability, load variation, cost, and dynamic response.

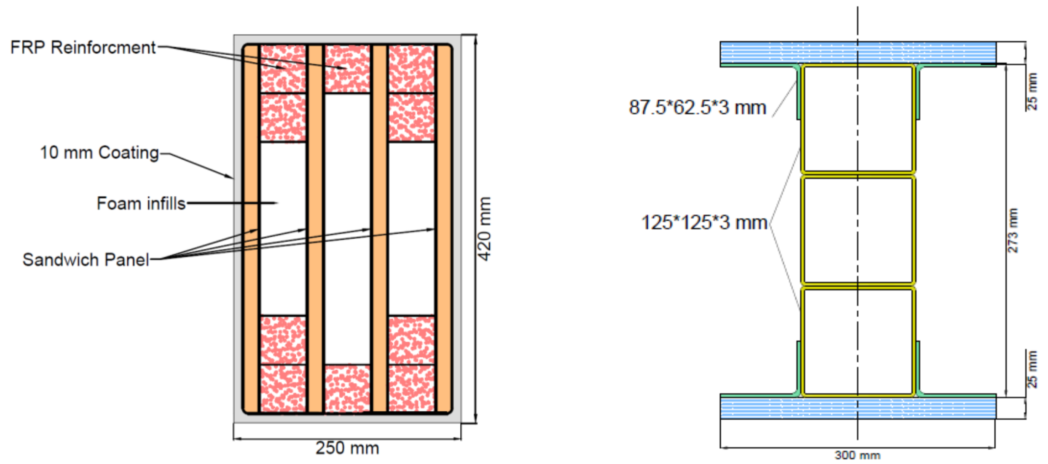

(a) Beam girder using sandwich panels.   (b) Beam girder using pultruded sections.

Figure 2.2 FRP girders for bridge applications in Australia (Aravinthan 2008, Aravinthan 2009).

A 900 mm (36-inch) double web FRP beam was developed at Virginia Tech as shown in Figure 2.3(a) (Schniepp et al. 2002). Extensive static testing and analysis was done on the double beam web (DWB). The objective of the study was to provide data for the design guide of the FRP DWB girder. The bending stiffness, shear stiffness, failure mode, and ultimate capacity were the main parameters conducted. Measuring and calculation of shear stiffness was the most challenge design parameter. An experimental investigation was done on the beam girder made from adhesively bonded fibre glass pultruded sections and sandwich panels as shown in Figure 2.3(b) (Keller et al. 2004). The girder length was 20 m and the cross section was made of sandwich panels web and pultruded sections flange. The experimental and analytical modelling found that beam of 20 m length is possible with this concept. This type of girder also can be used in pedestrian bridge and high-rise building applications.

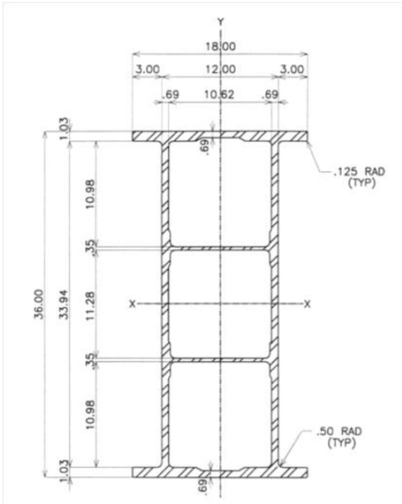

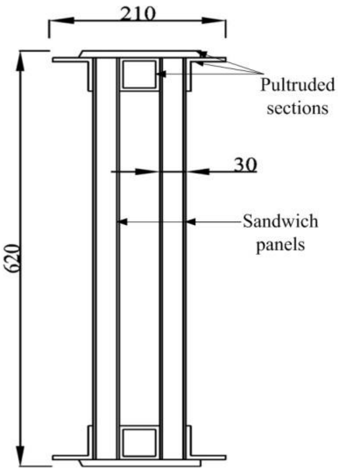

(a) FRP double web girder.

(b) Girder using pultruded sections and sandwich panels.

Figure 2.3 FRP composite girders.

The novel GFRP sandwich beam has been studied by Manalo et al. (2010b; 2010c; 2010d) for possible application as a railway sleeper. These investigations were carried out on the fixed beam span, and were focused on using edgewise and flatwise concepts as shown in Figure 2.4(a). However, these studies did not investigate the beam behaviour under a combined action of shear and flexural loading. The recommendation was made that the novel beam required an investigation for effect of combined shear and flexure in different shear-span to depth ratios (Manalo 2011). The application of the novel glue-laminated GFRP sandwich beam was extended for full-scale railway sleepers as shown in Figure 2.4(b) (Manalo 2011).

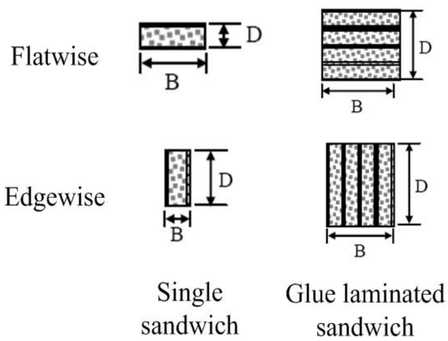

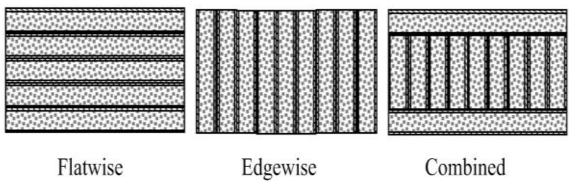

(a) Sandwich beam.

(b) Full scale railway sleeper cross sections.

Figure 2.4 Novel GFRP sandwich beam applications.

2.3.2 Fibre composite deck

Many countries have started to use fibre composite materials for bridge decks instead of conventional concrete, steel, and wood materials. The conventional decks showed degradation under the effects of cyclic loading and the environmental action (O'Connor 2008). Gan et al. (1999) evaluated available cross sections for the fibre composite deck. The research considered seven applicable composite deck sections as shown in Figure 2.5. The optimum section was found to be a triangular. This type of section enhanced both the global and local stiffness and improved buckling resistance. Jeong et al. (2007) on the other hand, tried to find the safety factor for fibre composite pultruded deck materials by static and fatigue tests to provide a comprehensive data for designers and engineers. The experimental test was conducted by applying a load equivalent to DB-24 truckload which provided a maximum load of 117.6 kN. The test showed that ultimate failure load was 431.2 kN with a service deflection of 1.74 mm less than span/800 and the strain is 13% of the ultimate strain. Kumar et al. (2004) conducted an experimental study to investigate the behaviour of a composite bridge deck with dimensions of 9.144 m x 2.743 m. The deck was made of square pultruded glass and carbon fibre tubes with dimensions of 76.2 mm x 76.2 mm x 3 mm as shown in Figure 2.6. The first version of this deck had 8-pultrusion layers. The experimental test indicated that the 8-pultrusion layers deck was over designed. The final decision was made that the deck comprised of 7-pultrusion layers in an I-beam configuration was able to carry the external load. The load of which the deck failed was about 155 kN, which was four times the design load of H-20 (35.587 kN).

Roy et al. (2005) started to develop a new bridge deck made from GFRP to replace an old timber deck. This deck was made of top and bottom layers of glass fibre with an intervening corrugated web as shown in Figure 2.7. The voids of the deck were filled with a structural foam (E=14.7 MPa). The final deck was optimised manually during the analysis to get good section parameters value. Tests revealed that such deck can carry twice the design load but the deflection was higher than the allowable limit span/400. CEEFC developed a new fibre composite bridge deck as shown in Figure 2.8. The new deck was made of pultruded sections with transverse post tension steel bars. Experimental verification was conducted on a small prototype with a 5 m span (Van-Erp et al. 2005).

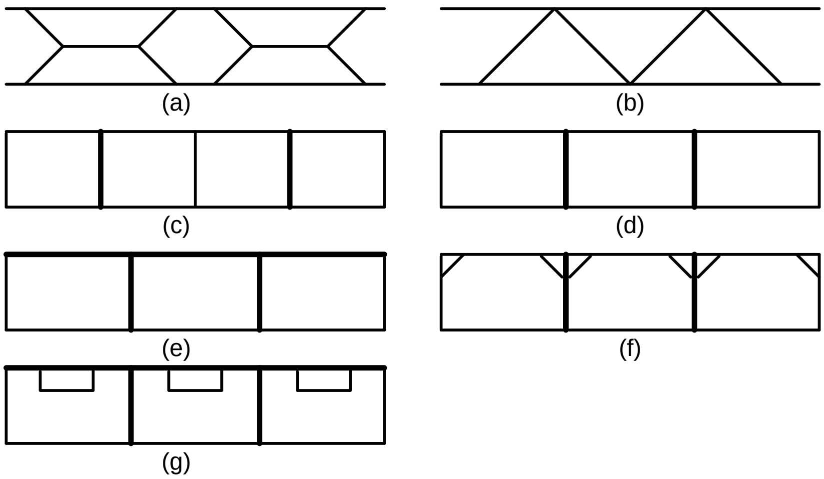

Figure 2.5 FRP deck sections (Gan et al. 1999).

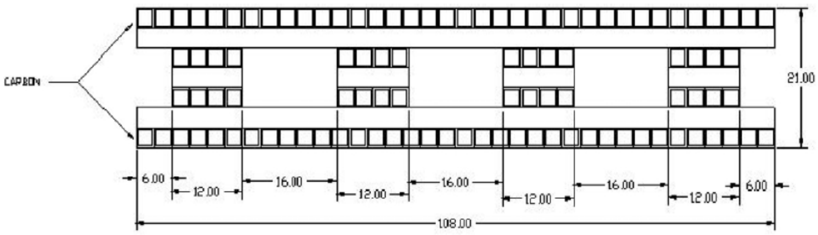

Figure 2.6 Assembly bridge deck (Kumar et al. 2004).

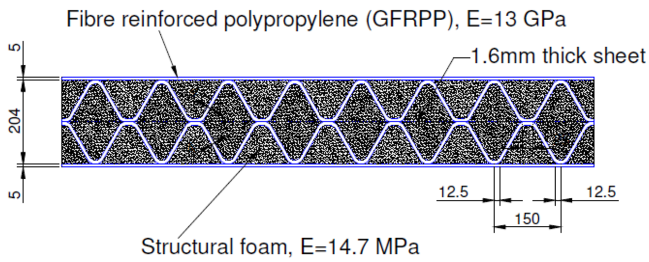

Figure 2.7 Bridge deck (Roy et al. 2005).

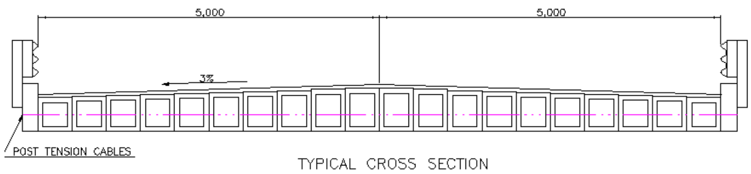

Figure 2.8 Bridge deck (Van-Erp et al. 2005).

An experimental investigation was conducted by Zi et al. (2008) on the effect of foam fill on the behaviour of rectangular GFRP bridge deck section as shown in Figure 2.9(a). It was found that using low modulus polyurethane foam enhances the structural behaviour in the transverse direction. Design and experimental investigations were conducted on the development of ASSET FRP bridge deck unit as shown in Figure 2.9(b) (Luke et al. 2002). This deck was used in the construction of West Mill Bridge in the UK. A similar deck system was used for the Friedberg Bridge in Germany (Knippers & Gabler 2006). It was tested experimentally for the material's mechanical properties and composite action with steel girder. They concluded that further investigation was required to cover the shortage of comprehensive design guidelines.

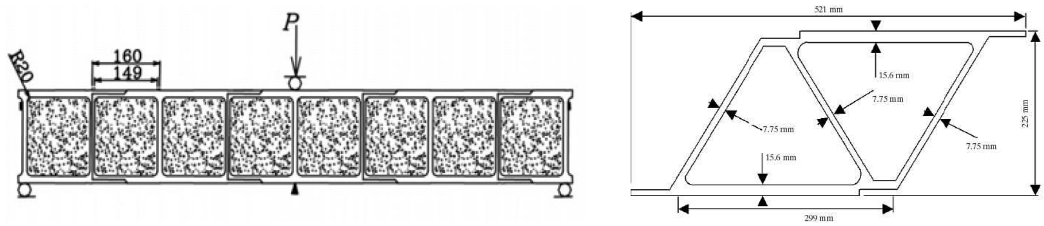

(a) Rectangular pultruded FRP unit (b) Triangular pultruded FRP unit

Figure 2.9 FRP deck units.

The novel GFRP sandwich panel was used in the construction of the floors and bridge decks as described in Chapter 1, and shown in Figure 1.4. Islam and Aravinthan (2010) studied the behaviour of the novel GFRP sandwich slab under point and distributed loading. Failure was noticed using the point load test as shown in Figure 2.10(a). However, due to the large deformation the timber joists buckled before the slab failure in the distributed load test as shown in Figure 2.10(b).

Experimental investigations are useful because they investigate the real behaviour of full scale structures. However, in real-life applications fibre composite structures have many aspects that cannot be covered by numerical simulation such as differences in fabrication quality, the effect of gluing on different parts of the structure, boundary conditions, and contact surfaces. On the other hand, there are some disadvantages associated with experimental investigations such as the high cost, longer time taken for testing, and the need for experimental test facilities. These tend to limit the number of test iterations to one or two, which is not sufficient to obtain an optimum design. In addition, it can be seen from the literature review that in some experimental investigations the structural design constraints for deflection criteria could not be met, resulting in non-compliance structure.

(a) Point load (b) Distributed load

Figure 2.10 Novel GFRP slab test.

2.4 Analytical methods of fibre composite structure

Fibre composite materials are anisotropic and its analysis different to the analysis of isotropic materials such as steel and concrete. In general, three different approaches were used in the modelling of fibre composite materials, the micro-level approach, in which the fibre and matrix simulated separately, the meso-level in which the layers are modelled, and finally, the macro-level, in which the performance of the complete homogenised laminated is considered. The meso-level approach was recommended because it provided a uniform way to model the fibre laminated composite. It also reduces the number of elements required compared to micro-level analysis (Linde et al. 2004). It is the simplest and most popular model for simulation of composite layers, and is sometimes called the Equivalent Single Layer (ESL) (Bosia et al. 2002).

Most of the analysis studies seek a fundamental understanding of the fibre composite materials behaviour using different materials models and formulations (Ochoa & Reddy 1992). Governing equations were used to analyse the laminated beam by assuming zero in-plane forces. Classical laminated plate theory (CLPT) is the most commonly used theory to describe the deformation behaviour of composite laminates. The formulation is based on the Kirchhoff theory, where normal plane remains straight and perpendicular to the mid surface after deformation (Reddy 2004). In the case of thick composites the shear deformation becomes significant and it cannot be ignored. Therefore, the Kirchhoff hypothesis requires a relaxation. This was achieved by assuming that the transverse normal is no longer perpendicular to the mid surface.

FEA method is considered a powerful numerical method in solving solid and structural mechanics problems (Ochoa & Reddy 1992). In the FEA method a complex structure can be divided into a series of small elements. In addition, complex properties and boundary conditions can be specified within each element. Laminated composite shell structures were used in the simulation of fibre composite structures (Noor et al. 1996). The layered plane stress shell elements allows to analyse different plies in different directions (Roy et al. 2010). However, the shell element is unsuitable for the simulation of thick composites, especially when the shear and normal stresses become dominant. Therefore, a three dimensional (3D) solid element was developed to simulate multi-layer composite materials (ABAQUS 2008). The 3D solid element allows the consideration of different layer thicknesses and different layer orientations within the overall element thickness (Donadon et al. 2009).

The shell element was used in the FE simulation of FRP composite beams, and plates (Huang 2007). On the other hand, a 3D continuum element was used for the simulation of the beams, shells, and sandwich structures (Sze 2002). Combined plane stress and 3D elements have also been used in the simulation of FRP composite structures (Altenbach 1998). The combination of plane stress and 3D element was used in the simulation of the sandwich structure (Mines & Alias 2002; Yoon et al. 2002). Whereas, the plane stress element was used for the skins and the 3D solid element was used for the core part.

Because fibre composite structures can accumulate damage before final failure, it is necessary to use the non-linear behaviour of quasi-brittle material to calculate the damage tolerance of the structure (Liu & Zheng 2010). There are few models that simulate FRP composite failure. These models are mainly based on the available "apparent" material data for lamina level. The theoretical plies thicknesses are calculated using fibre to matrix mixed ratio rules. Accordingly, the failure of composites can be determined based on the stress or strain components as follows (Knight Jr 2006; Sun et al. 1996):

- *Maximum stress criteria*: A non-interacting model, where a single stress component is compared to the ultimate strength of the composite.
- *Maximum strain criteria*: A non-interacting model, where a single strain component is compared to the ultimate strain of the composite.
- *Tsai-Wu failure polynomial*: An interaction model, where all stress components are used simultaneously to identified the material failure.
- *Hashin failure criteria*: An interaction model, where more than one single stress component is used to assess the material failure.

However, there are more failure models for FRP composite materials such as the Hill-Tsai and Hashin-Rotem models, which have been used for failure prediction (Hashin & Rotem 1973; Sun et al. 1996). Different studied conducted to justify the advantages and disadvantages of different failure models (Liu & Zheng 2010; Maimí et al. 2007; Matthews & Camanho 1999). In general, the conclusions were that maximum stress, maximum strain, and Hashin-Rotem models are suitable for composite with fibre dominance. Other failure criteria are suitable for the matrix dominant composite.

Analytical and numerical analyses methods have been combined with the optimisation methods to design FRP composite structures. Bending theory was used with some assumptions to optimise the FRP sandwich beams (Farkas & Jarmari 1998). The FE analysis method is the most popular analytical method used for the optimisation of the composite structures and it is suitable to deal with different objective functions (Fam & Son 2008; Procházka et al. 2009). Shell element and 3D brick element are used in the analysis of the fibre composite structures. The shell element allows considering the fibre layers in the model within the element thickness (Farshi & Rabiei 2007; Lund 2009). The 3D brick element allows the use of the incompatible mode and the layered solid section in the calculation of the flexural response of the element (Rahul et al. 2005).

2.5 Optimisation methods in fibre composite structural design

Optimising the design of civil engineering structures was done to meet specific design requirements or constraints for the structure over its design life. This section reviews the most popular optimisation methods used in the design of fibre composite structures for civil engineering applications.

2.5.1 Design Sensitivity Analysis (DSA)

Design sensitivity analysis (DSA) method has been used in the last two decades in automotive optimisation due to the increase of hardware capability. The DSA method requires the calculation of the gradient of the objective and the constraints with respect to the design variables. There are two methods used to find the variation of the objective function and the constraints; the finite difference method and the response surface method (RSM). The simple form of the finite difference for function *f(x)* and *x* variable is (Chiandussi et al. 1998):

$$\frac{df}{dx} \approx \frac{\Delta f}{\Delta x} = \frac{[f(x+\Delta x)-f(x)]}{\Delta x} \qquad 2.3$$

The RSM is a statistical method which depends on an approximation function to simulate the response of the variables. The relation between variable *x* and the real response ψ is:

$$\psi=f(x) \qquad 2.4$$

$$g(\psi)=f(x)+\zeta \qquad 2.5$$

where $g(\psi)$ is an estimate of the real response and ζ is the error.

Optimum design of FRP composite shell has been studied by using DSA method. Analytical, semi-analytical, and finite difference methods were used in the analysis. The investigators concluded that different optimisation objectives could be used with DSA method. They also found that using a higher order discrete model could enhance the accuracy (Correia et al. 1997; Mota-Soares et al. 1995). Wu and Burgueño (2006) studied the optimum shape and stacking sequence design of FRP composite shells using FEA and DSA. Lindgaard and Lund (2010) studied the non-linear buckling optimisation of fibre composite shells. The bucking behaviour was improved by using DSA method.

The FRP composite box beam was optimised to minimize the weight of the structure by Cardoso et al. (2002). The design constraints were stress, displacement, critical load, and natural frequency. Their optimisation variables were layer thicknesses and layer orientations of the rectangular beam sections. Geometrical non-linearity have been included in the design and optimisation of composite beam dome and in one study the optimum size of the domes was found to be 42.23 m in span and 6.1 m height (Valido & Cardoso 2003).

2.5.2 Genetic Algorithm (GA)

In the last few decades, Genetic Algorithms (GA) have been used in the structural design optimisation due to their capability to deal with complicated and large variable problems. The fundamental theorem of the genetic algorithm was developed by Holland (Burns 2002; Tabakov & Walker 2010). GA used to optimise the FRP composite plate as shown in Figure 2.11, and the objective was minimizing the weight and the cost of FRP plate. Two types of external load were applied, impact load (Rahul et al. 2005) and static load (Gillet et al. 2010). The optimisation of composite structures using parallel GA gives a relatively good convergence with low process time. In addition, the quality of the result depends on the size of the problem. He and Aref (2003) used GA to find the optimum selection of design parameters such as the number of stiffeners, layers thickness, and the orientation of outer skin layers of the fibre composite bridge deck, as shown in Figure 2.12. The weight decreased by 25% from the initial design weight, and the GA method was suitable method for handling this type of problem because its ability to accommodate both discrete and continuous design variables.

Kim et al. (2005) studied the optimum shape of hollow pultrusion fibre composite bridge deck subjected to a truck load DB-24. The objective function was the cost minimization, and the conclusion was made that the trapezoidal shape was the optimum shape for hollow deck bridge as shown in Figure 2.13. Their analysis showed that the sensitivity of deflection and buckling to the deck dimensions changing was higher than the material variables changing. However, the estimated cost of the optimised GFRP deck was twice as expensive when compared to a conventional concrete deck. The same authors (Kim et al. 2009) presented an optimisation design for a temporary FRP bridge deck. The optimum deck shape is shown in Figure 2.14.

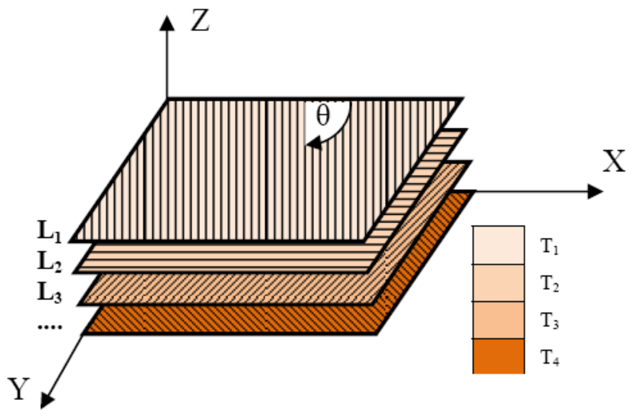

Figure 2.11 Composite laminate orientations.

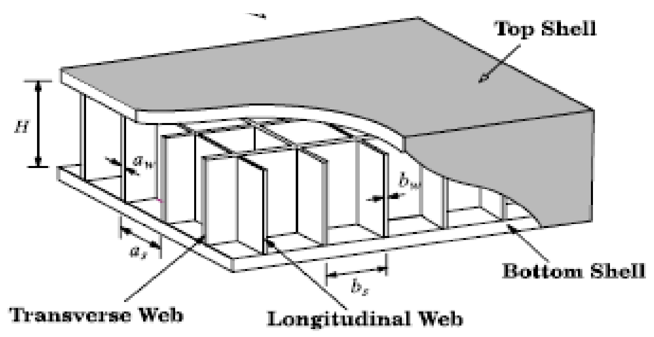

Figure 2.12 Sandwich bridge deck (He & Aref 2003).

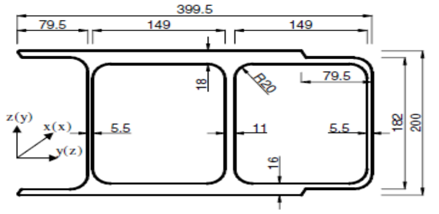

Figure 2.13 FRP deck (Kim et al. 2005).

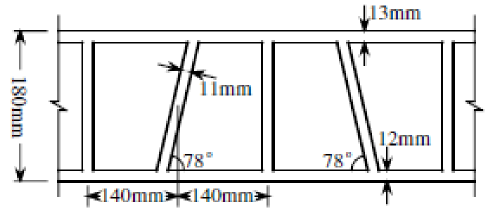

Figure 2.14 FRP deck (Kim et al. 2009).

2.5.3 Simulating Annealing method (SA)

In structural design, Simulating Annealing (SA) method was used to find the optimum design of fibre composite structures as an efficient method to solve problems with multiple-global optima (Hasançebi et al. 2010). Erdal and Sonmez (2005) discussed the optimum design of composite layer orientations in order to maximize the buckling load capacity of the laminated plate by using a direct SA algorithm. The optimum design enhanced the buckling load factor from 3973 to 4123 for the plate aspect ratio equal to one. Rao et al. (2002) optimised composite plate design in order to maximize the natural frequency as a dynamic consideration by using the SA method. They found that the SA method is a less expensive method to deal with complicated design optimisation, especially when the design considers the layup optimisation as well as the ply orientations. Ertas and Sonmez (2010) used the SA method to design fibre composite structure for maximum fatigue life. They found that increasing the number of fibre angles improved the fatigue life of the structure.

2.5.4 Reliability Based Design Optimisation (RBDO)

The Reliability-Based Design Optimisation (RBDO) method is different to other optimisation methods and it is called non-deterministic method or probabilistic method. The objective function is limited by probabilistic constraints instead of conventional deterministic constraints. It considers the uncertainty of the optimisation design in fibre composite structural problem. The mathematical form of the RBDO is described below (Nguyen et al. 2010) :

find x

$$\text{minimizing} \qquad f(x) \tag{2.6}$$

$$\text{subject to constraints} \quad \bar{P}(g_i(x) \leq 0 - \Phi(-\beta_i) \leq 0 \; (i = 1,2, \ldots, j) \tag{2.7}$$

$$x_{lower} \leq x \leq x_{upper} \tag{2.8}$$

where x is any design variable, $\bar{P}$ is the probability, Φ is the integral of the (0,1) standardized normal distribution and $\boldsymbol{\beta}_i$ is the so-called safety - index.

Since the application of FRP composite structures are new, the ultimate load and risk assessment for optimum design have become a critical consideration for engineers. Cost limits the use of full-scale testing, and there are not enough results for construction of probability distributions. Probability design methods have a research target to fill the design gap in the new technology. Thompson et al. (2006) used RBDO to design a FRP composite bridge deck panel. The objective function was to minimize the weight of the panel. Two types of constraints are used in the design, deterministic stress constraints and two probabilistic deflection constrains. The design optimisation achieved a 55% weight savings compared to the initial design. António and Hoffbauer (2009) carried out research on the optimisation of a FRP composite shallow shell reinforced with a composite beam which included a geometrical non-linearity. The objective function was weight minimization. The RDBO included the probabilistic stress, deflection and buckling constraints. They used the trade-off between the performance and the robustness in the decision making.

2.5.5 Particle Swarm Optimisation Algorithm (PSOA)

Particle Swarm Optimisation Algorithm (PSOA) method is an algorithm, which is based on swarm intelligence (Lee et al. 2012). It was developed from a research on the bird and fish flock movement behaviour. PSOA consists of group of particles and the position of each particle is affected by the surrounding most optimal position during its movement. The speed and position of each particle changes according to this equation for one-dimension (Parsopoulos & Vrahatis 2005):

$$v_{i+1} = \dot{a} \,.\, v_i + \bar{b}_1 \,.\, r_1(p_1 - \bar{x}_i) + \bar{b}_2 \,.\, r_2(p_2 - \bar{x}_i) \qquad 2.9$$

$$\bar{x}_{i+1} = \bar{c} \,.\, \bar{x}_i + \bar{d} \,.\, v_{i+1} \qquad 2.10$$

where v is the velocity, $\dot{a}$ is the momentum, i is the iteration, $\bar{b}$ is the strength of attraction coefficient, $\bar{x}$ is the particle position, and $\bar{c}$ and $\bar{d}$ are the position factors at velocity v_{k+1}.

Optimum design of a sandwich panel structure was conducted by Kovács et al. (2004) as shown in Figure 2.15. It was made of carbon fibre reinforced plastic polymer (CFRP) plate and aluminium sections. The PSOA was used to find the minimum cost and maximum stiffness of the structure. The CFRP was optimised by finding the layers' optimum orientations. The aluminium section was optimised for the wall thickness, and length of edges. Design constraints were the maximum allowable deflection and buckling of CFRP plate and aluminium stiffeners. Stresses in the CFRP and aluminium were included as well. The major finding was the CFRP plates increased the damping capacity of the aluminium section and the optimum design with plies oreintation $0^o/90^o$. FRP composite box beam was studied using PSOA method under single objective optimisation function (Kathiravan & Ganguli 2007) and multi-objective optimisation function (Suresh et al. 2007). They found that the box beam walls with different orientations had a better strength than the box walls with the same fibre orientations. Naik et al. (2011) used a Vector Evaluated Particle Swarm Optimisation (VEPSO) method to find the minimum weight of the composite structure under different failure criteria such as the Tsai-Wu, maximum stress and failure mechanism based failure criteria. Comparison between these criteria showed that the failure mechanism produced better results. The objective achieved a specific stiffness and maximum elastic coupling. The optimisation solution was compared with GA, and it showed a less computational time than GA.

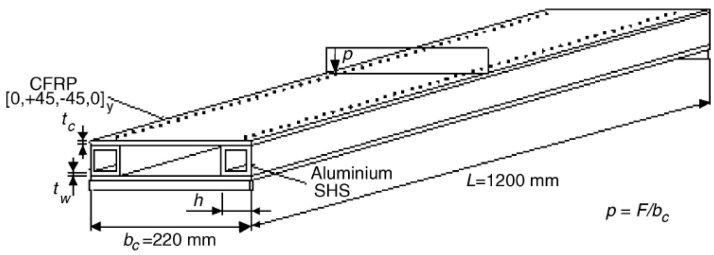

Figure 2.15 Panel details (Kovács et al. 2004).

2.5.6 Ant Colony Optimisation (ACO)

In each social insect colony, there is a system or plan to follow by all individuals and the overall groups seem to be well organized. This algorithm depends on the swarm intelligence to solve complicated problems. In the solution, the real ants try to find the shortest path from the nest to reach food. The procedure of the ACO is different to the GA, where in the ACO the ant tries to construct the solution step by step. Whereas, the GA method builds the coded solution candidate, and then does the evaluation. In ACO, each ant decides the direction of the next step. The state transition rule in ACO can be described as (Rao 2009):

$$l_{k+1} = \begin{cases} \arg max\{[\tilde{\tau}(l_k, l_i][l_k, l_i]^{\bar{\beta}}] & if\ q \leq q_o \\ \bar{P}\left(\frac{[\tilde{\tau}(l_k,l_i][l_k,l_i]^{\bar{\beta}}}{\sum[\tilde{\tau}(l_k,l_i][l_k,l_i]^{\bar{\beta}}}\right) & if\ q > q_o \end{cases} \quad 2.11$$

where $\tilde{\tau}$ is the pheromone, l_k is the latest chosen element, l_i belongs to the list of all possible candidatures, $\bar{\beta}$ is a parameter, $\bar{P}$ is the probability, q is a randomly generated number in the domain [0,1], and q_o is a constant parameter.

ACO has been used successfully in the optimisation of fibre composite structure. Abachizadeh and Tahani (2009) used ACO to maximize the fundamental frequency and minimize the cost of symmetric hybrid laminates. The sample was made of two graphite/epoxy stiff skins and a glass/epoxy core. Omkar et al. (2011) optimised FRP composite plate by using multi-objective ACO. Their objective was to achieve certain strength with minimizing the weight and the cost of the plate. The variables were ply numbers, stacking sequence and thicknesses. The ACO performance was compared with the GA, PSO and Artificial Immune System (AIS) performances and showed a good improvement. Wang et al. (2010) presented an optimal design of a composite stiffened panel with T-shape stiffeners. ACO and a finite strip method were used in the study to maximize panel buckling.

2.5.7 Multi-objective Robust Design Optimisation (MRDO)

Li et al. (2005) presented a new Robust Multi-Objective Genetic Algorithm (RMOGA) method. The advantages of this method are: i) it measures the optimum solution performances and ii) measures the robustness index. Messac and Yahaya (2002) developed a MRDO method under the consideration of physical meaningful term. The design showed that the MRDO allowed considering parameters which was not part of the normal optimisation process. The MRDO is different from the traditional optimisation method. The traditional optimisation methods provide a poor off-design solution and it becomes very critical to ensure the design requirements. The MRDO is an efficient tool for considering variation of input parameters in a range of circumstances. The simplest form of MRDO problem is (Li et al. 2005):

$$min_x \ f_v \ (f_2, f_2, \dots \dots ., f_m \ , g_1, \dots ., g_G) \qquad 2.12$$

$$max_x \ \eta = \frac{R}{R_E} \qquad 2.13$$

$$x^{lower} \leq x \leq x^{upper} \qquad 2.14$$

The f_v is the fitness value and is a function of the design objectives *(f_1,…, f_m)*, and constraints *(g1,…., g_G)*. η is the robust index, $\dot{R}$ is the optimum solution and R_E is the exterior radius of the normalized tolerance.

Application of the MRDO is very important in the design of fibre composite structures because it considers the uncertainty due to material properties and manufacturing processes. The uncertainty of the design variables and constraints can be included. MRDO enhances the design results by reducing the standard deviation of the design objectives. Choi et al. (2008) used MRDO to minimize the residual stresses in FRP composite plate. These stresses are the major cause of bond failure. Robust optimisation resulted in a reduction in the mean and standard deviation of the residual stresses thereby enhancing FRP plate production. Doltsinis et al. (2005) studied the design of non-linear structures by using MRDO. They expected to find design uncertainty or fluctuation of the material, fabrication, and load, which affected the design result. Optimisation of the structure using deterministic structural optimisation might become unreliable due to the deviation between the actual structure and the nominal one. The conclusion was that MRDO helped in reducing the structural performance sensitivity with respect to the design variables and noise parameters.

2.5.8 Other optimisation methods

There are several other optimisation methods that have been used in the design of fibre composite structures. Farkas and Jarmai (1998) presented an optimisation study to select a sandwich beam by using Rosenbrock's Hillclimb method. The expected beam should have a good damping capacity and low deflection. The optimum composite sandwich beam consisted of five layers consisting of a double box beam, rubber layer and two layers of FRP as shown in Figure 2.16. The objective of adding FRP layers was to increase the stiffness of the beam and to reduce the deflection. Optimisation focused on minimising the cost of the three sandwich beams. It was concluded that the five layers composite beam was the best one due to its high stiffness and its damping ratio.

Fam and Son (2008) presented a parametric study in the design of concrete-filled fibre composite poles and the problem was shown in Figure 2.17. Lund (2009) used Discrete Material Optimisation to design a multi-layered fibre composite shell. The conclusion was made that the middle layers required only ±45^{o} fibre in the corners to carry the shear forces and the top and bottom layers have fibre in different directions as shown in Figure 2.18. Ghiasi et al. (2010; 2009) presented a comparison study of the optimisation methods used in the constant and variable stiffness design of fibre composite structures. This work indicated that the Gradient - based methods are the best for the constant stiffness design. Furthermore, the optimality criterion and topology methods are the best for variable stiffness design.

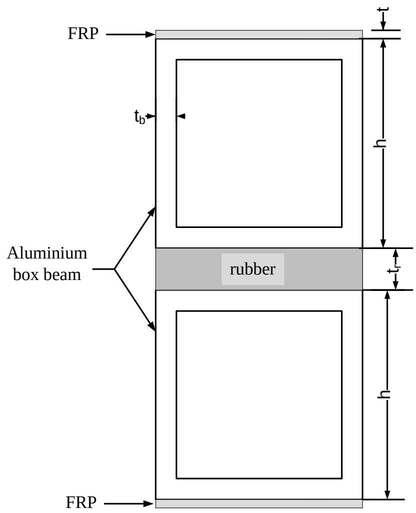

Figure 2.16 Five layers beam.

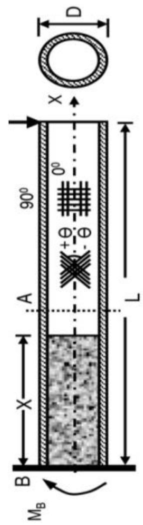

Figure 2.17 FRP poles.

(a) Top layer

(b) Middle layer

Figure 2.18 Fibre distributions (Lund 2009).

2.5.9 A comparison of optimisation methods

Various design optimization methods have been discussed in the previous sections. Many benefits are achieved by using different design methods and procedures. The optimisation formulation of composite structures leads to non-linear functions of the design variables such as number of plies, lamina thickness and fibre orientations. The DSA method relies on the gradient derivative to formulate the optimisation process, and it can optimise both discrete and continuous variables problems. The DSA was applied to geometry and lamina design problems. The DSA methods cannot solve multi-objective optimisation problem, but it can be used in the decision making of multi-objective optimisation as mentioned by Avila et al. (2006). Recently, engineering applications have shown increases interest in solving optimisation problems with multi-objective due to the multiple conflicting objectives.

SA was used on the fibre composite structures for multi-objective optimisation. The SA method showed a high ability to deal with non-linear optimisation problems. It is regarded as a general solution method that can be applied to a large number of problems. However, SA results are not able to produce the same results with another run and it might go for another solution. It is effective in achieving local optimum results, which are dependent on the initial configuration.

Researchers have used the GA method in several applications in FRP composite structural optimisation including multi-objective optimisation. GA is a global optimisation method, and it can work in a wide range of problems. In addition, it does not need to find the derivatives, and it is easy to parallelize. GA can store and use the information from previous steps. The disadvantage of GA is that it is very slow and cannot always find the exact solution, but it can find the best solution among populations.

RBDO is regarded as an expensive method in computational work because it includes evaluating more functions than corresponding deterministic optimisation methods. Using RBDO gives a reliable optimisation result because it considers the randomness of the problem variables and constraints. RBDO has a probabilistic distribution and this may lead to substantial errors in the reliability analysis. In this sense, RBDO might be less useful on the practical side, if the information about the random uncertainty is not available or not sufficient to authorize a reliability analysis of the problem.

PSOA is an evolutionary global algorithm that has been used recently for the optimisation of fibre composite structures. PSOA can solve the continuous global optimisation problem with a non-linear objective function. PSOA is quite similar to GA with a randomly generated population but GA is more popular due to its simplicity. The difference between PSOA and GA is that PSOA does not need complicated encoding and decoding and can work directly with real numbers. Moreover, both PSOA and GA start with randomly generated populations, evaluate the populations for fitness values, update the population and use random methods to search for the optimal solution. The main disadvantage of PSOA method is that the particles may follow wider cycles and may not converge when the individual best performance of the particles group is far from the local particles in the same swarm. In addition, when the inertia weight is decreased, the ability of the swarm to search for new areas becomes low because it is unable to create exploration mode.

ACO is regarded as a constructive search algorithm suited to deal with some complicated problems such as the Travelling Salesman problem. In addition, ACO has the advantage of giving positive and rapid feedback for the food solution. It can be used in dynamic applications. In contrast, there are some disadvantages of using ACO such as the probability distribution changes with each iteration, in spite of convergence being guaranteed, the time of convergence is uncertain and the theoretical analysis is difficult.

MRDO has been developed to optimise the products by reducing the effects of uncontrollable variation on the design parts. These uncontrollable variations can significantly reduce the design quality. Therefore, the robust solution is very important method to avoid small deviations in uncontrolled parameters. There is a trade-off between accuracy and efficiency and MRDO provides a good balance between these two. The disadvantage of robust design is that the problem size becomes large quickly, and it needs a long processing time to find the solution. MRDO optimisation can provide an efficient design procedure for complicated multi-objective problems by considering the types of controlled and uncontrolled variables. It relies on probabilities to improve design robustness and provides an attractive design framework of robustness. Design of fibre composite structures can use many variables eligible to be included in the design process. These variables come from the natural anisotropic of the fibre composite, different martials could be used, the fibre volume ratio is important, fibre orientations, geometry variable, sequence of layers, load position, load percentage at the service state, manufacturing quality and environmental effects. All these variables might affect the design of fibre composite structures. Under the consideration of multi-objective optimisation and the controlled and uncontrolled design variables of fibre composite structures, the MRDO method might represent an appropriate choice to design a complicated non linear optimisation problem. Finally, a comparison of the reviewed optimisation methods is shown in Table 2.1. This table compares the differences between each optimisation method according to its ability to solve the optimisation problems. The methods ranking is classified according to four categories such as multi-objective, probability, uncontrolled parameter, and free derivative. As indicated in Table 2.1, all the reviewed methods are able to solve the multi-objective optimisation except DSA method. In addition, the GA, SA, PSOA, ACO and MRDO methods do not require the derivative of the objective function, while the DSA and RBDO methods require the derivative of the objective function.

Table 2.1 Comparison of the optimisation methods

Method	Objective	Probability	Uncontrolled parameters	Free derivative	Solution cost	Optimum solution remark	Overall ranking
DSA	Single	x	x	x	Moderate	Discrete and continuous variables	Low
GA	Multi-objective	√	x	√	Low in parallel optimisation	Global	High
SA	Multi-objective	√	x	√	Low	Multiple global optimum	Moderate
RBDO	Multi-objective	√	x	x	High	Convergence difficulties	Moderate
PSOA	Multi-objective	x	x	√	Less than GA for single objective	-Global -Convergence difficulties	High
ACO	Multi-objective	√	x	√	Moderate	Good performance	Moderate
MRDO	Multi-objective	√	√	√	High	Enhance the design objectives	High

2.6 Proposed optimisation approach for civil infrastructures

The previous sections reviewed various optimisation methods and the design objectives associated with. The selected design optimisation method might be the right choice to find an economic, light weight and serviceable fibre composite structure. But in some of the studies the designer did not adopt the guidelines in their actual case study in the form of dimensions, external applied load, and serviceability requirements. Civil engineering structural design requires special constraints and limitations in the design compared to other structures such as automobiles and aircraft. These requirements focus on the service load level of the structure. In addition, the literature review showed that there is no limitation for the stresses at the service load level. Several structural design standards give some recommendations for the external applied service load and allowable deflection. Such recommendations depend on the type of structural materials. For fibre composite structures, the only available guideline is EUROCOMP which recommends allowable deflection, allowable stresses and a safety factor of some structural applications (Clarke 1996).

The design optimisation of fibre composite structures is important to get an economical and safe structure. To achieve this objective, this methodology suggests an optimisation procedure that links different design steps so as to achieve an optimum design. These steps are, experimental material testing, FEA, design codes and standards, and optimisation methods. Figure 2.19 shows the proposed optimisation methodology to address the shortcomings of the current optimisation procedures. The suggested methodology focuses on different parts of the structural design process. Initially, experimental investigation will be carried out on the available FRP material to find the basic design data such as strength, strain, modulus of elasticity, density, and failure mode. Then, the behaviour of the structural elements such as beam and plate made from this material will be investigated. Thirdly, FE method will be employed to simulate the tested FRP composite element. The major part of the simulation is to select the most appropriate material model and type of element. A review of the available design standards, design guides, and previous structural data follows. This will identify the most suitable and critical design constraints. The design process should also satisfy the recommendation of the standards with regard to dimensions, loads, allowable stresses and deflections. It is expected that the design simulation satisfies all the requirements, the results produced from the design optimisation will be more realistic and useful to the practicing engineers.

A certain type of GFRP sandwich structure will be selected for the design from the existing fibre composite materials. The design process started with the experimental investigation of behaviour of the existing GFRP sandwich beams and slabs. Then, it well be followed by the FE modelling and design optimisation.

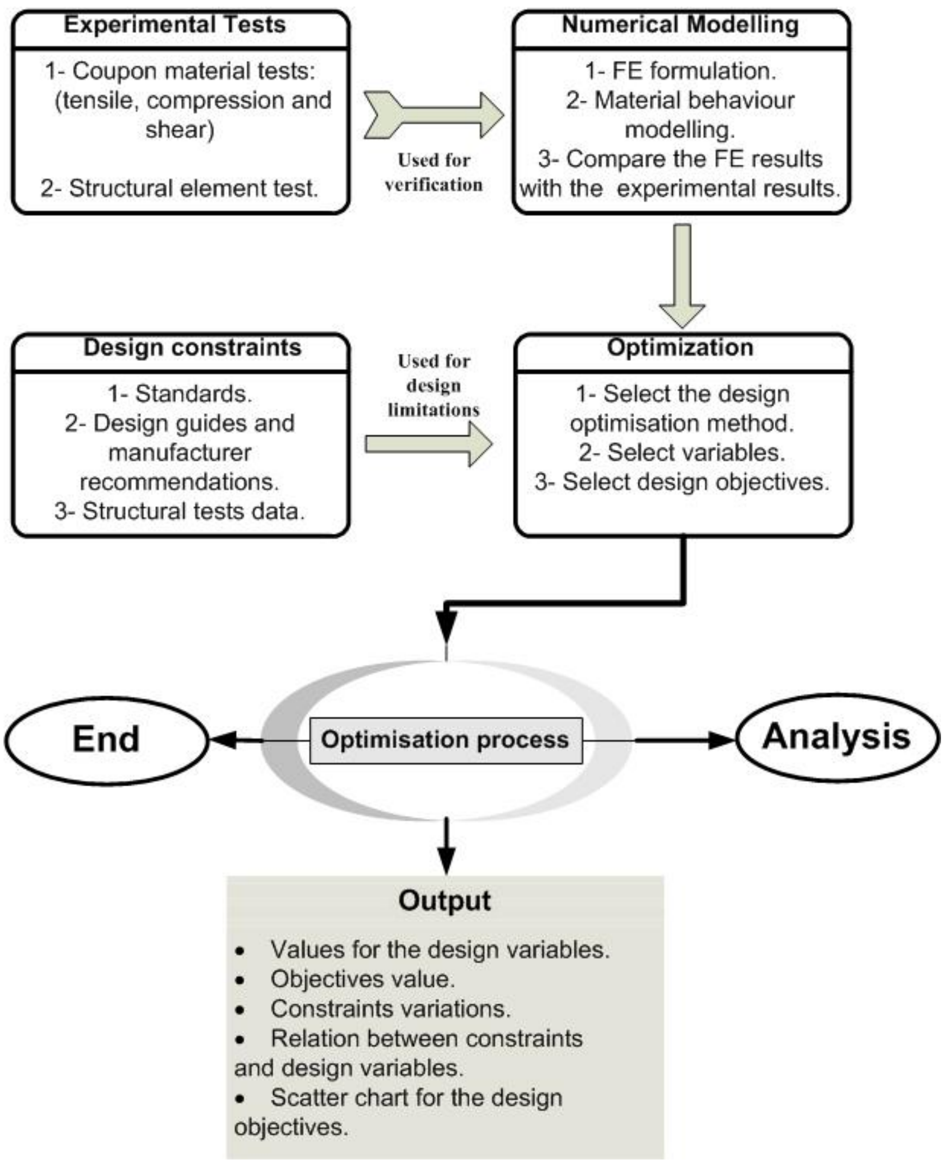

Figure 2.19 Proposed design optimisation methodology of FRP structures.

2.7 Chapter conclusions

The advantages of fibre composite structures make them attractive for use in the building and construction industries. Many full-scale fibre composite structures have been built over the last two decades. They are significantly lighter compared to the traditional structures. Experimental investigation and numerical analysis have been used to get an understanding of FRP structural behaviour and providing a sound base of information for designers. The FEA method was developed to achieve an acceptable analysis prediction. Two and three dimensional composite elements were implemented in the FE simulation.

The challenge was to optimise the fibre composite structures to achieve both structural performance and minimum cost. The application of optimisation methods offers many benefits in the design of fibre composite for civil engineering structures. The literature review found that the DSA method was used with single objective function and the GA, PSOA, ACO, RBDO, and MRDO methods were used when there are multiple objectives optimisation.

These methods have been applied successfully to different fibre composite structures such as plate, beam, box beam, sandwich panel, bridge girder, and bridge deck. In the multi-objective, GA optimisation methods were found to be more suitable for the design optimisation of FRP composite structures because it allows to consider variable and constraint uncertainty in the design. Considering the limitations of the existing optimisation procedures, a proposed methodology is developed for optimisation of civil infrastructure. Finally, it is important that the designers consider several objectives in their quest to find the optimum solution for civil engineering applications.

The literature review showed that the novel GFRP sandwich panel was used for beams and slabs applications. In addition, the literature showed that there is a lack of design studies to optimise the design of the novel GFRP sandwich panel in many applications. Present work has focused on slab and beam applications of the novel GFRP sandwich panel. The following chapters are focused on the experimental testing of the beams and slabs structures made from the novel GFRP sandwich panel, FE simulation, and design optimisation.

Chapter 3

Behaviour of single and glue laminated GFRP sandwich beams

3.1 Introduction

Fibre Reinforced Polymer (FRP) composite sandwich panels have been used extensively in different applications such as aerospace, automobile, and building construction (Hudson et al. 2010). Recently, an Australian manufacturer fabricated a new type of structural Glass Fibre Reinforced Polymer (GFRP) sandwich panel for use in the civil engineering applications such as slabs, pedestrian bridges, bridge girders and railway sleepers. These applications require the use of the panel in the form of single and glue laminated configurations. The sandwich panel is made from ECR-glass fibre for the top and bottom skins and a modified phenolic solid core material (Van-Erp et al. 2005).

There is an increasing interest in the application of the GFRP sandwich panels for structural beams. The main function of the top and bottom skin in a sandwich beam is to carry the normal stresses, while the core is used to connect the two faces and carries the shear force (Johannes et al. 2009). A single sandwich beam can be made by cutting a large panel into small strips, with each beam having a thickness equal to the original thickness of the sandwich panel. Large sandwich beam section can be produced by gluing layers of single sandwich beams together in different forms such as flatwise, edgewise and a combination of edgewise and flatwise. The concept of using smaller sections to produce a larger section has been used effectively in structural glue-laminated timber (Ayhan 2009). Glue laminated structural member is defined by the ASTM D3737 standard (ASTM 2008) as materials glued together from smaller pieces of any material with the fibres of all the laminations essentially parallel to the length of the member (Freas & Selbo 1954). This type of construction has been used in bridge construction for more than 30 years due to the benefits such as high strength, lower cost, ease of installation, and time savings (Lopez-Anido & Xu 2002).

The diminishing supply of good quality hardwood for structural applications has resulted in research on combining timber with fibre composite materials. The GFRP glue-laminated (glulam) timber beam has been taken a big attention from researchers investigating its mechanical properties. The GFRP associated with glulam beams provides a considerable gain in terms of strength and stiffness, and also modified the failure mode of the structural elements (Issa & Kmeid 2005). Different types of reinforcement could be used with the glue-laminated timber beams such as carbon and glass fibres (Lorenzis et al. 2005). Similarly, several studies were conducted to investigate the behaviour, mode of failure, and strength of fibre composite sandwich structures and to determine their potential use for structural beam applications (Chen et al. 2001; Konsta-Gdoutos & Gdoutos 2005; Petras & Sutcliffe 1999; Steeves & Fleck 2004; Tagarielli et al. 2004). These studies showed that the failure mode of sandwich beams depends on the core to skin thickness ratio, span length, skin to core density, and strength of the core and skins. However, the application of FRP sandwich panels in civil construction is very limited because the nature of core material of existing sandwich structures is not appropriate for structural applications.

Manalo et al. (2010b; 2010c; 2010d) conducted an experimental investigation to determine the behaviour of single and glue-laminated beams made from novel GFRP sandwich panels in pure shear and pure flexure loads. However, in real applications, the structural beams are normally subjected to combined shear and flexural loading conditions. Therefore, investigating the behaviour of the single and glue-laminated GFRP sandwich beams under combined shear and flexural loading is more realistic.

Published literature contains no record of investigations of the effect of beam shear span to depth ratio (a/d) and combined shear and flexural loading on the behaviour of the novel GFRP sandwich beams. In the following experiments, the variation in the beam geometry was obtained by glue laminating the panels into 2, 3, 4 and 5 layers in different spans length while maintaining the same width. The present chapter investigates the behaviour of the single and glue laminated GFRP sandwich beams under the combined shear and bending loading. The effects of variation of shear span to depth ratio on the behaviour of the beam under four-point static bending tests were determined.

3.2 Materials and specimens

The GFRP sandwich panel is being produced with a nominal thickness of 18 mm. The top and bottom skin is made of 3 mm thick, and the middle core is made of 12 mm thick. The materials and manufacturing details are described below:

3.2.1 GFRP skin and modified phenolic core

The details of the GFRP skin plies are shown in Figure 3.1. The GFRP skin is made from 6-plies. These plies have a bi-axial E-CR glass with $0^{o}/90^{o}$ orientations and chopped strand mat. The skin is designed to provide strength and stiffness to the panel. The fibre content of $0^{o}/90^{o}$/chopped layers are 400/300/300 gsm. The core is designed to be solid to carry the shear forces. It has a density of around 950 kg/m^3. The modified phenolic core material is formulated by LOC Composites Pty. Ltd., Australia (Manalo et al. 2010b). The phenolic foam core comes from natural plant products derived from vegetable oils and plant extracts and chemically bonded within the polymer resin. Tensile, compression, and shear tests were done on the GFRP skin and modified phenolic core coupons, based on the ISO and ASTM standards to determine their mechanical properties. A summary of the material's mechanical properties is presented in Table 3.1, while the full details of the mechanical properties test results are shown in Appendix-A.

3.2.2 Manufacturing process

The GFRP sandwich panels used in this study are manufactured by the LOC Composite Pty. Ltd. in their manufacturing facility. The glass fibre composite skins and the modified phenolic core are co-cured using a toughened phenol formaldehyde resin. This is an automated manufacturing process developed by the manufacturer. The accompanying intellectual patent for this new core material and resin prevent the authors from divulging any information related to the chemical composition. This process provides an environmentally sustainable panel with the ability to be recycled at the end of its life.

3.2.3 Samples preparation

The single sandwich beam specimens were prepared by cutting the panel into 50 mm widths with lengths as listed in Table 3.2. The glue-laminated GFRP sandwich beams were prepared by gluing together 2, 3, 4, and 5 layers of sandwich panels using Techniglue HP (RA5) glue. The sandwich panels were clamped together after gluing for at least 24 hours. Figure 3.2 shows samples of single and glue-laminated GFRP sandwich beams.

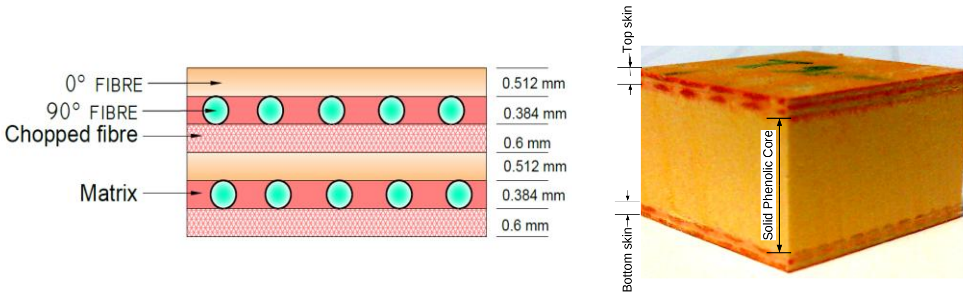

(a) GFRP skin plies (b) Sandwich panel solid core

Figure 3.1 GFRP sandwich panel.

Table 3.1 Properties of GFRP sandwich panel.

Property	GFRP Skin	Modified phenolic core
Density (kg/m^3)	1425	950
Modulus of elasticity (MPa) (Tensile test)	11750	1350
Compressive strength (MPa)	194.77	24.50
Tensile strength (MPa)	239.70	8.50
Shear strength (MPa)	22.82(Manalo, et al. 2010d)	8.80

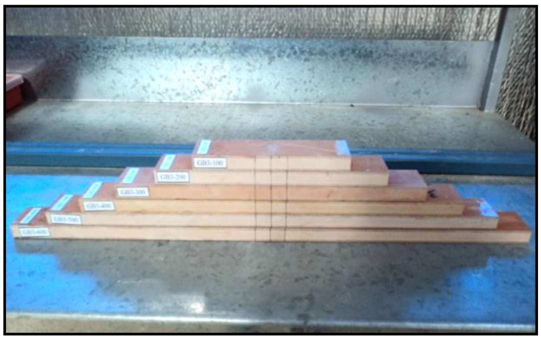

(a) Single GFRP sandwich beam.

(b) Four layers glue laminated GFRP sandwich beam.

Figure 3.2 Samples of sandwich beam.

Table 3.2 GFRP sandwich beam specimen details.

Number of layers	Specimen name	Span, L (mm)	Shear span, a (mm)	Nominal width, b (mm)	Nominal depth, d (mm)	Illustration
One	GB3-60	60	10	50	18	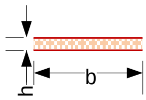
	GB3-100	100	30			
	GB3-150	150	55			
	GB3-200	200	80			
	GB3-250	250	105			
	GB3-300	300	130			
	GB3-300	350	155			
	GB3-400	400	180			
Two	GB4-70	70	15	50	36	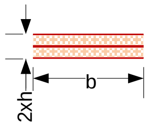
	GB4-100	100	30			
	GB4-200	200	80			
	GB4-300	300	130			
	GB4-400	400	180			
	GB4-500	500	230			
	GB4-600	600	280			
Three	GB6-100	100	30	50	54	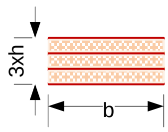
	GB6-125	125	42.4			
	GB6-200	200	80			
	GB6-250	250	105			
	GB6-350	350	155			
	GB6-500	350	230			
Four	GB5-100	100	30	50	72	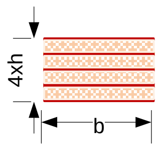
	GB5-200	200	80			
	GB5-300	300	130			
	GB5-400	400	180			
	GB5-500	500	230			
	GB5-600	600	280			
Five	GB7-500	500	230	50	90	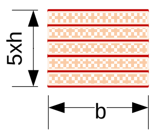
	GB7-600	600	280			
	GB7-700	700	330			

3.3 Experimental procedure

The static flexural test of the GFRP sandwich beam was conducted under four-point bending (Figure 3.3) following the ASTM D7250 (ASTM-Standard 2006) standards. The load was applied at two points with a load span of 40 mm. A constant load span was used to keep the top skin under the same conditions for sandwich beam specimens with different spans. This also allowed putting the strain gauges on the top of the skin at mid span to measure the longitudinal strain. The MTS 100 kN testing machine was used for applying the load. A uni-axial strain gauges type KYOWA- KFG-3-120-C1-11L1M2R were provided in selected specimens to measure the strain on the top and bottom faces of the GFRP sandwich beam. The strain gauges were fixed in the mid span of the beam. The applied load and the displacement of the loading ram were measured and recorded using a data logger System-5000.

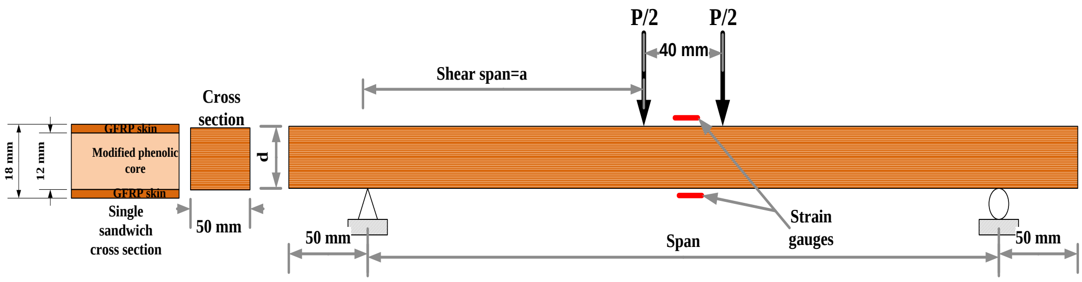

Figure 3.3 Schematic illustration of flexural test.

3.4 Experimental results

3.4.1 Load-displacement behaviour

Figure 3.4 shows the load-displacement behaviour of the single GFRP sandwich beams. Eight beams were tested for different span to depth ratio (a/d). The a/d ratio starts from 0.55 and goes up to 10. It can be seen from the figure that the behaviour of the single GFRP sandwich beams is linear up to failure. However, there is a non-linear response before the final failure for the beam with spans of 200, 300, and 400 mm length due to either initiation of compression failure of the top skin or shear failure of the core followed by bottom skin debonding. The variation of the shear span to depth ratio (a/d) affects the load carrying capacity of the beam. The load carrying capacity of the GFRP sandwich beam decreases with increasing a/d ratio. The single GFRP sandwich beams show approximately brittle failure in both flexural and shear failure modes. When the maximum load was reached, an abrupt drop in the load was observed and the specimens failed subsequently. There was no change in the slope of the load-deflection curve up to failure.

The load-displacement curves of the Glue-laminated GFRP sandwich beams with two, three, four, and five layers are shown in Figures 3.5-3.8. The figures demonstrate that the load-displacement curves are approximately linear for two layers beam and it show a non-linear behaviour with the increasing of the sandwich layers. One the other hand, the load-displacement curves for GB5 showed a non-linear behaviour for short spans, and then starts to be approximately linear with increasing of span length. However, most of the glue-laminated beams show a drop in the last stage of their load carrying behaviour. This drop in load-displacement behaviour is due to the initiation of failure in the beam such as core shear cracks, core tension cracks, and top skin failure.

For the beams with shorter shear span (GB5-100 and GB6-100), the non-linear behaviour is due to initiation of crushing and shear cracking of the core. For the beams with intermediate spans (200 mm to 300 mm), the drop in the load is due to shear cracking of the core and the final failure due to transverse shear. For longer beams (500 and 600), the slight drop in the load and stiffness is due to flexural cracking of the core with final failure due to compressive failure of the top skin. It was noticed in the experiments that core cracking in the bottom sandwich layer affects the load-displacement behaviour of the glue laminated GFRP sandwich beam. Furthermore, the specimens GB5-100 and GB6-100 showed different failure behaviour compared to other samples. This failure mode is classified as a core crushing, and the beam carries higher load with a non-linear load-displacement. These beams with a/d equal to 0.41 and 0.55 show a relatively higher load with more deformation than the other beams. The higher load on this beam can be attributed to the very low a/d that results in compression shear failure. The larger deformation observed in this case is mainly caused by crushing of the core, resulting in local deformation of the top skin. Furthermore, the glue-laminated GFRP sandwich beams with 1, 2, 3, 4, and 5 layers showed the same behaviour. The full details of the failure load, displacement, and failure mode of the tested beams are shown in Table 3.3.

The failure mode of three layers glue laminated GFRP sandwich beam with an a/d equal to 0.55 (GB6-100) is classified as core crushing failure. It shows the same behaviour as four layers glue laminated beam (GB5-100) as provided in Table 3.3. It appears to show that the beams with low a/d have different load-displacement behaviour compared to the beams with core shear and skin failure and this is due to the core crushing failure mechanism.

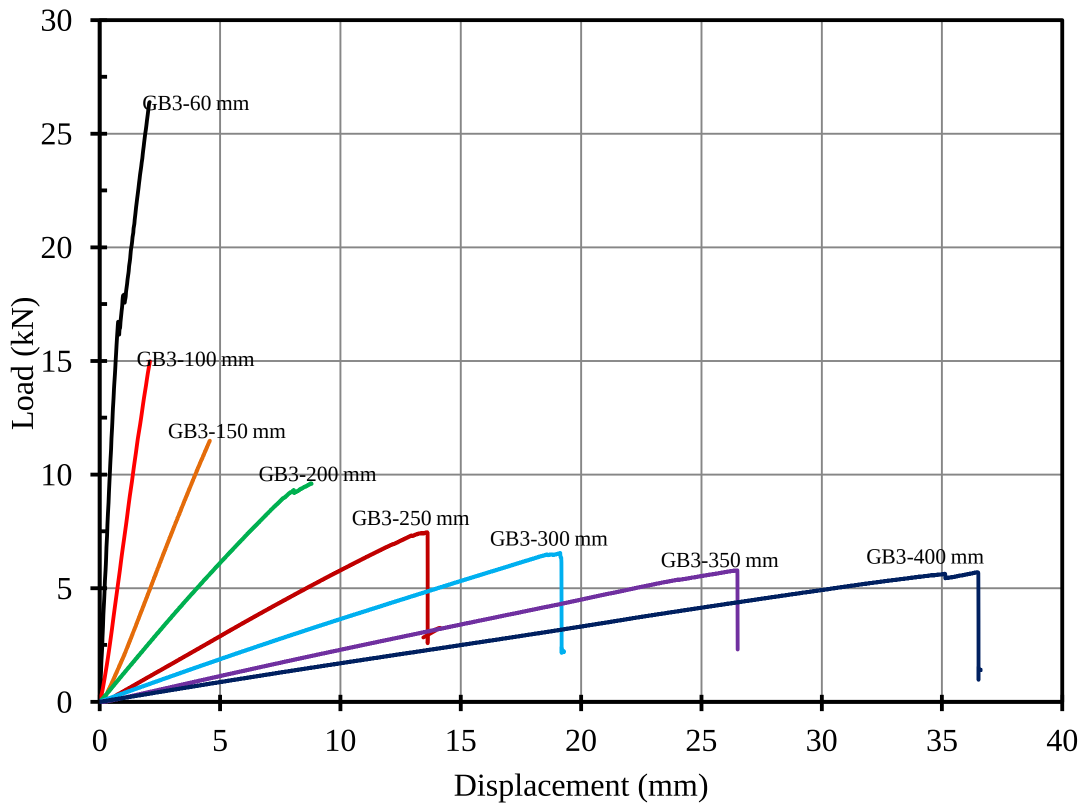

Figure 3.4 Load-displacement curves for single sandwich beams (GB3).

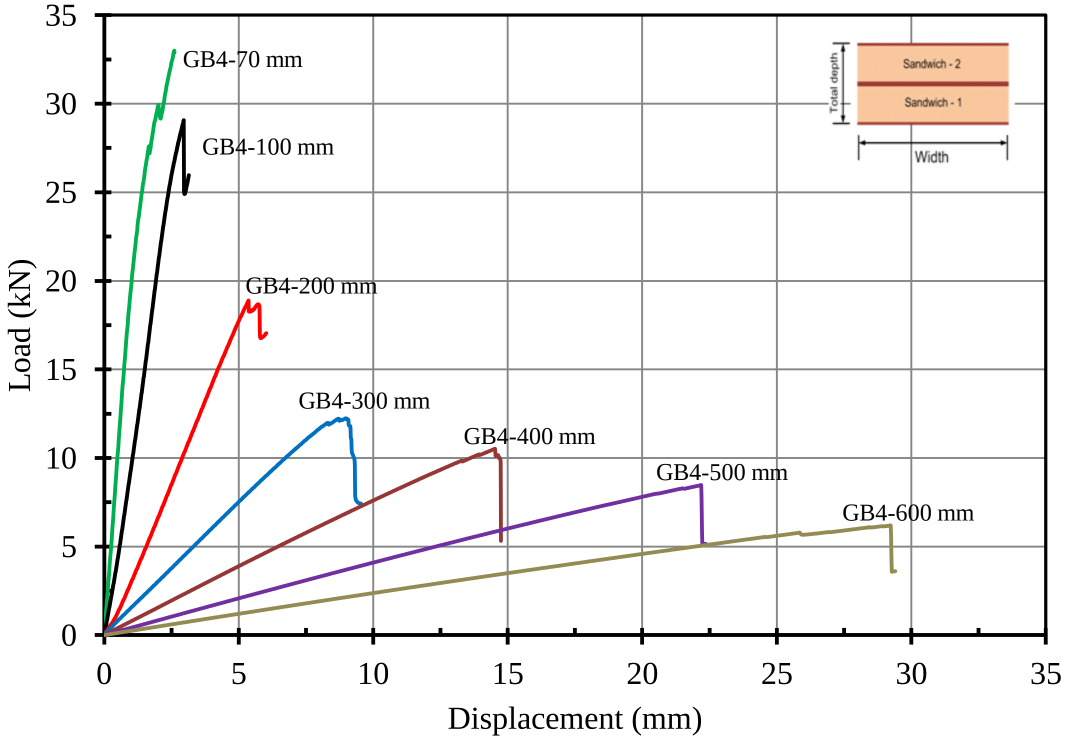

Figure 3.5 Load-displacement curves of two layers GFRP sandwich beams (GB4).

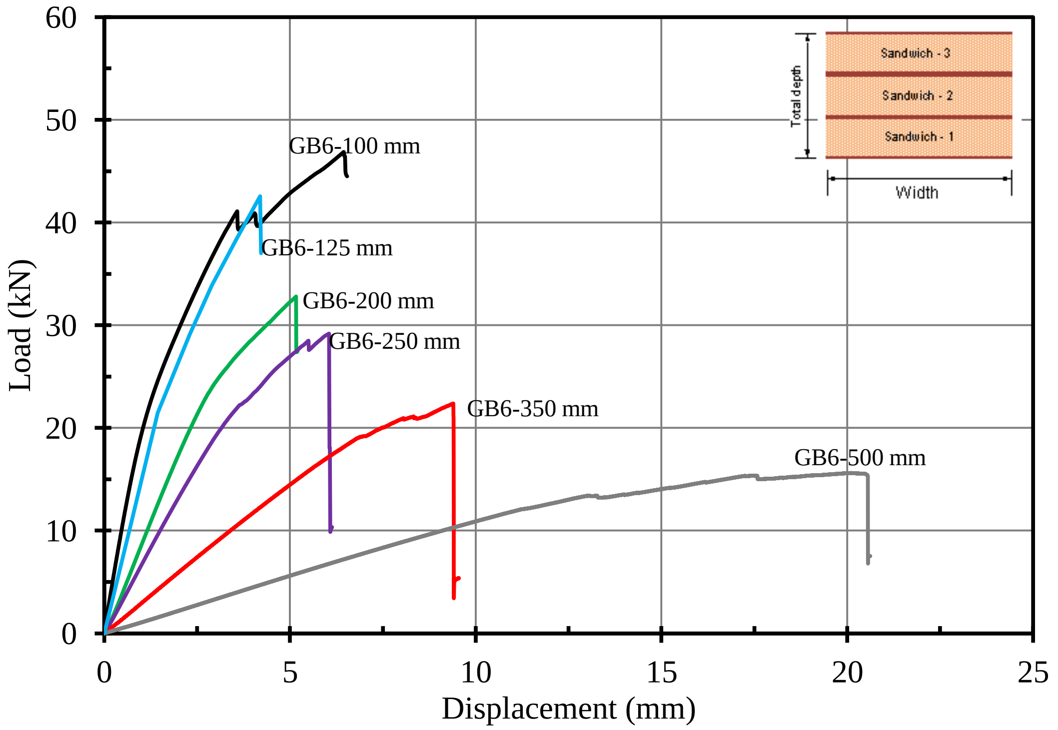

Figure 3.6 Load-displacement curves of three layers GFRP sandwich beams (GB6).

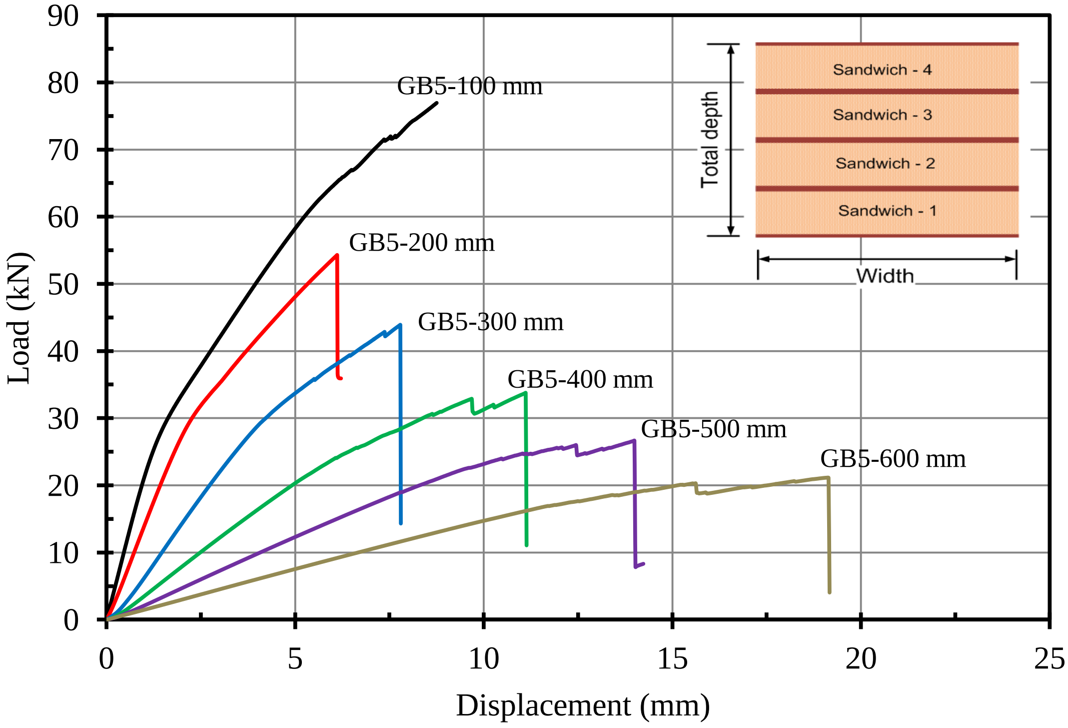

Figure 3.7 Load-displacement curves of four layers GFRP sandwich beams (GB5).

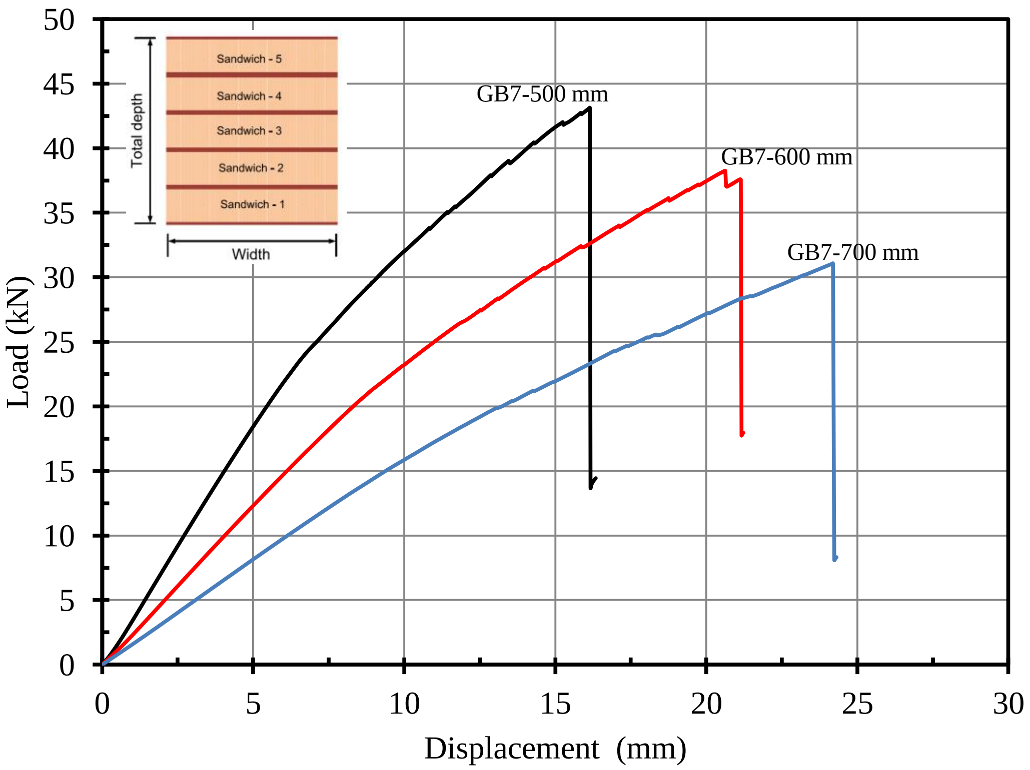

Figure 3.8 Load-displacement curves of five layers GFRP sandwich beams (GB7).

Table 3.3 GFRP sandwich beams experimental results.

No. of layers	Specimen name	Span (mm)	Shear span (mm)	Nominal width (mm)	Nominal depth (mm)	a/d	Failure load kN	Displa-cement mm	Failure mode
One	GB3-60	60	10	50	18	0.55	26.4	2.05	CS
	GB3-100	100	30			1.66	14.9	2.13	CS
	GB3-150	150	55			3.05	11.4	4.56	CS
	GB3-200	200	80			4.44	10.2	7.5	CS
	GB3-250	250	105			5.83	7.4	13.62	TS
	GB3-300	300	130			7.22	6.31	16.13	TS
	GB3-350	350	155			8.61	5.7	26.49	TS
	GB3-400	400	180			10	5.6	31.1	TS
Two	GB4-70	70	15	50	36	0.41	36.5	2.46	CS
	GB4-100	100	30			0.83	29.0	2.96	CS
	GB4-200	200	80			2.22	18.6	5.72	CS
	GB4-300	300	130			3.61	12.2	8.97	TS
	GB4-400	400	180			5	10.5	14.53	TS
	GB4-500	500	230			6.38	8.4	22.19	TS
	GB4-600	600	280			7.77	6.6	29.23	TS
Three	GB6-100	100	30	50	54	0.55	46.8	6.45	CC
	GB6-125	125	42.4			0.78	43.8	4.05	CS
	GB6-20	200	80			1.48	32.8	5.17	CS
	GB6-250	250	105			1.94	29.1	6.06	CS
	GB6-350	350	155			2.87	22.3	9.40	TS
	GB6-500	500	230			4.25	15.6	20.12	TS
Four	GB5-100	100	30	50	72	0.41	76.9	2.96	CC
	GB5-200	200	80			1.11	54.3	5.72	CS
	GB5-300	300	130			1.80	43.9	8.97	CS
	GB5-400	400	180			2.50	33.7	14.53	TS
	GB5-500	500	230			3.19	26.6	22.19	TS
	GB5-600	600	280			3.88	21.0	29.23	TS
Five	GB7-500	500	230	50	90	2.55	43.1	15.95	TS
	GB7-600	600	280			3.11	37.5	20.26	TS
	GB7-700	700	330			3.66	32.0	23.81	TS

CS: core shear
CC: core crushing
TS: top skin

3.4.2 Failure mechanism

Figure 3.9 shows the different failure modes for single GFRP sandwich beams with different shear spans. These failure modes are classified as core shear and skin compression failure. The single sandwich beam exhibits different failure mechanism based on the shear span to depth ratio a/d. The shorter beams showed core shear failure without any degradation in the skin and debonding between core and skin. The sandwich beam with an a/d equal to 0.55 showed a shear compression failure as shown in Figure 3.9(a). The beams with an a/d equal to 1.66 showed a diagonal shear failure with no debonding between the skins and core as shown in Figure 3.9(b). On the other hand, the beams with a/d equal to 3.05 and 4.5 showed core shear and bottom skin delamination failure as shown in Figures 3.9(c) and (d) respectively. This shown that once the beam failed by core shear, all the forces transfer to the bottom skin. The bottom skin carries the load up to its debonding strength and finally, it fails by the debonding of the bottom skin.

Increasing the shear span to depth ratio causes an increase in beam deformation. Top skin failure was noticed for beams with a span to depth ratio a/d greater than 4.5 as shown in Figures 3.9(e) and (f). The top skin failed by compression with no failure symptoms noticed in the core. The flexural failure starts in the top skin and then followed by the top skin debonding as shown in Figures 3.9(e) and (f).

Strain measurements for the single layer GB3 beams at the top and bottom skins is shown in Figure 3.10. It can be seen that the tensile strain in the bottom skin is higher than the top skin compressive strain. Furthermore, the shorter beam has a smaller failure strain compared to longer beams. The maximum compressive strain of the top skin of GB3-300 and GB3-400 was around 1.6%. Based on the elastic modulus of skin (11750 MPa) the compression stress is 188 MPa, which is very close to the skin compressive strength (194.77 MPa) as shown in Table 3.1. The beam with smaller a/d such as GB3-100 showed a strain equal to 0.4% and 0.9% in compression and tension respectively. This gives stress values of 47 MPa and 105 MPa for compression and tension respectively. This confirms that the skin stress is smaller than its ultimate strength, and there is no skin failure but core cracking causing shear dominant failure. As observed in specimen GB3-60, the tensile and compressive strains decreased after a load of 16 kN. This is due to the initiation of crushing of the core material. The shorter beam exhibited a small deflection in the mid span, and showed core shear failure. In addition, the beams with flexural failure of the top skin (300 and 400 mm) show approximately the same final compression strain. Beams with an a/d less than 4.5 show a small compression strain compared to beams with an a/d greater than 4.5. The bottom and top strains decrease with decreasing of the a/d for the specimens with core failure mode. The 200 mm beam with core shear failure and bottom skin de-bonding (Figure 3.9(d)) shows a high tension strain at bottom skin compared to the compression strain in the top skin as shown in Figure 3.10. The 200 mm span exhibits the tension shear mode of failure and it is very close to the flexural failure mode. It can be seen that the failure mode changes from core shear at 200 mm (a/d equal to 4.44) to top skin flexural failure at 300 mm span length (a/d equal to 7.22). Strain measurement values show the contribution of the skins to the bending strength of the GFRP sandwich beams. This means that the contribution of the GFRP skins to the shorter beam bending is lower than it is for the longer beam bending.

Glue-laminated beams exhibit a different behaviour with regarding to the a/d as shown in Figures 3.11-3.14. The specimens with two layers and an a/d less than 1.0 showed core shear cracking as shown in Figure 3.11(a-b) while, the three and four layered specimens exhibited core crushing in the top and bottom layers for a/d values less than 1.0 as shown in Figures 3.12(a) and 3.13(a). The core crushing happened due to load concentration and a higher load level under point loads. The core crushing occurs when the applied load exceeds the core compressive strength. From the experimental results, it can be seen that the core crushing appears in the beams with a/d less than 1.0 and an applied load of more than 45 kN as shown in Table 3.3. This is the reason why the core crushing does not appear in the single and double sandwich beams with a/d ratio less than 1.0 is because of the low load level.

The core shear failure has been noticed in the GFRP sandwich beams with different cross sections and spans. The glue laminated beams showed core shear failure followed by bottom skin delamination as illustrated in Figures 3.11(c), 3.12(d-e), and 3.13(c). Glue laminated beams exhibit top skin failure and core cracking as seen in Figures 3.11(d), 3.12(e), 3.13(d), and 3.14(a-c). The tested beams showed a different shear failure load due to the effect of shear span to the depth ratio. The beams with lower shear to depth ratios showed a higher load capacity than beams with higher shear span to the depth ratios.

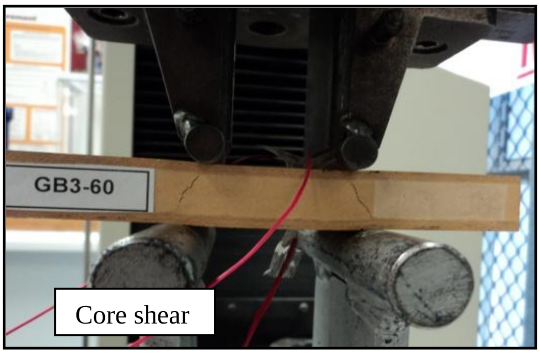

(a) a/d =0.55

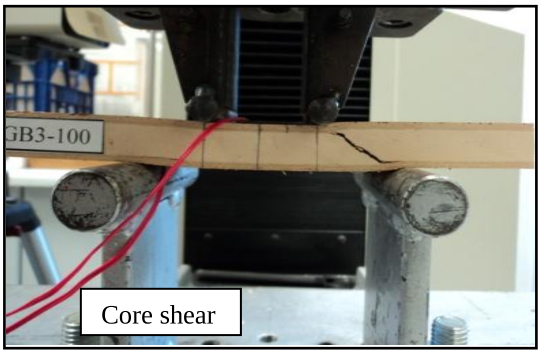

(b) a/d = 1.66

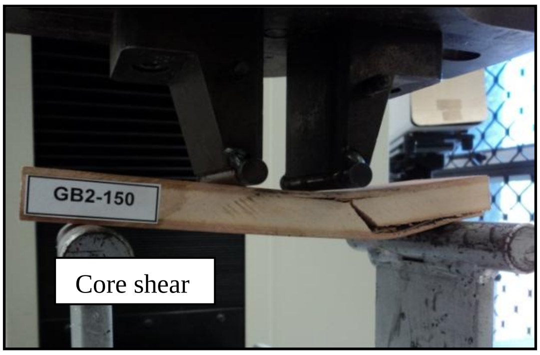

(c) a/d = 3.05

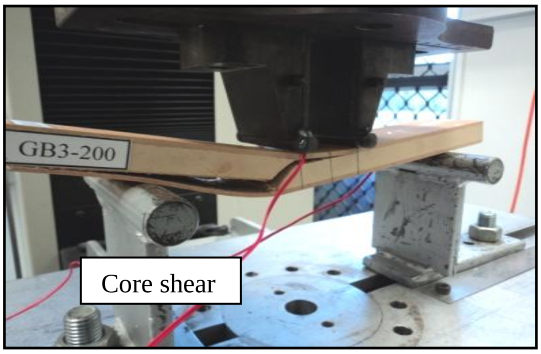

(d) a/d =4.44

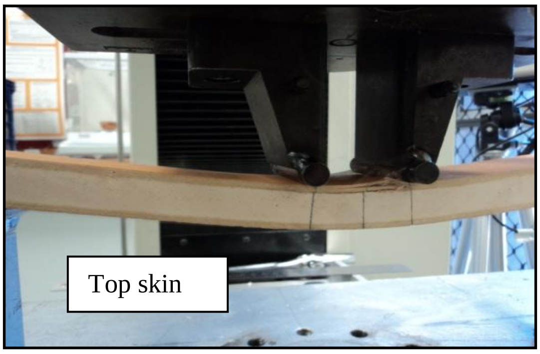

(e) a/d = 7.22

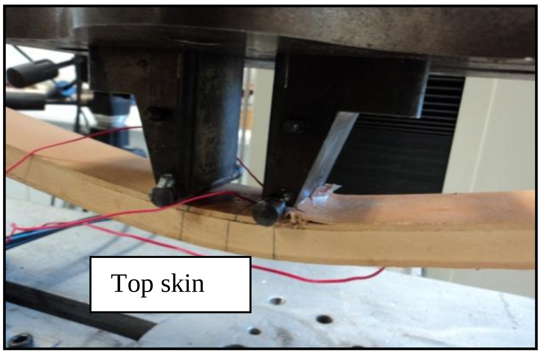

(f) a/d =10

Figure 3.9 Failure modes of single sandwich beams with different shear span to depth ratios (a/d).

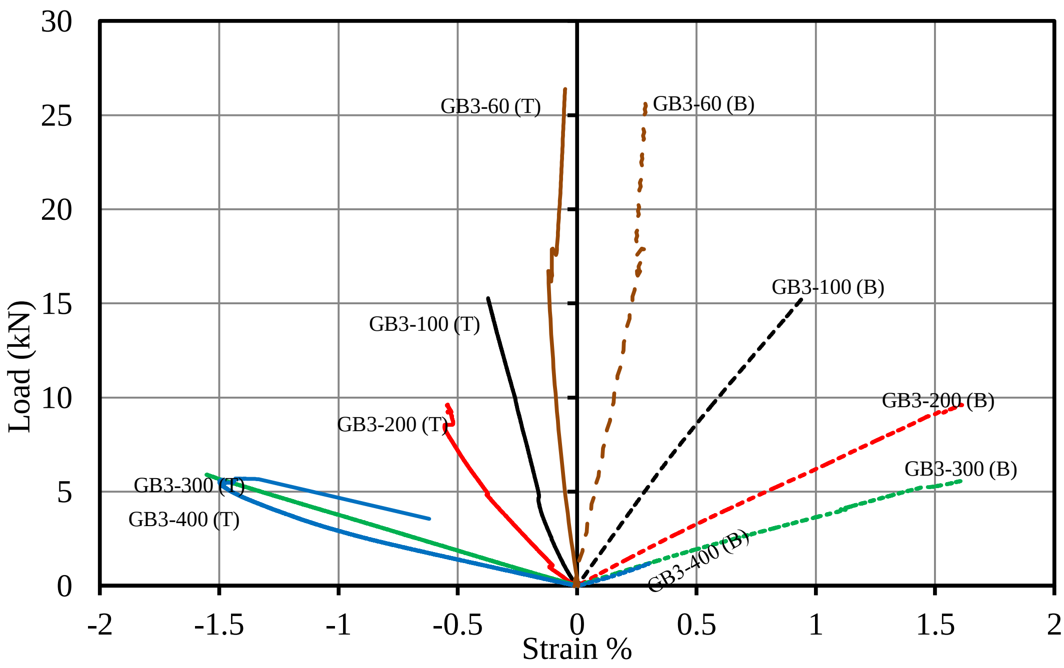

Figure 3.10 Strain-load curves for single layer sandwich beams (GB3).

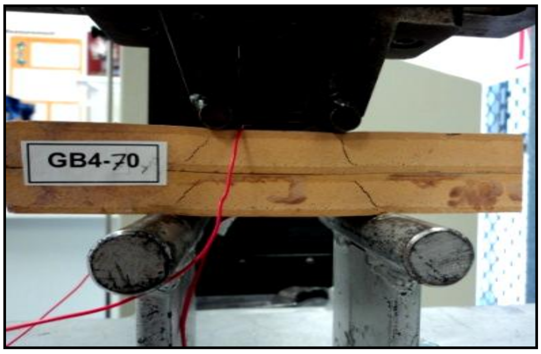

(a) a/d = 0.41

(b) a/d =0.83

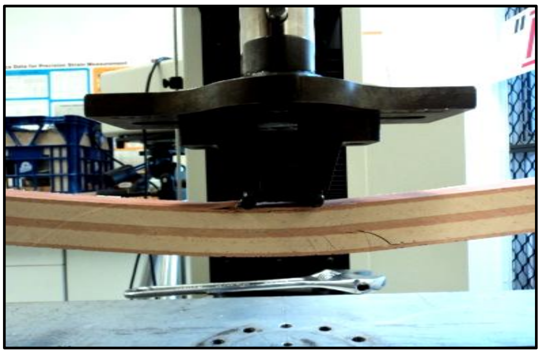

(c) a/d = 2.22

(d) a/d =6.38

Figure 3.11 Failure modes of two layers glue laminated sandwich beam with different shear span to depth ratios (a/d).

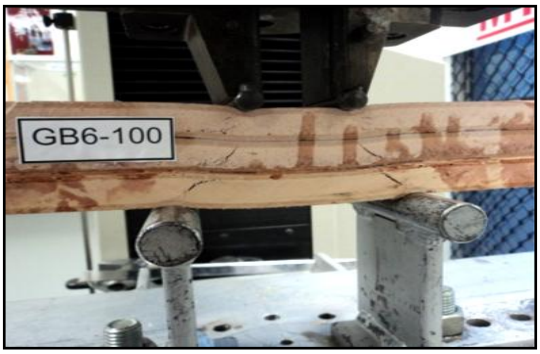

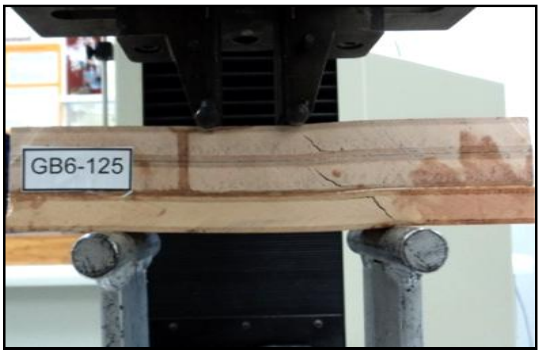

(a) a/d = 0.55

(b) a/d =0.78

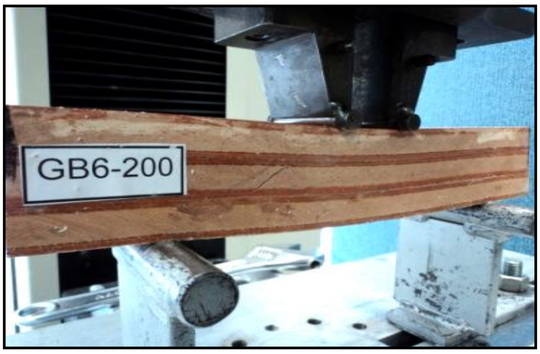

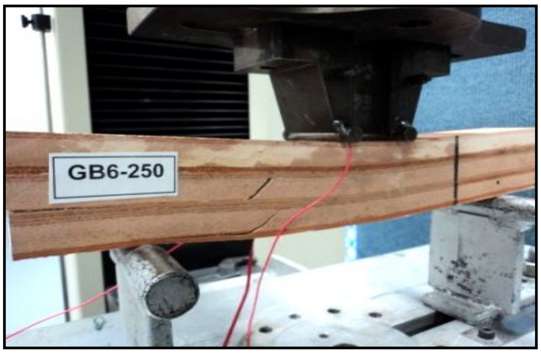

(c) a/d = 1.48

(d) a/d =1.94

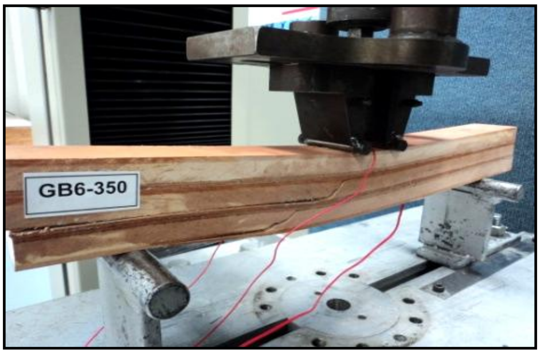

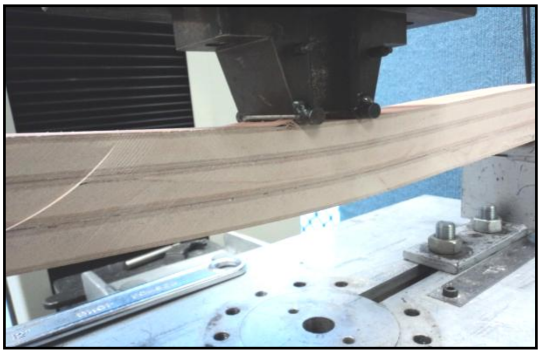

(e) a/d = 2.87

(f) a/d =4.25

Figure 3.12 Failure modes of three layers glue laminated sandwich beam with different shear span to depth ratios (a/d).

.

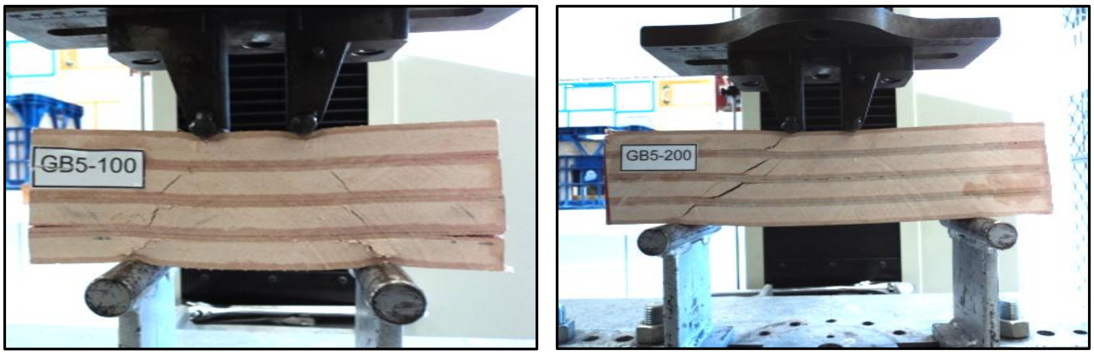

(a) a/d = 0.41 (b) a/d = 1.11

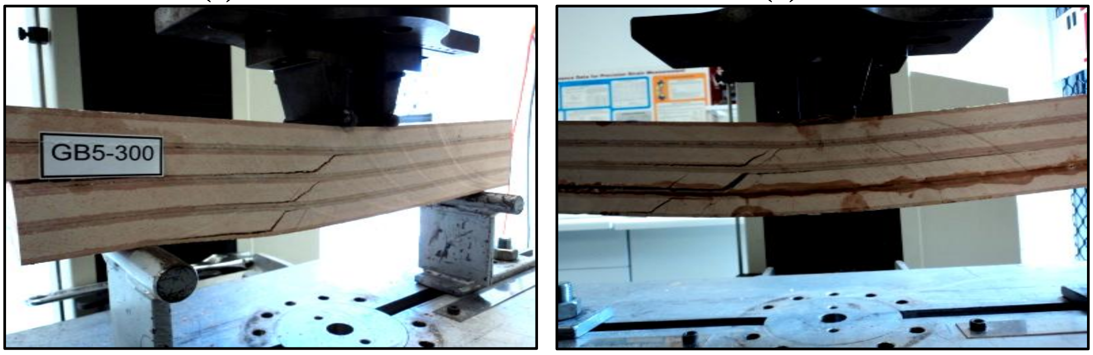

(c) a/d = 1.80 (d) a/d = 3.88

Figure 3.13 Failure modes of four layers glue laminated sandwich beams with different shear span to depth ratios (a/d).

(a) a/d = 2.55 (b) a/d = 3.11

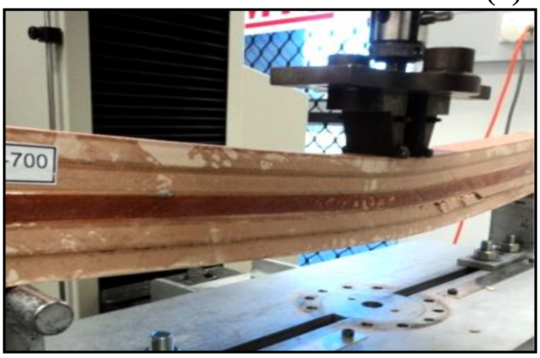

(c) a/d=3.66

Figure 3.14 Failure modes of five layers glue laminated sandwich beams with different shear span to depth ratios (a/d).

3.5 Discussion

3.5.1 Effect of shear span to depth ratio on shear capacity

The effect of a/d ratio on the shear capacity of individual and glue-laminated sandwich beams was determined. The shear strength of all tested beams has been normalised by using the transformed section in Equation 3.1 as indicated by Triantafillou (1998). According to this author, the normalised shear for composite can be calculated by transforming the composite material into an equivalent core material based on their elastic modulus.

$$\tau = \frac{VQ_t}{b_t I_t} \qquad 3.1$$

where V is the shear force, Q_t is the first moment of area, I_t is the moment of inertia, b is the width, and subscript t is refer to the transformed section.

The normalised shear strength of the GFRP beams was calculated using Equation 3.1 and presented in Figure 3.15. The normalisation for the shear strength is necessary to compare between single and glue-laminated beams having different depths. It can be seen that the normalised shear strength decreases with increase in a/d ratio. The single sandwich beam has a slightly higher normalise shear strength than the glue-laminated sandwich beam. The reason is that the core in the single sandwich beam failed completely then followed by debonding between the skin and the core as shown in Figure 3.9. Furthermore, glue-laminated GFRP sandwich beams with 2, 3, 4, and 5 layers have the same normalised shear strength at the same shear span to the depth ratio. The bottom layers of the glue-laminated beams have core cracks due to shear, but the top layer does not show core cracking as shown in Figures 3.12(c-d) and 3.13(c). Initially, the crack developed in the core layers but did not extend directly into the core of the below and above sandwich layers because of the presence of the GFRP skin. The GFRP skin has higher shear strength than the phenolic core. As a consequence of increasing the applied load, the horizontal shear stress increases. The increase in the horizontal shear stress causes a debonding between the skin and the core in both directions of the crack as shown in Figure 3.16. Therefore, part of the core cracks in the glue-laminated GFRP sandwich beam is due to the shear, and the rest of the cracks are due to the debonding between the phenolic core and GFRP skin. Debonding is clear in the beams with a shear span to depth ratio greater than 2, and above this level of shear span to depth ratio the effects of flexure become bigger. This results in lower normalised shear strength at failure. The debonding of the core to intermediate skin interaction occurs before the shear crack developed in all core layers as shown in Figures 3.12(d-e) and 3.13(c). The normalised shear strength of beams with an a/d greater than 1.0 and less than 2 is between 8 and 10 MPa which is similar to the core shear strength established from the coupon tests. For beams with an a/d less than 1.0, the high normalised shear strength indicates the initiation of crushing in the core material. On the other hand, the lower normalised shear strength for beams with an a/d greater than 2 indicates that the increasing contribution of flexural stresses.

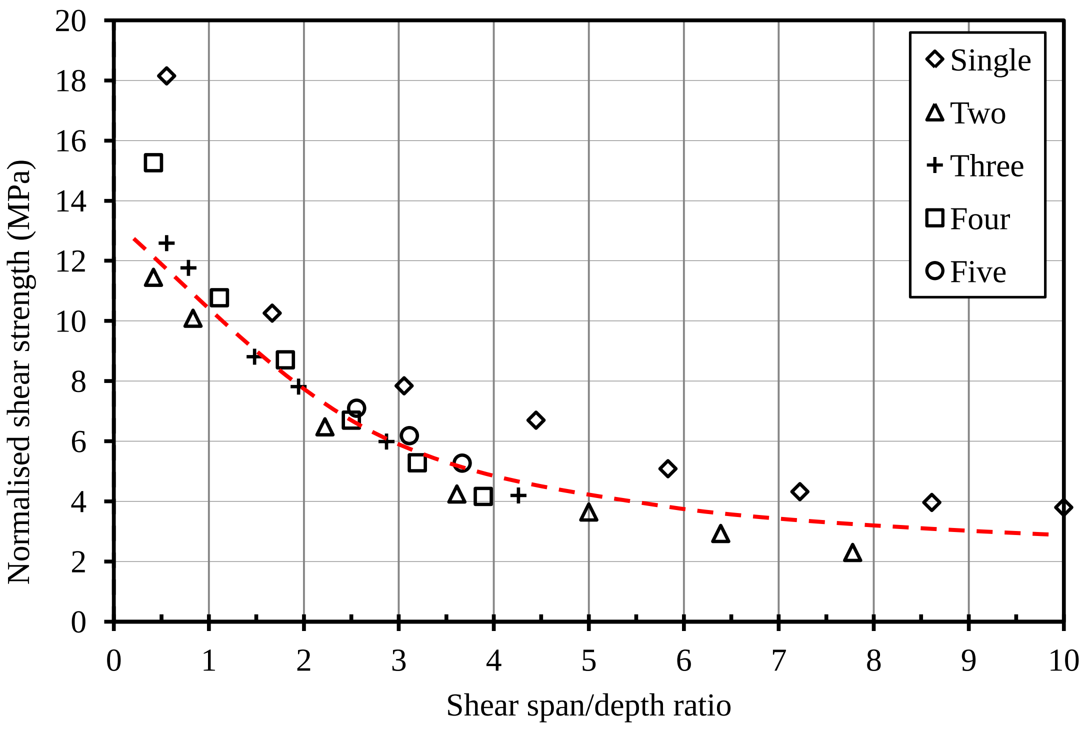

Figure 3.15 Normalised shear strength versus shear span to depth ratios.

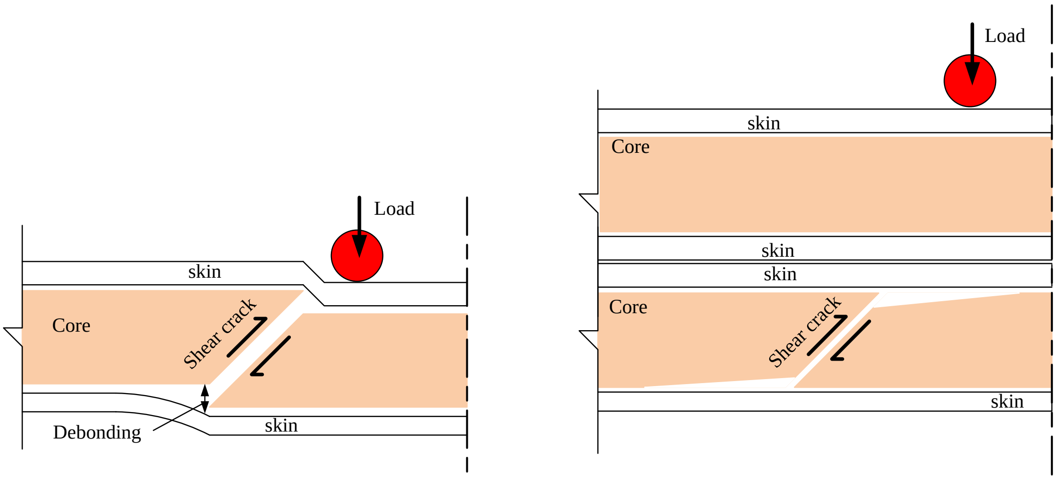

(a) Single sandwich (b) Glue laminated sandwich beam

Figure 3.16 Schematic diagrams for the shear failure in the beams.

3.5.2 Effect of shear span to depth on flexural behaviour

The bending behaviour of the single and glue laminated GFRP sandwich beams have studied under four-point bending. The bending stress in the top and bottom skins is presented for comparison as calculated using equation below:

$$Skin\ stress = \frac{M_b z E_{skin}}{EI} \qquad 3.2$$

where M_b is the bending moment, z is the distance from neutral axis to the outer top skin, E_{skin} is the elastic modulus of the skin, and EI is the flexural rigidity.

The normalized bending stress of the single sandwich beams was calculated using Equation 3.2 and it is shown in Figure 3.17. The normalisation was used to compare between single and glue-laminated beams with different depths. Three different zones have been noticed in relation to the effect of shear span to depth ratio in bending. The GFRP sandwich beams exhibit approximately a pure flexural failure when the shear span to depth ratio is greater than 4.5. This is indicated by the calculated bending strength having almost similar to the compression strength of the skin as determined from the tests. Core shear zone failure occurs in the beams with shear span to the depth ratios less than 2, and the behaviour seems to be linear. In the zone of shear span to depth ratio from 2 to 4.5, there is a transition zone between the core failure and flexural top skin failure. Both single and glue-laminated GFRP sandwich beams show similar stress behaviour as shown in Figure 3.17.

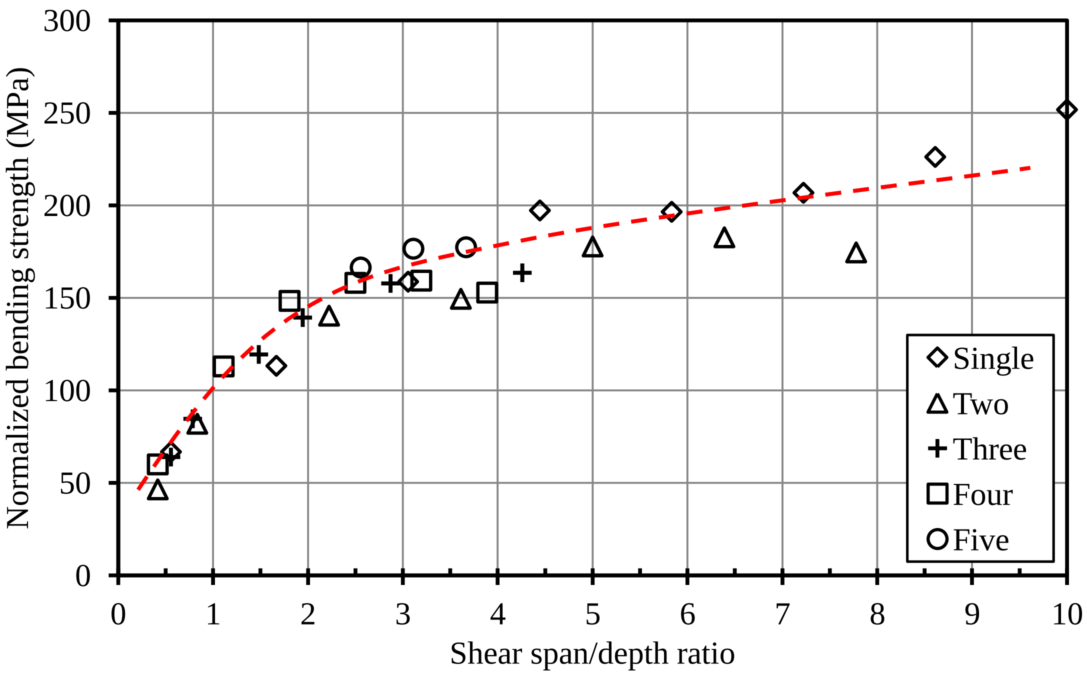

Figure 3.17 Normalised bending strength versus shear span to depth ratio.

3.5.3 Effect of shear span to depth ratio on failure behaviour

The single GFRP sandwich beam showed a sudden or brittle behaviour in all modes of failure. The failure of the GFRP single sandwich beam is controlled by either the core shear failure or the compressive failure of the skin. The single sandwich beams with an a/d less than 2 showed core shear failure as shown in Figures 3.9(a-b). In addition, beams with an a/d greater than 2.0 and less than 4.5 showed core shear failure and bottom skin debonding as shown in Figures 3.9(c-d). The top skin compressive failure happens in beams with an a/d greater than 4.5. In some cases, it can be seen that there are some drops at failure stage for the beams with spans of 200, 250, 300, 350, and 400 mm. This failure response is due to the core cracking followed by debonding of the bottom skin or the failure of the top skins followed by the debonding as it is noticed in the experiments as shown in Figures 3.9(c) and (d).

The glue-laminated GFRP sandwich beams showed different failure behaviours. Core crushing was noticed for beams with a/d less than 0.7. The core starts to fail by crushing under the point load or through a line between the point load and the support position as shown in Figures 3.12(a) and 3.13(a). In addition, the beam shows a ductile behaviour with a high load capacity but small displacement. The second failure behaviour is core shear for beams with a/d greater than 0.7 and less than 2.0 as shown in Figures 3.11(b-c), 3.12(b-d), and 3.13(b-c). The core cracked in the bottom layers and no core crack in the top layer. This is due to the mechanism of the failure. The core cracks in the bottom and middle layers, and it is restricted by the intermediate GFRP skin layers. Due to the presence of the inner GFRP skin layer, the debonding tends to initiate between the core and the skin. Decreases and changes in load-displacement have been noticed due to this failure behaviour as shown in Figures 3.5-3.8. In relation with the point load, it seems that the core cracking position is closer to the top point load than the support, and the core cracks by an angle approximately equal to 45^o.

The third failure mode is top skin compression with a/d greater than 2.0. The top skin compression happens for GFRP sandwich beams, between the loading points. The top skin failure for different beams is shown in Figures 3.5-3.8. The glue-laminated GFRP sandwich beams show a bottom layer core cracking before the final failure of the beam. These tension cracks affect the beam behaviour and it gives some non-linearity to the beam behaviour. The glue-laminated beams showed a core diagonal cracking and top skin failure as shown in Figures 3.11(d), 3.12(e), 3.13(d), and 3.14(a-c).

3.5.4 Comparison with theoretical predictions

The simply supported beam with 4-point bending has a particular bending equation to find the mid span deflection (δ) as below (Granet 1973):

$$\delta = \frac{Pa(3L^2 - 4a^2)}{48EI} \qquad 3.3$$

where P is the load, a is the shear span.

The overall rigidity EI of single sandwich beams can be calculated from the following equation by assuming that there is full interaction between the skin and the core (Mohan et al. 2005; Steeves & Fleck 2004):

$$EI_{single} = \left(\frac{\mathrm{b}t^3}{12} + btd^2\right)E_{skin} + \left(\frac{bC^3}{12}\right)E_{core} \qquad 3.4$$

where EI_{single} is calculated in the neutral axis of the cross section, and c is the core thickness.

In the same way, the rigidity of the glue-laminated sandwich beam (EI_{glued}) is equal to the summation of the rigidities of the N-layers (Manalo et al. 2010b):

$$EI_{glued} = \sum_{i=1}^{N}\left(\left(\frac{\mathrm{b}t^2}{12} + bt(d_{st}^2 + d_{sb}^2)\right)E_{skin}\right)_i + \left(\left(\frac{bC^3}{12} + bcd_c^2\right)E_{core}\right)_i \qquad 3.5$$

where b is the width. The terms d_{st}, d_{sb}, and d_c are the distances from the centre of the top skin, bottom skin, and core to the neutral axis, respectively.

Bending stress is another important aspect in the sandwich beam analysis. The bending stress equation for sandwich beams is shown in Equation 3.2. The load capacity for beam bending (P_b) can be calculated from Equation 3.2 based on four-point bending as follow:

$$P_b = \frac{2\sigma_f EI}{a\, z\, E_{skin}} \qquad 3.6$$

The load capacity for shear (P_s) of the single sandwich beam in 4-point bending can be predicted by multiplying the core shear strength to the cross-sectional area of the core (Petras & Sutcliffe 1999):

$$P_{s1} = 2bc\tau_c \qquad 3.7$$

where P_{s1} is the load capacity, and τ_c is the core shear strength.

Manalo et al. (2010c) studied the in-plane shear behaviour of the novel GFRP sandwich panel with the skin contributing to the shear. The proposed equation is:

$$P_{s2} = 2\tau_c(2t\,\frac{G_{core}}{G_{skin}} + c)b \qquad 3.8$$

where P_{s2} is the load capacity, and G_{core} and G_{skin} are the shear module of the core and skin, respectively.

Mohan et al. (2005) suggested an equation for the shear prediction of single sandwich beam. In addition to the shear capacity of the core, this equation considers the contribution of bending created by the top and bottom skins in the calculation as shown below:

$$P_{s3} = 2bc\tau_c + \frac{8bt^2\sigma_f}{3a} \qquad 3.9$$

where P_{s3} is the load capacity.

For the glue-laminated sandwich beams, it can be assumed that the overall shear capacity (P_G) is equal to the capacity of the single sandwich beam layer multiplied by the number of layers as follows:

$$P_G = N \times capacity\ of\ single\ sandwich \qquad 3.10$$

These analytical equations are used to predict the behaviour of the single and glue-laminated sandwich beams. The bending failure load is predicted by using Equation 3.6, and the results are shown in Table 3.4. The pure shear capacity estimation of the cross section was predicted using Equations 3.7 and 3.8, and the results are shown in Table 3.4. The tested beam showed a different shear failure load due to the effect of different shear span to depth ratio. Using Equation 3.6 shows that the predicted bending load capacity of the beam is compatible with the experimental results when the higher a/d ratio in the flexural failure zone. Beams with lower shear to the depth ratios showed higher load capacities than the beams with higher shear span to depth ratios as shown in Table 3.4. Comparison between the predicted values and the experimental results shows that considering the core only gives lower values than considering the core and the skins in the shear. Additionally, the calculated value of the shear capacity does not agree with the experimental value for the same cross section. This is due to the effect of bending on the shear behaviour of the sandwich beam.

The bending Equation 3.6 was used to predict the failure load of the single and glue-laminated GFRP sandwich beams, and the results are shown in Figures 3.18 and 3.19. It can be seen that the bending equation provides a good estimate of the failure load in the flexural failure zone. Equation 3.9 proposed by Mohan et al. (2005) was used to predict the failure load of single and three layers sandwich GFRP beam. It showed an acceptable prediction in the core shear failure zone (a/d less than 2.0) as shown in Figures 3.18 and 3.19. However, the bending Equation 3.6 gives a very high load prediction when the a/d ratios less than 2. However, both analytical equations could not predict accurately the failure load of the beams in the combined zone of the shear and flexural. It can be seen that the combined zone between shear and flexural is approximately in the range of 1.5 to 4.5 shear span to depth ratio. On the other hand, the bending Equation 3.6 gives a better estimation of the failure load of beams with an a/d ratio greater than 4.5. The slightly higher predicted failure load compared to actual failure load is due to the effect of cracking in the core which was not considered in the flexural analysis.

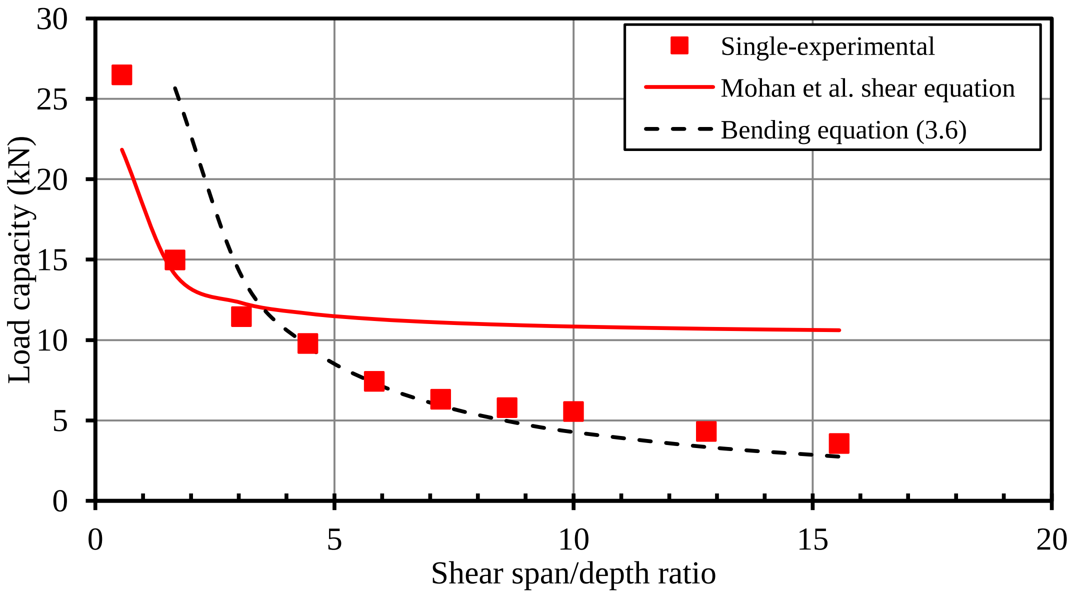

Figure 3.18 Experimental and predicted failure loads of GFRP sandwich beams.

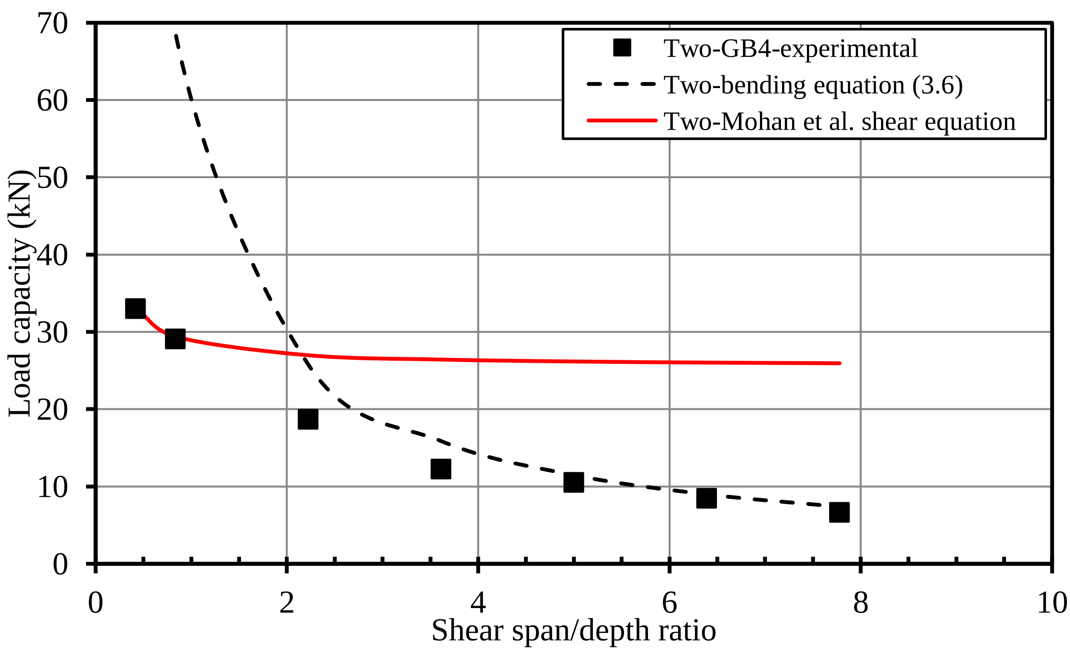

Figure 3.19 Experimental and predicted failure loads of two and three layers GFRP sandwich beams.

The apparent stiffness of the sandwich beam is another factor affected by the span to depth ratio. The EI of the different GFRP sandwich beams was calculated using the bending Equation 3.3 from the failure load and corresponding deflection values as measured in the experimental tests. The apparent stiffness modulus (E_a) was found by dividing the EI by the gross moment of inertia of the section. The E_a values of the beams with cross sections of one, two, three, four, and five sandwich layers were calculated, and are shown in Figure 3.20. Figure 3.20 shows that the E_a of the GFRP sandwich beam increases with increasing of a/d ratio. This behaviour can be attributed to the higher shear deformation in small a/d ratio beams contributing to larger overall deformation. The E_a value becomes constant as the a/d ratio increases and this means that the shear deformation is very small. Single sandwich beams have a higher E_a compared to glue-laminated beams. This is due to the sandwich effect or the presence of the top and bottom skins which increases the flexural stiffness of a sandwich structure. The apparent E_a of glue-laminated GFRP sandwich beams with 2, 3, 4, and 5 layers at the same a/d ratio is nearly the same.

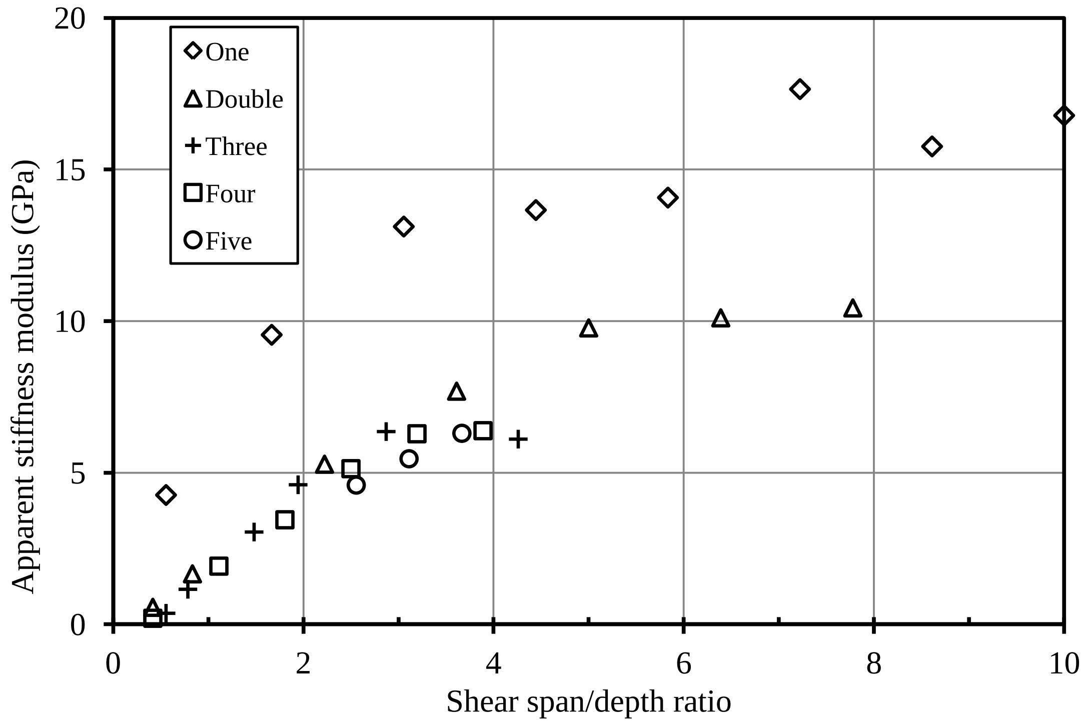

Figure 3.20 Apparent stiffness modulus versus the a/d ratio for GFRP sandwich beams.

Table 3.4 Failure load of GFRP sandwich beams.

Number of layers	Specimen	a/d	Failure load (kN)	P_b (kN)	P_{s1} (kN)	P_{s2} (kN)	P_{s3} (kN)
One	GB3-60	0.55	26.4	87.7	10.2	11.7	21.8
	GB3-100	1.66	14.9	29.4			14.0
	GB3-150	3.05	11.4	16.2			12.3
	GB3-200	4.44	10.2	11.2			11.6
	GB3-250	5.83	7.4	8.6			11.3
	GB3-300	7.22	6.31	7.0			11.0
	GB3-350	8.61	5.7	5.9			10.9
	GB3-400	10	5.6	5.2			10.8
Two	GB4-70	0.41	36.5	130.3	20.4	23.4	33.2
	GB4-100	0.83	29.0	66.3			29.3
	GB4-200	2.22	18.6	26.2			26.9
	GB4-300	3.61	12.2	17.0			26.3
	GB4-400	5	10.5	12.9			26.1
	GB4-500	6.38	8.4	10.6			26.0
	GB4-600	7.77	6.6	9.1			25.9
Three	GB6-100	0.55	46.8	126.7	30.6	35.2	44.6
	GB6-125	0.78	43.8	91.3			43.5
	GB6-200	1.48	32.8	51.1			42.2
	GB6-250	1.94	29.1	40.3			41.9
	GB6-350	2.87	22.3	29.1			41.5
	GB6-500	4.25	15.6	21.5			41.3
Four	GB5-100	0.41	76.9	17.8	40.8	46.9	59.9
	GB5-200	1.11	54.3	73.6			57.5
	GB5-300	1.80	43.9	49.5			56.9
	GB5-400	2.50	33.7	38.7			56.7
	GB5-500	3.19	26.6	32.7			56.6
	GB5-600	3.88	21.0	28.8			56.5
Five	GB7-500	2.55	43.1	49.7	51.0	58.0	71.9
	GB7-600	3.11	37.5	44.0			71.8
	GB7-700	3.66	32.0	40.0			71.7

3.6 Failure map of GFRP sandwich beams

A failure map is a diagram that shows the different failure modes of composite sandwich beams. It can be developed by plotting the relationship between the geometric non-dimensional variable or geometric variables against physical variables (Petras & Sutcliffe 1999). In this study, the non-dimensional geometric properties of sandwich beams are the number of the sandwich layers and the shear span total to depth ratio. Failure maps of single sandwich beam have been studied by many researchers to find the governing failure modes of different sandwich beams materials. Their finding was that the failure modes of the sandwich beams are core crushing, core shear, skin-core debonding, and skin failure (Chen et al. 2001; Gibson 1984; Lim et al. 2009; Tagarielli et al. 2004).

In the present study, the failure mode of glue-laminated sandwich beams is affected by the shear span and the depth ratio variations. Thus, a failure map with two non-dimensional axes (shear span total to depth ratio in the x-axis, and number of sandwich layers in the y-axis) has been created to represent the potential mechanisms of failure for sandwich beams with different geometries and shear spans. The total depth depends on the number of sandwich layers. The experimental results from the earlier works of Manalo et al. (2010b; 2010d) have been included to add more details to the failure map.

Three failure modes (core crushing, core shear, and top skin flexural failure) have been defined in the failure map of the glue-laminated GFRP sandwich beam using the theoretical prediction equations for bending and shear in section 3.5.4. The predicted equation was developed in this work and it represents the transition from the flexure and core shear failure, which was determined by equating the flexural bending equation with the shear equation as shown below:

$$\frac{a}{d} = \frac{\sigma_f \, d}{6 \, c \, \tau_c} \qquad 3.11$$

The final failure map of the glue-laminated GFRP sandwich beams is shown in Figure 3.21. Two zones have been identified using Equations 3.11. Equation 3.11 is drawn to identify the zone that separates between core shear and flexural failure. It can be seen in the core failure zone that the two points corresponding to the specimen where core crushing was observed at higher load. This failure mode explains the expected behaviour of the single and glue-laminated GFRP sandwich beams with regards to the beam geometry. The failure map shows that in single sandwich beams, the failure mode changes from flexure to core shear when a/d is approximately 6.0. However, for glue laminated sandwich beams, the failure mode change is occurring at a much lower a/d ratio. Moreover, with increasing number of panels, the a/d ratio is reduced. This could be attributed to the presence of inner GFPR skin layers restricting the core shear failure in glue laminated beams.

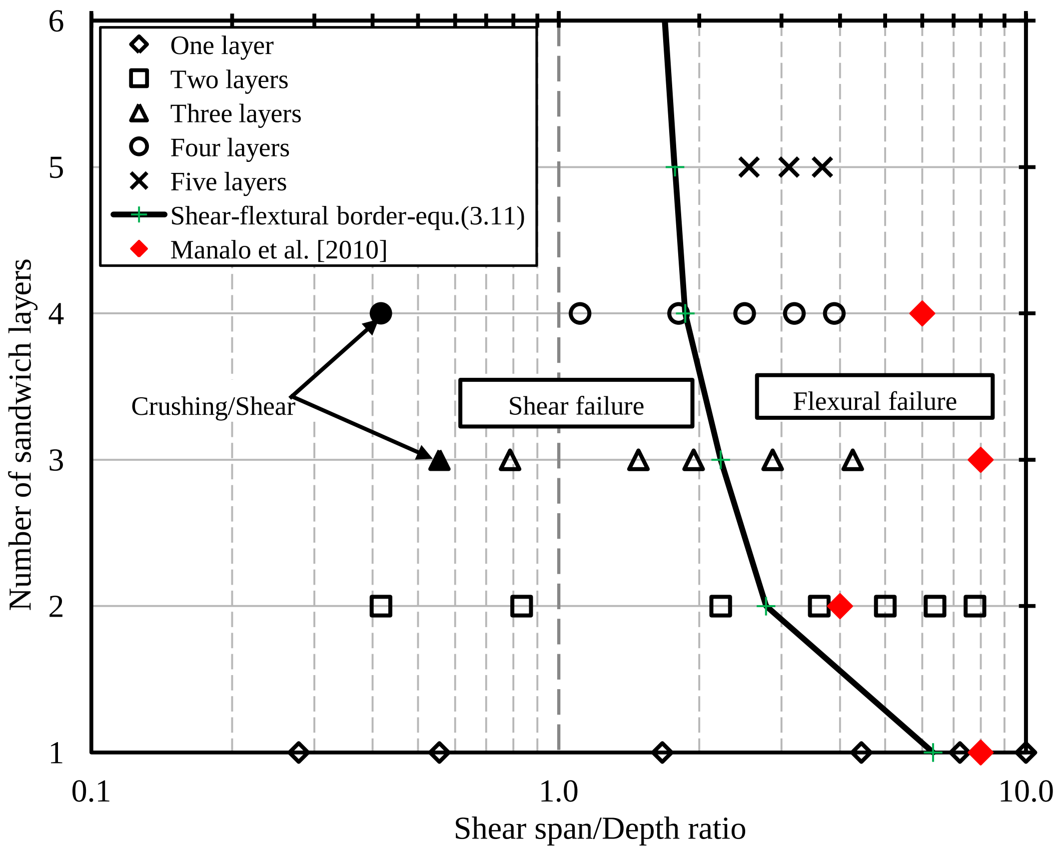

Figure 3.21 Failure-map of GFRP sandwich beams (x-axis in logarithm scale).

3.6 Chapter conclusions

The behaviour of single sandwich and glue-laminated GFRP sandwich beams with different cross sections and shear spans was investigated under four-point bending. The results of the experimental investigation provide a better understanding of the behaviour of GFRP sandwich beams under combined shear and flexure. The load carrying capacity of GFRP sandwich beams decreases as the shear span to depth ratio increases. The single sandwich beams showed slightly higher bending and shear capacities than the glue-laminated beams and this is attributed to debonding effects within the interim layers. The effect of shear span to depth ratio also impacted the apparent flexural stiffness of the sandwich beams. Higher apparent stiffness was observed for larger a/d.

The analytical equations proposed by other researchers for shear show an acceptable prediction for the specimens with a/d less than 2 while the prediction using the bending equation is better for a/d greater than 4.5. Moreover, it is clear that the analytical equations have limitations, especially in the combined shear and flexural failure zone (a/d greater than 2.0 and less than 4.5). Three different failure modes were reported, core crushing, core shear, and top skin compression failure. A failure map developed for different number of sandwich layers indicates that the failure mode changes with a/d ratio. It is recommended that further study is needed to predict the strength of such beams under combined failure modes.

This chapter is followed by the experimental investigation of two-dimensional GFRP sandwich slabs. The slabs were subjected to a point load test with different boundary restraints and sizes. The following work provides more information about the behaviour of sandwich slab structure.

Chapter 4

Behaviour of GFRP sandwich slabs

4.1 Introduction

Traditionally timber material has been used in different for civil engineering applications such as slabs and decks. The novel GFRP sandwich panel has become a possible alternative to replace timber in these structural applications. The GFRP sandwich panel is a material of light weight, high stiffness, long life, and with an ability to be cut, drilled and shaped on site (Van-Erp 2010). Experimental investigation of the behaviour of the GFRP sandwich slab is necessary to use the panel more widely. Islam and Aravinthan (2010) studied the behaviour of novel GFRP rectangular sandwich slabs with a fibre orientation design of $0^o/90^o$. The experimental work included applying both a point load and a distributed load on the slab with a width to length ratio (L_y/L_x) equal to two, and a total thickness of 15 mm. The work was done using screw and glue restraints. They concluded that the slabs behaved similarly under both types of load, and that the glue restraint does not provide much stiffness to the slab. Xiong et al. (2011) studied the mechanical behaviour of the sandwich panels with Al-Si tube cores and found that the bending behaviour is non-linear due to the membrane action and debonding.

The previous Chapter 3 discussed the experimental behaviour of the GFRP sandwich beams. The beams showed different failure modes based on the a/d ratio. The beam represents a one-dimensional element, and there is no variation of forces with respect to beam width. Extending the experimental tests is necessary for the slabs investigation as two-dimensional structural elements. In this chapter, the effect of slab width to length on the overall slab behaviour is discussed. In addition, the boundary restraints are considered along longitudinal and transverse dimensions of the slab. The variables are width to length (L_y/L_x) ratio, one-way and two-way supports, restraint types and fibre orientations. The tests were conducted using a static point load.

4.2 Samples preparation

The manufacturing process and the components of the GFRP sandwich slab were explained in Chapter 3. The GFRP sandwich slab was fabricated with the major fibre parallel to the longitudinal direction and the lesser fibre in the transverse direction. Samples were cut from the original GFRP sandwich panel with different dimensions as shown in Figure 4.1 Two types of sandwich panel with two different fibre orientations were generated as shown in Figure 4.1. The samples were prepared with $0^o/90^o$ fibre orientation and fibre orientation. The $\pm45^o$ slab was prepared by cutting the panel at 45^o because there is no fabricated panel with $\pm45^o$ orientation.

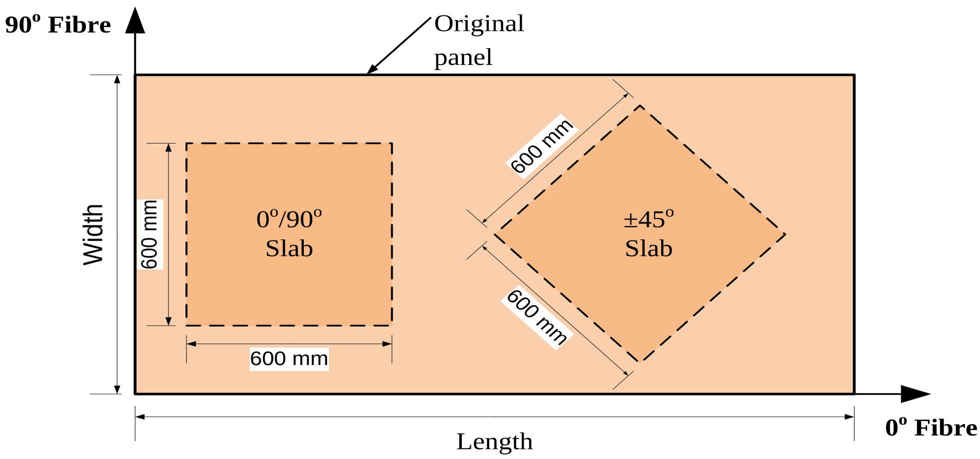

Figure 4.1 Fibre orientation of the GFRP sandwich slabs.

One-way and two-way supports were prepared with cross-section of 45 mm x 150 mm as shown in Figure 4.2. The difference between one-way support and two-way support is that the one-way support provides restraint to the slab in two sides along its width, while the two-way support provides a restraint for all sides of the slab. Few slabs prepared for the tests with different sizes and fibre orientations. The details of the tested samples are shown in Table 4.1. The cross-section details of the 15 mm and 18 mm slabs are shown in Figure 4.3. This was considered in order to find the effect of the cross section on the overall slab behaviour. The 15 mm slab has a GFRP skin and core thicknesses equal to 2 mm and 11 mm respectively. The 18 mm slab has a higher GFRP skin and core thickness of 3 mm and 12 mm respectively. Two types of boundary restraints, simple and screw were conducted to find the behaviour of the slab with different restraint conditions. Steel screws (8G x 65 mm) were used to fix the GFRP sandwich slabs to the timber support. The distance between the screws is approximately 275 mm.

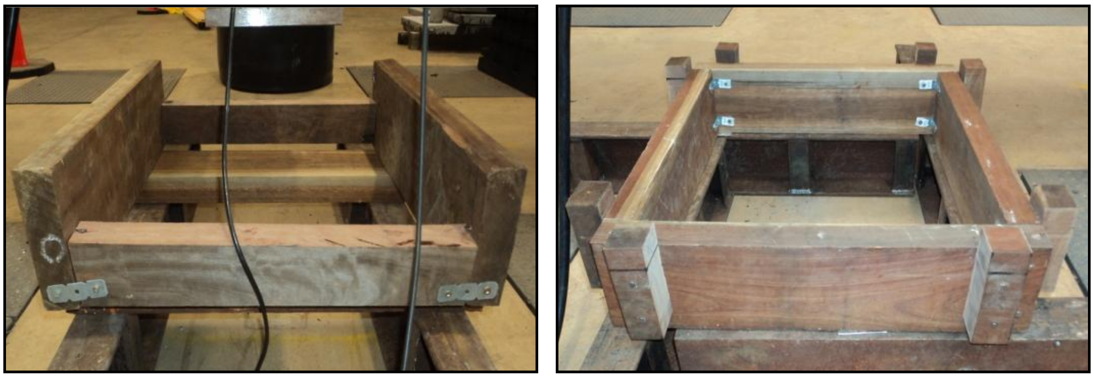

(a) One-way support (b) Two-way support

Figure 4.2 Timber supports for slab tests.

Table 4.1 GFRP sandwich slab samples

Name	Support conditions	Fibre orientations	Slab thickness mm	Dimensions mm	Restraint type
P1	Two sides (one-way)	$0^o/90^o$	15	600 x 600	Simple
P2	Two sides (one-way)	$0^o/90^o$	18	600 x 600	Simple
P3	Two sides (one-way)	$0^o/90^o$	18	600 x 600	Screw
P4	Four sides (two-way)	$0^o/90^o$	18	600 x 600	Simple
P5	Four sides (two-way)	$0^o/90^o$	18	600 x 600	Screw
P6	Four sides (two-way)	$-45^o/+45^o$	18	600 x 600	Simple
P7	Four sides (two-way)	$-45^o/+45^o$	18	600 x 600	Screw
P8	Four sides (two-way)	$0^o/90^o$	18	600 x 900	Simple
P9	Four sides (two-way)	$0^o/90^o$	18	600 x 900	Screw
P10	Four sides (two-way)	$0^o/90^o$	18	600 x 1200	Simple
P11	Four sides (two-way)	$0^o/90^o$	18	600 x 1200	Screw

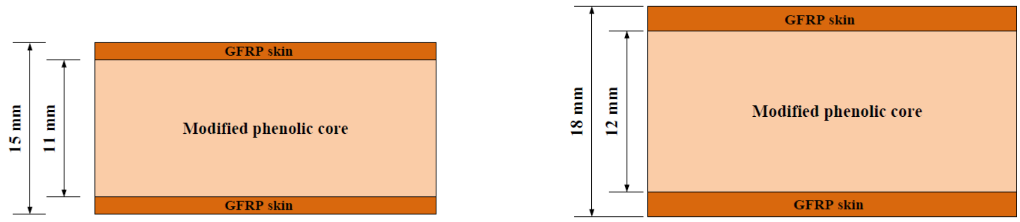

(a) 15 mm thickness (b) 18 mm thickness

Figure 4.3 GFRP sandwich slabs cross sections.

4.3 Experimental procedure

Different slabs were tested with two and four sided supports as shown in Figure 4.2. The strain gauges were used with different positions as shown in Figures 4.4-4.6. The strain position in Figure 4.4 was used for all slabs except the two-way 600 x 600 mm slabs. The strain positions for the two-way 600 x 600 mm slabs are shown in Figures 4.5 and 4.6. The strain gauges were fixed at the centre of the slab under the point load and in the edge of the slab (for one-way 15 mm slab) as shown in Figure 4.4. Figures 4.5-4.6 show that the strain gauges position at a distance of 120 mm from the slab centre. Strain gauge type KYOWA- KFG-3-120-C1-11L1M2R was used in the tests to measure the strain in the top and bottom faces of the GFRP sandwich slab. The experimental setup for one-way and two-way GFRP sandwich slabs is shown in Figure 4.7. A 100 x 100 mm steel plate was used under the point load, and a rubber pad was used to protect the strain gages in the top skin. A 500 kN load cell was used to apply the load to the slab.

A 600 mm x 600 mm single span one-way GFRP sandwich slabs were tested under point load in the mid-span. The 15 mm one-way GFRP sandwich slabs were tested with a simple boundary restraint and the 15 mm GFRP sandwich slabs were tested with simple and screw boundary restraints. Eight two-way GFRP sandwich slabs were tested with simple and screw restraints. The slabs are; P4, P5, P6, P7, P8 P9, P10, and P11, as shown in Table 4.1.

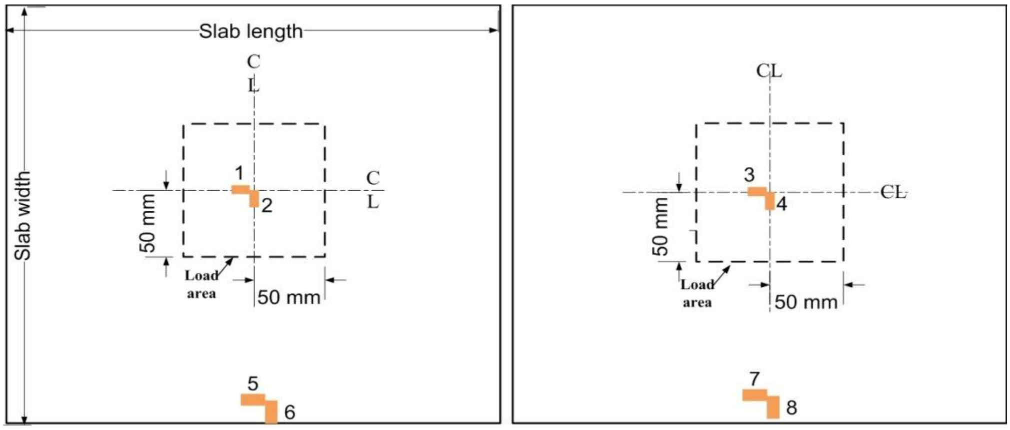

(a) Bottom skin (b) Top skin

Figure 4.4 Strain gauge positions for slabs P1, P2, P3, P8, P9, P10, and P11.

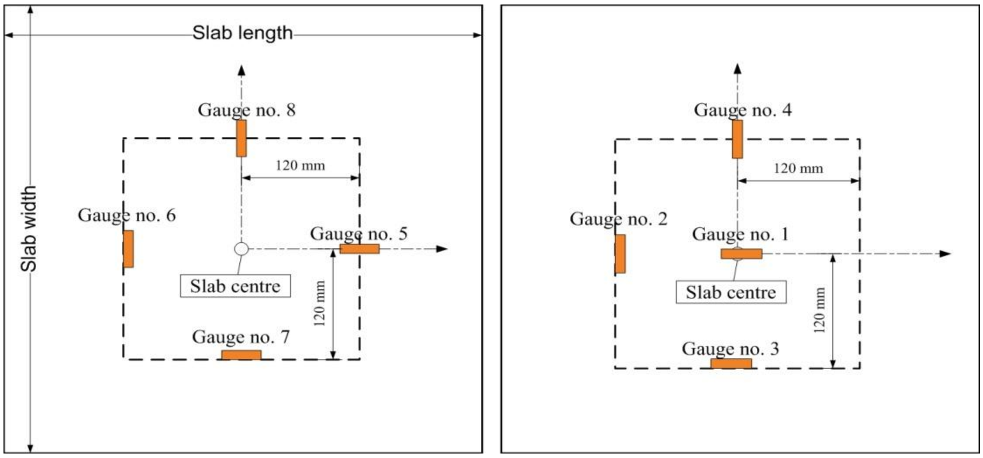

(a) Bottom skin (b) Top skin

Figure 4.5 Strain gauge positions for slabs P4 and P5.

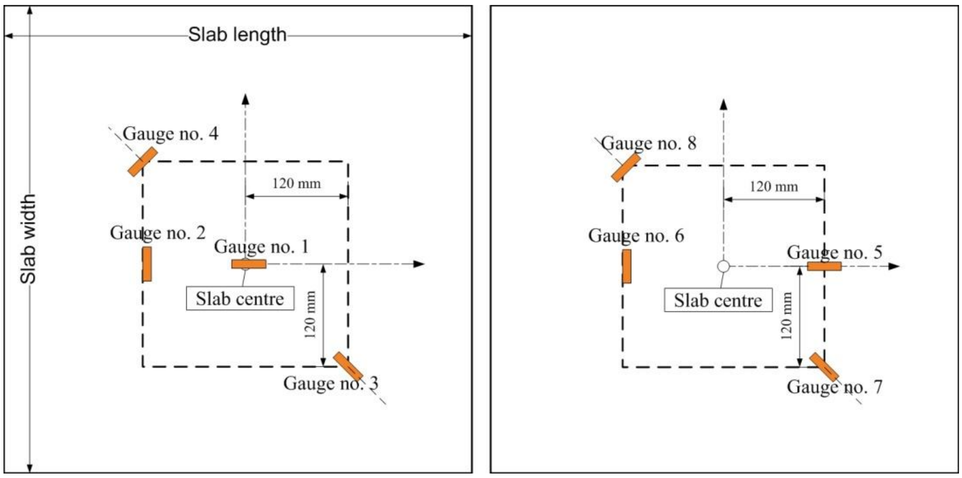

(a) Bottom skin (b) Top skin

Figure 4.6 Strain gauge positions for slabs P6 and P7.

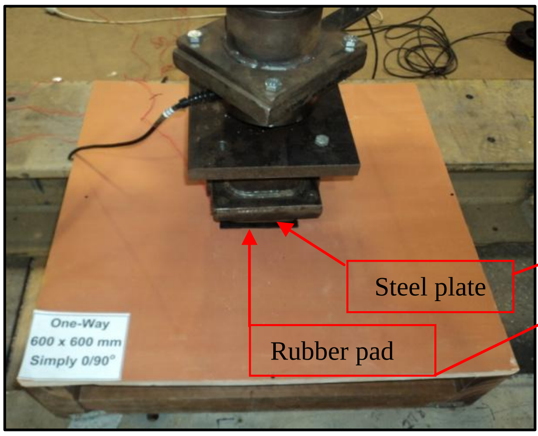

(a) One-way

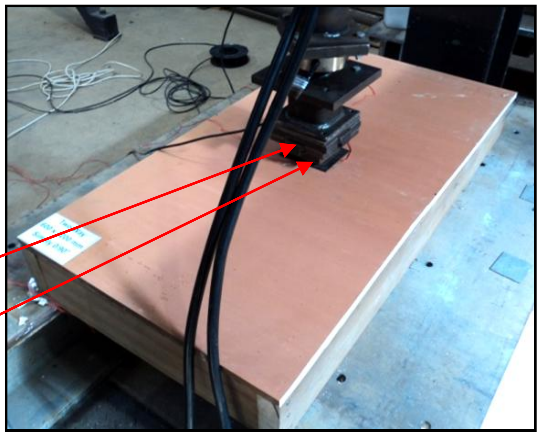

(b) Two-way

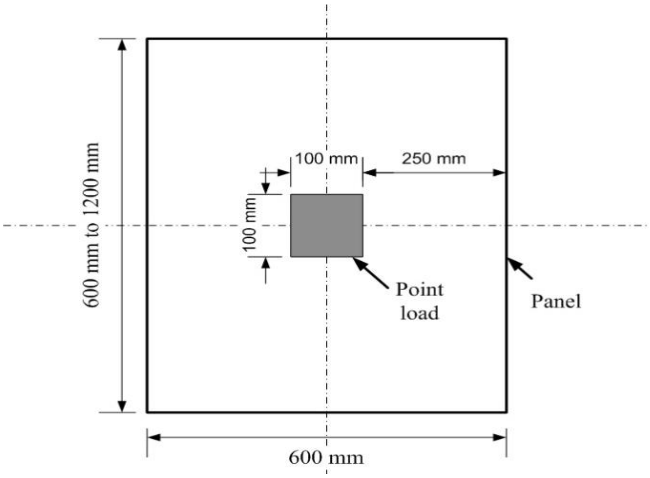

(c) Schematic diagram of the slab's test.

Figure 4.7 Slab setup.

4.4 Experimental results

4.4.1 One-way GFRP sandwich slab

Three samples of 15 mm thickness GFRP sandwich slab of were tested under simple restraints and two samples of 18 mm slabs thickness were tested with simple and screw restraints. The comparison between the slab test results is shown in Figure 4.8. The load-deflection curves show that the GFRP sandwich slab behave approximately linearly up to 75% of the ultimate failure load. At this load level all slabs have drops at points K and F, of which stage it is expected that the core part is cracking. Then, both slabs show a small drop, and continue with approximately linear behaviour in the last 25% of the ultimate load. The effect of the screws was tested on the 18 mm thickness slab behaviour as shown in the Figure 4.8, and this effect mainly contributes to the deflection of the GFRP sandwich slab as a support condition effect. The slab with the screw restraint showed an ultimate load similar to the simple restraint slab. The 18 mm thickness GFRP sandwich slab showed an ultimate load capacity approximately equal to twice the 15 mm slab thickness. In addition, the stiffness of 18 mm slab is 43% higher than the stiffness of 15 mm slab. The edge slab deflection was measured for the 15 mm slab thickness, and it is shown in Figure 4.9, compared to the central deflection. It can be seen that the edge deflection is 30% less than the central deflection of the slab.

The load-strain measurements for the GFRP slabs of 15 mm and 18 mm thicknesses are shown in Figures 4.10 and 4.11 respectively. The comparison between the centre and edge strain of the one-way slab is shown in Figure 4.12. The load-strain measurement of the one-way slab with screw restraints is shown in Figure 4.13. It shows that the strain reading shifts around points F and K for both slabs and this is expected to be due to the expecting core cracking. The load-strain measurements show that the 0^o-direction strain is higher than the 90^o-direction strain. Furthermore, the bottom strain is higher than the top strain due to the cracking of the core on the bottom side and the difference in the tension and compression elastic modulus of the GFRP skin. The one-way GFRP sandwich slab showed a centre strain higher than the edge strain in both directions as shown in Figure 4.13. A summary of all static point load tests on the GFRP sandwich slabs is shown in Table 4.2.

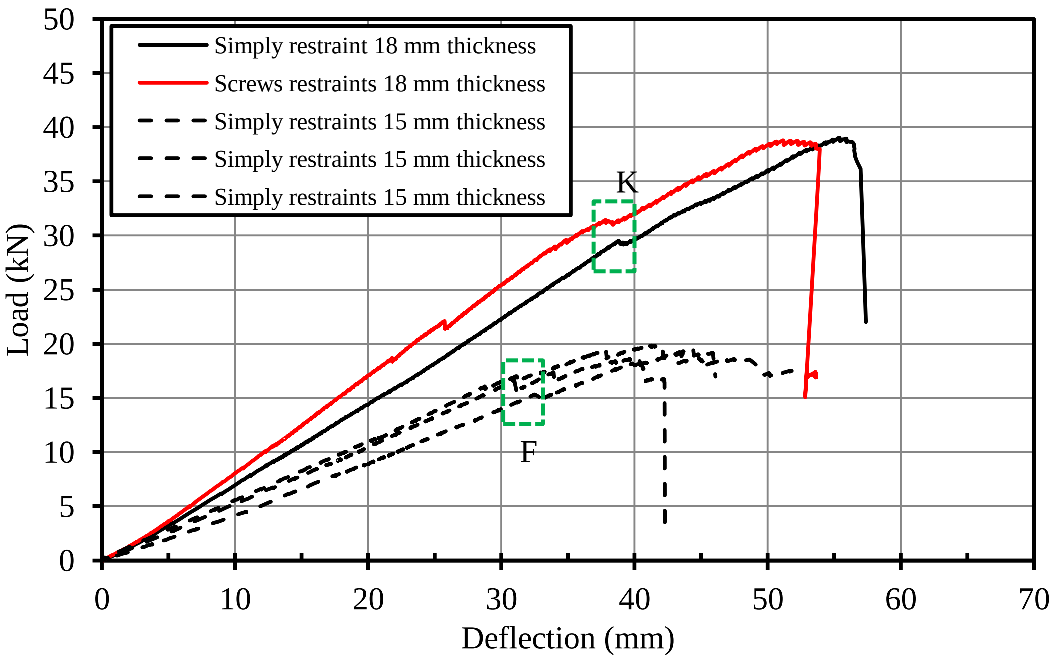

Figure 4.8 Load-deflection curves of single span sandwich slabs (15 mm and 18 mm thicknesses).

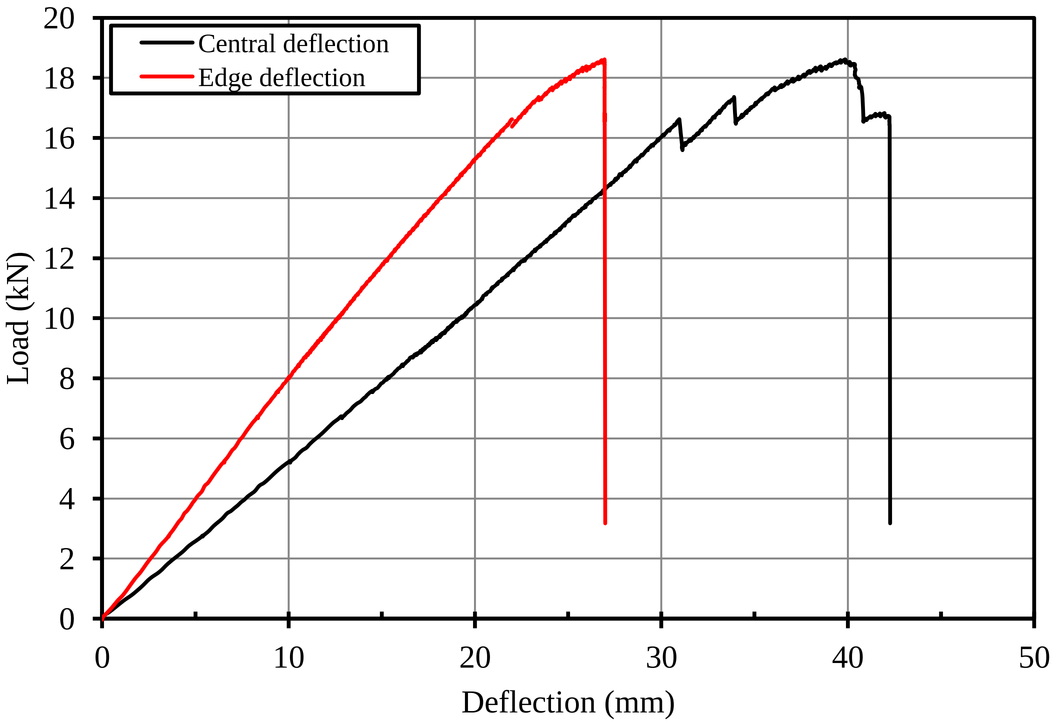

Figure 4.9 Central deflection and edge deflection of 15 mm thickness one-way slab.

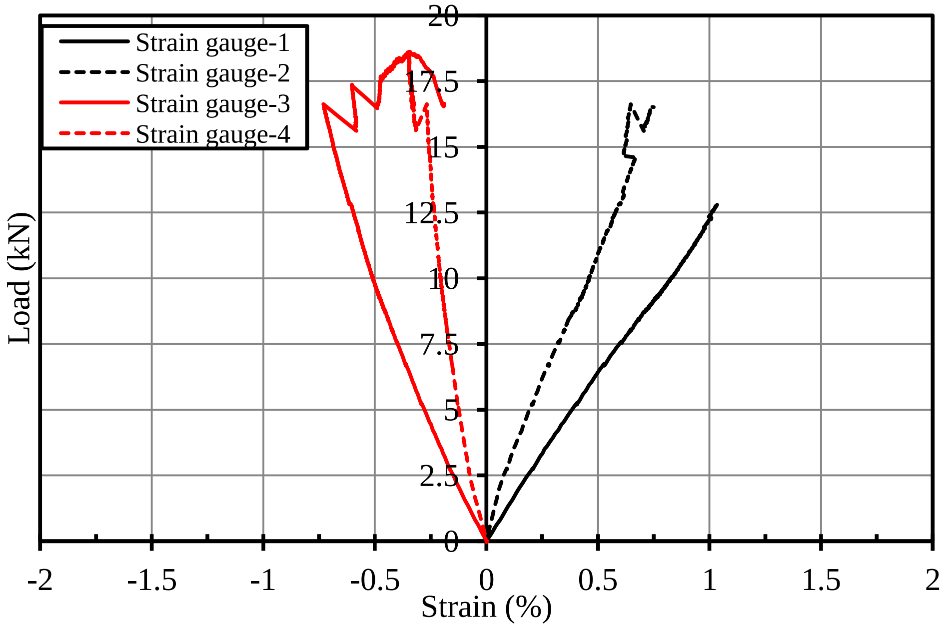

Figure 4.10 Load-strain of simple restraint slab (15 mm thickness).

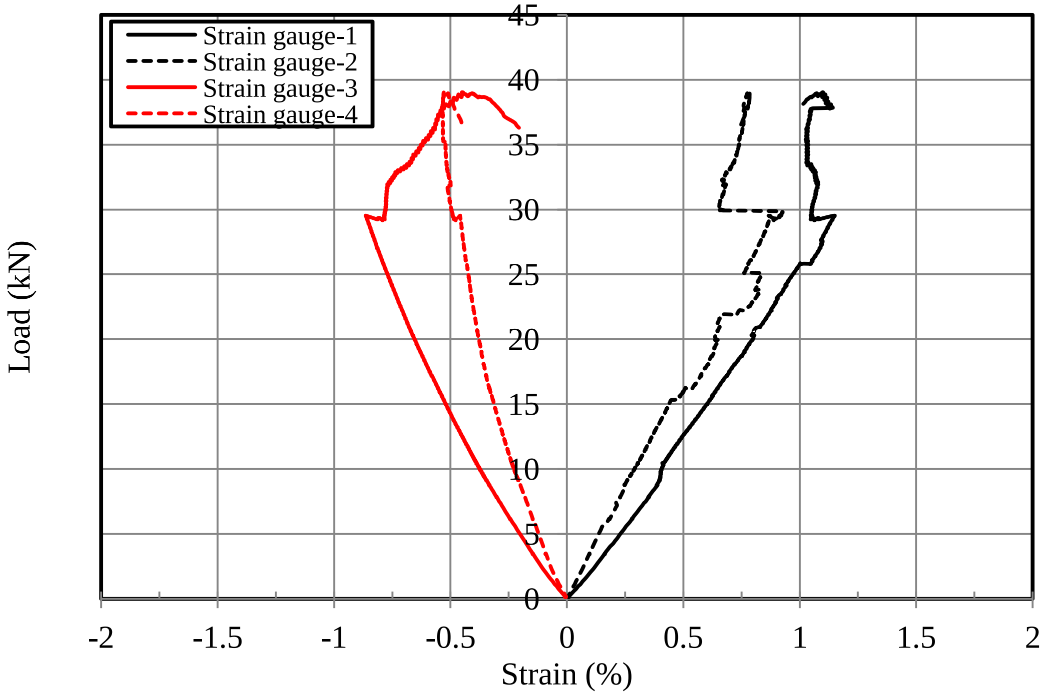

Figure 4.11 Load-strain of simple restraint slab (18 mm thickness).

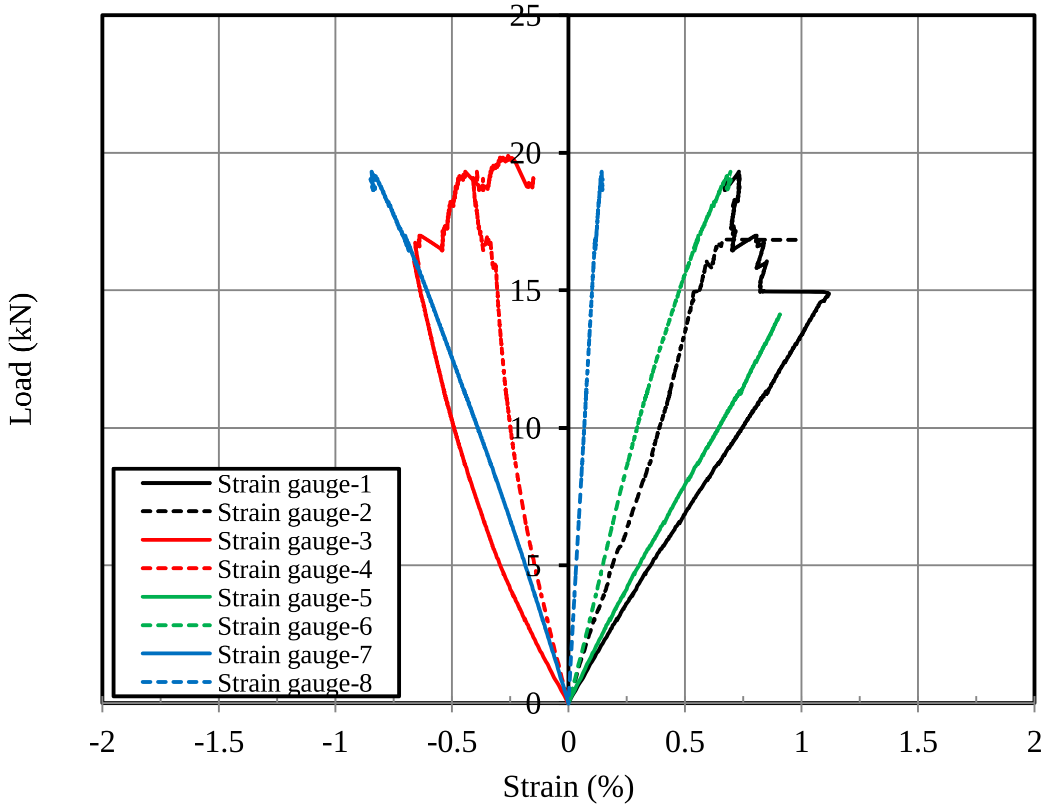

Figure 4.12 Comparison between strain at centre and edge of one-way slab.

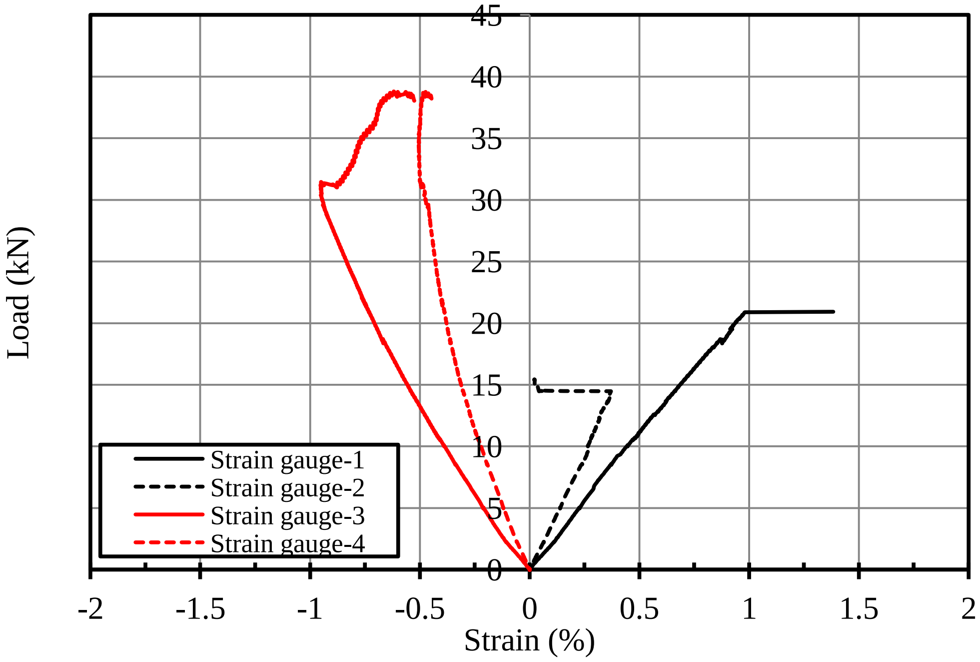

Figure 4.13 Load-strain of screw restraint slab (18 mm thickness).

4.4.2 Two-way GFRP sandwich slab

During the testing, the first cracking sound was heard around 27-30 kN of load for all the slabs. The load-deflection curves for the $0^o/90^o$ (P4 and P5) and $\pm45^o$ (P6 and P7) slabs are shown in Figures 4.14 and 4.15. There is a drop in the load-deflection curves around 27-30 kN for all slabs. This drop is due to the core cracking. The screw boundary restraints have a small effect for on the deformation of the two-way square GFRP sandwich slab. The effect of the slab width to length ratio was conducted on slabs P8, P9, P10, and P11. Load-deflection curves are shown in Figures 4.16 for the GFRP sandwich slabs P8 and P9. Figure 4.16 shows the comparison between simple and screw restraints on the two-way (600 x 900 mm) GFRP sandwich slabs. The same comparison was done for the two-way (600 x 1200 mm) GFRP sandwich slab, and the results are shown in Figure 4.17. In general, the effect of the screw restraint on the behaviour of the two-way GFRP sandwich slab is not significant, and the slabs behave in a similar way with both simple and screw restraints.

The comparison between the two-way slabs shows that the square slabs have a slightly different behaviour at failure compare to the rectangular slabs. The strain reading for the two-way square slab tests, P4 ($0^o/90^o$) and P6 ($\pm45^o$) are shown in Figures 4.18 (a) and (b), and the strain position is shown in Figures 4.5 and 4.6. Both slabs at the load level 27-30 kN show the top and bottom strains reach the value of 0.6% and 1.0% respectively. In general, the bottom strain is higher than the top strain for both slabs due to the core cracking and the difference between tension and compression module of the GFRP skin. In addition, the $\pm45^o$ bottom skin strain is lower than the $0^o/90^o$ bottom strain because the $\pm45^o$ has a lower deformation than the $0^o/90^o$ slab. The strain readings for the two-way rectangular GFRP sandwich slabs P8, P9, P10, and P11 are shown in Figures 4.19 and 4.20. It can be seen that the central strain in top skin reaches a maximum value at the load between 27-30 kN, then the strain decreases. This is due to core cracking and bottom skin relaxation under point load. The maximum value of the central strain of the bottom skin is about 1.1% at this load level. Furthermore, the top strain or the compression strain is around 0.75%. It was noticed that some of the strain gauges in the tension side were broken before final failure. A summary of the two-way slab tests are shown in Table 4.2.

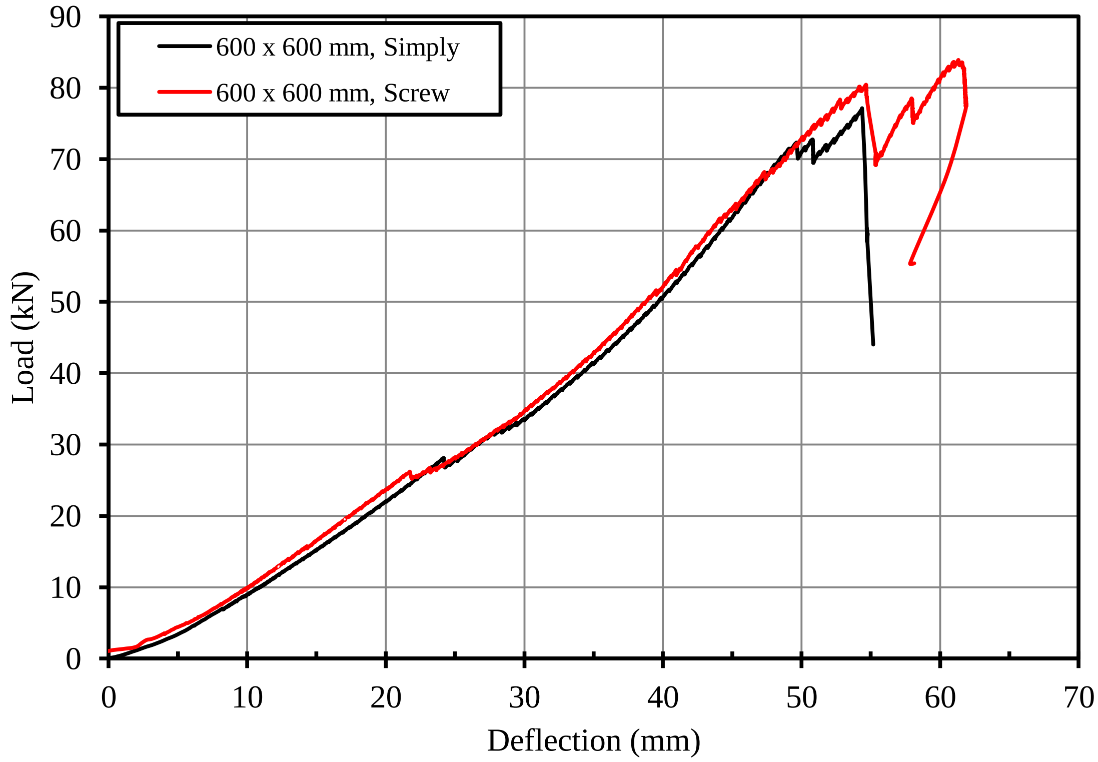

Figure 4.14 Load - deflection for 600 x 600 mm slab $0^o/90^o$ fibre orientation.

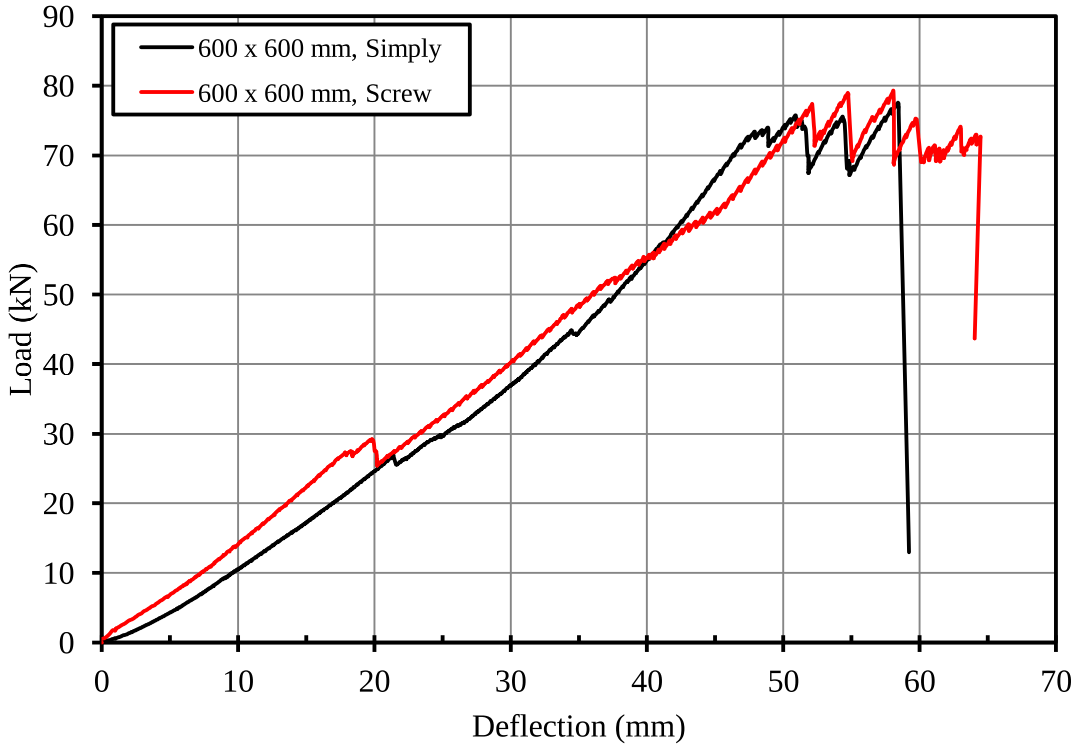

Figure 4.15 Load - deflection for 600 x 600 mm slab $\pm 45^o$ fibre orientation.

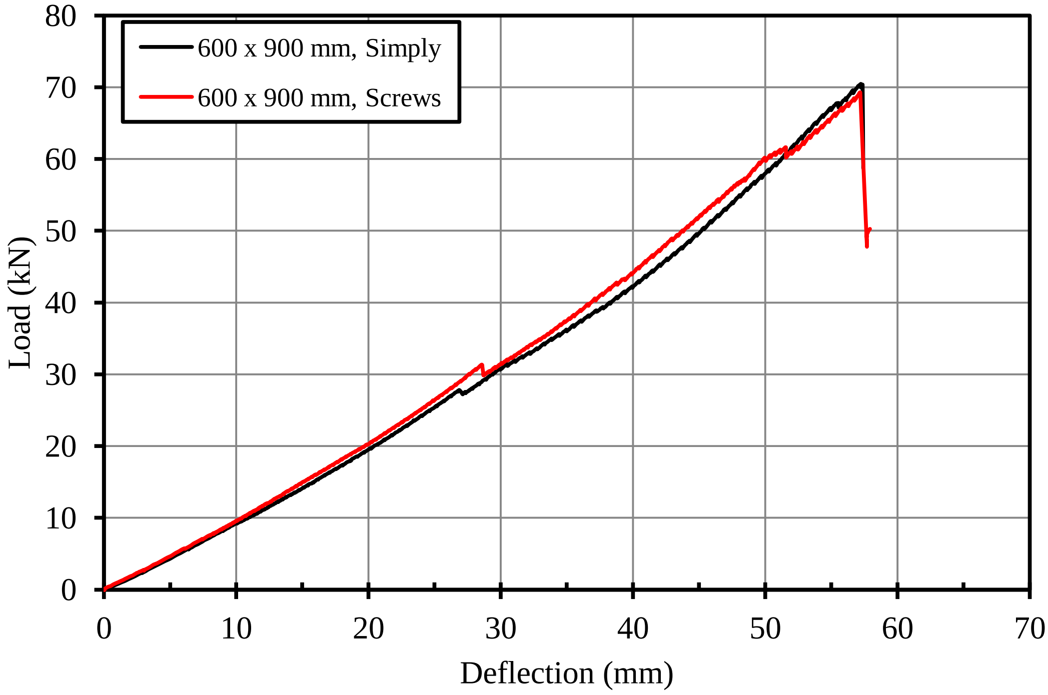

Figure 4.16 Load-deflection curves for 600 x 900 mm slab.

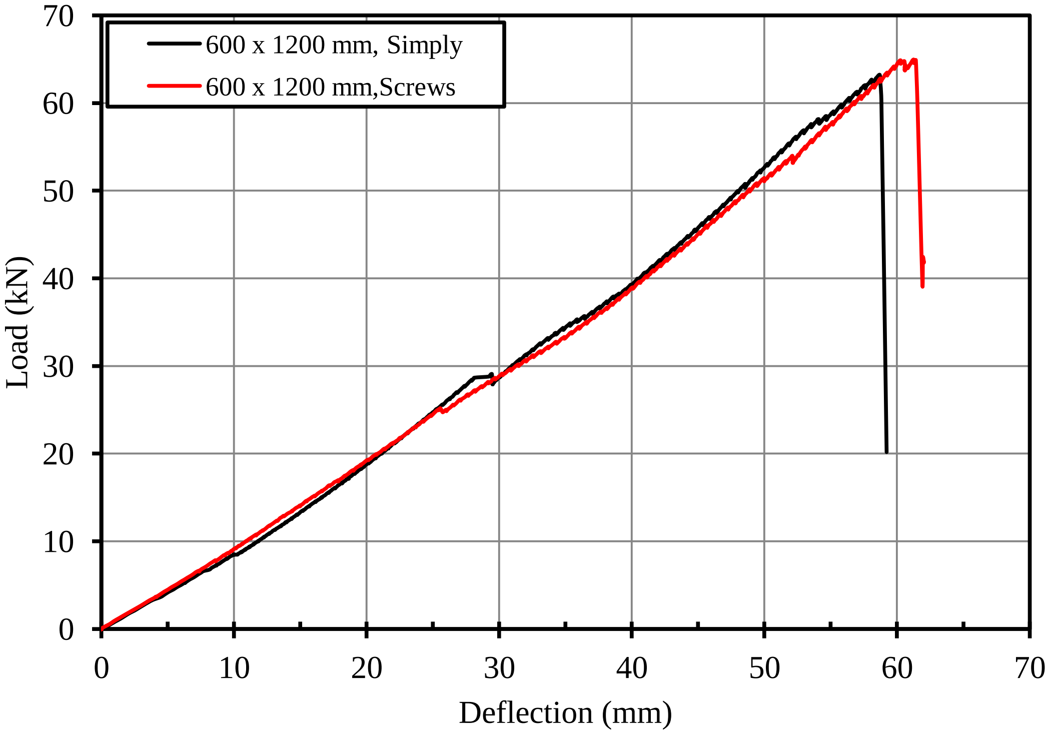

Figure 4.17 Load-deflection curves for 600 x 1200 mm slab.

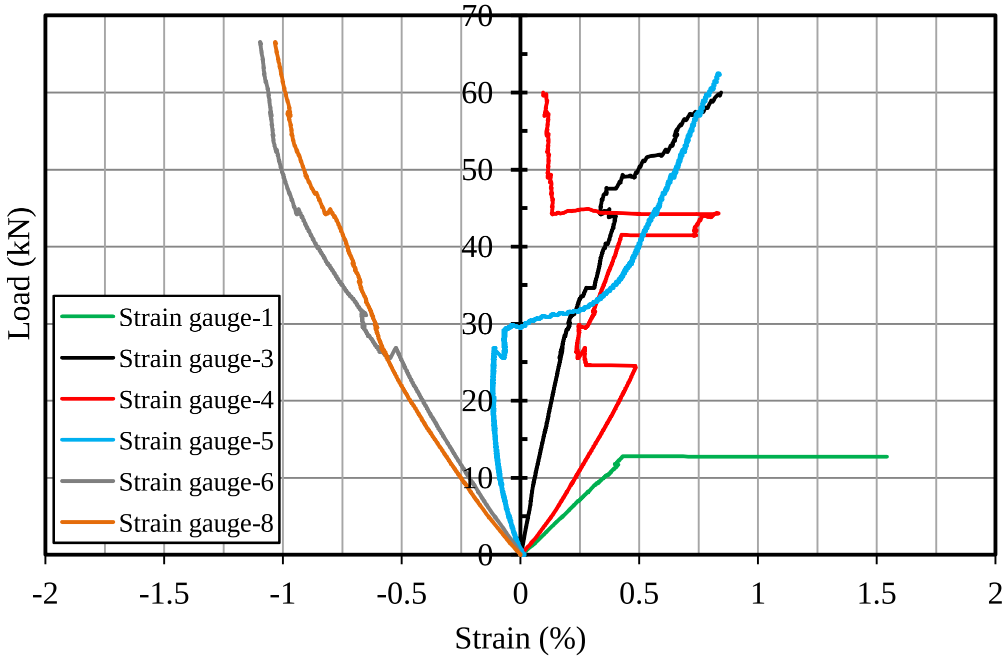

(a) ±45° fibre orientation.

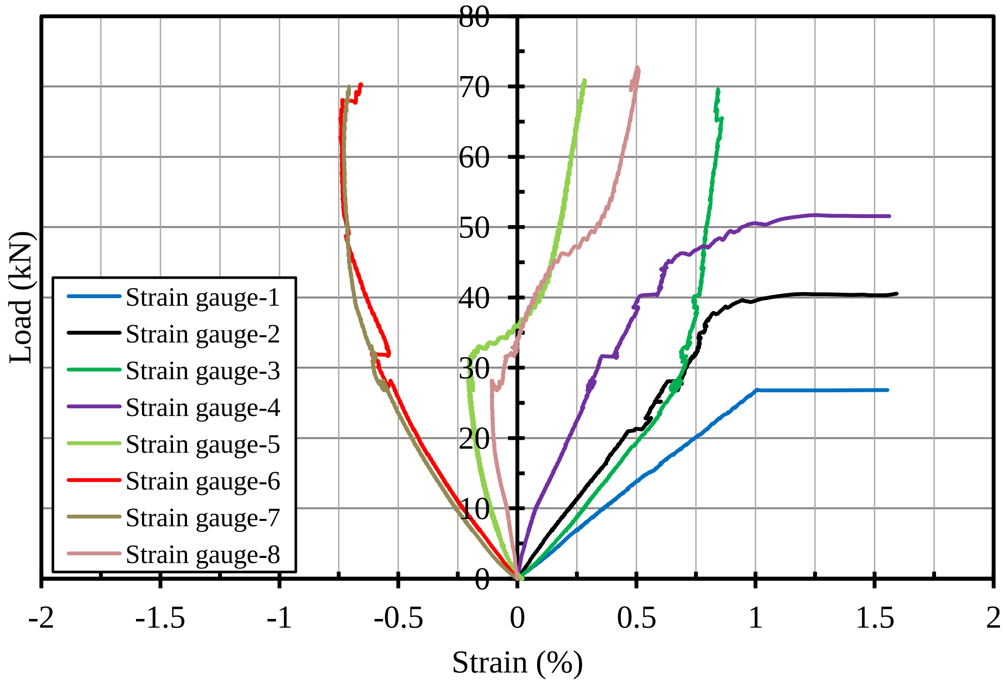

(b) 0°/90° fibre orientation.

Figure 4.18 Load-strain for 600 x 600 simple restraint slabs.

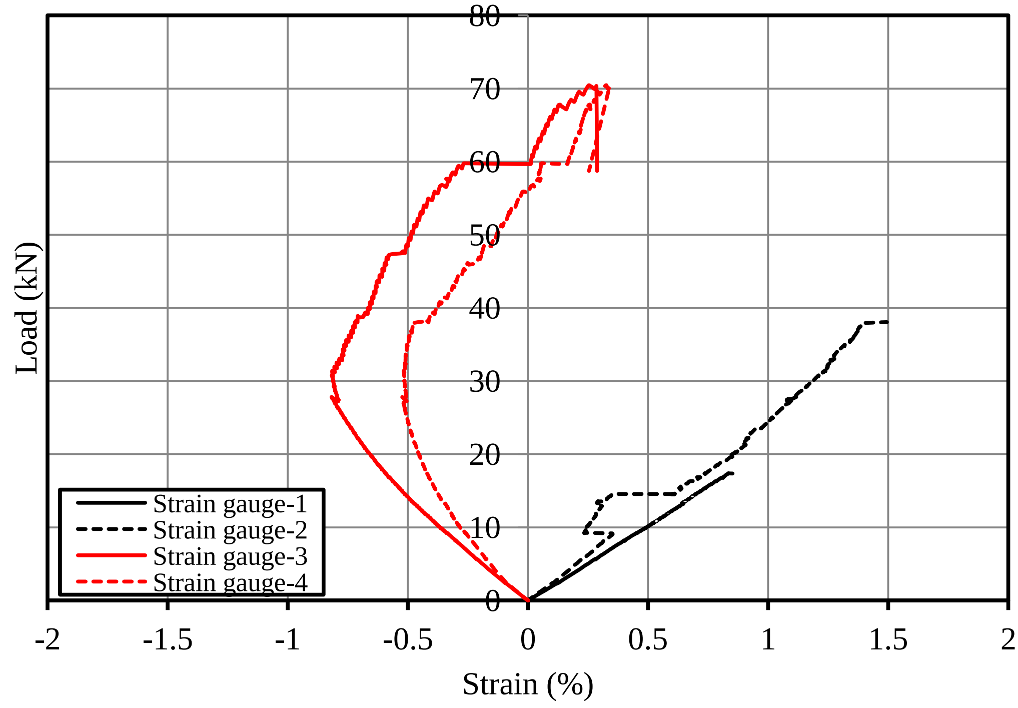

(a) 600 x 900 mm slab dimensions.

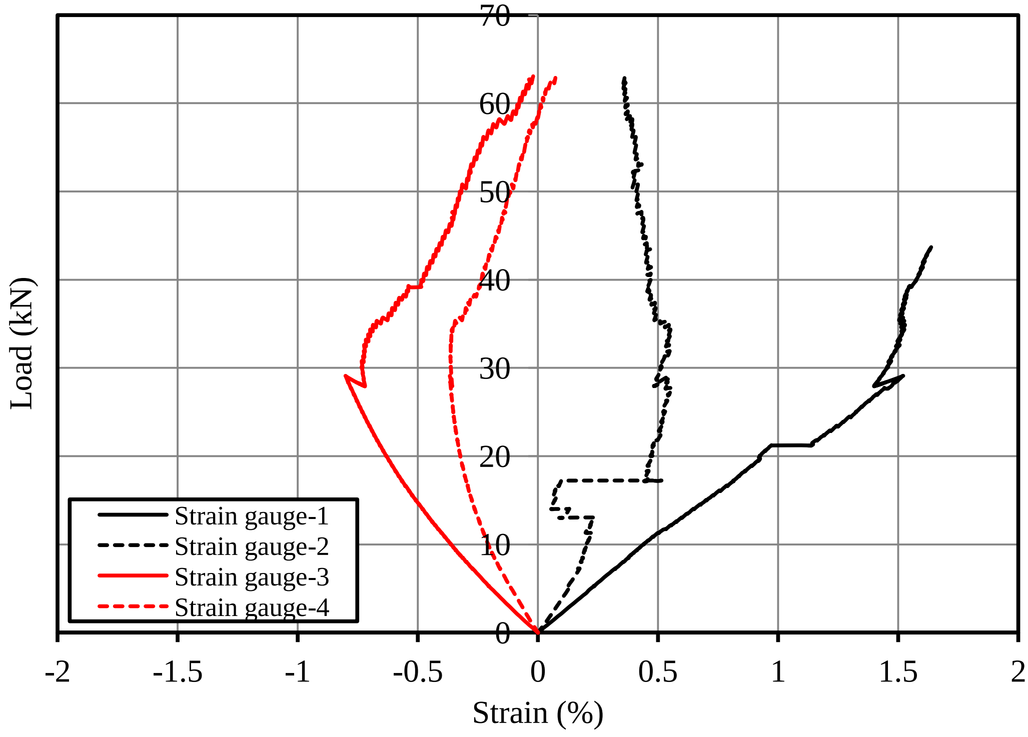

(b) 600 x 1200 mm slab dimensions.

Figure 4.19 Load-strain curves for simple restraint GFRP slabs.

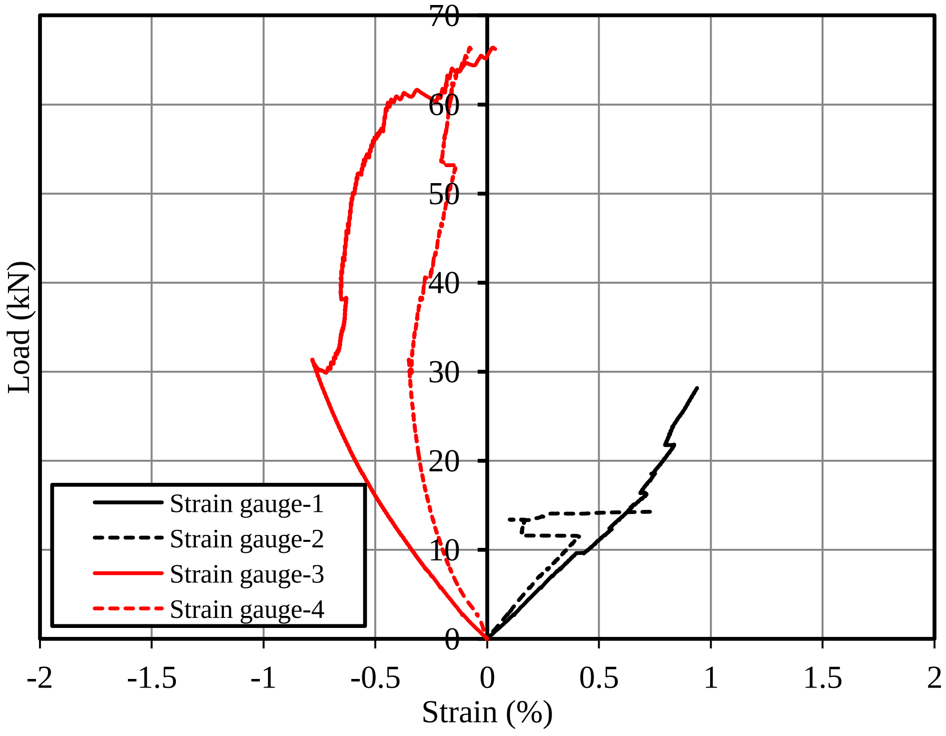

(a) 600 x 900 mm slab dimensions.

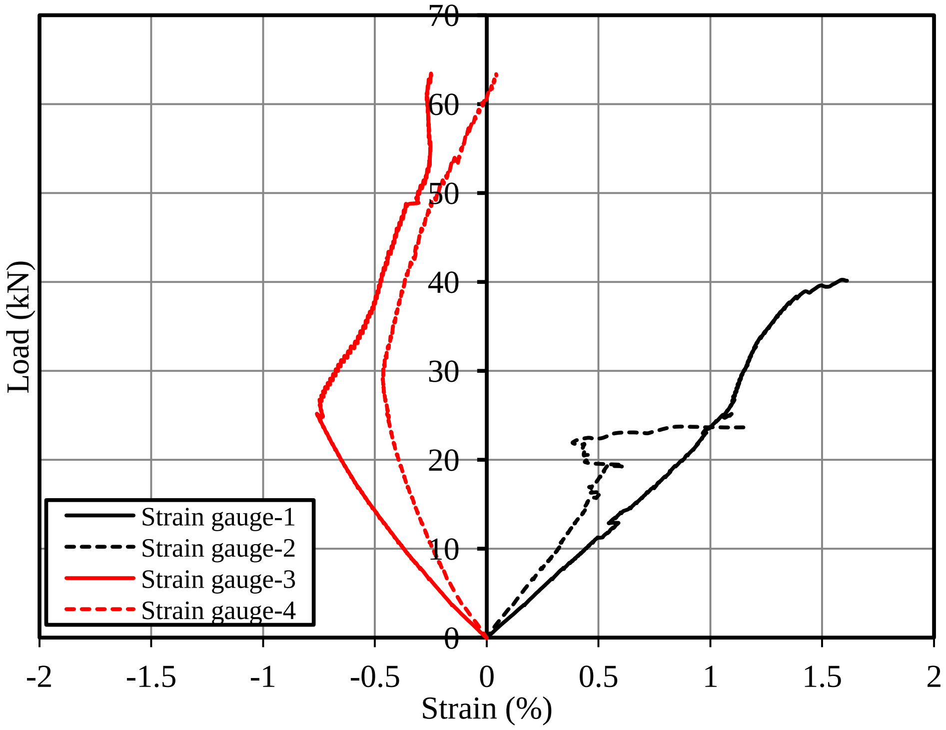

(b) 600 x 1200 mm slab dimensions.

Figure 4.20 Load-strain curves for screw restraint two-way slabs.

Table 4.2 Experimental results summary

Name	Size mm x mm	Support	Restraint type	Fibre orientation	Ultimate load kN	Deflection at ultimate load mm	Stiffness N/mm	Major notice at failure
P1	600 x 600	one-way	Simple	$0^o/90^o$	19.60	40.50	500.12	Failure line is parallel to the support
P2	600 x 600	one-way	Simple	$0^o/90^o$	38.74	54.99	715.60	=
P3	600 x 600	one-way	Screw	$0^o/90^o$	38.32	49.94	875.53	=
P4	600 x 600	two-way	Simple	$0^o/90^o$	78.51	53.73	1252.14	Core crack and bottom skin debonding
P5	600 x 600	two-way	Screw	$0^o/90^o$	82.95	60.63	1253.21	Core crack parallel to the support
P6	600 x 600	two-way	Simple	$\pm 45^o$	77.93	57.58	1574.80	Diagonal cracking
P7	600 x 600	two-way	Screw	$\pm 45^o$	77.81	57.67	1584.71	Diagonal cracking
P8	600 x 900	two-way	Simple	$0^o/90^o$	70.45	57.24	1111.12	Core cracks towards the corners
P9	600 x 900	two-way	Screw	$0^o/90^o$	69.29	57.19	1119.23	Core crack is limited between the restraints points
P10	600 x 1200	two-way	Simple	$0^o/90^o$	63.24	58.65	869.56	Core cracks in 45^o towards the corners
P11	600 x 1200	two-way	Screw	$0^o/90^o$	64.86	60.01	871.31	Core cracks at restraint points

4.5 Discussion

4.5.1 Comparison of slabs load-deflection behaviour

The experimental results of one-way slabs showed two drop points in the load-deflection curve as shown in Figure 4.8. Both slabs showed a small drop at 75% of the ultimate load at points F and K. For the 15 mm and 18 mm thickness GFRP slabs, the first drop happened at mid-span deflection equal to 30.80 mm in point F and mid-span deflection equal to 37.64 mm in point K respectively. The drop happened because of core cracking. The slope of the load-deflection curve represents the overall stiffness of the structure. The stiffness of the slab after the first drop F and K is approximately the same as before drop points F and K. As a consequence, there is no major stiffness degradation of the slab after the points F and K up to failure. Final failure of the slab happened at an ultimate load equal to 19.6 kN and 38.74 kN for 15 mm and 18 mm slab thicknesses respectively. The 15 mm one-way slab showed a difference between the central and edge deformation. Therefore, the one-way slab does not behave like a beam when it is loaded by a point load. This happened due to the contribution of the transverse direction and the variation of forces distribution along the width of the slab.

All GFRP sandwich slabs show approximately similar behaviour under both simple and screw restraints. The comparisons between the simple restraint slabs are shown in Figure 4.21. The three slabs show approximately the same behaviour with different ultimate loads. The ultimate load of two-way slabs decreases with increase in the transverse length of the slab as shown in Figure 4.21. Increasing the width to length (L_y/L_x) ratio of the slab reduces the effect of the supports along the length of the slab (L_x) on the behaviour of the slab and this causes the reduction in ultimate load.

The non-linear behaviour of the slabs is due to two factors. The first factor is the two-way support effect and the second is related to the membrane action. The effect of material behaviour is shown at the first drop in the load-deflection curve, where the first drop of all slabs happened between 27 - 30 kN. The drop is due to the core cracking under the point load. This leads to the redistribution of the forces through the GFRP skin. One-way and two-way 600 x 600 mm GFRP sandwich slab load-deflection curves are compared in Figure 4.21. The two-way slab showed an ultimate load almost double the ultimate load of the one-way slab. Furthermore, the membrane effect on the two-way GFRP sandwich slab is higher than the one-way GFRP slab as shown from Figure 4.21.

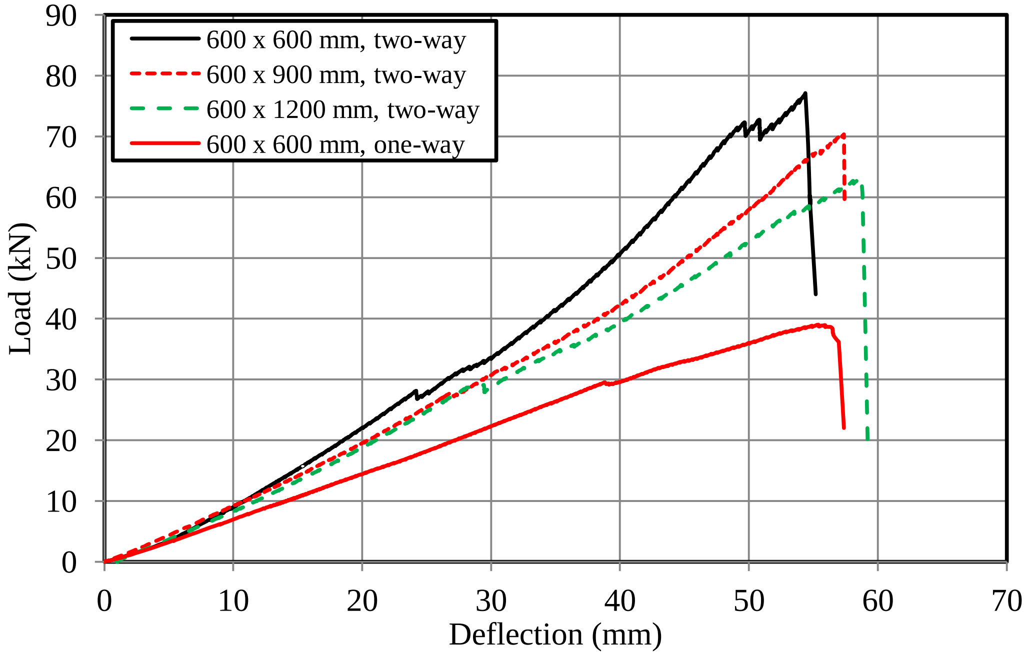

Figure 4.21 Load-deflection curves for two-way and one-way slabs.

The experimental load-deflection behaviour of different slabs shows that the mid-span deflections of the slabs are affected by different variables. These are the number of supports, fibre orientation, restrain types, and width to length ratio. From the previous load-deflection curves in Figures 4.8, and 4.14-17, the deflection of the mid-span was determined at load of 20 kN. The load of 20 kN was selected because this is before any cracks happen in the slab. The comparison between the 18 mm slabs mid-span deflection is shown in Figure 4.22. It can be seen that the one-way slab shows a higher deflection than the others. The square slabs (L_y/Lx=1.0) with a screw boundary restraint have a lower deflection than the simple restraint slabs. Furthermore, there is a small difference in the deflection between the simple and screw restrained rectangular slabs (L_y/L_x=1.5 and L_y/Lx=2.0) at this stage of loading. In addition, the square slabs with $0^o/90^o$ fibre orientation have a higher deflection than the slabs with a $\pm45^o$ fibre orientation. The stiffness of the simple and screw restrained one-way and two-way slabs are shown in Figure 4.23. The stiffness of the two-way slab is higher than the stiffness of the one-way slab. Furthermore, the stiffness of the $\pm45^o$ slab is higher than the stiffness of $0^o/90^o$ slab. The stiffness of the two-way slab is reduced by increasing the width to length ratio.

The strain behaviour showed that the bottom strain is greater than the top strain. The one-way slab with 18 mm thickness showed a bottom and top strain equal to 1.1% and 0.8% at the first drop at load level 30 kN. The bottom strain is located on the bottom skin at the tension zone. The converted stress using the skin elastic modulus (11750 MPa) shows that the top skin and bottom skin stresses are equal to 94 MPa and 129 MPa respectively. These values are below the ultimate strength of the skin and it confirms that the failure is initiated by the core. In addition, the strain values observed in the two-way slabs is equal to 1.1% and 0.75% at a load of around 30 kN for the bottom and top skins respectively. The core cracking strain in tension is equal to 0.62% as shown in Appendix-A. It can be concluded that the strain the bottom exceeds the cracking strain of the phenolic core. The drops in the load-deflection curves are due to core cracking. The maximum strain values observed at failure is equal to 1.1% and 1.5% for compression and tension respectively. Similarly, the top and bottom skin stresses are equal to 130 MPa and 176 MPa respectively, which confirm that the skin stress is below the ultimate strength.

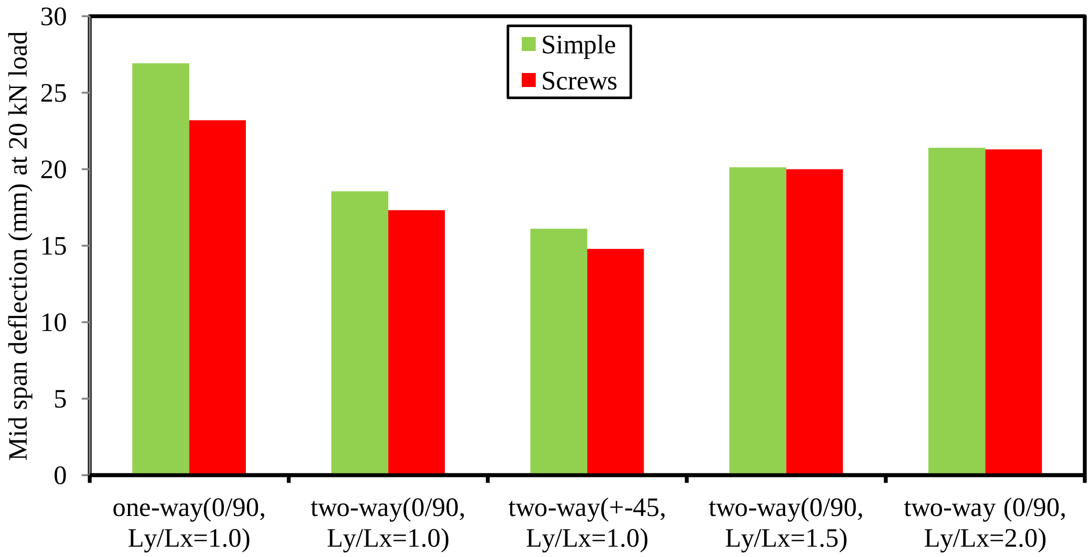

Figure 4.22 Mid-span deflection of slabs at load equal to 20 kN.

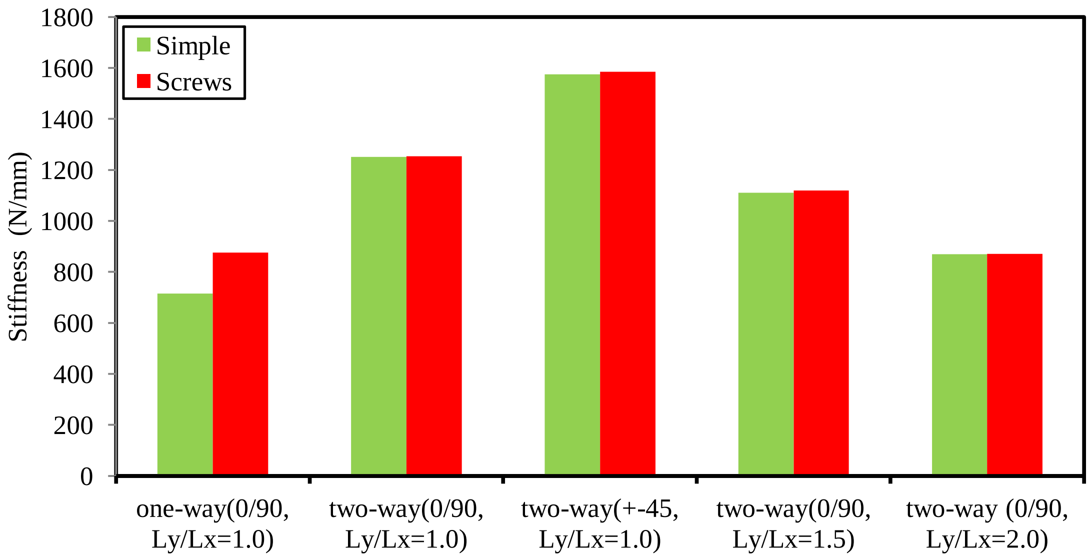

Figure 4.23 Stiffness of simple and screw restraints slabs.

4.5.2 Effect of fibre orientations

Effect of fibre orientation is very clear from the load - deflection curves in Figures 4.24 and 4.25. The slabs with $\pm 45^{o}$ fibre orientation have a lower deflection than slabs with $0^{o}/90^{o}$ fibre orientation. The stiffness of the slab was calculated at an early load level of the load-deflection curve as shown previously in Table 4.2. These stiffness calculations indicate that the fibre orientation has an obvious effect on the stiffness of the GFRP sandwich slab. The ±45° slab is 25% stiffer than the 0°/90° slab under both types of restraint. Finally, the deflection shape is different between ±45° and 0°/90° GFRP sandwich slabs as shown in Figure 4.26. The ±45° slab showed a concave type of deflection. In contrast, the 0°/90° GFRP sandwich slab showed a convex type of deflection. This is due to the forces distribution through the slab skins. In the ±45° slab, the force distribution become diagonal and causes a stretching to the slab from the corners. In 0°/90° slab the forces become parallel to the supports and causes stretching of the slab from the middle of each side.

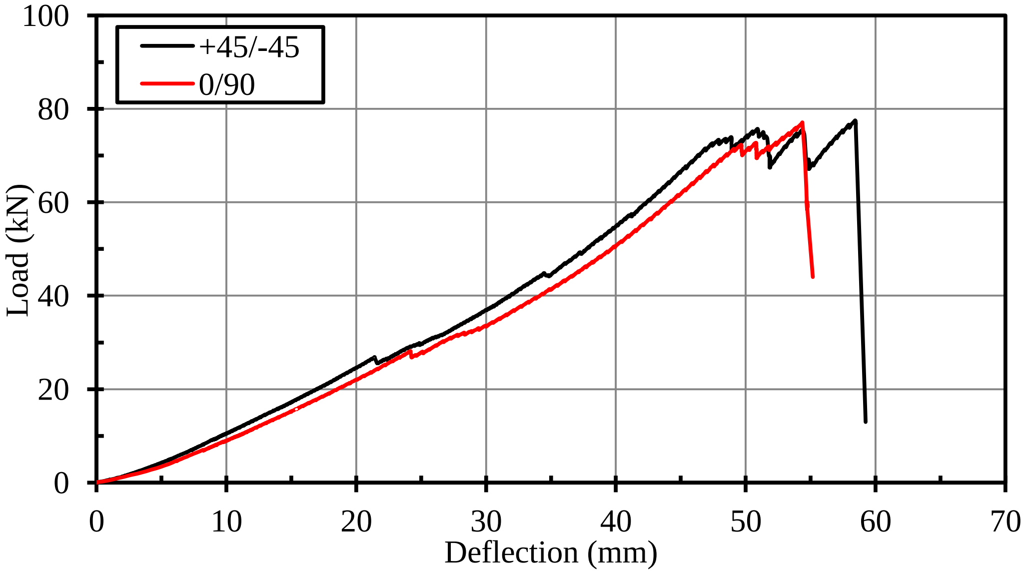

Figure 4.24 Load-deflection for two-way 600 x 600 mm simple restraint slabs.

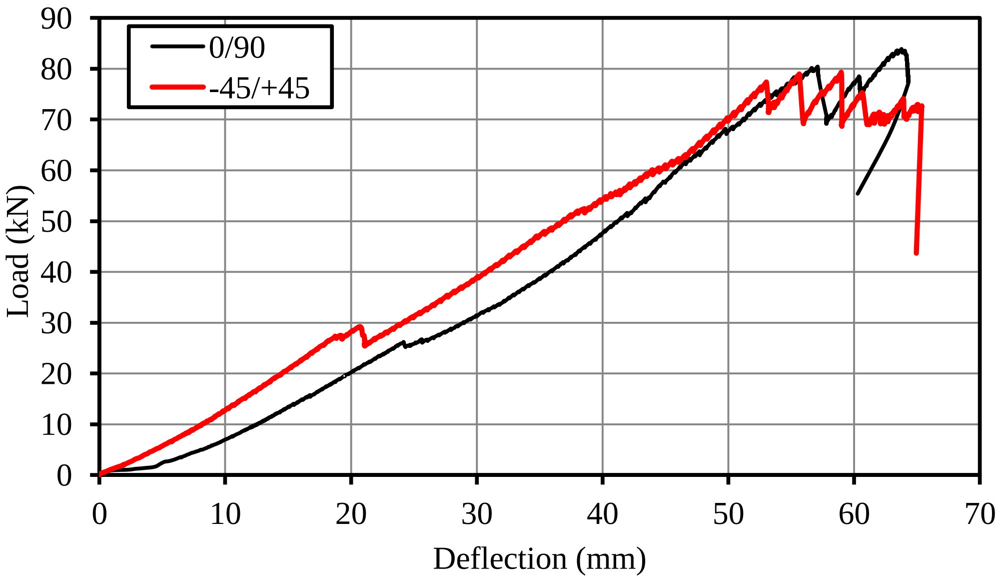

Figure 4.25 Load-deflection for two-way 600 x 600 mm simple restraint slabs.

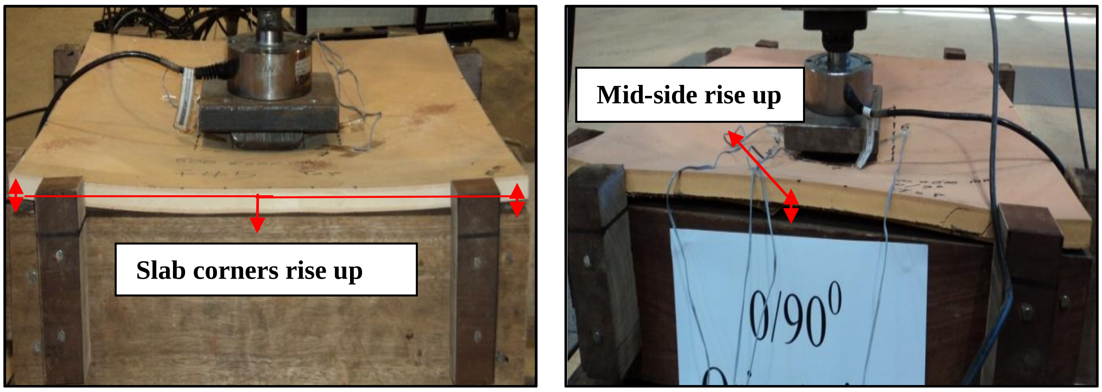

(a) ±45^{o} fibre orientation. (b) 0^{o}/90^{o} fibre orientation.

Figure 4.26 Deformation shapes of simple restraint slabs.

4.5.3 Effect of restraint conditions

Steel screws were used to fix GFRP sandwich slabs in building construction. This slab was fabricated with a high core density to enhance its strength and ability to hold screws. A load of 20 kN was selected to compare the deflection of ±45^{o} and 0^{o}/90^{o} GFRP sandwich slabs under different restraint conditions. The 20 kN load represents about 25% of the ultimate failure load. The ratio of central deflection for simple restraint slabs and screw restrained slabs are shown in Figure 4.22. It can be seen that using screws to fix the square GFRP sandwich slabs has a small effect on the mid-span deflection. In addition, both slabs in one-way and two-way configurations show the same behaviour. However, the effect of screw restraint is insignificant for the rectangular GFRP sandwich slabs.

The largest deformation in the ±45^{o} slab is located at the corners as shown in Figure 4.26(a). In contrast, the largest deformation in the 0^{o}/90^{o} slab is located in the middle as shown in Figure 4.26(b). Restraining those points has different effects on the behaviour of the slabs. The distance between the point load and the restraint screw is the key factor. For ±45^{o} slab, this distance is greater than the distance for 0^{o}/90^{o} slab, and the reaction moment is higher in the ±45^{o} slab than the 0^{o}/90^{o} slab. The deformation shape for simple and screw restrained one-way slabs are shown in Figure 4.27. Simple and screw restrained two-way slabs are compared in Figure 4.28 for 0^{o}/90^{o} fibre orientation. The deformation shape is similar for the rectangular slabs with L_y/L_x=1.5 and L_y/L_x=2.0.

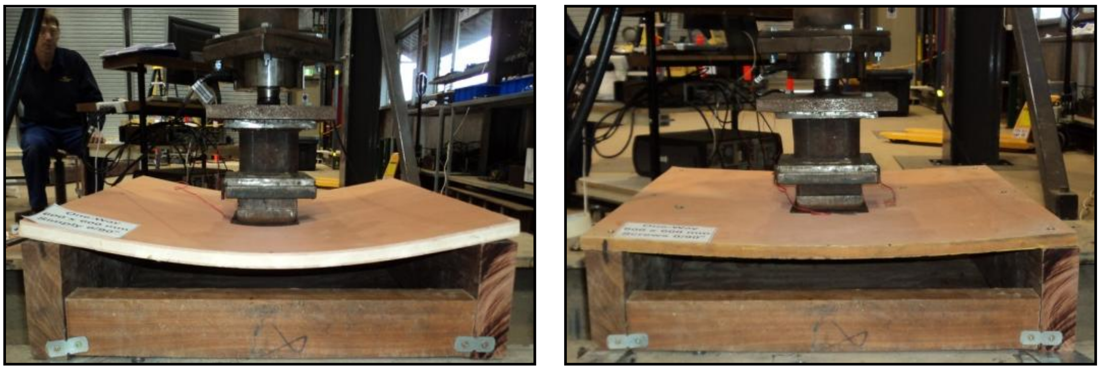

(a) Simple restraint. (b) Screw restraint.

Figure 4.27 Deformation shapes of $0^o/90^o$ one-way slabs (600 x 600 mm).

(a) Two-way simple (600 x 600 mm). (b) Two-way screw (600 x 600 mm).

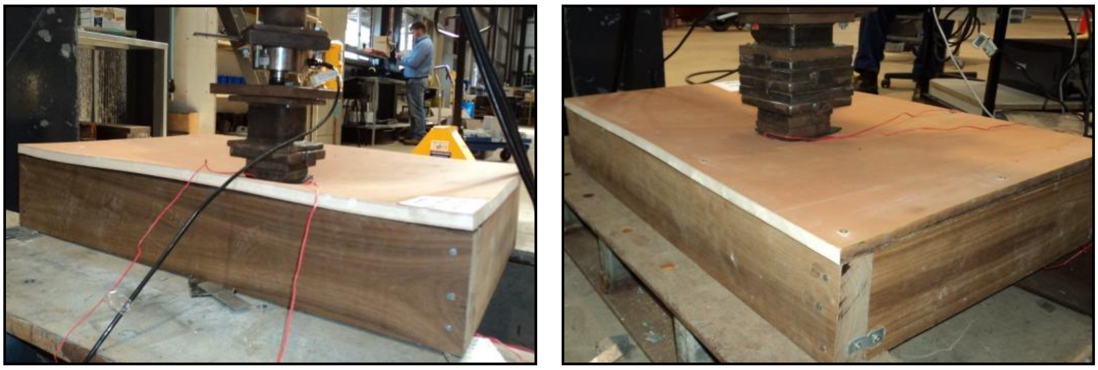

(c) Two-way simple (600 x 900 mm). (d) Two-way screw (600 x 900 mm).

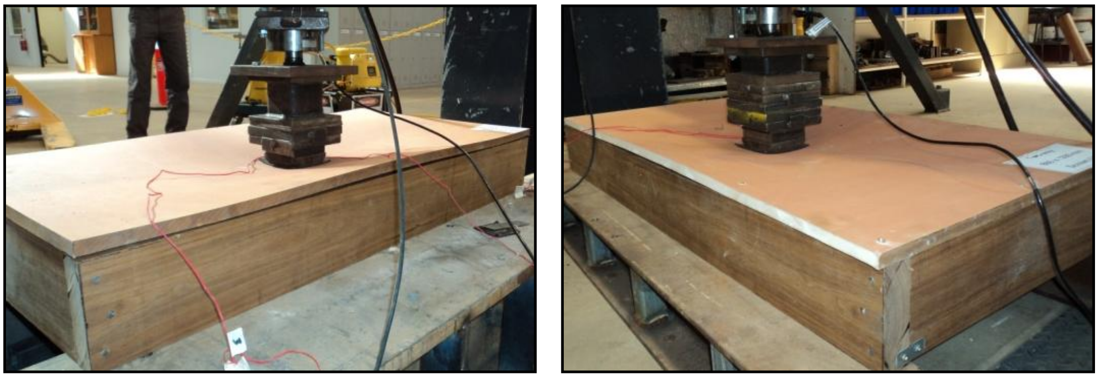

(e) Two-way simple (600 x 1200 mm). (f) Two-way screw (600 x 1200 mm).

Figure 4.28 Deformation shapes of simple and screw restraints two-way slabs.

4.5.4 Mode of failure

Two types of GFRP sandwich slabs have been tested in a one-way support configuration. The 15 mm and 18 mm slab thicknesses show a similar failure mode as shown in Figure 4.29. Experimental tests showed that the failure happened at an ultimate load of 19.60 kN and 38.74 kN for 15 mm and 18 mm slab thicknesses respectively. The comparison between the failure mode of one-way simple and screw restrained slabs is shown in Figure 4.30. The failure of both simple and screw restraint slabs are similar. Failure occurred due to cracking of the top skin and the cracking of the core. The failure line starts at the middle of the slab and progress towards the edge of the slab, parallel to the supports.

Two-way GFRP sandwich slabs showed different failure modes depending on the fibre orientations, restraint types, and slab width to length ratio. Mode of failure seems to be different between $\pm 45^o$ and $0^o/90^o$ GFRP sandwich slabs. Figure 4.31 shows the failure of $0/90^o$ and $\pm 45^o$ simply restrained slabs. Failure in the $\pm 45^o$ GFRP sandwich slabs occurs diagonally as shown in Figure 4.31(a). Failure of $0^o/90^o$ slabs is due to bottom skin delamination as shown in Figure 4.31(b). In addition, the failure mode was also affected by the deflection shape for $\pm 45^o$ slab. Increasing the deflection beyond the level of ($\delta \geq 0.30$ x slab thickness), causes stretching of the slab surfaces and this restrains the corners or full edges against the in-plane motion. Furthermore, the membrane forces developed by stretching could participate in carying the lateral load. Once the slab corners rise up as shown in Figure 4.26(a), the restraint is allocated on the mid-sides of four edges. Then, the prospective failure line will be parallel to the tension zone.

The failure of the two-way GFRP sandwich slab is affected by the type of restraint. Differences between the failure modes of the 600 x 600 mm GFRP sandwich slabs are shown in Figure 4.31. The $\pm 45^o$ GFRP sandwich slab did not show much difference between simple and screw restraints in terms of failure mode. The failure in both cases was diagonal and followed the line between the corners and parallel to the fibre orientations as shown in Figure 4.31 (a) and (c). In the case of $0^o/90^o$ GFRP sandwich slabs, there is a difference between the simple and screw restrained slabs. The slab with the simple restraint failed due to the core cracking near the corners and delamination of the bottom fibre in the middle of the span as shown in Figure 4.31(a). The slab with screw restraint showed a different failure mode with the cracking of the core and skins in the main direction (zero direction) as shown in Figure 4.31(d). The location of the crack was near the point load with a distance equal to 60 mm from the plate load side.

(a) 15 mm thickness. (b) 18 mm thickness.

Figure 4.29 Failure mode of one-way slabs.

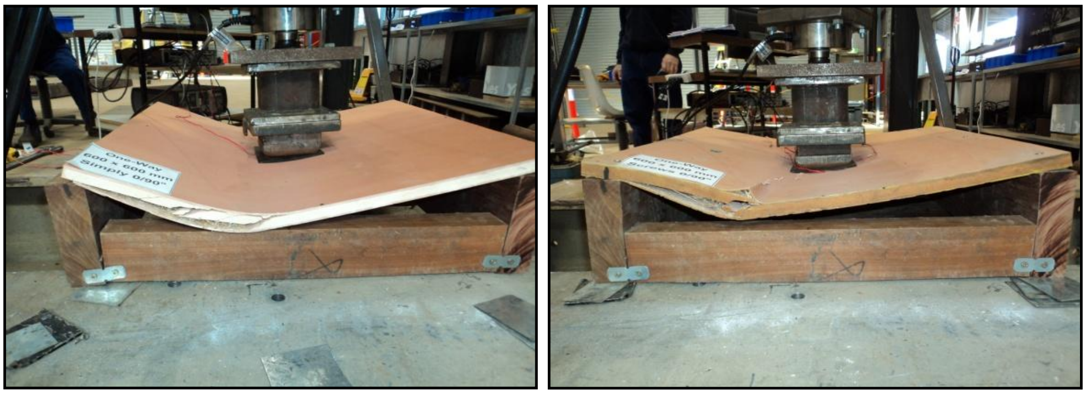

(a) Simple restraint. (b) Screw restraint.

Figure 4.30 Failure mode of one-way 18 mm thickness slabs.

The failure modes of 600 x 900 mm and 600 x 1200 mm rectangular GFRP sandwich slabs are affected by the slab width to length ratio and the type of boundary restraints. Comparison between simple and screw restraints of the two-way 600 x 900 mm are shown in Figure 4.32. The failure of the simply restrained slab is continued towards the corner of the slab. In contrast, the failure of the screw restraint slab is limited to the middle of the span due to the constraint of the screw as shown in Figure 4.32(b). The 600 x 1200 mm simple GFRP sandwich slab showed a failure mode as shown in Figure 4.33(a). The core cracks appear symmetrically at the edge of the slab in two positions with a distance of 30 cm from both corners. The 600 x 1200 mm screw slab failed in different mode compared to the simple restraint slab as shown in Figure 4.33(b). The effect of screw restraint is very clear on the failure mode. The screws in the mid-side try to limit the deformation of the slab at mid-side. The schematic diagram of the possible failure mode of the GFRP slab is shown in Figure 4.34.

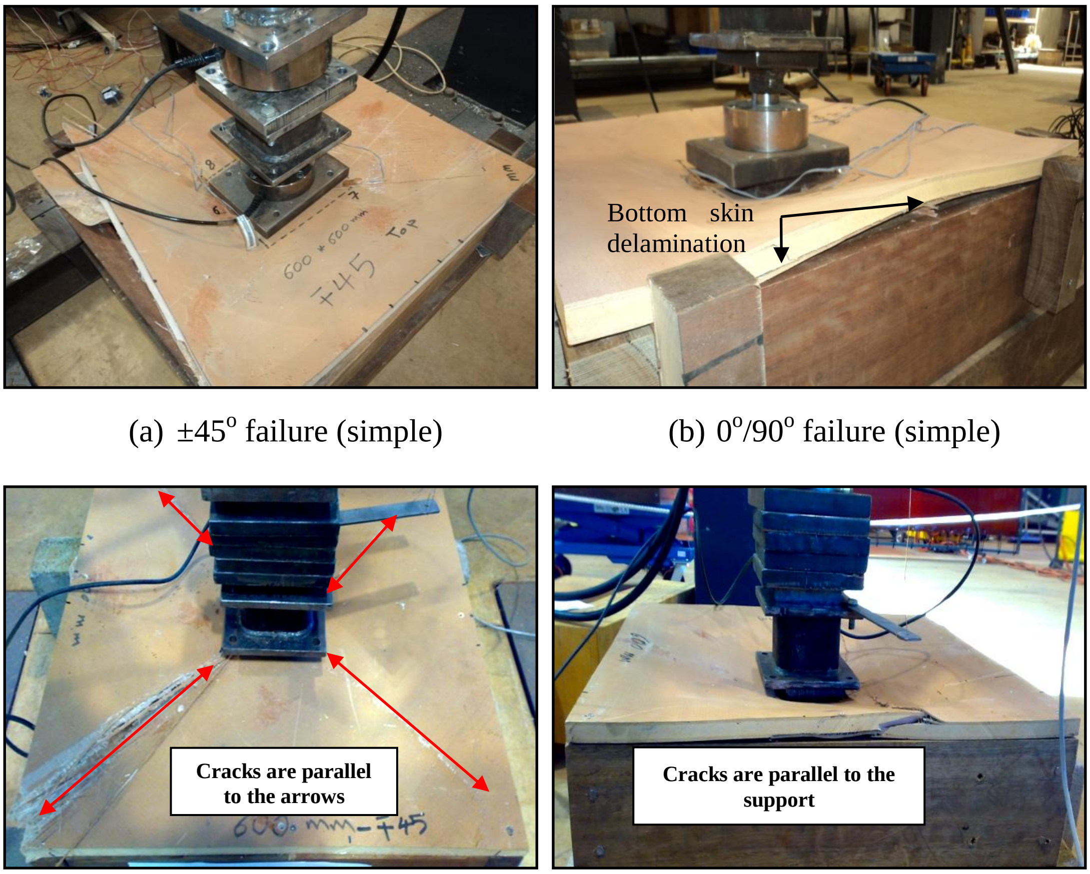

(a) ±45° failure (simple)

(b) 0°/90° failure (simple)

(c) ±45° failure (screw)

(d) 0°/90° failure (screw)

Figure 4.31 Failure mode of 600 x 600 mm two-way slab.

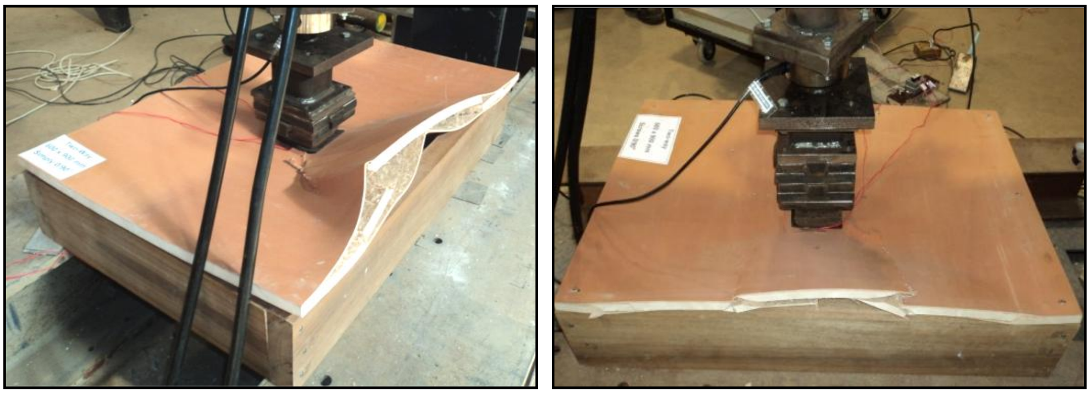

(a) Simple restraint. (b) Screw restraint.

Figure 4.32 Failure mode of 600 x 900 mm two-way slab.

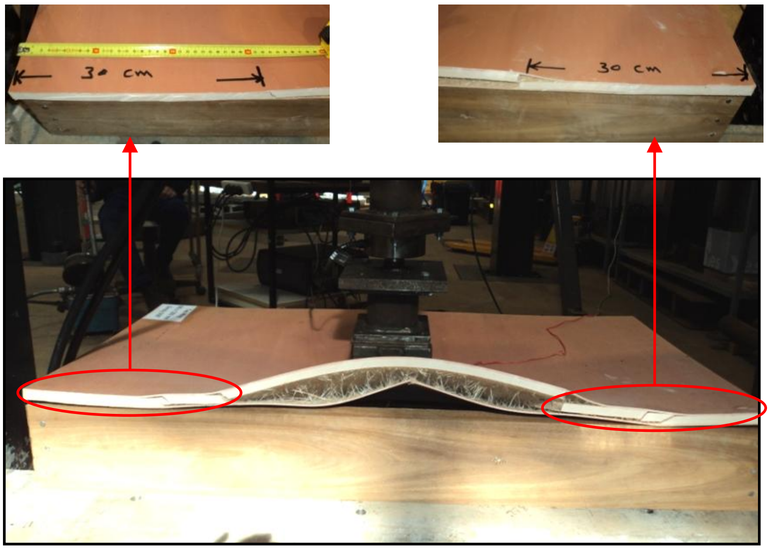

(a) Simple restraint

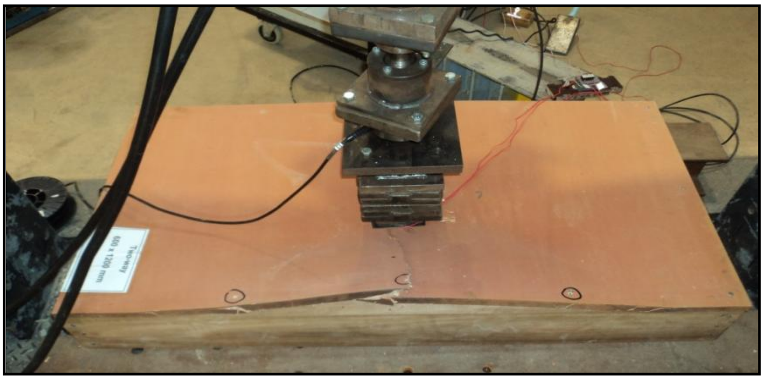

(b) Screw restraint

Figure 4.33 Failure mode of simple restraint 600 x 1200 mm two-way slab.

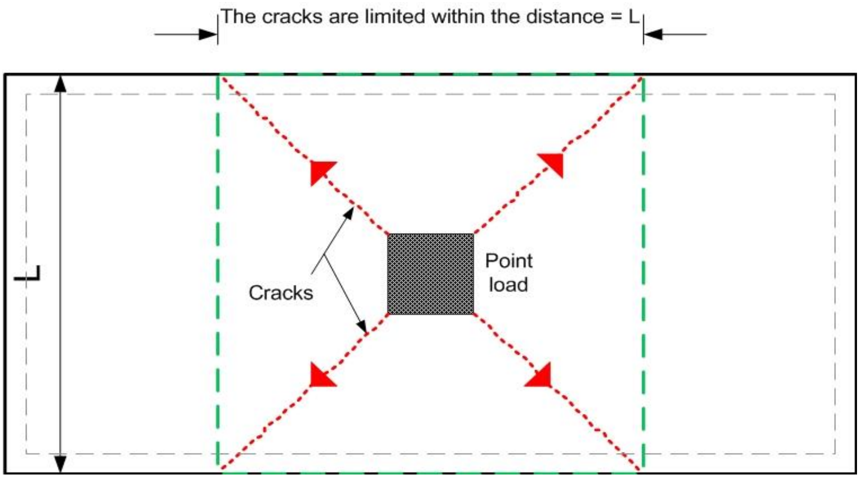

Figure 4.34 Schematic diagram for the possible failure in two-way slab.

4.5.5 Membrane action

Deflection of the GFRP sandwich slab can be classified as a large deflection problem because the final deflection is greater than the total thickness of the slab (Szilard 1974). The two way bending behaviour of the square sandwich slab can be divided into two parts; plate bending behaviour and membrane behaviour. The plate membrane behaviour can be calculated by Equation 4.5 and the plate bending behaviour under point load can be calculated by Equation 4.6. The plate bending theory can be applied to the sandwich plate only when the transverse deflection is small compared to the slab thickness. Otherwise, the membrane action should be considered as an effect of large deformation (Allen 1969; ASCE 1984).

$$P_{mem} = \frac{2(Et)_{skin}}{L^2}\left(\frac{\delta}{0.4386}\right)^3 \qquad 4.1$$

$$P_{plate} = \frac{\delta.EI}{4kL^2\sum_{i=0}^{m}\sum_{i=0}^{n}C_{mn}} \qquad m,n = 1, 3,\ldots \qquad 4.2$$

where,

$$C_{mn} = \frac{\left[\frac{6(1+r)^2}{r\bar{R}}\right](m^2+n^2k^2)+1}{2\pi^4 k}$$

$$k_{mn} = \left[\frac{6(1+r)^2}{r\bar{R}}\right](m^2+n^2k^2)^3 + [3(1+r)^2+1](m^2+n^2k^2)^2$$

$$EI = D = \frac{Et^3}{12(1-\nu^2)}$$

$$\bar{R} = \frac{GtL^2}{\pi^2 EI} \ , \ r = \frac{c}{t}$$

P_{plate} and P_{mem} are the plate load and membrane load, D is the rigidity, E is the elastic modulus of the skin. t is the thickness of the skin, L_x is the length of the slab, G is the shear modulus of the core, υ is the Poisons ratio of the skin, r is ratio of the core to the overall thickness of the slab, and k is equal to L_x/L_y.

Figure 4.35 shows the comparison between plate behaviour, combined plate and membrane behaviour, and experimental behaviour of the GFRP sandwich slab. The results of the experimental deflection were used in Equations 4.1 and 4.2 to find the corresponding plate and membrane load (Dawood et al. 2010; Timoshenko & Woinowsky-Krieger 1959). It showed that the GFRP sandwich slab was controlled by the plate bending behaviour up to 8 mm deflection or deflection equal to span/66. Then, the membrane action started to affect the load-deflection curve, and the slope of the load-deflection curve starts to increase. Figure 4.21 shows that the membrane effect decreases with increase in the transverse slab length in the cases of rectangular two-way GFRP slabs.

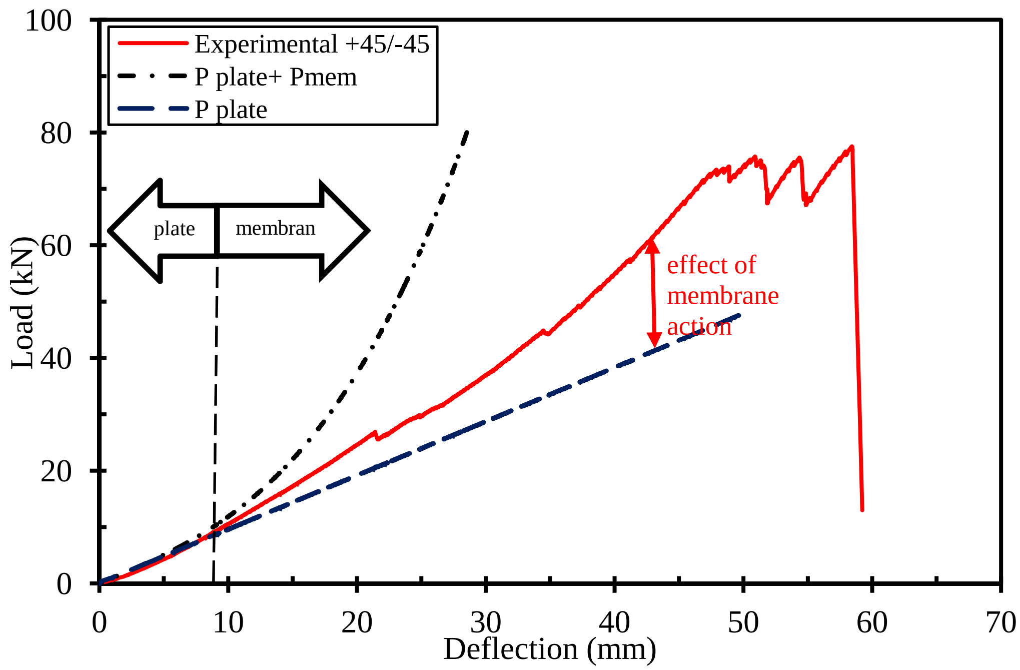

Figure 4.35 Effect of plate and membrane action.

4.6 Chapter conclusions

Experimental static point load tests were conducted on novel GFRP sandwich slabs. Eleven slabs were tested under static point load. Different parameters were studied such as one-way spaning, two-way spaning, fibre orientations, restraint types and slab width to length ratio. In conclusion, the two-way slab showed a load capacity twice the load capacity of the one-way slab. The effect of the screw restraint is not significant, especially at low load level for the rectangular two-way slab. Furthermore, static point load tests confirmed the $\pm 45^{o}$ slab has a higher stiffness than $0^{o}/90^{o}$ slab for both restraint types. The two-way GFRP sandwich slabs showed a similar behaviour with different (L_y/L_x) ratios. However, the ultimate load capacity is reduced by increasing the transverse length of the slab.

All slabs show a drop in the load-deflection curve around the load level 27-30 kN and the strain reading at bottom skin was 1.1%. This value of strain gives an indication that the core reaches the cracking strain. As a consequence, the core cracking at this load level cause drop in the load-deflection curve. However, the slabs show a reduction or small variation in the top strains after core cracking towards the final failure. This gives an indication that cracking of the core causes redistribution to the forces carried by the sandwich skins and this leads to this strain behaviour.

One-way slabs exhibited a similar failure mode for the simple and screw restraint types. Two-way square slabs showed a straight-line failure and diagonal failure for the $0^{o}/90^{o}$ and $\pm 45^{o}$ fibre orientations respectively. However, the rectangular slabs showed a small difference in failure mode between simple and screw restraint slabs. Moreover, the simply restraints slabs showed cracks with approximately 45^{o} towards the external long edge of the slab. The square two-way slabs revealed membrane behaviour in its load-deflection. Slab behaviour is controlled by membrane action after the mid-span deflection exceeds the value of clear span/66.

Results of experimental investigations in Chapter 3 and Chapter 4 lead to understanding of the static behaviour of the GFRP sandwich slabs. To enhance the knowledge about the GFRP sandwich structures behaviour, free vibration tests are discussed in Chapter 5.

Chapter 5

Free vibration behaviour of GFRP sandwich slabs

5.1 Introduction

Recently, resonance has become one of the design criteria for floors and footbridges. Walking and rhythmic activities cause several resonance problems in structures. The ISO-10137 standard indicates that the value of free vibration applied that accurse in building due to human activities usually lies between 1.2-12 Hz (ISO:10137 2007). Cunningham et al. (2000) studied the effect of design variables on the free vibration of a double curved free edge fibre composite sandwich panel. Their parametric study involved the design variables such as the core properties, fibre orientations and curvature. Lee et al. (2007) studied the free vibration of fibre composite sandwich plates with a symmetric layup. The objective of the study was to identify the material constants of the sandwich plate.

In addition to the free vibration limitation, the stiffness of the slab can be used as design criteria to avoid the undesired free vibration. A minimum stiffness of 1 kN per mm is recommended for steel structure design when the slab carries a concentrated force (Murray et al. 1997). AASHTO (2008) recommended that the span to depth ratio greater than 20 should be avoided in the design of FRP pedestrian bridges to prevent undesired vibration.

There are existing formulae for the free vibration of beams and plates. The general equation of Euler-Bernoulli beam is described below:

$$\overline{w} = \left(\frac{a_n}{L}\right)^2 * \sqrt{\frac{EI}{\rho A}} \qquad 5.1$$

where $\overline{w}$ is the circular frequency. *A* is the cross section area, *EI* is the rigidity, ρ is the density, *L* is the span, and a_n is the boundary conditions parameters.

The general equation of natural frequency for multi-layer plates is (Reddy 2004):

$$\overline{w} = \frac{\pi^2}{b^2}\sqrt{\frac{D}{I_o}}\left[\left(\frac{b}{a}\right)^2 + 1\right] \qquad 5.2$$

$$f = \frac{\overline{w}}{2\pi} \qquad 5.3$$

where *f* is the natural frequency Hz, *a* is the plate length, *b* is the plate width, *D* and I_o are:

$$D = \frac{Eh^3}{12(1-\upsilon^2)} \qquad 5.4$$

$$I_o = \sum_{k=1}^{N} \rho_o^k h^k \qquad 5.5$$

where *N* is the number of layers, ρ_o is the mass of the layer, υ is the Poisson's ratio, and *h* is the thickness of the layer.

Although the novel GFRP sandwich slab has been accepted by the design engineers for use as a structural member due to it is good mechanical properties, there is a lack of information about the free vibration behaviour of the GFRP sandwich slabs. The literature review showed that no such research has been done on a slab with different support conditions and restraints. The present study has been conducted to investigate the free vibration behaviour of the GFRP sandwich slab with different variables.

Chapters 3 and 4 discussed the mechanical behaviour of GFRP sandwich beams and slabs. Destructive static load tests were conducted on them. Experimental tests provided valuable information towards understanding the static behaviour of the GFRP sandwich beams and slabs.

In this chapter, series of free vibration investigations are presented for the GFRP sandwich slabs. Slab variables were considered in the experimental investigation are, span of the slab, single spans, continuous spans, support restraint types and skin fibre orientations. These parameters provide a better understanding to the free vibration characteristics of GFRP sandwich slabs. In addition, this information provides the design engineers with basic knowledge about the free vibration of the novel GFRP sandwich structure.

5.2 Experimental procedure

Comprehensive experimental testing has been conducted to investigate the free vibration behaviour of the novel GFRP sandwich slab. The objective of this study is to find the effect of different variables on the free vibration behaviour of the GFRP sandwich slab. The variables are; span length, single spans, continuous spans, restraint types and skin fibre orientations. All variables are explained in this section.

5.2.1 Samples preparations

The preparation of sandwich slabs and supports were explained in Chapter 4. The cross section of timber joist dimensions is 70 mm x 35 mm. Timber supports were prepared for a one-way single span, two-way single span, and continuous slabs. Four types of support, two sided, four sided, and continuous were used in the experiments as shown in Figure 5.1. Three different restraint types, simple, screw and glue restraints were used to connect the GFRP slabs to the supports as shown in Figure 5.2. Steel screws (8G x 65 mm) were used in the fixing of the restraint type R2, and Sikaflex-221 glue was used in the glued restraint type R3.

Square GFRP sandwich slabs were cut to specific sizes of 400, 600, 800 and 1000 mm. The total thickness of the slabs was 18 mm. Samples of the slabs are shown in Figure 5.3(a). Sikaflex-221 was applied in the glue restraint tests to connect the slab to the support as shown in Figure 5.3(b). The timber supports were connected to steel channels using steel clamps to increase the stiffness of as shown in Figure 5.3(c). The combinations of timber support configuration, restraint types and fibre orientations produced 42 cases as shown in Table 5.1.

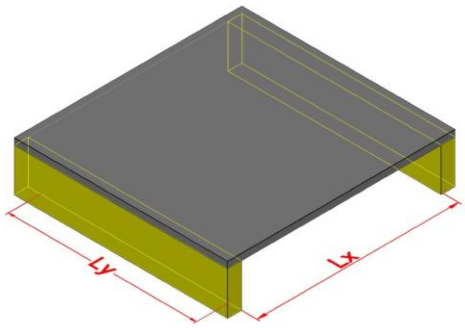

(a) Support type S1 (one-way)

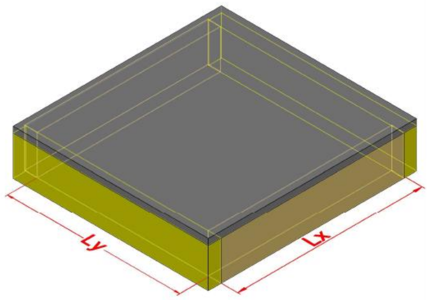

(b) Support type S2 (Two-way)

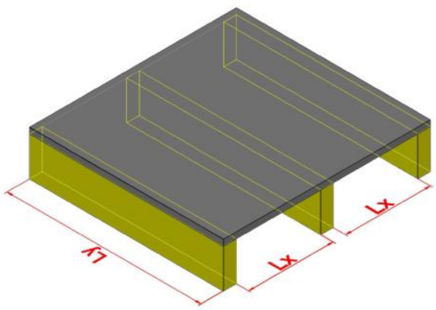

(c) Support type S3 (One-way continuous)

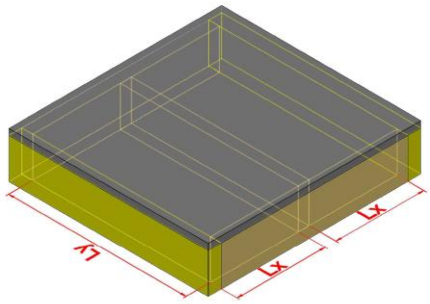

(d) Support type S4 (Two-way continuous)

Figure 5.1 Timber support types.

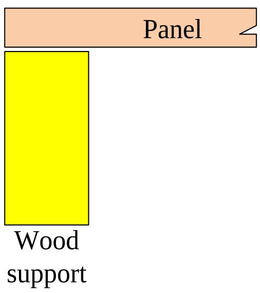

(a) Simple restraint: R1.

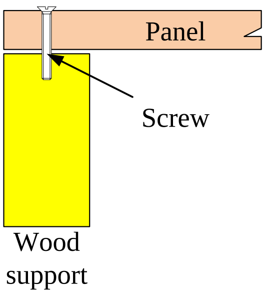

(b) Screw restraint: R2.

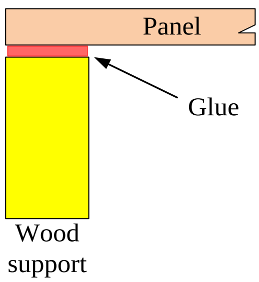

(c) Glue restraint: R3.

Figure 5.2 Boundary restraint types.

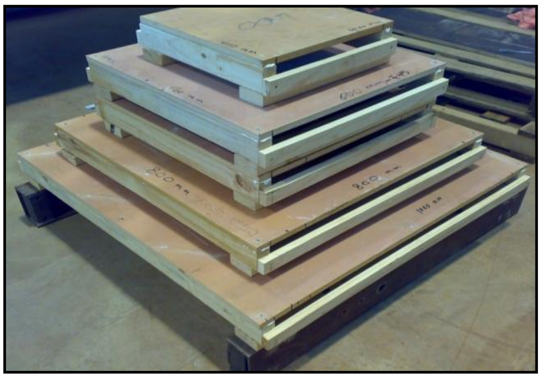

(a) Different slab sizes

(b) Glue restraint support

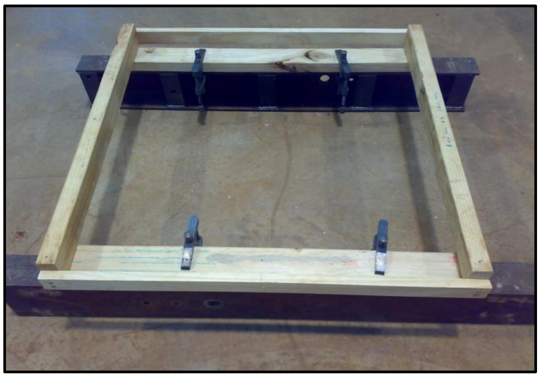

(c) Support clamped to steel channel

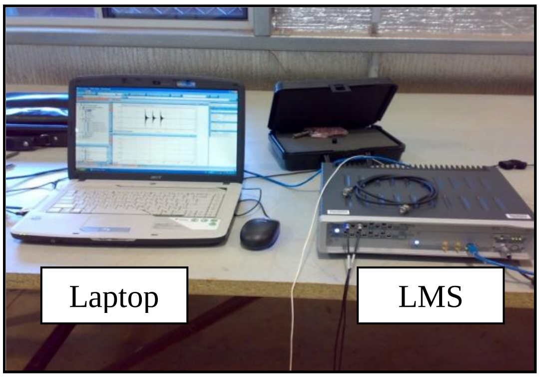

(d) LMS instrument test

Figure 5.3 Experimental setup.

Table 5.1 GFRP sandwich slab samples

Name	Support type	Restraint type	Skin fibre orientation	Slab size mm x mm	Short span (L_x) mm
T1	One-way (S1)	Simple (R1)	$0^o/90^o$	400 x 400	330
T2			$0^o/90^o$	600 x 600	530
T3			$0^o/90^o$	800 x 800	730
T4			$0^o/90^o$	1000 x 1000	930
T5			$-45^o/+45^o$	600 x 600	530
T6	Two-way (S2)	Simple (R1)	$0^o/90^o$	400 x 400	330
T7			$0^o/90^o$	600 x 600	530
T8			$0^o/90^o$	800 x 800	730
T9			$0^o/90^o$	1000 x 1000	930
T10			$-45^o/+45^o$	600 x 600	530
TS1	One-way (S1)	Screw (R2)	$0^o/90^o$	400 x 400	330
TS2			$0^o/90^o$	600 x 600	530
TS3			$0^o/90^o$	800 x 800	730
TS4			$0^o/90^o$	1000 x 1000	930
TS5			$-45^o/+45^o$	600 x 600	530
TS6	Two-way (S2)	Screw (R2)	$0^o/90^o$	400 x 400	330
TS7			$0^o/90^o$	600 x 600	530
TS8			$0^o/90^o$	800 x 800	730
TS9			$0^o/90^o$	1000 x 1000	930
TS10			$-45^o/+45^o$	600 x 600	530
TG1	One-way (S1)	Glue (R3)	$0^o/90^o$	400 x 400	330
TG2			$0^o/90^o$	600 x 600	530
TG3			$0^o/90^o$	800 x 800	730
TG4			$0^o/90^o$	1000 x 1000	930
TG5			$-45^o/+45^o$	600 x 600	530
TG6	Two-way (S2)	Glue (R3)	$0^o/90^o$	400 x 400	330
TG7			$0^o/90^o$	600 x 600	530
TG8			$0^o/90^o$	800 x 800	730
TG9			$0^o/90^o$	1000 x 1000	930
TG10			$-45^o/+45^o$	600 x 600	530
TC1	One-way continuous (S3)	Simple (R1)	$0^o/90^o$	800 x 800	347.5
TC2			$0^o/90^o$	1000 x 1000	447.5
TCS1	One-way continuous (S3)	Screw (R2)	$0^o/90^o$	800 x 800	347.5
TCS2			$0^o/90^o$	1000 x 1000	447.5
TCG1	One-way continuous (S3)	Glue (R3)	$0^o/90^o$	800 x 800	347.5
TCG2			$0^o/90^o$	1000 x 1000	447.5
TTC1	Two-way continuous (S4)	Simple (R1)	$0^o/90^o$	800 x 800	347.5
TTC2			$0^o/90^o$	1000 x 1000	447.5
TTCS1	Two-way continuous (S4)	Screw (R2)	$0^o/90^o$	800 x 800	347.5
TTCS2			$0^o/90^o$	1000 x 1000	447.5
TTCG1	Two-way continuous (S4)	Glue (R3)	$0^o/90^o$	800 x 800	347.5
TTCG2			$0^o/90^o$	1000 x 1000	447.5

5.2.2 Test setup

Measuring free vibration needs a specific type of instrumentation for creating excitation and for finding the structural response. In the present experimental program, the LMS Test Lab instrument and LMS SCADAS system were used to measure the natural frequency of the GFRP sandwich slabs. Two channels were used in the reading, one for the hammer reading and the other for the accelerometer reading. The LMS instrument was connected to the computer to transfer the data as shown in Figure 5.3(d).

The accelerometer was fitted in different positions depending on the slab support as shown in Figure 5.4. It was attached to the top skin with glue. Three hits or impacts were used for each reading to develop the vibration in the GFRP sandwich slabs. The excitation was initiated using the hammer and the response was measured using the accelerometer.

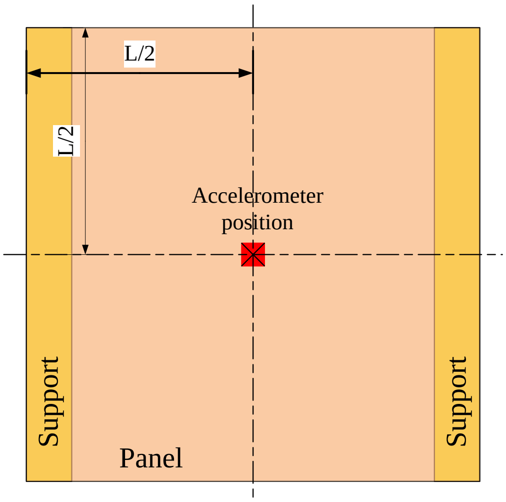

(a) Single span

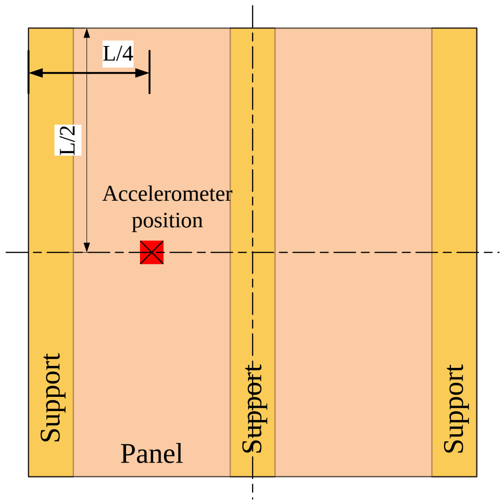

(b) Continuous span

Figure 5.4 Accelerometer position.

5.3 Experimental results and discussion

5.3.1 Effect of span length

The span length of the slab has been investigated by the researchers as an effective variable to determine the value of the natural frequency of any structure (Murphy 1997). The span length of the square GFRP sandwich has been selected as a variable in this study. One-way and two-way slabs were studied with different span lengths. All sample details are shown in section 5.2. Slab results are discussed in this section for $0^o/90^o$ fibre orientation.

The results of the free vibration tests can be divided into three parts. Part one is the result of the slab one-way support type (S1) as shown in Figure 5.5 and Table 5.2. The second part is the result of the slabs having two-way support (S2) as shown in Figure 5.6 and Table 5.3. The third part is for the slabs with support types S3 and S4, with continuous spans as shown in Figure 5.7 and Table 5.4. It can be seen from the experimental results that the slab has a non-linear frequency variation with span length. The frequency decreased with the increase in length of the span. In addition, all GFRP sandwich slabs with different restraint types follow the same behaviour with the increase in length of the span.

The free vibration frequencies *f1*, *f2* and *f3* are decreasing with the increase of the slab span length. In general, decreasing the slab span length by half would increase the natural frequency by about 3-4 times as shown from the experimental results in Figures 5.5 and 5.6. For example, the frequency (*f1*) of the one-way 400 mm slab size (T1) is three times the frequency (*f1*) of one-way 800 mm slab size (T3) as shown in Table 5.2.

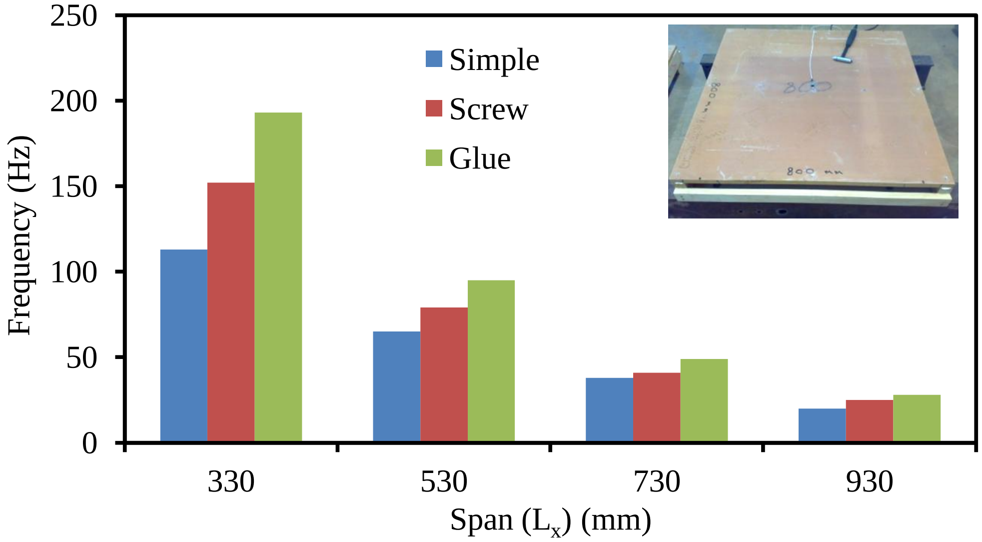

Figure 5.5 First natural frequency for one-way (S1) slabs.

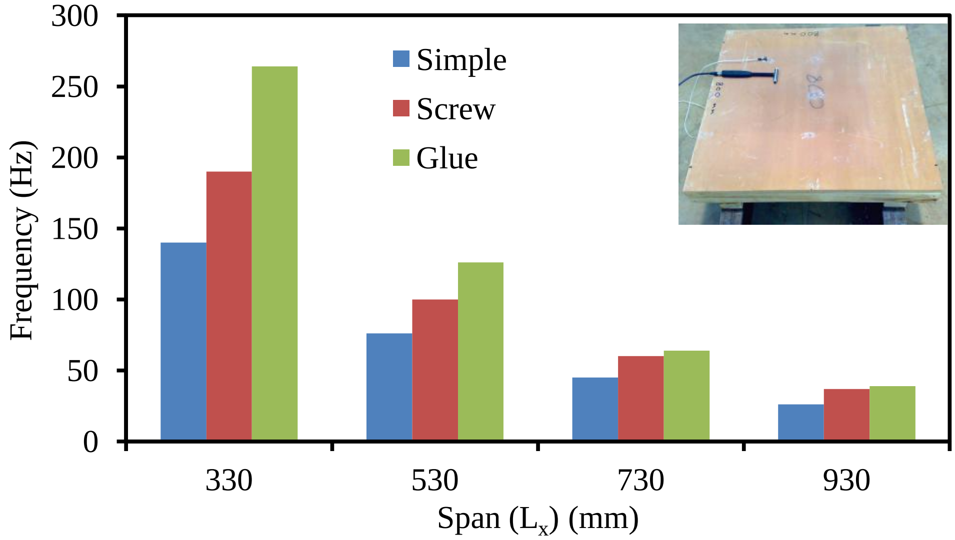

Figure 5.6 First natural frequency for two-way (S2) slabs.

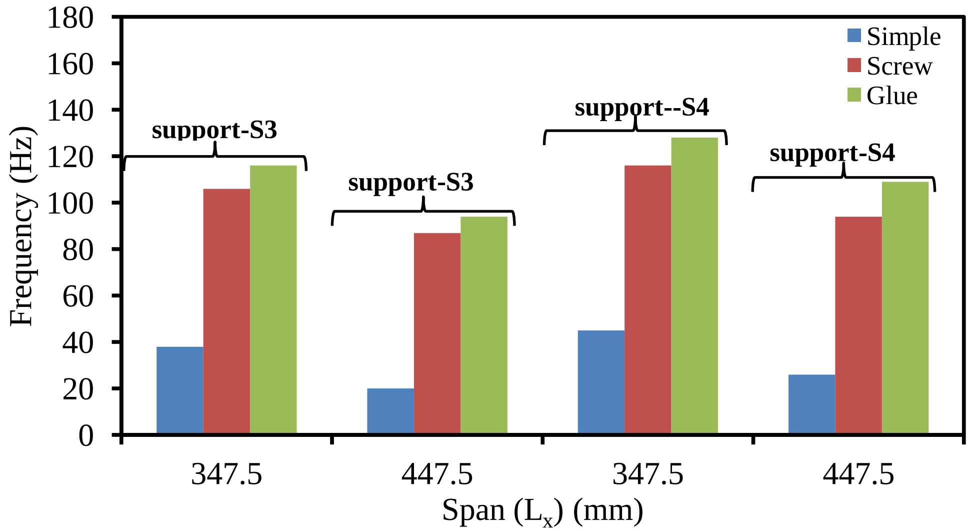

Figure 5.7 First natural frequencies for continuous (S3 and S4) slabs.

Table 5.2 Natural frequency of one-way (S1) slabs.

Slab name	Size mm x mm	Short span (L_x) mm	*f1* Hz	*f2* Hz	*f3* Hz
T1	400 x 400	330	113	127	232
T2	600 x 600	530	65	82	146
T3	800 x 800	730	38	54	99
T4	1000 x 1000	930	20	32	57
TS1	400 x 400	330	152	200	270
TS2	600 x 600	530	79	111	166
TS3	800 x 800	730	41	57	95
TS4	1000 x 1000	930	25	38	72
TG1	400 x 400	330	193	230	380
TG2	600 x 600	530	95	123	210
TG3	800 x 800	730	49	70	124
TG4	1000 x 1000	930	28	41	75

Table 5.3 Natural frequency of two-way (S2) slabs.

Slab name	Size mm x mm	Short span (L_x) mm	*f1* Hz	*f2* Hz	*f3* Hz
T6	400 x 400	330	140	164	260
T7	600 x 600	530	76	104	140
T8	800 x 800	730	45	59	82
T9	1000 x 1000	930	26	40	53
TS6	400 x 400	330	190	308	384
TS7	600 x 600	530	100	174	220
TS8	800 x 800	730	60	116	136
TS9	1000 x 1000	930	37	84	98
TG6	400 x 400	330	264	392	414
TG7	600 x 600	530	126	286	314
TG8	800 x 800	730	64	138	154
TG9	1000 x 1000	930	39	86	93

Table 5.4 Natural frequency of continuous (S3 and S4) slabs.

Slab name	Size mm x mm	Short span (L_x) mm	*f1* Hz	*f2* Hz	*f3* Hz
TC1	800 x 800	347.5	38	54	103
TC2	1000 x 1000	447.5	20	32	66
TCS1	800 x 800	347.5	106	123	129
TCS2	1000 x 1000	447.5	87	97	111
TCG1	800 x 800	347.5	128	140	181
TCG2	1000 x 1000	447.5	109	117	144
TTC1	800 x 800	347.5	45	59	84
TTC2	1000 x 1000	447.5	26	42	54
TTCS1	800 x 800	347.5	116	124	128
TTCS2	1000 x 1000	447.5	94	120	140
TTCG1	800 x 800	347.5	152	185	207
TTCG2	1000 x 1000	447.5	96	126	138

5.3.2 Effect of support restraint

The restraint types represent one of the important aspects in the analysis of structural free vibration. As shown in section 5.2, three different boundary restraints were investigated, simple, screw and glue restraints. In real construction, builders use both screws and glue to fix the slab. The novel GFRP sandwich slab was designed to be suitable for drilling and gluing installation. The effect of the boundary conditions was included in the Euler-Bernoulli beam as described in Equation 5.1 for simply support and fixed support slabs. The effects of different restraint types on the first natural frequency are also shown in Figure 5.8(a) and (b) for the one-way and two-way slabs respectively. The simple restraint gives the lowest frequency for all support types. The glue restraint gives the highest frequency for all support types.

However, it can also be seen from both figures that there is divergence between the three types of restraint and that this divergence increases with decrease of slab span length. This is explained by the effective span length which depends on the support restraint type. In the case of the simple restraint, the effective span of the slab is increased by half the width of the support on both sides as shown in Figure 5.9(a).

In the case of screw restrained slabs, the effective span of the mode shape remains the same as actual span as shown in Figure 5.9(b). The glue restraint has the largest effect on the mode shape. The effective span is reduced by half the width of the support from both sides as shown in Figure 5.9(c). To enhance the presentation of results, some modifications were made on the x-axis in the Figures 5.9(a) and (b). The span length was modified to the effective span length as discussed above. This shows that the divergence decreases which enhances the results as shown in Figure 5.10(a) and (b).

In the case of simple restrained slabs, the comparison between one-way, single span slabs (S1) and one-way, continuous span slabs (S3) indicates that there is only a small difference between the first natural frequencies of the samples. This was observed in both the one-way, single span sample with 800 mm span length (T3) and the one-way, continuous span sample with 400 mm span length (TC1). In the same way, the first natural frequency of the slab T4 (with 1000 mm span) and TC2 slab with continuous span (with 500 mm span) were the same. In addition, the same behaviour has been noticed with the two-way, single span slab (S2) and two-way, continuous span slab (S4). The single span (T8) and continuous span (TTC1) two-way slabs show the same first natural frequency with slab sizes of 800 mm. Similarly, the single span slab (T9) has the same frequency as the continuous span slab (TTC2) with slab size of 1000 mm. This happens because there is no contact between the slabs (TTC1 and TTC2) and the middle support in the case of simple restrained slabs despite having a support in the middle. There is no restraint to prevent the slab from moving upward. In addition, this behaviour is expected for the upward deflection only. These causes of the continuous slab show the same behaviour as a single span slab in the first mode of frequency.

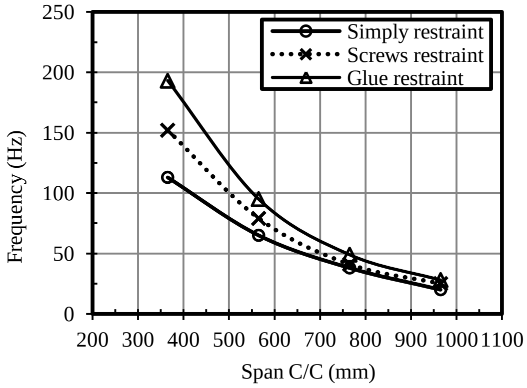

(a) One-way.

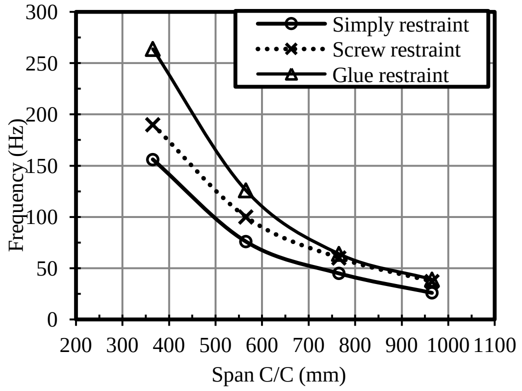

(b) Two-way.

Figure 5.8 Frequency-span relationship of the slab with span centre to centre.

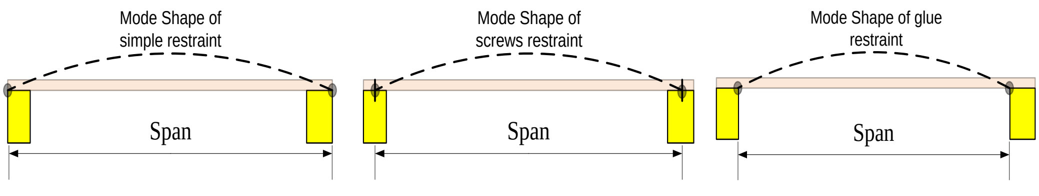

(a) Simple restraint. (b) Screws restraint. (c) Glue restraint.

Figure 5.9 Schematic drawings for the effective span.

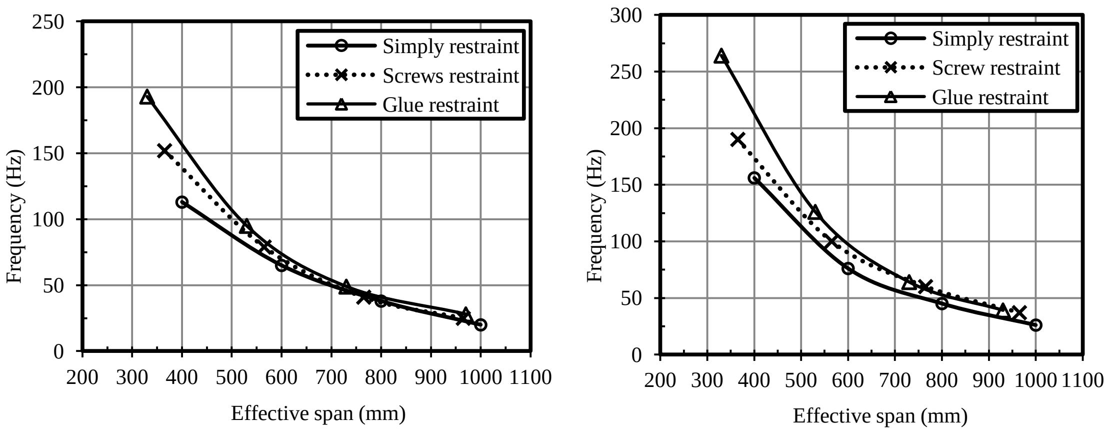

(a) One-way. (b) Two-way.

Figure 5.10 Frequency-span relationship of the slab with effective span.

5.3.3 Effect of one-way and two-way spanning supports

This section presents the behaviour of the slabs with the sizes of 800 mm and 1000 mm. Comparison between these GFRP sandwich slabs shows that there is a big difference between the one-way span slabs (S1) and two-way span slabs (S2). The differences in natural frequency between them are shown in Figure 5.11. It can be seen that the difference is very clear for all types of restraint. The simple restraint gives a lowest frequency and the glue restraint gives the highest frequency. A simple equation that considers the support type was used in the design of timber slabs. This equation has a modification factor (β) for two-way and one-way slabs. These factors are equal to 0.65 and 0.77 for one-way and two-way respectively. This equation is shown below (Smith 2003):

$$f = \frac{1}{2\pi}\sqrt{\frac{9.81}{\beta(\delta_b+\delta_G)+\delta_s}} \qquad 5.6$$

where,

β=0.77 (one-way support)

β=0.65(two-way support)

The δ_b is the slab deflection due to bending. δ_G is the girder deflection due to shear and δ_s is the elastic shortening of the support.

The effect of the β factor on the difference between one-way and two-way frequencies is 18% for a timber slab. However, the experimental results in Figure 5.11 show that the difference ratio between one-way (S1) and two-way (S2) supports of the GFRP sandwich slab is not constant, and it lies between 17% to 44%. For support types S3 and S4, the slab becomes continuous with two spans by adding a middle support. The comparison of the first natural frequency was presented in section 5.3.1 as shown in Figure 5.7. It can be seen that there is a big improvement in increasing the first natural frequency by adding the middle support in the case of screws and glue restraint boundary conditions.

The comparison between the one-way, single span slab T3 and one-way, continuous span slab TC1 shows an increase in the natural frequencies. The one-way, continues span TC2 shows the same behaviour compare the single span slab T4. Similarly, the two-way, continuous span slabs (TTC1 and TTC2) show higher frequencies than the two-way, single span slabs (T8 and T9). However, it was found that in the case of simple restrained slabs, there is no effect on the first natural frequency by making the slab continuous with an extra support in the middle. This behaviour due to the upward deflection in the first mode.

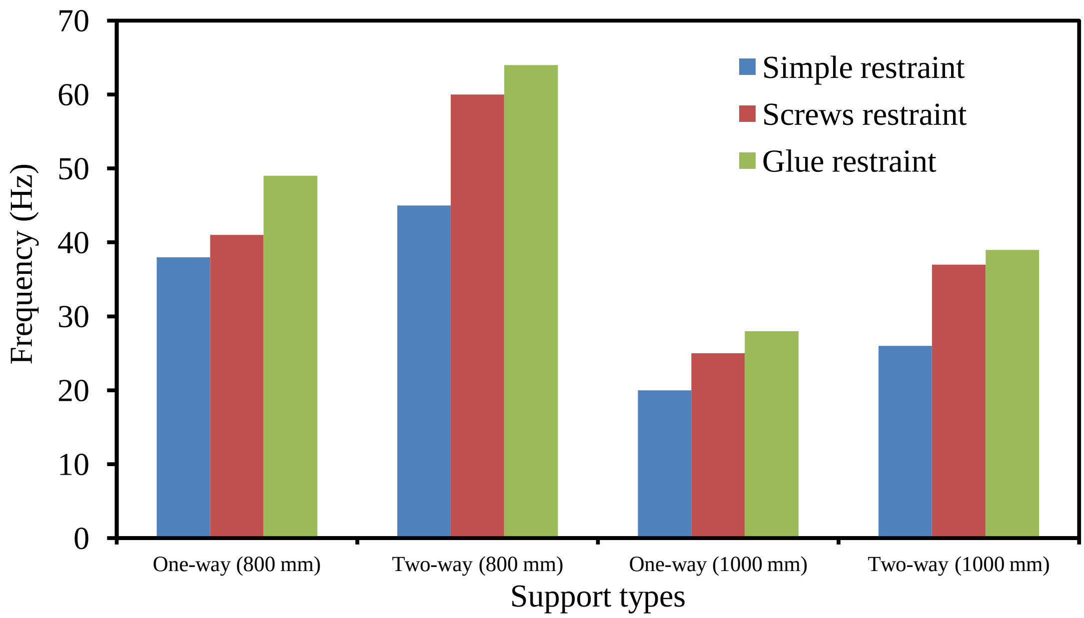

Figure 5.11 Comparison between one-way and two-way slabs.

5.3.4 Effect of fibre orientations

The last objective of the free vibration experimental work was to investigate the effect of skin fibre orientation on the free vibration behaviour of the GFRP sandwich slab. Two types of skin orientations, $0^o/90^o$ and $\pm45^o$ with one-way and two-way sandwich slabs were investigated. The total number of comparisons with the fibre orientation variables was 12. The results of the free vibration of the different fibre orientations are shown in Table 5.5.

The frequency variation between the one-way span slab and two-way span slab is given in Figures 5.12 and 5.18 respectively. It can be seen from the test results that the $0^o/90^o$ slab fibre orientation has a higher frequency than the $\pm45^o$ slab fibre orientation in the cases of one-way spanning slab (S1). By contrast, the $0^o/90^o$ slab fibre orientation has a lower frequency than the $\pm45^o$ slab fibre orientation in the cases of the two-way span slab (S2). All slabs with different restraints showed similar behaviour. The same slabs of $0^o/90^o$ and $\pm45^o$ fibre orientations were tested in Chapter 4 under point load static test. The $\pm45^o$ slab showed a lower deflection than the $0^o/90^o$ slab in the case of a two-way support system. This behaviour attributed to the fibre orientation in the skins. In the one-way support, the best fibre orientation is $0^o/90^o$ which is parallel to the carrying load direction. The two-way slab has four sided support and the $\pm45^o$ can participate more effectively in load carrying.

Table 5.5 Natural frequency of 600 x 600 mm slabs.

Slab name	Orientation	*f1* Hz	*f2* Hz	*f3* Hz
T2 T5	$0^o/90^o$ $\pm45^o$	65 44	82 74	146 132
T7 T10	$0^o/90^o$ $\pm45^o$	76 87.5	104 122	140 156
TS2 TS5	$0^o/90^o$ $\pm45^o$	79 65	111 111	166 150
TS7 TS10	$0^o/90^o$ $\pm45^o$	100 118	174 176	220 262
TG2 TG5	$0^o/90^o$ $\pm45^o$	95 77	123 119	210 170
TG7 TG10	$0^o/90^o$ $\pm45^o$	126 136	286 295	314 390

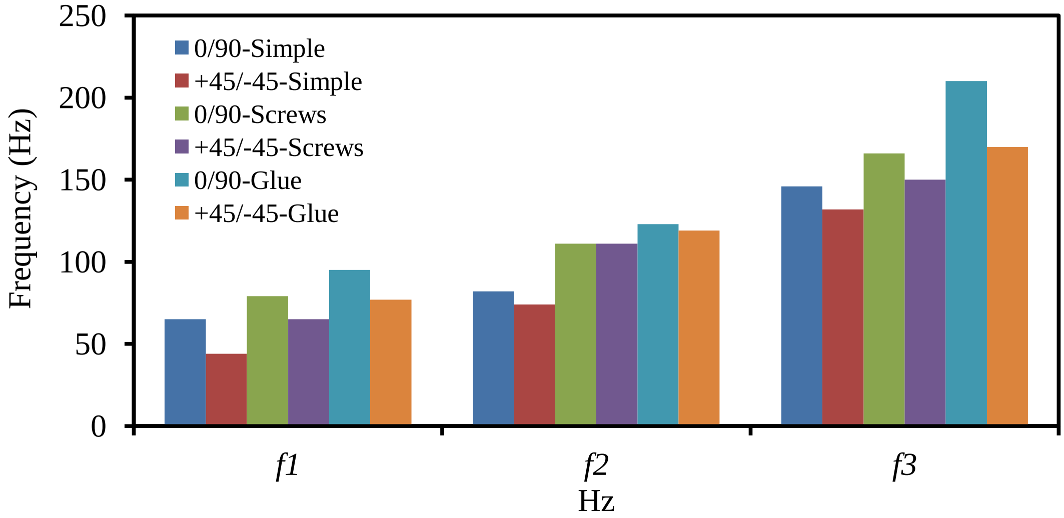

Figure 5.12 One-way support (S1) slabs.

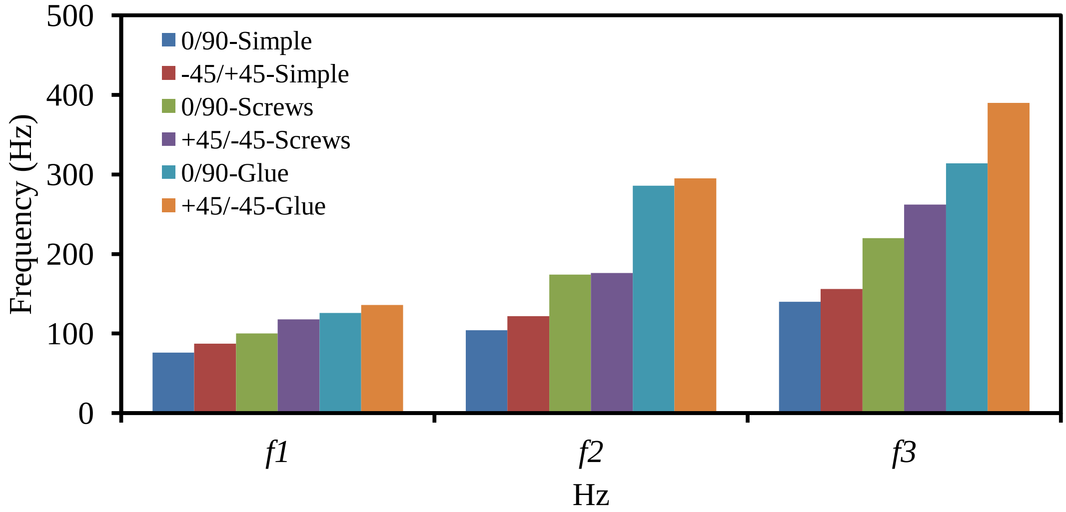

Figure 5.13 Two-way support (S2) slabs.

It was shown in Equation 5.1 that the rigidity of the beam is expressed as *EI*. In Equation 5.2 the rigidity of the slab is expressed as *D*. Beam Equation 5.1 can be used to calculate the rigidity of the one-way slab, and the Equation 5.2 can be used for the calculation of the rigidity of the slabs. Equations 5.1 and 5.2 can be rearranged to calculate the *EI* and *D* values of the for a square GFRP sandwich slab (a=b=L) as given below:

$$EI_\theta = \frac{4 f_\theta^2 L^4 \rho A \pi^2}{a_n^4} \qquad \text{One-way slab} \qquad 5.7$$

$$D_\theta = \frac{f^2 L^4 I_o}{\pi^2} \qquad \text{Two-way slab} \qquad 5.8$$

where θ is the fibre orientation, f is the frequency, and L is the span.

The core density of this slab was measured and found to be 950 kg/m^3. The GFRP skin density was determined as 1425 kg/m^3. Details of the materials properties are shown in Appendix-A. Equation 5.8 can be used to estimate the rigidity (*EI*) ratio of the ±45^o GFRP sandwich slab (T5) to the rigidity of 0^o/90^o fibre orientation slab (T2) where they have the same one-way span (S1). Since both slabs have the same material properties, dimensions, and the cross sections, Equation 5.7 indicates that the rigidity EI of skin orientation ±45^o is lower than the rigidity of skin orientation 0^o/90^o. In the case of two-way span slabs (S2) Equation 5.8 can be used to estimate the D values when the fibre orientation is ±45^o or 0^o/90^o. The D value of slab T10 with skin orientation ±45^o is higher than the D value of slab T7 with fibre orientation 0^o/90^o, which is in contrast to the results for one-way span slabs.

The ratio between the rigidity of slabs with ±45^o fibre orientation to the slab with 0^o/90^o fibre orientation for the first natural frequency is calculated below.

$$\left(\frac{EI_{\mp 45^o}}{EI_{0/90^o}}\right) = 0.67 \quad simple\ restraint \quad \text{(One-way support type-S1)}$$

$$\left(\frac{D_{\mp 45^o}}{D_{0/90^o}}\right) = 1.15 \quad simple\ restraint \quad \text{(Two-way support type-S2)}$$

From the above equations, it can be seen that the ±45^o orientation provides more gain in the D value than the 0^o/90^o orientation for the two-way span slabs. The ±45^o orientation shows a lower rigidity (*EI*) than the 0^o/90^o in the case of one-way span slabs.

5.3.5 Comparison with theoretical prediction

The literature review revealed that there are two popular equations for natural frequency calculations. The first one is for simple supported beams as shown in Equation 5.1, and this equation can be used for the one-way slab support type (S1). The second Equation 5.2 is for the simple supported slab structures, similar to slabs with two-way support (S2). These equations depend on the geometry and material property to find the natural frequency. These equations have been applied to the simple supported GFRP sandwich slab. Equation 5.1 was used for the one-way simple supported GFRP sandwich slab, and the results are shown in Figure 5.14. It can be seen that the divergence between the predicted values for the one-way single span GFRP floor slab and the experimental observation increases when the span to depth ratio decreases. The reason is that the sandwich slab becomes thick when the span to the depth ratio is less than 20 (Kant & Babu 2000). Equation 5.2 was used to find the frequency of the two-way simple supported sandwich slab. This equation gives very low values of natural frequency when using Equation 5.4 to calculate the *D*. The value of *D* was derived by Timoshenko and Woinowsky-Krieger for homogenous plates (Timoshenko & Woinowsky-Krieger 1959). Applying the same procedure of Timoshenko and Woinowsky-Krieger for calculating the *D* for the sandwich slab consisting of core and skins gives a different value of *D* as follows:

$$D = D_{core} + D_{skins} \qquad 5.9$$

$$D = \left(\frac{Ec^3}{1-\upsilon^2}\right)_{core} + \left(\frac{Ed^2 t}{1-\upsilon^2}\right)_{skins} \qquad 5.10$$

$$d = c + t \qquad 5.11$$

where *c* is the core thickness, *t* is the skin thickness and *d* is the centre to centre distance between the top and bottom skins.

Equation 5.10 was used to calculate the *D* of the sandwich and this was substituted in Equation 5.2 to find the frequency. The results are shown in Figure 5.15. It can be seen there is some divergence between the predicted and experimental values of the two-way single span GFRP sandwich slab. This divergence increases when the span to depth ratio decreases.

From the literature, the ratio between the fixed-fixed and simply-simply supported beam frequencies is 1.5. In addition, the ratio between the fixed-simply and simply-simply frequencies is 1.25 (Reddy 2004). It can be assumed the glue restraint slab has approximately fixed-fixed support behaviour, and the screw restraint slab has fixed-simply support behaviour. These assumptions give an opportunity to predicate the frequency of the screw and glue restraints GFRP sandwich slab. The value of α is equal to; 1.0, 1.25, and 1.5 for simple, screw and glue restraints respectively. The two Equations 5.1 and 5.2 can be re-written in the following forms:

$$w = \alpha * \left(\frac{a_n}{L}\right)^2 * \sqrt{\frac{EI}{\rho A}} \qquad \textit{One-way slab} \qquad 5.12$$

$$w = \alpha * \frac{\pi^2}{b^2} * \sqrt{\frac{D}{I_o}} * \left[\left(\frac{b}{a}\right)^2 + 1\right] \qquad \textit{Two-way slab} \qquad 5.13$$

where α is a variable which depends on the support restraint types.

Equations 5.12 and 5.13 were used to predict the frequency of the screw and glue restrained slab, and the results are shown in Figures 5.14, and 5.15. It can be seen that the restraint types of the GFRP sandwich slab are an important factor to be considered in the slab design. It can be seen from Figures 5.14 and 5.15 that the prediction equations diverge around the lower span slabs and this divergence reduces with increase of the slab span. In the low span length the ratio of the ratio of the span (L_x) to the depth of the slab is less than 20.

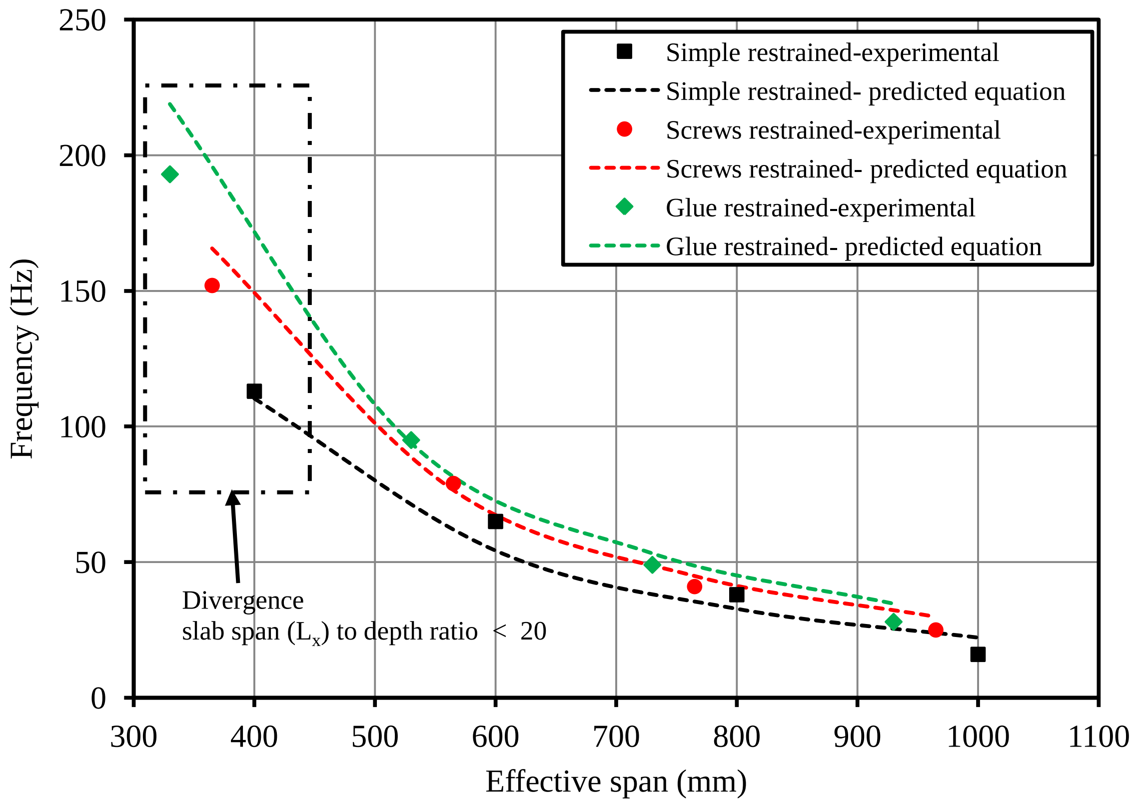

Figure 5.14 Prediction of one-way GFRP slab frequency.

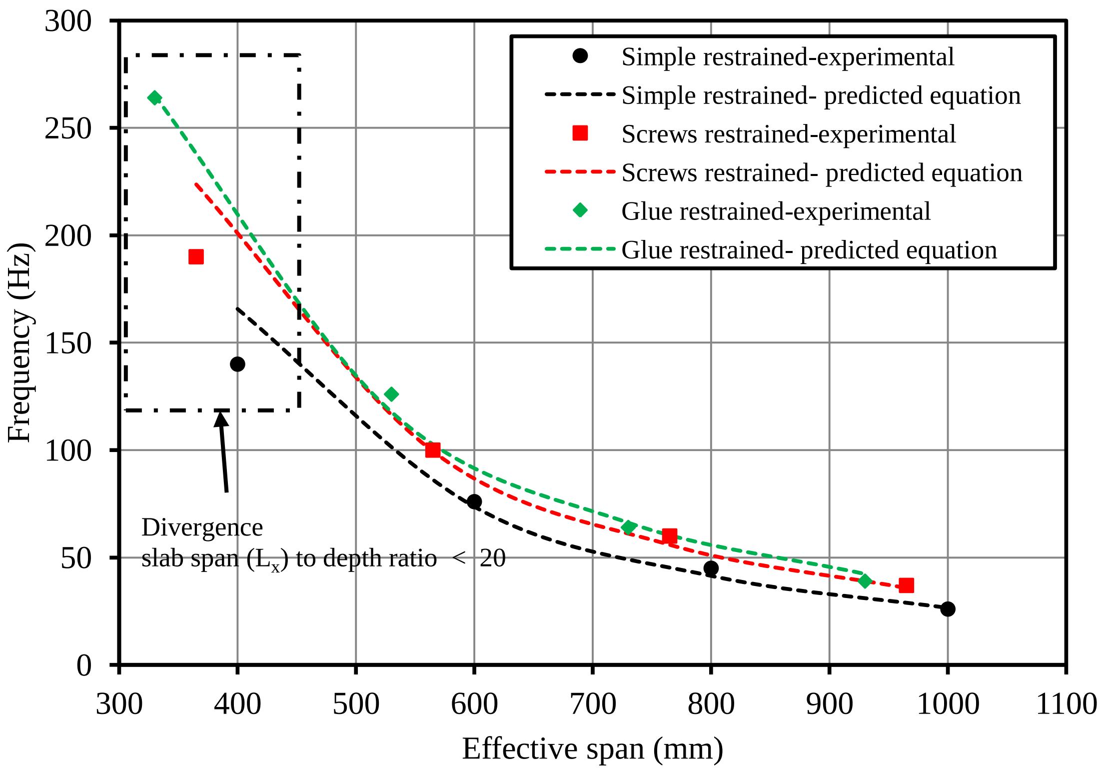

Figure 5.15 Prediction of two-way GFRP slab frequency.

5.4 Chapter conclusions

Free vibration tests were conducted on novel GFRP sandwich slabs. Different parameters have been studied for the slabs such as one-way spans, two-way spans, fibre orientations, restraint types and slab dimension aspect ratio. Several points were discovered in the free vibration slabs testing. The $0^o/90^o$ fibre orientation gives higher frequency than $\pm45^o$ fibre orientation in one-way support slab type S1. In contrast, $\pm45^o$ fibre orientation gives higher frequency than $0^o/90^o$ fibre orientation for two-way support slab type S2. Simple restrained slabs have the lowest frequency, and glue restrained slabs have the highest frequency.

Slab frequency decreases with increase in span length in a non-linear manner. Increasing the number of supports increases the natural frequency values of the slab. Finally, there is no impact on the frequency value by adding more supports in the mid span to the slabs T3, T4, T8, and T9 in the case of simple restrained slabs. The theoretical equations provide a reasonable prediction when the span to depth ratio greater than 20.

The current chapter provides important information for the designer about the behaviour of GFRP sandwich slabs. The free vibration behaviour of single and glue GFRP sandwich laminated beams is presented in Appendix-B. The testing of single and glue laminated beams provide more information about the free vibration behaviour. In addition, the beams experimental behaviour was compared with predicted theoretical equations. Chapters 3, 4, and 5 described the experimental behaviour of beams and slabs in both static and free vibration situations. The following Chapter 6 focuses on the development of FEA modelling and simulation. FEA is justified for the static and free vibration tests.

Chapter 6

FE simulation and modelling verifications

6.1 Introduction

The Finite Element Analysis (FEA) method offers a numerical solution for the analysis of fibre reinforce polymer (FRP) composite structures, with the analysis results showing the deformations, stresses, and strains through complex structures (Kollár & Springer 2003). The success of the new civil engineering technology depends on the ability to determine the behaviour of the structures with an acceptable level of accuracy. In the civil engineering applications, different forms of FRP composite structural elements have been developed such as, sandwich panels, pultrusion and plates. To model FRP materials, FEA method has been developed in two forms, two-dimensional (2D) and three-dimensional (3D) simulations. Shell element represents a common application of 2D FRP composite structural analysis (Hoo Fatt & Pothula 2010; Kollár & Springer 2003; Roy et al. 2010). A 3D composite solid element is used for the simulation of thick composite structure. Multi-layer of different materials arranged in different orientations can be specified in each shell and in each 3D solid element (ABAQUS 2008; Panigrahi & Pradhan 2009; Pyo & Lee 2009).

Previous Chapters 3, 4, and 5 discussed the experimental behaviour of the GFRP sandwich beams and slabs. Following the methodology developed in Chapter 2, FEA modelling needs verification before using it for design optimisation. This chapter covers FEA formulation for the 3D composite solid elements, the interaction model, material modelling, user subroutine, static and dynamic simulation.

6.2 Finite Element formulation

FEA method is attractive to researchers because it is a powerful numerical technique for the analysis of solid mechanics (Ochoa & Reddy 1992). The nature of FRP composite materials requires a certain type of element for the simulation of layers combination. It would be possible in theory to stack several brick elements to simulate the plies. Each brick element represents one ply of composite. However, it would be very difficult and expensive to run this simulation for the whole composite structure. In addition, using brick element layers to simulate a very thin plate would lead to ill-conditioned sets of equations (Matthews 2000). The 3D continuum solid element solves this problem for large composite structure.

6.2.1 Continuum 3D solid element

Creation of 3D solid continuum element model requires more attention with a computational time more than the conventional shell element model. The continuum 3D element can be derived depending on the brick element formulations. This element can be used with single homogenous material or can include layers of different materials. The continuum element has only displacement degrees of freedom without rotations at nodes. Its advantages are: i) boundary conditions can be specified on top or bottom of the solid element ii) it is compatible with the three-dimensions CAD software and iii) it provides a better description for the inter-laminar shear and normal stresses than shell element (Klinkel et al. 1999). Continuum 3D solid element analysis is required for these cases:

1. Transverse shear effects predominate.
2. Normal stress cannot be ignored.
3. Accurate inter-laminar stresses are required.

Material layers could be stacked in any direction within the continuum 3D solid element. Stacking direction, associated element faces, and the positions of element integration point output variables in the layer plane are shown in Figure 6.1. Numerical integration is used to develop element matrixes. Gauss's quadrature is used in the plane of the layers or plies, and Simpson's rule is used in the stacking direction (ABAQUS 2008).

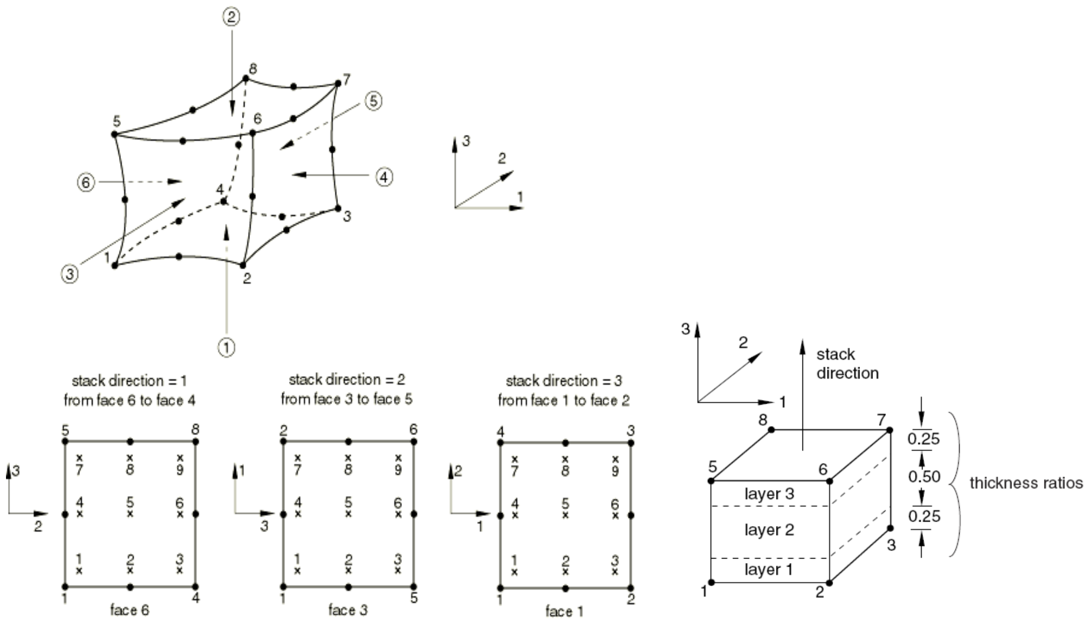

(a) Stacking directions. (b) Multi-layer element.

Figure 6.1 3D continuum solid element.

In the 3D stress-strain relationships for orthotropic linear elastic material is described below (Donadon et al. 2009; Knight Jr 2006):

$$\{\varepsilon\} = \begin{Bmatrix} \varepsilon_{11} \\ \varepsilon_{22} \\ \varepsilon_{33} \\ \varepsilon_{12} \\ \varepsilon_{13} \\ \varepsilon_{23} \end{Bmatrix} = \begin{bmatrix} S_{11} & S_{12} & S_{13} & 0 & 0 & 0 \\ S_{21} & S_{22} & S_{23} & 0 & 0 & 0 \\ S_{31} & S_{32} & S_{33} & 0 & 0 & 0 \\ 0 & 0 & 0 & S_{44} & 0 & 0 \\ 0 & 0 & 0 & 0 & S_{55} & 0 \\ 0 & 0 & 0 & 0 & 0 & S_{66} \end{bmatrix} \begin{Bmatrix} \sigma_{11} \\ \sigma_{22} \\ \sigma_{33} \\ \sigma_{12} \\ \sigma_{13} \\ \sigma_{23} \end{Bmatrix} = [S]\{\sigma\} \qquad 6.1$$

where $\boldsymbol{\varepsilon}$ is the strain. σ is the stress. The non-zero S_{ij} are:

$$S_{11} = \frac{1}{E_{11}} \qquad 6.2$$

$$S_{22} = \frac{1}{E_{22}} \qquad 6.3$$

$$S_{33} = \frac{1}{E_{33}} \qquad 6.4$$

$$S_{12} = S_{21} = -\frac{v_{21}}{E_{22}} = -\frac{v_{12}}{E_{11}} \qquad 6.5$$

$$S_{13} = S_{31} = -\frac{v_{31}}{E_{33}} = -\frac{v_{13}}{E_{11}} \qquad 6.6$$

$$S_{23} = S_{32} = -\frac{v_{23}}{E_{33}} = -\frac{v_{32}}{E_{22}} \qquad 6.7$$

$$S_{44} = \frac{1}{G_{12}} \qquad 6.8$$

$$S_{55} = \frac{1}{G_{13}} \qquad 6.9$$

$$S_{66} = \frac{1}{G_{23}} \qquad 6.10$$

$$v_{12} = v_{21}\frac{E_{22}}{E_{11}} \qquad 6.11$$

$$v_{31} = v_{13}\frac{E_{33}}{E_{11}} \qquad 6.12$$

$$v_{32} = v_{23}\frac{E_{33}}{E_{22}} \qquad 6.13$$

where v_{ij} is Poisson's ratio of the material.

Hence, the stress-strain relation can be obtained from the Equation 6.1:

$$\{\sigma\} = \begin{Bmatrix} \sigma_{11} \\ \sigma_{22} \\ \sigma_{33} \\ \sigma_{12} \\ \sigma_{13} \\ \sigma_{23} \end{Bmatrix} = \begin{bmatrix} C_{11} & C_{12} & C_{13} & 0 & 0 & 0 \\ C_{21} & C_{22} & C_{23} & 0 & 0 & 0 \\ C_{31} & C_{32} & C_{33} & 0 & 0 & 0 \\ 0 & 0 & 0 & C_{44} & 0 & 0 \\ 0 & 0 & 0 & 0 & C_{55} & 0 \\ 0 & 0 & 0 & 0 & 0 & C_{66} \end{bmatrix} \begin{Bmatrix} \varepsilon_{11} \\ \varepsilon_{22} \\ \varepsilon_{33} \\ \varepsilon_{12} \\ \varepsilon_{13} \\ \varepsilon_{23} \end{Bmatrix} = [S]\{\varepsilon\} \qquad 6.14$$

The stiffness coefficient C_{ij} in the above stress-strain relation can be explained by using the elastic material constants:

$$C_{11} = \frac{(1-v_{23}v_{32})E_{11}}{\Delta} \qquad 6.15$$

$$C_{22} = \frac{(1-v_{13}v_{31})E_{22}}{\Delta} \qquad 6.16$$

$$C_{33} = \frac{(1-v_{12}v_{21})E_{33}}{\Delta} \qquad 6.17$$

$$C_{12} = C_{21} = \frac{(v_{12}-v_{13}v_{32})E_{22}}{\Delta} = \frac{(v_{21}-v_{31}v_{23})E_{11}}{\Delta} \qquad 6.18$$

$$C_{13} = C_{31} = \frac{(v_{13}-v_{12}v_{32})E_{33}}{\Delta} = \frac{(v_{31}-v_{21}v_{23})E_{11}}{\Delta} \qquad 6.19$$

$$C_{23} = C_{32} = \frac{(v_{23} - v_{13}v_{21})E_{33}}{\Delta} = \frac{(v_{32} - v_{31}v_{12})E_{22}}{\Delta} \quad 6.20$$

$$C_{44} = G_{12} \quad 6.21$$

$$C_{55} = G_{13} \quad 6.22$$

$$C_{66} = G_{23} \quad 6.23$$

$$\Delta = 1 - v_{12}v_{21} - v_{23}v_{32} - v_{13}v_{31} - 2v_{21}v_{32}v_{13} \quad 6.24$$

where E_{11}, E_{22} and E_{33} are the material elastic module in three dimensions as shown in Figure 6.2.

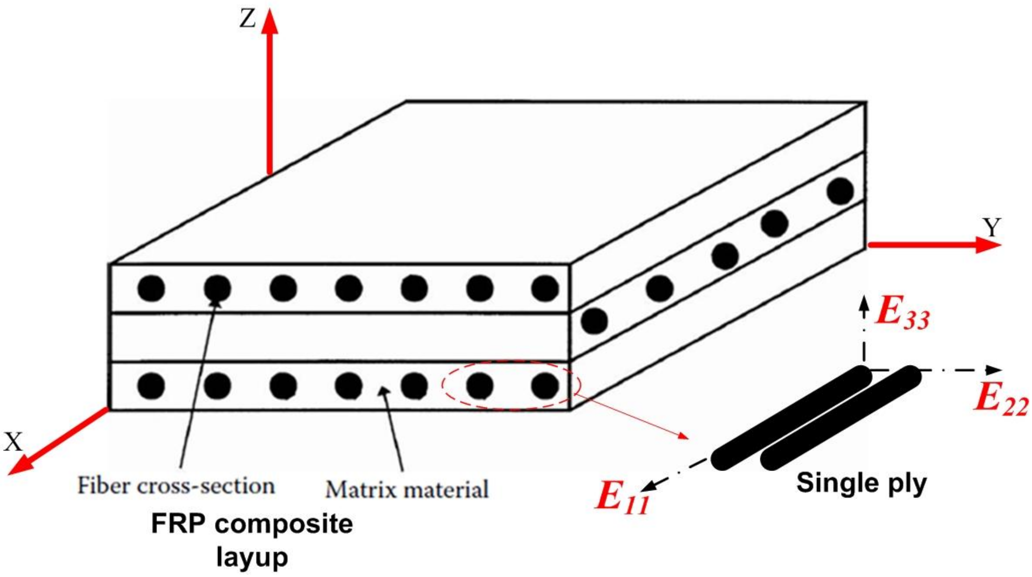

Figure 6.2 Fibre composite material in 3D model.

6.2.2 Contact Interaction

Contact interaction is a very essential part in the FEA simulation because it provides the right understanding to the force transmissions between the components of the single structures and between structures. Surface to surface contact interaction model was used in the interaction simulation. Whereas, the surface might interact with the other surfaces and such surfaces should be extended far enough to be included in the interaction developed during the FEA. One of the surfaces is called master surface, and the other is called slave surface as shown in Figure 6.3. Extending the interaction surfaces might affect the cost analysis and any nodes separated from the master surface during the analysis could increase computational memory usage. The master surface might be an analytical rigid surface, while the slave surface might be attached to deformable bodies. When both surfaces are attached to deformable bodies, the master surface should be the larger surface, and the slave is the smaller surface. If both surfaces have the same area, the master surface is the stiffer body, and the slave surface is the softer one. Interaction between any nodes in the master surface and slave surface is shown in Figure 6.4. The unit vector N can be calculated for each point on the segment 1-2 and 2-3. The unit vector N_2 is the average vector of the segments 1-2 and 2-3. An anchor point for each node of slave surface should be calculated on the master surface. At distance X_o the anchor point for the slave point 103 the contact u_2 vector of master surface is calculated.

$$X_0 = (1 - u_0)X_1^m + u_0 X_2^m \qquad 6.25$$

where $X_1^m$and X_2^m are the coordinates of master nodes 1 and 2 respectively. The contact vector v_0 in tangential direction is perpendicular to $N(X_0^m)$.

$$v_0 = T(X_1^m - X_2^m) \qquad 6.26$$

where T is a rotation matrix (ABAQUS 2008).

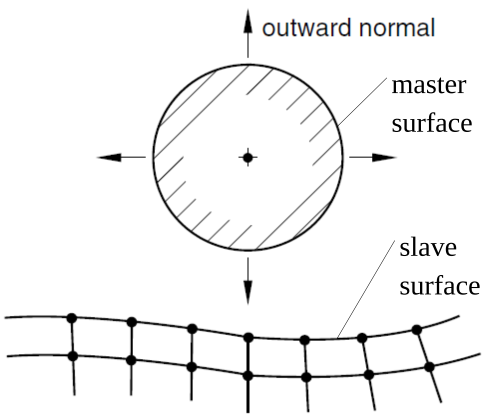

Figure 6.3 Master and slave surfaces.

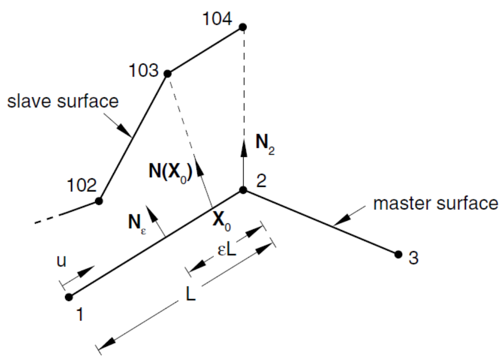

Figure 6.4 Interaction between nodes in master and slave surfaces.

There are two contact models used in the FEA, tied interface and Lagrange multiplier. The Lagrange multiplier is formulated by using the gap (*g*) between the two surfaces multiplied by the Lagrange multiplier as shown below.

$$g = X_i^s - X_i^m \tag{6.27}$$

$$if\ g = \begin{cases} > 0; No\ contact \\ = 0; Contact \\ < 0; Pentration \end{cases} \tag{6.28}$$

$$\Pi_c = \int_{\Gamma_c} \lambda_\Gamma^T (x^s - x^m) d\Gamma \ \approx \ \lambda_n g \tag{6.29}$$

where t_Γ is the surface traction, x^s is the position on the slave surface, x^m is the position on the master surface and λ_n is the Lagrange multiplier. The first derivative is:

$$\delta\Pi_c = \delta\lambda_n g + (\delta u^s - \delta u^m)\lambda_n = [\delta u^s \quad \delta u^m \quad \delta\lambda_n] \begin{Bmatrix} \lambda_n \\ -\lambda_n \\ g \end{Bmatrix} \tag{6.30}$$

where *u* is the deformation. λ_n represents the required "force" to prevent the penetration between surfaces. Linearization is required for the Newton solution process and the tangent form for the nodal contact element is (Zienkiewicz & Taylor 2005):

$$\begin{bmatrix} 0 & 0 & 1 \\ 0 & 0 & -1 \\ 1 & -1 & 0 \end{bmatrix} \begin{Bmatrix} du^s \\ du^m \\ d\lambda_n \end{Bmatrix} = \begin{Bmatrix} -\lambda_n \\ \lambda_n \\ -g \end{Bmatrix} \tag{6.31}$$

The tie interface is explained by Figure 6.5, where the line AB is the interface part between the two regions. Those two regions have different mesh size and AB should have the following conditions:

- Coordinate deformation (x^i) at both surfaces are the same.

$$x^1|^{AB} = x^2|^{AB} \tag{6.32}$$

- Traction interface (t^i) summation for both regions is equal to zero.

$$t^1|^{AB} + t^2|^{AB} = 0 \tag{6.33}$$

To achieved these conditions, the Lagrange multiplier function is introduced as:

$$\Pi_1 = \int_{\Gamma_1} \lambda^T (x^1 - x^2) d\Gamma^1 \qquad 6.34$$

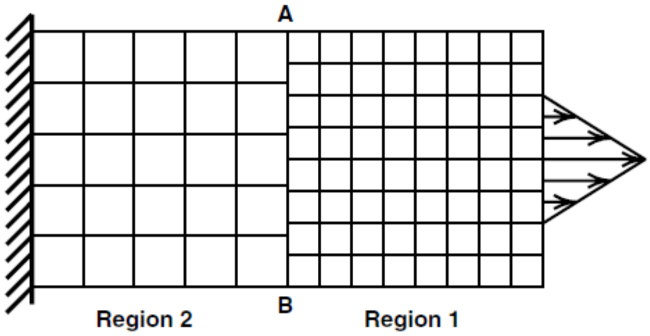

Figure 6.5 Tied interface between two regions (Zienkiewicz & Taylor 2005).

The tie model was used in contact interaction modelling in this study. In FEA of the GFRP sandwich beams and slabs, some parts are attached to each other with no relative movement between them. The tied model represents the right option for this type of contact. The tie model was used in the interaction simulation between the glue-laminated sandwich beam layers, and the interaction between the slab and the support in the glue restraint cases. The Lagrange multiplier was used with the interaction between GFRP skin and the loading and supporting parts.

6.2.3 Core-skin interaction

The traction separation law was used for the damage evolution of the core - skin interaction. The elastic behaviour of the model is written in terms of an elastic constitutive matrix that relates the normal and shear stresses across the interface. The corresponding separations are denoted by δ_n, δ_s, and δ_t. Where, n and s refer to local 2D displacements and t refers to the third displacement. The elastic behaviour can be written as:

$$\begin{Bmatrix} t_n \\ t_s \\ t_t \end{Bmatrix} = \begin{pmatrix} K_{nn} & K_{ns} & K_{nt} \\ K_{ns} & K_{ss} & K_{st} \\ K_{nt} & K_{st} & K_{tt} \end{pmatrix} \begin{Bmatrix} \delta_n \\ \delta_s \\ \delta_t \end{Bmatrix} \qquad 6.35$$

where t_n, t_s and t_t are the nominal traction stresses, and K is the stiffness of the cohesive layer.

A cohesive element is used to connect two different parts, skin and core and it depends on the traction separation law. In novel GFRP sandwich panel, there is no adhesive used to connect the skin and core. Therefore, using a zero-thickness cohesive element approach is more practical. The cohesive element has three components, two shear forces parallel to the plan of interaction and the third force is normal to the interaction plane. Degradation starts with damage initiation of the cohesive at contact points. A stress based traction separation approach was used in this study. Damage is assumed to start when the maximum contact ratio reaches one of the maximum values:

$$max\left[\frac{\langle t_n\rangle}{t_n^0},\frac{t_s}{t_s^0},\frac{t_t}{t_t^0}\right]=1 \qquad 6.36$$

where $t_n^0, t_s^0\ and\ t_t^0$ are the peak normal, first and second shear stress values for the contact surface respectively. $\langle\ \rangle$ is Macauluny bracket with the usual interpretation. Damage evolution in this model is calculated for the cohesive surfaces. The contact stress components after damage initiation are described below (ABAQUS 2008).

$$t_n=\begin{cases}(1-R)\bar{t}_n, & \bar{t}_n\geq 0\\ \bar{t}_n\ , & no\ damge\ in\ compressive\ stiffness\end{cases} \qquad 6.37$$

$$t_s=(1-R)\bar{t}_s \qquad 6.38$$

$$t_t=(1-R)\bar{t}_t \qquad 6.39$$

where $\bar{t}_n, \bar{t}_s\ and\ \bar{t}_t$ are the contact stress components calculated at the current stage of load for elastic behaviour. R is a scalar damage variable ($0 \leq R \leq 1$).

6.2.4 Extended Finite Element Method

An Extended Finite Element Method (XFEM) is a re-meshing finite element method based on cracking location and discontinuity. The XFEM was developed by Belytschko and Black (1999) for crack growth in the FEA model. It is an extension of the conventional finite element method based on the concept of partition of unity which allows discontinuous enrichment functions to be incorporated into the FEA model (ABAQUS 2008). Fracture analysis requires the enhancement of using the enrichment functions to capture the singularity around the crack tip and a discontinuous function that represents the jump in displacement across the crack surfaces. The approximation for a displacement vector function (u) with the partition of unity enrichment is:

$$u = \sum_{I=1}^{N} N_I(x)[u_I + H(x)a_I + \sum_{\alpha=1}^{4} F_\alpha(x) b_I^\alpha] \qquad 6.40$$

where $N_I(x)$ is the usual nodal shape functions, a_I is the nodal enriched degree of freedom vector, $H(x)$ is the associated discontinuous jump function across the crack surfaces, b_I^α is the product of the nodal enriched degree of freedom vector, and $F_\alpha(x)$ is the asymptotic crack-tip function.

Crack initiation is the beginning of material degradation in an enriched element. Degradation starts when the stresses satisfy the crack initiation criteria. The maximum principal stress criterion is conducted as the crack initiation criteria. When the maximum principal stress is maintained, a new crack is created and it is always orthogonal to the maximum principal stress direction. The XFEM works with the 3D element type C3D8R in Abaqus. A traction separation is adopted based on the ultimate principle tensile stress.

6.3 Material constitutive models

6.3.1 Core constitutive model

The phenolic core material is the middle part of the FRP sandwich panel and is expected to carry the shear forces. The behaviour of the modified phenolic core material is different in tension and in compression. It is non-linear in compression while it is approximately linear up to failure in tension. The uni-axial tension and compression behaviour are shown in Figure 6.6(a) (details are provided in Appendix-A). The behaviour of the modified phenolic core follows the behaviour of foam materials (Gibson & Ashby 1999). Rizov (2006) presented a numerical and experimental studies on the non-linear simulation of sandwich foam core material. The conclusion was made that using a CRUSHABLE FOAM model with a hardening is suitable way to simulate the foam core.

The CRUSHABLE FOAM model was used to simulate the non-linear behaviour of the present sandwich panel core. The uni-axial behaviour of the modified phenolic core is divided into three stages, an elastic stage from the point O to point A, a core crushing stage from the point A to B and the compression of compacted core from point B to C. The compression curve ABC represents the plastic behaviour of the material as shown in Figure 6.6(a). The CRUSHABLE FOAM model is shown in Figure 6.6(b). It uses a uni-axial hardening to simulate material in the plastic state. There are three surfaces, original surface, yield surface and flow potential surface. The yield surface is defined by the following (ABAQUS 2008; Deshpande & Fleck 2000):

$$F = \sqrt{q^2 + \alpha^2 (p - p_0)^2} - B = 0 \quad 6.41$$

$$p = -\frac{1}{3}\,\sigma \quad 6.42$$

$$q = \sqrt{\frac{3}{2}S} \quad 6.43$$

$$\alpha = \frac{B}{A} \quad 6.44$$

$$B = \alpha\, A = \alpha\, \frac{p_c + p_t}{2} \quad 6.45$$

$$p_o = \frac{p_c + p_t}{2} \quad 6.46$$

where p is the pressure stress, q is the Mises stress, S is the deviatoric stress α is the shape factor of the yield surface, p_0, p_t and p_c are the centre of the yield surface, hydrostatic tension and hydrostatic compression, A and B is the size of the horizontal and vertical yield ellipse (ABAQUS 2008).

Hardening happens after core crushing. The yield surface intersects with the horizontal axes at p_c and p_t. p_t is assumed constant while p_c represents the compaction of core material and increase in density, or p_c is a dilation of the material with decrease in density. The hardening of the core material can be expressed in terms of volumetric strain:

$$p_c = \frac{\sigma_c\left[\sigma_c\left(\frac{1}{\alpha^2}+\frac{1}{9}\right)+\frac{p_t}{3}\right]}{p_t+\frac{\sigma_c}{3}} \quad 6.47$$

The plastic part of the mechanical behaviour of the core is adopted from the uni-axial compression behaviour of the core. A calibration of the model parameters is recommended by the Abaqus manual (ABAQUS 2008).

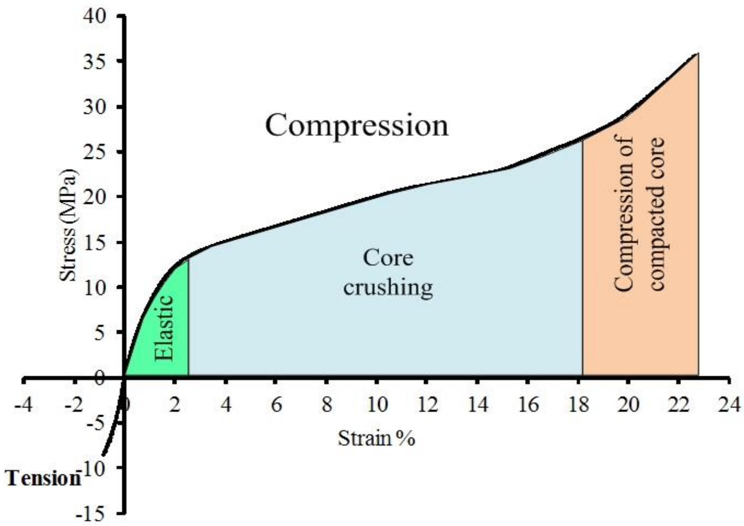

(a) Uni-axial model.

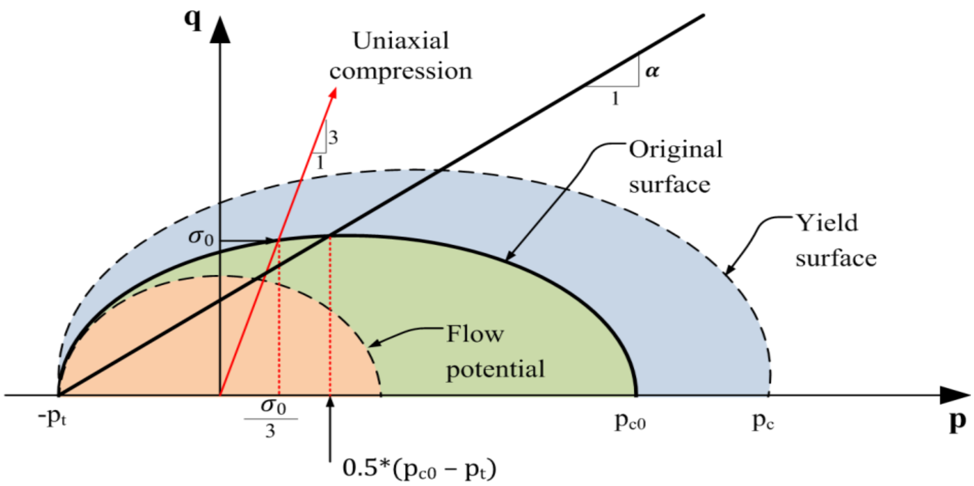

(b) CRUSHABLE FOAM model.

Figure 6.6 Phenolic core modelling.

6.3.2 GFRP skin model

Modelling of fibre composite material is very important in the failure analysis of fibre composite structures. Many materials exhibit elastic-brittle behaviour and the damage is initiated without significant plastic deformation. Camanho and Matthews (1999) used the Hashin model to simulate progressive damage of fastened joint composite laminates. Karakuzu et al. (2008) used the Hashin model to simulate a fibre composite plate with pin-loaded holes. Santiuste et al. (2010) compared the results between the Hou and Hashin models in the prediction of dynamic bending failure of fibre composite laminated beams. They concluded that the Hashin model was more progressive than the Hou model, and Hashin model gives a good ability to simulate the GFRP skin behaviour. Mines and Alias (2002) presented a numerical simulation of sandwich beam progressive collapse by using the Hashin model to simulate GFRP skins. Their study found that the Hashin model works well with FRP sandwich modelling.

Experimental analysis of the present two layers of biaxial GFRP skins showed an approximately linear behaviour with sudden failure at the maximum stress (Manalo et al. 2010d). Therefore, the Hashin model was used to simulate the elastic–brittle behaviour of the glass fibre composite in this work. The same tension elastic modulus is used for the GFRP skin in tension and compression as shown in Figure 6.7. In each ply, the fibre is assumed to be parallel and four different failure modes were considered: i) fibre in tension ii) fibre in compression iii) matrix cracks under transverse tension and iv) matrix crushing under transverse compression. The response of the material is assumed to be (ABAQUS 2008; Hashin & Rotem 1973):

$$\tilde{\sigma} = C_d \varepsilon \tag{6.48}$$

where $\tilde{\sigma}$ is the nominal stresses, $\boldsymbol{\varepsilon}$ is the strain and C_d is:

$$C_d = \begin{pmatrix} (1-d_f)E_1 & (1-d_f)(1-d_m)\upsilon_{12}E_1 & 0 \\ (1-d_f)(1-d_m)\upsilon_{12}E_2 & (1-d_m)E_2 & 0 \\ a_0 & 0 & (1-d_s)GR \end{pmatrix} \tag{6.49}$$

$$R = 1-(1-d_f)(1-d_m)\upsilon_{12}\upsilon_{21} \tag{6.50}$$

where d_f, d_m and d_s is the damage state in the fibre, matrix and shear. G is the shear modulus, and v_{12} and v_{21} are the Poisson ratios. The failure point is fixed by creating an initiation failure as a brittle failure. The general forms of damage initiations are (ABAQUS 2008; Hashin & Rotem 1973):

Fibre tension ($\sigma_{11} \geq 0$)

$$F_f^t = \left(\frac{\sigma_{11}}{X^T}\right)^2 + \alpha\left(\frac{\tau_{12}}{S^L}\right)^2 \tag{6.51}$$

Fibre Compression ($\sigma_{11} < 0$)

$$F_f^c = (\frac{\sigma_{11}}{X^C})^2 \quad 6.52$$

Matrix tension ($\sigma_{22} \geq 0$)

$$F_m^t = (\frac{\sigma_{22}}{Y^T})^2 + \beta(\frac{\tau_{12}}{S^L})^2 \quad 6.53$$

Matrix Compression ($\sigma_{22} < 0$)

$$F_m^c = (\frac{\sigma_{22}}{2S^T})^2 + [(\frac{Y^C}{2S^T})^2 - 1]\frac{\sigma_{22}}{Y^C} + (\frac{\tau_{12}}{S^L})^2 \quad 6.54$$

where X^T and X^c refer to the longitudinal fibre tension and compression strength, Y^T and Y^c refer to the transverse matrix tension and compression strength and S^L and S^T refer to the longitudinal and transverse shear strength. α is the shear contribution factor, and σ_{11}, σ_{22}, and τ_{12} are the effective stresses tensor components.

The Hashin failure model was developed for uni-directional lamina. The extended Hashin model was developed to include the third direction stress σ_{33}. The three-dimensional model for Hashin failure criteria is described below (Hashin 1980; Linde et al. 2004):

Fibre tension ($\sigma_{11} \geq 0$)

$$F_f^t = (\frac{\sigma_{11}}{X^T})^2 + (\frac{\tau_{12}}{S^L})^2 + (\frac{\tau_{13}}{S^L})^2 \quad 6.55$$

Fibre Compression ($\sigma_{11} < 0$)

$$F_f^c = (\frac{\sigma_{11}}{X^C})^2 \quad 6.56$$

Matrix tension ($\sigma_{22}+\sigma_{33} \geq 0$)

$$F_m^t = \frac{(\sigma_{22})^2 + (\sigma_{33})^2}{(Y^T)^2} + (\frac{\tau_{23}}{S_{23}})^2 - \frac{\sigma_{22}\sigma_{33}}{S_{23}{}^2} + \frac{\tau_{12}{}^2 + \tau_{13}{}^2}{S_{12}{}^2} \quad 6.57$$

Matrix Compression ($\sigma_{22}+\sigma_{33} < 0$)

$$F_m^c = [(\frac{Y^C}{2S_{23}})^2 - 1]\frac{\sigma_{22}+\sigma_{33}}{Y^C} + \frac{(\sigma_{22}+\sigma_{33})^2}{4S_{23}^2} + \frac{(\sigma_{23}^2 - \sigma_{22}\sigma_{33})}{S_{23}^2} + \frac{\sigma_{12}^2+\sigma_{13}^2}{S_{12}^2} \quad 6.58$$

Inter-laminar normal tensile failure ($\sigma_{33} \geq 0$)

$$F_l^t = (\frac{\sigma_{33}}{Z^T})^2 \quad 6.59$$

Inter-laminar normal compression failure ($\sigma_{33} < 0$)

$$F_l^c = (\frac{\sigma_{33}}{Z^C})^2 \quad 6.60$$

where Z^T and Z^c are the normal strengths of the composite layers in tension and compression respectively.

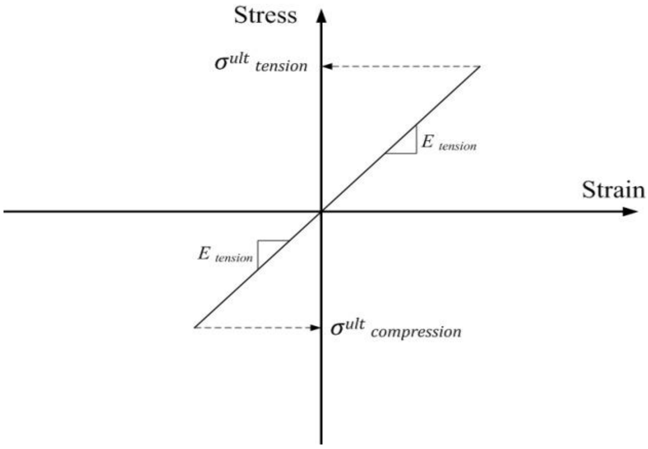

Figure 6.7 GFRP skin model.

6.3.3 User subroutine UMAT

Analysis of fibre composite structures requires predicting the failure of the composite itself. ABAQUS does not provide a built-in failure model for 3D-solid element simulation. However, ABAQUS offers the ability to use a special material constitutive model through a material subroutine called UMAT. Use of UMAT is necessary because none of the existing material models included in the ABAQUS material library could represent the FRP material behaviour up to failure. The present work involves writing a constitutive GFRP composite material model through the UMAT external subroutine. This subroutine provides the ability to do a non-linear FRP composite analysis of the 3D-solid FE model and such subroutine calls user-defined subroutine (Linde et al. 2004).

UMAT can be used to define the mechanical constitutive behaviour of GFRP skin materials. This includes material degradation and progressive damage developed in the material. The UMAT subroutine also simulates the failure in different modes and therefore, cannot be easily represented by one smooth function. The Hashin three-dimension stress-based model is widely accepted (Matthews 2000). The role of this subroutine is to update the stresses and solution-dependent state variables values at the end of the non-linear loading increment. The UMAT subroutine provides the numerical ability to use the Hashin failure model in the prediction of 3D composite solid element. It also contains six failure modes for the GFRP material which are fibre compression, fibre tension, matrix compression, matrix tension, tension de-lamination, and out of plane compression failure. In addition, it must provide a Jacobian matrix in Equation 6.1 for the composite material. Running UMAT is required to set up the FORTRAN environment and to manage the interaction with the external data files that are used in conjunction with the user subroutines. The ABAQUS execution procedure finds the subroutine file and compiles and links it with the rest of ABAQUS. The UMAT Fortran code file is described in Appendix-C. The UMAT loop is explained in Figure 6.8. The strain and stress need to be updated at a certain stage in the loop as follows (ABAQUS 2008):

$$\text{Strain update: } \varepsilon^{k+1} = \varepsilon^{k} + \Delta\varepsilon^{k+1} \qquad 6.61$$

$$\text{Stress update: } \sigma^{k+1} = \sigma(\varepsilon^{k}) + \Delta\sigma(\varepsilon^{k+1}) \qquad 6.62$$

where $\sigma(\varepsilon^{k})$ represent the stress at increment k and $\Delta\sigma(\varepsilon^{k+1})$ represents the delta stress at increment $k+1$.

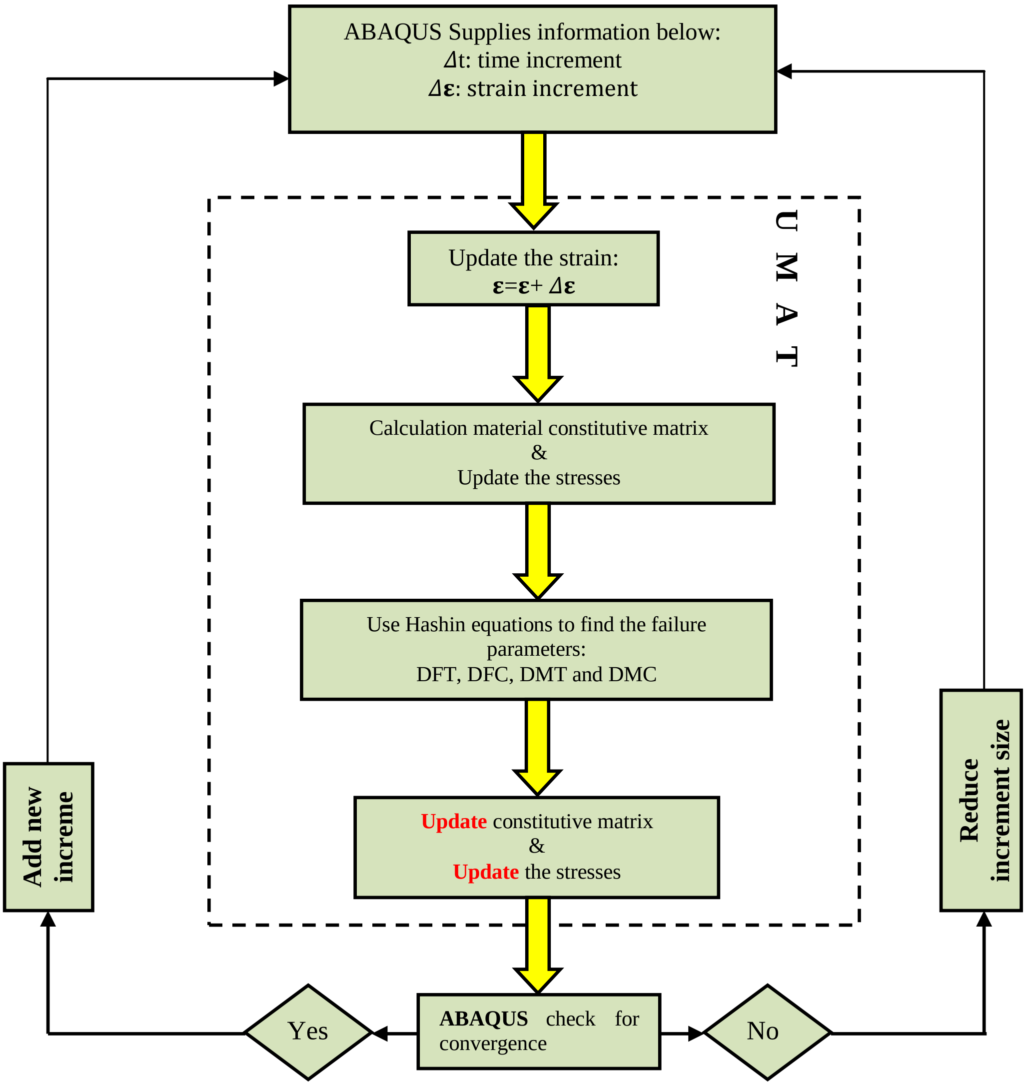

Figure 6.8 UMAT subroutine flow chart.

6.4 Validation of the FEA models

In this section, Full 3D FEA modelling is conducted to simulate the GFRP sandwich beam. The 3D solid continuum element is used for the core simulation and for the GFRP skin simulation. The simulation of the GFRP skin thickness is important in beam simulation, especially for the multi-layers glue-laminated sandwich beams. In the glue-laminated sandwich beam, the thickness of the skins contributes to the total thickness of the beam. The C3D20R solid continuum element was used for the GFRP skin. The C3D8R solid continuum element was used for the core simulation to get the option of cracking creation by using XFEM in Abaqus. Abaqus provides a

Hourglassing control, to overcome the problems of Hourglassing in the first-order reduce integration element,. In addition to the Hourglassing control, a second-order accuracy control can be used to get a smooth solution (ABAQUS 2008).

The GFRP skin experimental tests are explained in Appendix-A. The rules of mixture and micromechanics were used to calculate the ply properties of the GFRP skin for the FEA input is explained in Appendix-A as well. Sandwich panel properties for 15 mm and 18 mm thicknesses as are described in Table 6.1. The calculation of the skin mechanical properties is based on a fibre to matrix volume ratio equal to 27.77 %. The calculated ply properties represent the input of the FE model. Different cases from the experimental results are verified which include the individual materials modelling, UMAT subroutine, and mesh sensitivity.

Table 6.1 Materials mechanical properties.

Material	Elastic module MPa			Poisson's ratio	Shear strength MPa	Tensile stress MPa	Compressive stress MPa
	E_{11}	E_{22}	E_{33}				
Slab thickness =15 mm							
GFRP skin ply (theoretical)	24,021.7	3,420.1	3,420.1	0.35	45.1	480.4	432.3
Phenolic core	1,154.4	…….	…….	0.3	4.25	5.95	21.3
Slab thickness =18 mm							
GFRP skin ply (theoretical)	24,021.7	3,420.1	3,420.1	0.35	45.1	480.4	432.3
Chopped fibre ply (Manufacturer)	7,500	7,500	3,420.1	0.32	45.1	105	160
Phenolic core	1350.2	……	……	0.3	8.8	8.5	24.5

6.4.1 Modified phenolic core

The FEA model was developed to predict the uni-axial compression and tension behaviour of the modified phenolic core by using the CRUSABLE FOAM model with XFEM. The traction separation was adopted to create the tension cracks, which is based on the maximum principle stress in tension. The CRUSABLE FOAM model considers the non-linearity of the material and structural non-linearity in the simulation. No hydrostatic tests were done on the modified phenolic solid core in tension or compression. Implementing hydrostatic tensile tests is hardly ever applicable on high-density foams (ABAQUS 2008). Calibration of the model was managed based on previous studies that used the CUSHABLE FOAM model (Li et al. 2000; Rizzi et al. 2000). Model calibration showed an acceptably accurate prediction when the plastic Poisson's ratio (υ_p) is assumed equal to zero (ABAQUS 2008; Deshpande & Fleck 2000).

Experimental compression and tension tests were conducted as discussed in Appendix-A. The dog bone of the modified phenolic core material was simulated using a 3D brick element (C3D8R). A fine mesh was used to ensure the accuracy of the results. 2644 elements were used and the results are shown in Figure 6.9(a). This show that the FEA model shows a linear behaviour compared to the experimental tests. A GFRP sandwich sample with dimensions of 26 mm length, 26 mm width, and 18 mm thickness was modelled using 2D nonlinear FEA (Rizov 2006). A CPE4R element was used to simulate the core and skins (Rizov 2006). The core part was divided into 390 elements. Full interaction was assumed between the skin and core. Core hardening was used in the material modelling and the experimental stress-strain curve was used to calibrate the CRUSHABLE FOAM HARDENING model. To include hardening, few points were selected along the experimental curve as shown in Table 6.2. The results of the FEA simulation compared to the experimental result are shown in Figure 6.9(b). It shows that the CRUSHABLE FOAM model can simulate the axial core compression behaviour with an acceptable level of accuracy, especially in the elastic zone.

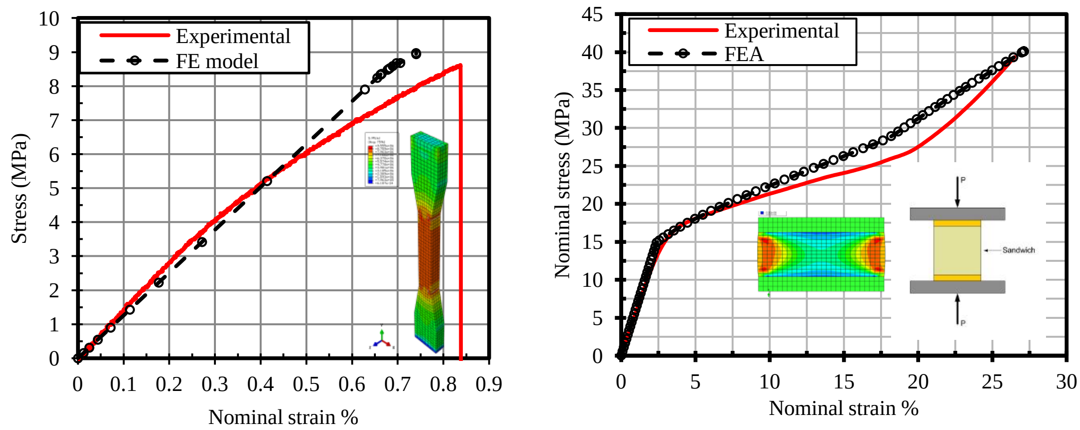

(a) Tension (b) Compression

Figure 6.9 Core tension and compression simulation.

Table 6.2 Modified phenolic core hardening.

Slab thickness	15 mm			18 mm		
Plastic stress (MPa)	22.0	22.5	35	15	24	38
Plastic strain %	0	0.2	0.31	0	0.12	0.2

6.4.2 GFRP skin

Using Hashin model was verified with the tensile test of the GFRP skin coupon. The thickness of the skin was 3 mm, and the GFRP skin had 6-plies. The experimental test and the details of the GFRP skin are provided in Appendix-A and Table 6.1. The 3D solid element type C3D20R was used in the simulation of the GFRP skin. The result of the test simulation is shown in Figure 6.10. The Hashin model parameter (α) is equal to 1.0. The sample was failed when the longitudinal stress reach the ultimate strength of the GFRP plies. The FEA results revealed that the Hashin model is able to predict the GFRP skin behaviour of the current product.

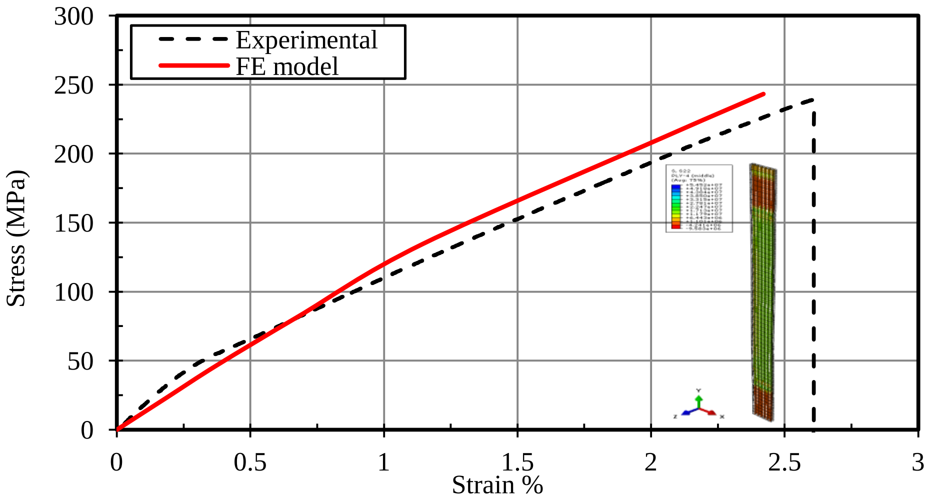

Figure 6.10 GFRP skin tensile FEA simulation.

6.4.3 Skin - core interaction

Skin - core interaction is very important in the simulation of GFRP sandwich panel, and the numerical modelling requires special attention to represent this interaction (Moreira & Rodrigues 2010). The present GFRP sandwich panel is fabricated in one stage, with no adhesive used to connect the core and the skins in the fabrication. Therefore, assessment of the skin-core interaction of this type of GFRP sandwich panel is more challenging. A numerical analysis was developed to simulate the behaviour of the skin-core interaction. A traction separation law was used to represent the damage evolution of the skin-core interaction. The skin-core interaction model was discussed in section 5.2.3. In this section, the model is verified with the skin-core interaction experimental test which is described in Appendix-A. The 3D FE model is shown in Figure 6.11(a). The 3D shell element type S8R was used in the simulation of the GFRP skin. The 3D solid element was used to simulate the core material.

The shear values of the traction separation model were used in the simulation are equal to 8.8 MPa and it was adopted from the experimental tests as shown in Appendix-A. The result of model verification is shown in Figure 6.11(a), and (b). This shows that the interaction separation model can deal with this type of core-skin interaction in GFRP sandwich panel. In addition, the stress - strain curve shows a good agreement with the experimental result.

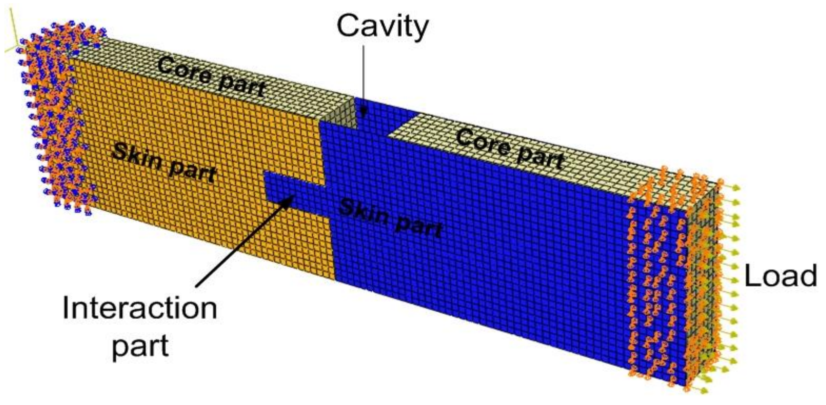

(a) FE 3D model of skin-core interaction test.

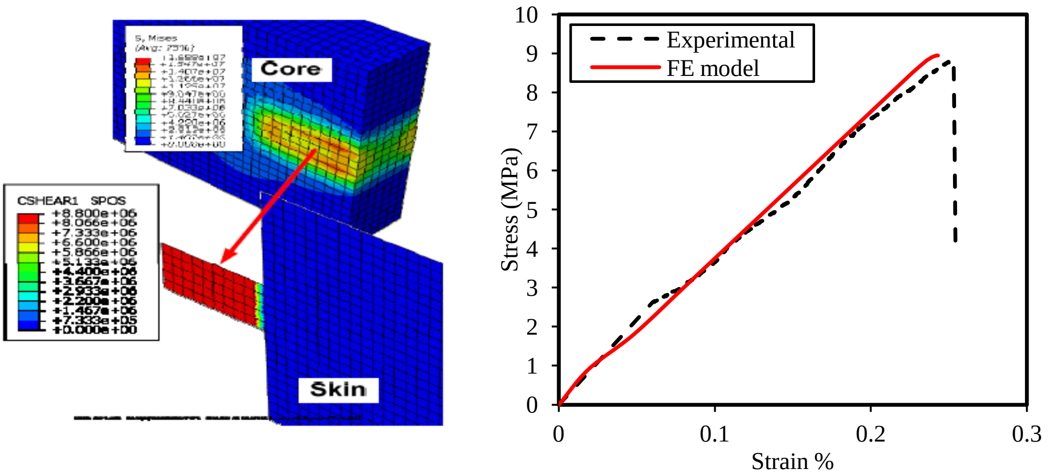

(a) Stresses in the skin and core. (b) Stress-strain.

Figure 6.11 Skin-core interaction.

6.4.4 UMAT subroutine verification

An external subroutine was written for material modelling of the 3D GFRP skin as shown in Appendix-B. The UMAT subroutine has been connected to the ABAQUS software through FORTRAN language. A comparison has been done in the simulation of the flexural test of a 400 mm single sandwich beam. Two analyses were performed by using the shell element (type S8R) and 3D continuum brick element (type C3D20R) to simulate the top and bottom skins of the GFRP sandwich beams.

Using the shell element to model the top and bottom skins of the GFRP sandwich beam does not require external material modelling, and it can use the available Hashin failure model for plan stress element in ABAQUS. The analysis of the glue laminated sandwich beams required the 3D continuum brick element to simulate the GFRP skin because of the influence of the skin thickness on the full depth of the beam. The FEA results are shown in Figure 6.12. It can be seen that the UMAT subroutine works very well in the simulation of the GFRP skin compare to the shell element. The FEA model with the shell element gives a lower estimate for the final load than the 3D solid continuum element. This is due to the effect of simulating the full thickness of the skin, shear contribution, and load distribution through the 3D skin.

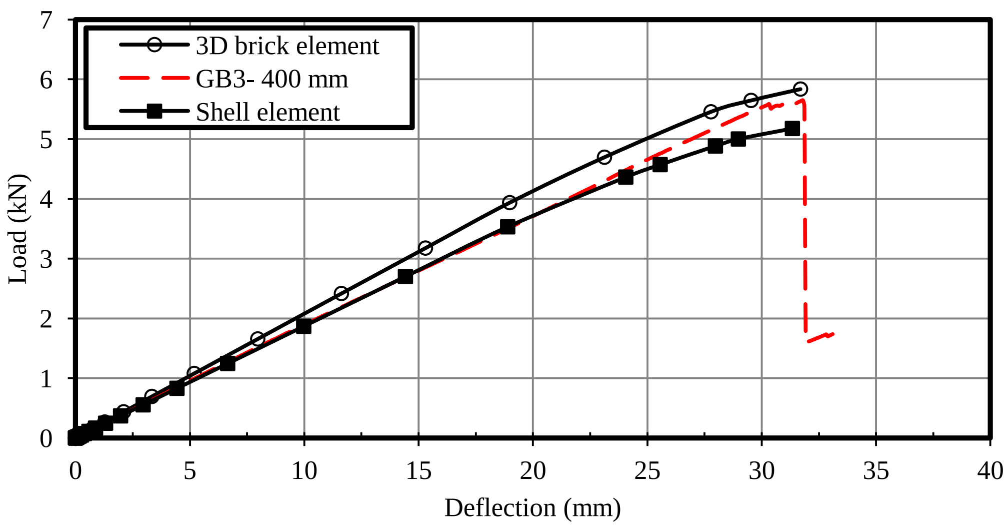

Figure 6.12 Comparison between shell and 3D continuum solid element (UMAT) in the simulation of GFRP skin.

6.4.5 Mesh size sensitivity

In order to determine appropriate mesh density for FEA, the GFRP sandwich beam was tested with three different mesh sizes. Coarse, medium, and fine meshes were chosen as shown in Figure 6.13(a). The same model was used to analyze the different meshes. The C3D20R element type was used for the GFRP skins and C3D8R core parts. The skin thickness is divided into two elements and this is kept constant for all models. There are 1296 elements for the coarse mesh, 2736 elements for the medium mesh, and 6816 elements for the fine mesh. A traction separation model was used to simulate the interaction between the skin and the core. A Lagrange multiplier was used to simulate the interaction between the GFRP skin and the loading and supporting steel parts.

The FEA analysis results for the three different meshed are presented as the final calculated failure load of the beam as shown in Figure 6.13(b). The coarse mesh shows a higher failure load than the others. The medium mesh shows a reasonable solution compared to the fine mesh. In addition, the medium mesh required less computational time than the fine mesh. As a result, the medium mesh size is sufficient to simulate such structures.

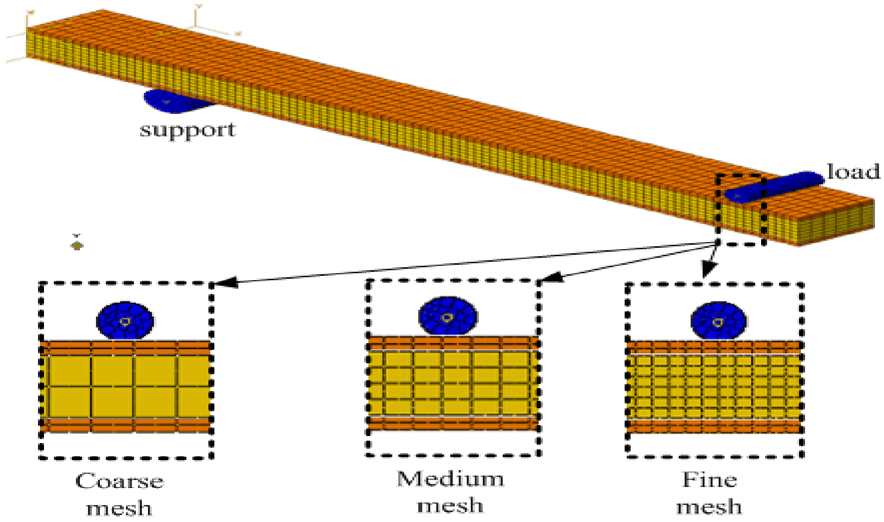

(a) Mesh sensitivity.

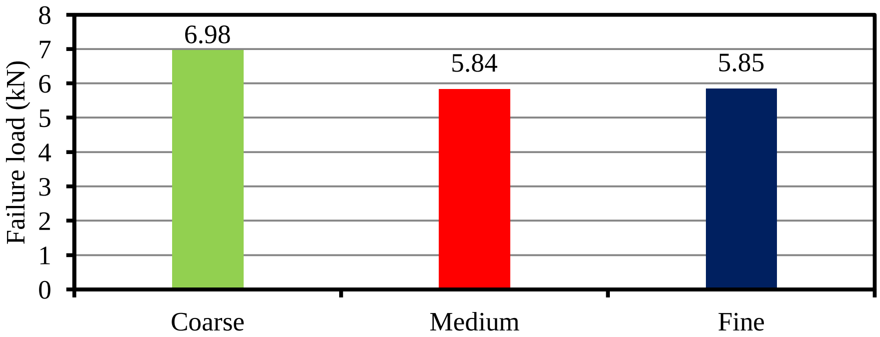

(b) Failure loads.

Figure 6.13 GB3-400 mm GFRP sandwich beam.

6.5 GFRP sandwich beam simulation

6.5.1 Single sandwich beam

The experimental investigation on the behaviour of a single GFRP sandwich beam was made under four point bending with different span lengths. The static load test was conducted to find the effect of the a/d on the failure behaviour of the beams. Span length were varied from 60 mm up to 400 mm as explained in Chapter 3. Two different failure zones were found in this experiment. These were, shear failure and top skin failure as shown previously in Chapter 3. The present section summarise two experiments, one sample in each zone. The experiments are GB3-100 mm and GB3-300 mm for core shear and top skin failure respectively.

The 3D FEA model of a single sandwich beam is shown in Figure 6.14, and a quarter of the beam is simulated due to the symmetry. Figure 6.14(a) shows the 3D

FE model of the GFRP sandwich beam, and Figure 6.14(b) presents the modelling of the GFRP skin plies. The C3D20R brick element was used in the simulation of the GFRP skins and element type C3D8R was used to simulate the core parts. The GFRP skin is divided into 6-plies with different orientations and thicknesses. The plies are distributed within the skin thickness based on the individual ply thickness. The plies mechanical properties were mentioned in Table 6.1. UMAT user subroutine was used for the GFRP skin modelling. An interaction model was used to connect between skin, core, load and support parts. The Lagrange multiplier model was used to simulate the interaction between the beam skins and the loading and support steel parts. A traction-separation model was used to simulate the interaction between skin and core parts. The default Abaqus automatic loading increment was used in the model to apply the load.

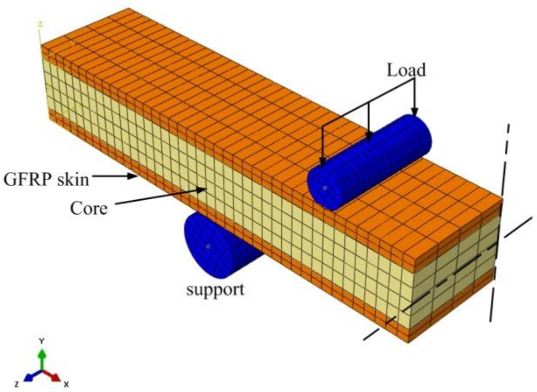

(a) Single sandwich beam.

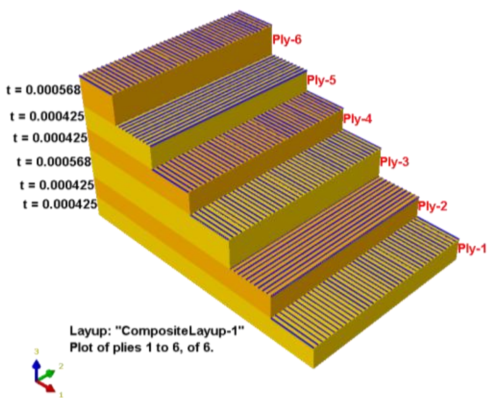

(b) GFRP skin plies model.

Figure 6.14 3D FEA model of four point bending sandwich beam.

The load-displacement curves of the FEA results are shown in Figure 6.15. The experimental curve at Figure 6.15(a) had a small fixture error at initial loading stage and this was corrected. For the two tests, it can be seen that there is good agreement between the FEA results and the experimental results. The load-strain curves for the comparison are shown in Figure 6.16. It shows that the bottom strain is linear with the applied load. The comparison between the cross section stresses for the beams is shown in Figure 6.17. This figure explains that the GFRP skin stresses in the short span beam (GB3-100 mm) are less than the stresses in the longer span beam (GB3-300 mm). In addition, the 100 mm beam GFRP skin stress is less than its strength.

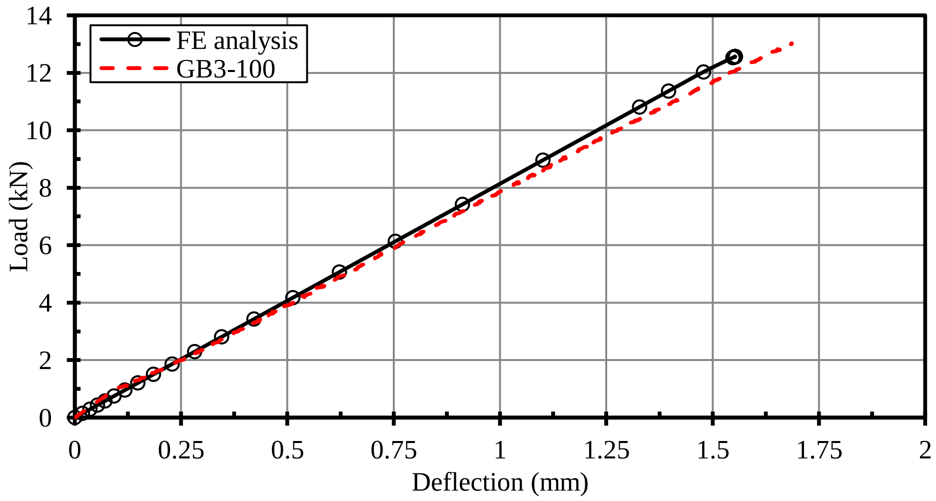

(a) Span = 100 mm

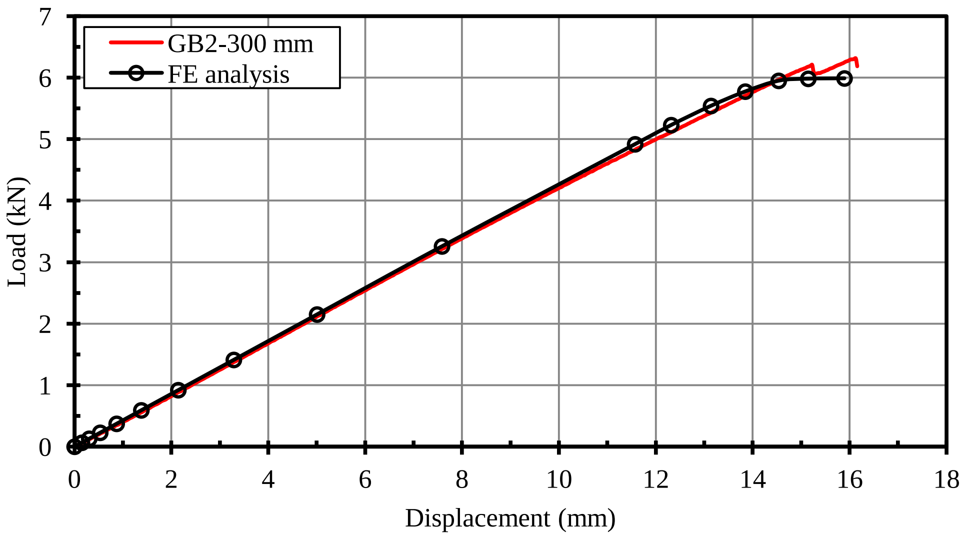

(b) Span = 300 mm

Figure 6.15 Load-displacement for single sandwich beam.

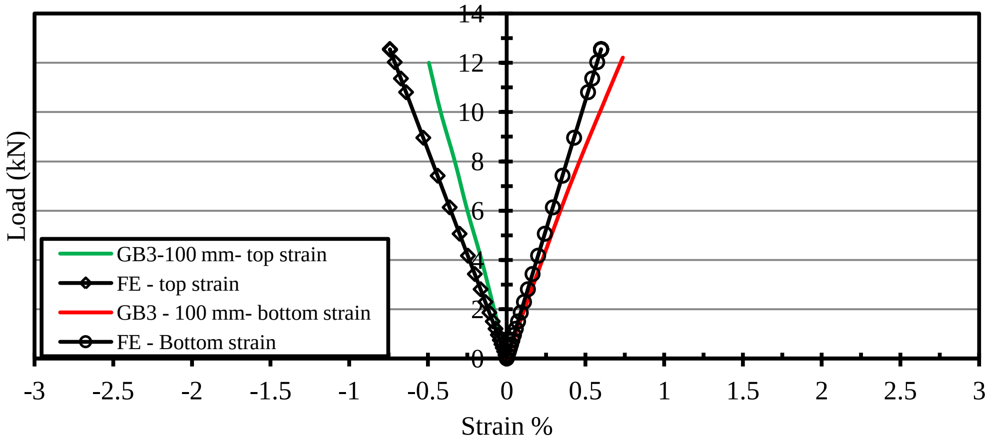

(a) Span = 100 mm.

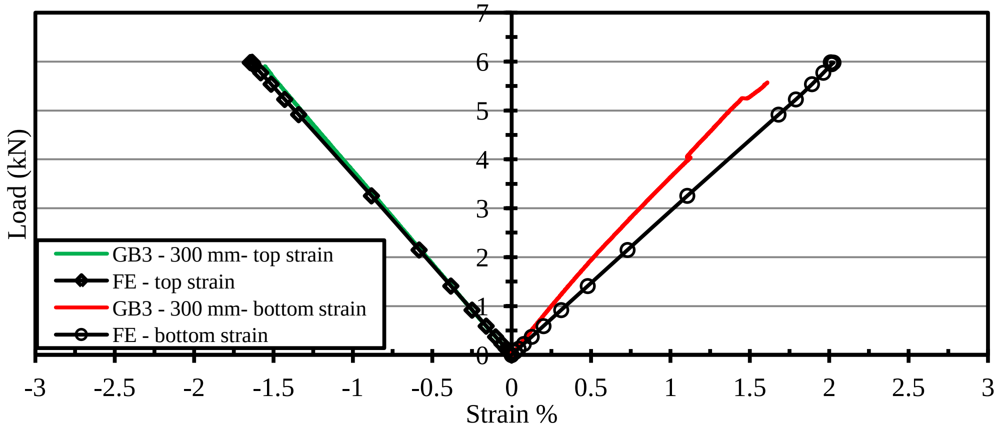

(b) Span = 300 mm.

Figure 6.16 Load-strain for single sandwich beam.

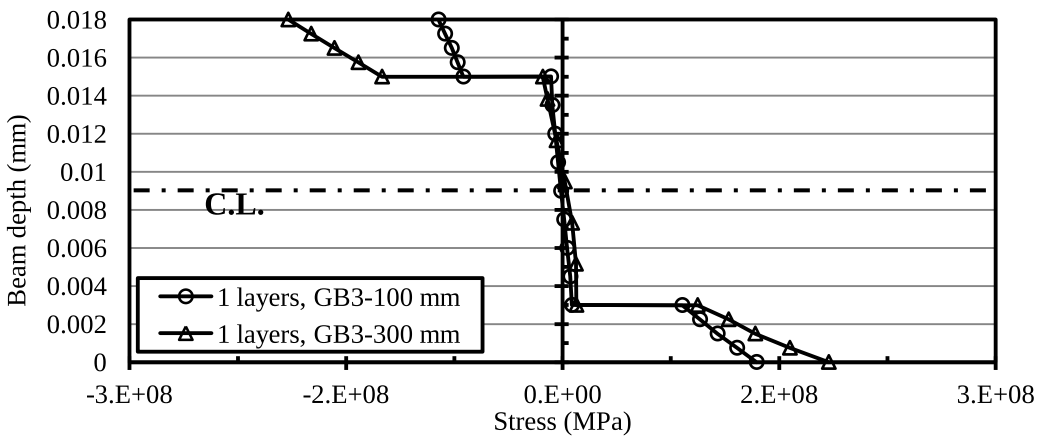

Figure 6.17 Stresses distribution in the mid span gross section.

The comparison of failure modes is shown in Figure 6.18. Core shear failure can be simulated using this model as shown in Figure 6.18(a). The FEA programme stopped after the core cracks due to the excessive failure by shear forces, and the structure is not able to carry more loads. The core cracked in the position of the maximum shear stress as shown in Figure 6.18(a). The core shear stresses reach the failure shear stress of the shear coupons tested previously. However, the core compression strain shows that the value of the strain is less than 0.5 % as shown in Figure 6.18 (a). In addition, based on the CRUSHABLE FOAM model in Figure 6.6 (b), the core part in the compression zone is located in the elastic zone behaviour. Figures 6.18(b) shows that the failure happens in the top skin at the span between loading points. Debonding happened in the experimental tests for long beams as shown in Figure 6.18(b). The FEA model shows that the top skin reaches its strength before the skin-core interaction achieves its debonding strength. Therefore, it is concluded that the debonding in the experimental tests happened after the failure of the top skin in compression.

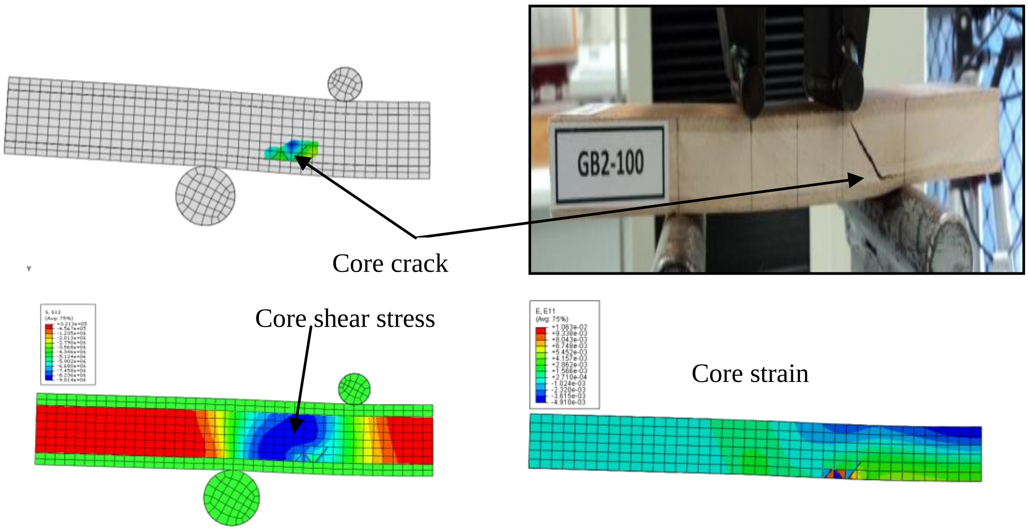

(a) Failure of sandwich beam span = 100 mm.

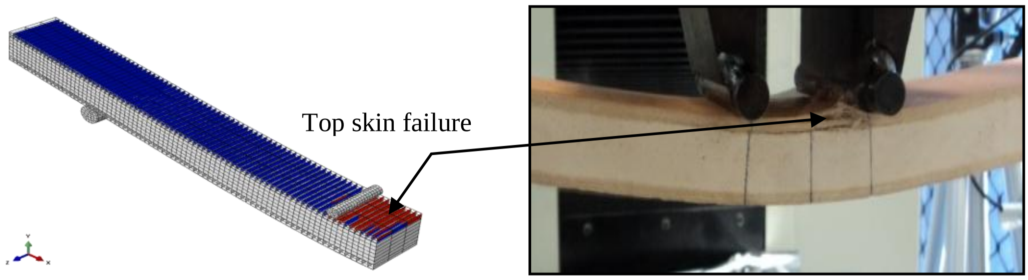

(b) Failure of sandwich beam span = 300 mm.

Figure 6.18 Comparison of single sandwich failure prediction.

The FEA simulation results of different span length single sandwich beams show that the current FEA model can predict different failure modes of single GFRP sandwich beam. The present FEA model shows an ability to find the failure of the skin and the core. The full details of the analysis results for single GFRP sandwich beams are shown in Table 6.3. All single sandwich beams were simulated using the same 3D FEA model. However, only two cases of the beam failure are presented in this section for the justification of the simulation. The error of the FE ultimate failure load prediction is presented in Table 6.3 as well.

The conclusion in Chapter 3 was that the a/d ratio affects the behaviour and failure mode of GFRP sandwich beams. Therefore, using the 3D FEA model is more applicable to deal with different a/d ratios. The FEA results for different measurements were justified in this section, and these aspects are, ultimate load, stress-strain behaviour, load-displacement behaviour, and failure mode predictions.

Table 6.3 Experimental and FEA prediction results of GFRP sandwich beams

Name	Number of layers	Span mm	Depth mm	Experimental failure		FE results		
				Load kN	Deflection mm	Load kN	Deflection mm	Load error %
GB3-60	1	60	18	16.34	0.73	17.56	0.78	7.5
GB3-100		100		12.79	1.75	12.91	1.70	0.9
GB3-200		200		9.54	8.67	10.00	8.49	4.8
GB3-300		300		6.31	16.20	6.54	16.10	3.6
GB3-400		400		5.60	31.24	5.60	32.01	0.0
GB4-100	2	100	36	29.06	2.96	29.67	2.67	2.1
GB4-200		200		18.66	5.28	18.87	5.15	1.1
GB4-300		300		12.23	8.51	12.72	8.27	4.0
GB4-400		400		10.50	14.25	10.86	14.32	3.4
GB4-500		500		8.45	21.59	8.44	21.06	-0.1
GB4-600		600		6.80	28.59	6.17	27.86	-9.3
GB6-100	3	100	54	39.99	3.38	44.24	3.44	10.6
GB6-125		125		30.15	2.89	32.78	3.44	8.7
GB6-200		200		25.58	3.23	27.14	3.34	6.1
GB6-250		250		20.28	5.17	21.66	3.56	6.8
GB6-350		350		19.32	7.11	19.92	6.92	3.1
GB5-100	4	100	72	71.62	7.47	72.15	7.24	0.7
GB5-200		200		54.30	6.01	53.54	5.96	-1.4
GB5-300		300		43.90	7.46	42.56	6.83	-3.1
GB5-400		400		33.79	9.46	33.51	8.75	-0.8
GB5-500		500		25.99	13.59	25.98	11.54	0.0
GB5-600		600		20.11	15.17	19.89	14.19	-1.1
GB7-500	5	500	90	42.47	15.69	43.16	13.81	1.6
GB7-600		600		39.27	20.31	38.67	19.81	-1.5
GB7-700		700		31.06	24.19	32.48	23.88	4.6

6.5.2 Glue laminated sandwich beam

In Chapter 3, several tests were done on the behaviour of GFRP glue laminated sandwich beams. The glue laminated GFRP sandwich beams showed different failure modes depending on the number of sandwich layers and the shear span to depth ratio (a/d).The failure mode of the glue laminated beam mainly depends on the a/d ratio. These modes are, core crushing, core shear and GFRP skin compression failure. Three different cases have been selected to be used for the presentation of the non-linear FEA simulations. These samples are, GB5-100 mm, Gb4-100 mm and GB5-500 mm, for core crushing, core shear and skin failure respectively. The 3D FEA model was conducted to simulate the glued GFRP sandwich beams using the same model in the previous section. Full interaction between the sandwich layers is assumed using tie model, and the interaction between the core and the skin is considered using the traction separation model. The Lagrange multiplier interaction is used between the skin and the loading and supporting steel parts. The experimental tests and FEA simulation were made for four points bending with a static load test.

Load-displacement behaviour for different beams is shown in Figure 6.19. The GB5-100 mm beam showed core crushing in the experimental test. The result of the FEA numerical simulation shows the core crushing under loading points and supports as shown in Figure 6.19(a). It can be seen that there is a difference between the loading point displacement and the mid-span displacement. The shorter beam with an a/d ratio equal to 0.41 showed a core crushing type of failure. The core crushed under the loading point and the support, and the FEA stress prediction shows that the core is reaching the plastic stress at the loading point and the support. Therefore, it is clear that the deformation in the mid-span is relatively low. In addition, part of the deformation under the loading point is a local deformation due to the core crushing. The load-displacement of the GB4-200 mm beam is shown in Figure 6.19(b). It can be seen that the FEA model shows a good prediction to the ultimate load with a lower deformation than the real experiment. The failure of the two layers beam was due to the core shear. The load-displacement of the longer beam (GB5-500 mm) is shown in Figure 6.19(c). It shows a small difference between the loading point and mid-span displacements.

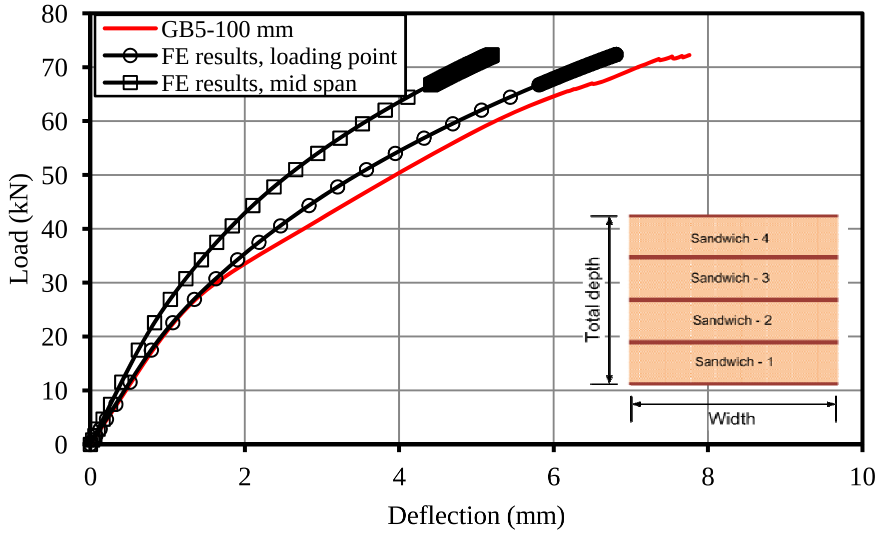

(a) Four sandwich layers, span = 100 mm.

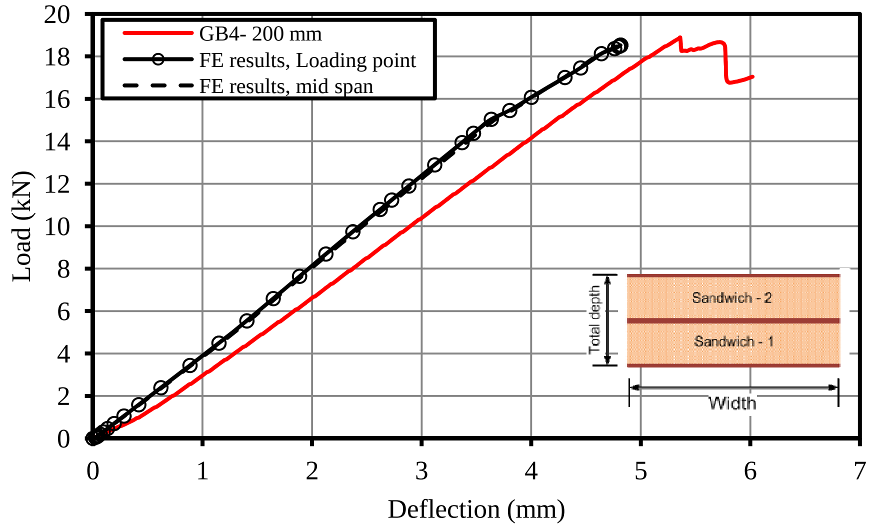

(b) Two sandwich layers, span = 200 mm

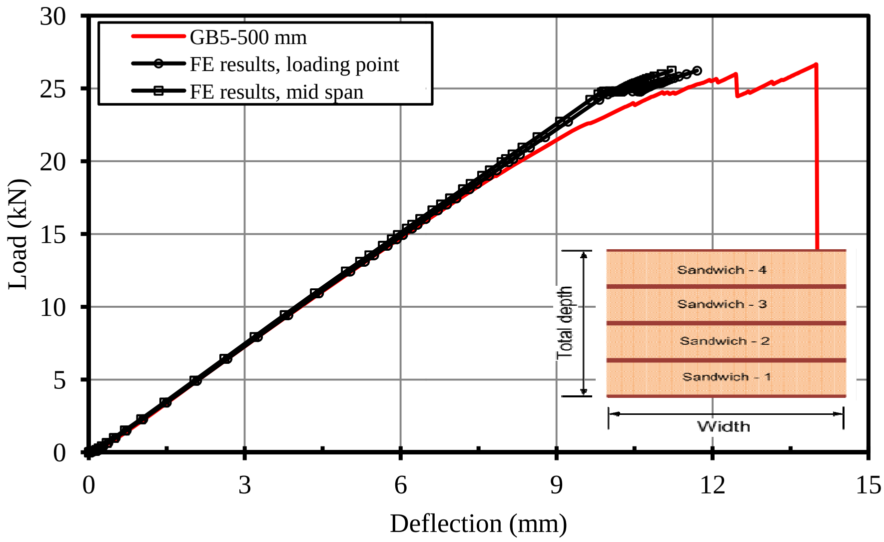

(c) Four sandwich layers, span = 500 mm

Figure 6.19 Load-displacement for glue laminated sandwich beam.

The difference between the mid-span deflection and the loading point deflection of the longer beam is small compare to the shorter beam. This difference in the GB5-500 beam is due to the curvature of the beam and not due to the local deformation of the core under loading point. In addition, the failure load of the GB5-500 mm beam is about 30 % of the GB5-100 mm failure load. Therefore, the load level in the GB5-100 mm is enough to create crushing in the core part.

The stress distribution of the beams cross-section confirms that the vertical stress developed in the short beam (GB5-100 mm) is much higher than the vertical stresses in the longer beam (GB5-500 mm) as shown in Figure 6.20(a-b). The maximum core vertical stresses are 36.4 MPa and 21.0 MPa for the 100-mm and 500 mm GB5 beams respectively. The FEA failure prediction is shown in Figure 6.21. The indentation failure is shown in Figure 6.21(a). The major core crushing failure is located at the positions of the loads and supports. The elements in the top and bottom core parts are crushed in the FEA model. The FEA model shows that shear failure developed at the lower core part and the upper core part near the loading point as shown in Figure 6.21(b). In the case of skin failure, the FEA model shows only the initial failure of the top skin and did not show the latest failure of the core failure as shown in Figure 6.21(c). The load-displacement curve shows an initial drop as shown in Figure 6.19(c). Then, the beam tried to continue carrying the load with more deformation after the first drop. The drop in load-displacement before the failure is due to the top skin compression failure as it is indicated from the experimental tests. The details of the full FEA modelling simulation are shown in Table 6.3.

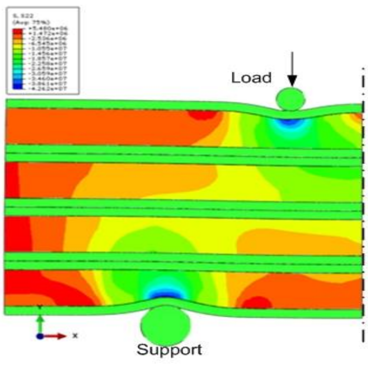

(a) GB5-100 mm span.

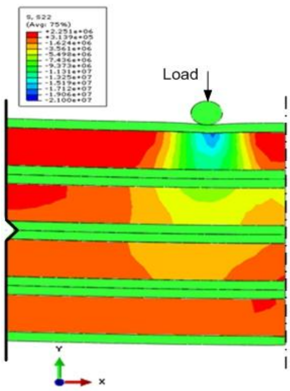

(b) GB5-500 mm span.

Figure 6.20 Vertical stress in the core under loading point and support.

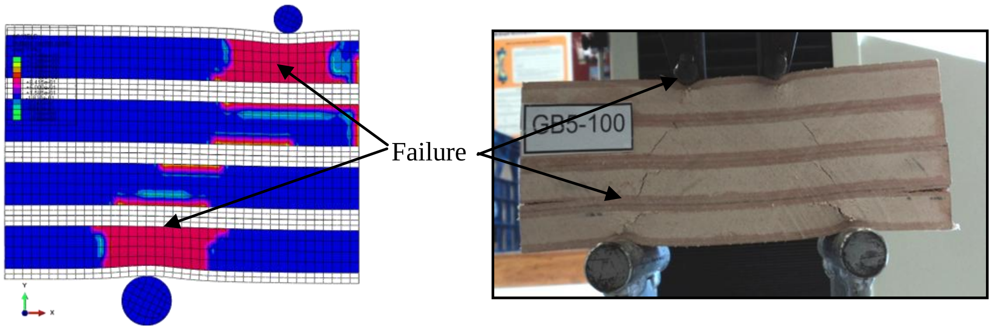

(a) Core crushing failure of four layers glue laminated sandwich beam, span = 100 mm.

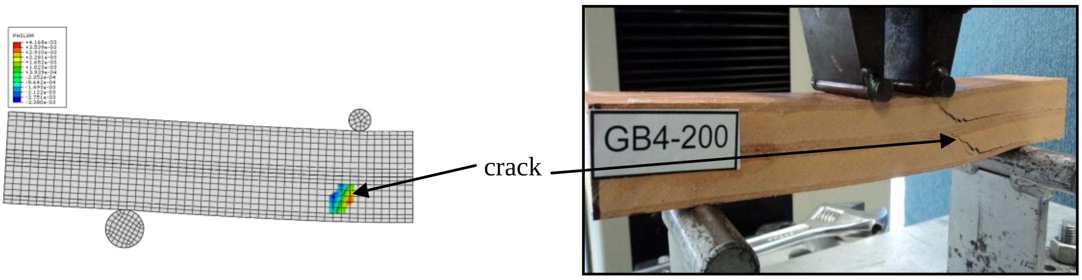

(b) Failure of two layers sandwich beam, span = 200 mm.

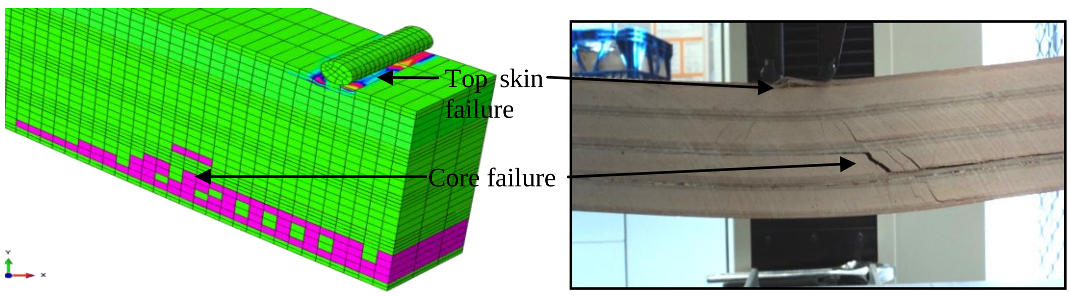

(c) Flexural failure of four layers GFRP sandwich beam, span = 500 mm.

Figure 6.21 Comparison of glue laminated failure prediction.

The present FEA model proves the ability of finding different failure modes in the glue laminated GFRP sandwich beams. The FEA model can simulate the core crushing, core shear, and skin failure. There is a small difference between the FEA model and the experimental behaviour, especially in the post skin failure zone. In the post skin failure behaviour, some of the glue laminated sandwich beams show a different behaviour compared to single sandwich beam. The post skin failure behaviour is very complicated due to the failure of the skin, core failure initiation, and the interaction failure between skin and core. The comparison of the axial stress (σ_{11}) distribution of the single and four layers glue laminated GFRP sandwich beams is shown in Figure 6.22. It can be seen from the figure that the core contribution to the axial stress is small compare to the contribution of the GFRP skins. The stress distribution is different between single and glue laminated GFRP sandwich beams. In the single GFRP sandwich beam, the main contribution to the bending strength comes from the upper and lower parts with a small contribution from the middle part or the core. While, the glue laminated beam has fewer layers through all the beam thickness to contribute to the bending strength. Furthermore, the core contribution in the bending strength of the GFRP sandwich beam is relatively small compared to the GFRP skin layers. In addition, there is a very small contribution by the GFRP skin layers located on the neutral axis of the glue-laminated beam as shown in Figure 6.22(b).

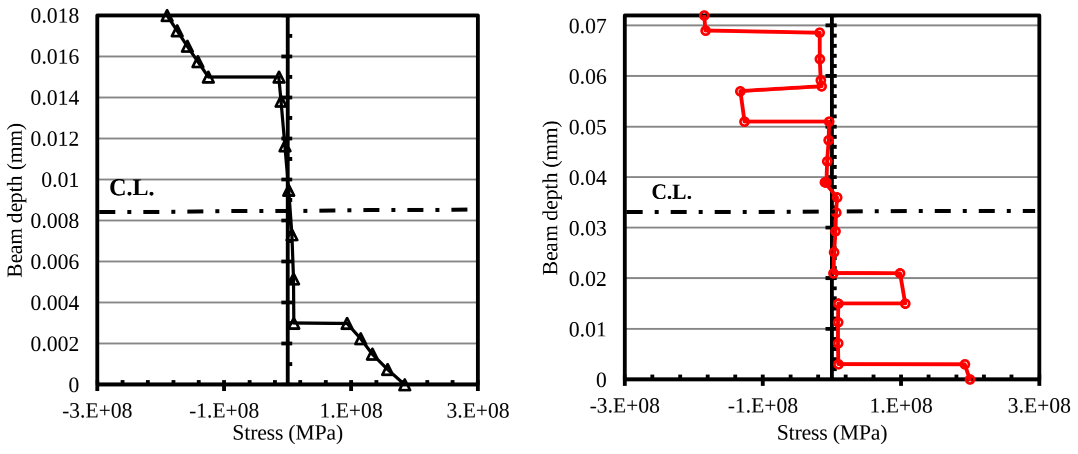

(a) Single layer sandwich, GB3-300 mm. (b) Four layers sandwich, GB5-500mm.

Figure 6.22 Mid span cross section beams axial stress distribution.

6.6 GFRP sandwich slab simulation

6.6.1 One-way slab

One-way GFRP sandwich slabs were tested in Chapter 4. The non-linear FEA model was applied to a single span GFRP sandwich slab under a point load test. Two different slabs were simulated, 15 mm and 18 mm thicknesses. The FEA analysis was utilised to find the non-linear behaviour of the GFRP sandwich slab. The 3D solid brick element type C3D20R was used to simulate the GFRP skin. The skin was divided into plies, and each ply has a property with a longitudinal elastic modulus in the glass direction (E_1) and a transverse elastic modulus (E_2) in the matrix dominant. The orthotropic properties are connected to the Hashin failure model. The 3D solid element type C3D8R was used to simulate the solid core material. The 3D FE model for the one-way GFRP sandwich slab is shown in Figure 6.23. The interaction between the core and the skins is considered in the simulation, and the traction separation model was used. The Lagrange multiplier interaction model was used between the GFRP skin and the steel plate and support parts. In addition, a fastener point-to-point available option in Abaqus was used to simulate the screws (ABAQUS 2008). The comparison of the load deflection curve between numerical and experimental test is shown in Figures 6.24 and 6.25 for the 15 mm and 18 mm slab thicknesses respectively. In addition, a sample of the numerical and experimental comparison of load-strain curves is shown in Figure 6.26 for the 15 mm slab thickness.

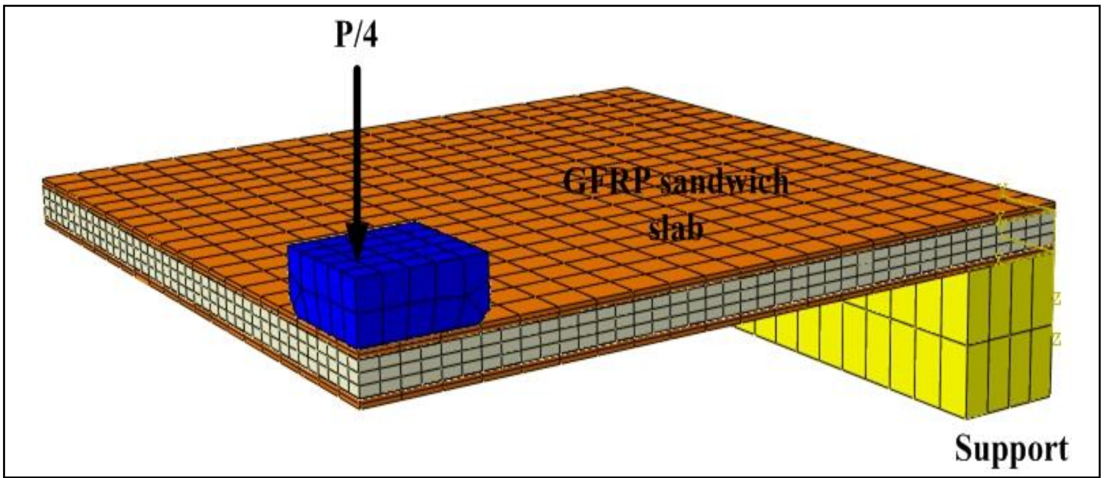

Figure 6.23 3D FEA model for the one-way GFRP sandwich slab.

It can be seen that the stiffness of the slab after the first drop F is approximately the same as before the drop point F. As a consequence, there is no major stiffness degradation of the slab after the point F up to the final failure. The FEA shows good agreement with the experimental test. Both FEA and the experimental load-deflection curves show approximately linear behaviour up to failure. The FEA model shows an initial core cracking happened around a load equal to 15 kN and 28 kN for 15 mm and 18 mm slab thicknesses respectively. After core cracking, there is no reduction in the slope of the load-deflection curve.

The GFRP sandwich slab exhibits a large deformation due to the high failure deflection to a thickness ratio, and this ratio is approximately equal to 3. The core failure is shown in Figure 6.27, and it can be seen that the crack is parallel to the support. The failure of the top skin is shown in Figure 6.28(a), and it shows that the failure index is greater than one. The failure line starts in the middle of the slab and progresses towards the edge of the slab as shown in the experimental picture in Figure 6.29(b). The effect of the screws on the behaviour of the one-way GFRP sandwich slab is limited to the stiffness of the slab as shown in Figure 6.25. In addition, the effect of the screw restraints is not significant on the ultimate failure load. A comparison between the Von-Mises stress distribution in the simple and screw restraint one-way slabs are shown in Figure 6.29. The load and deflection curves of the experimental tests and FE results are shown in Table 6.3 for the one-way slabs.

The current loading applied on the slab is a concentrated load using 100 x 100 mm loading plate in the middle. This generally has caused the failure to be dominant by core cracking. However, depending on the type of loading such as uniformly distributed loads, the slab failure mode may be dominated by skin failure. Such failure modes have been verified for beams using the FEA model in section 6.5. Hence, the same approach can be applied to the simulation of different types of slab loadings.

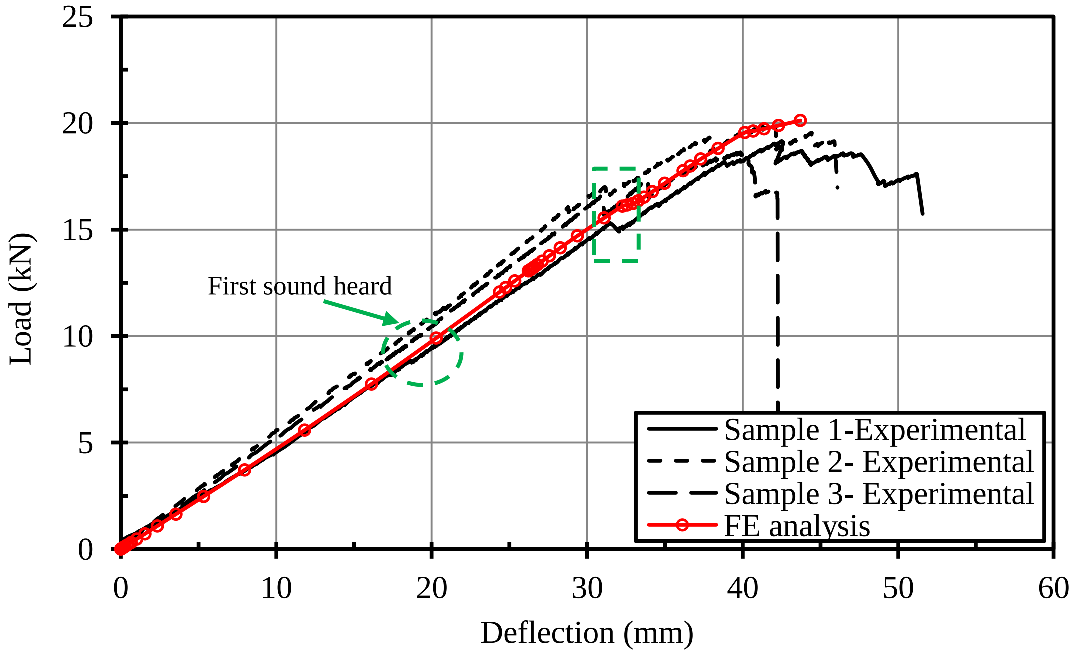

Figure 6.24 Load-deflection curve of single span 15 mm slab.

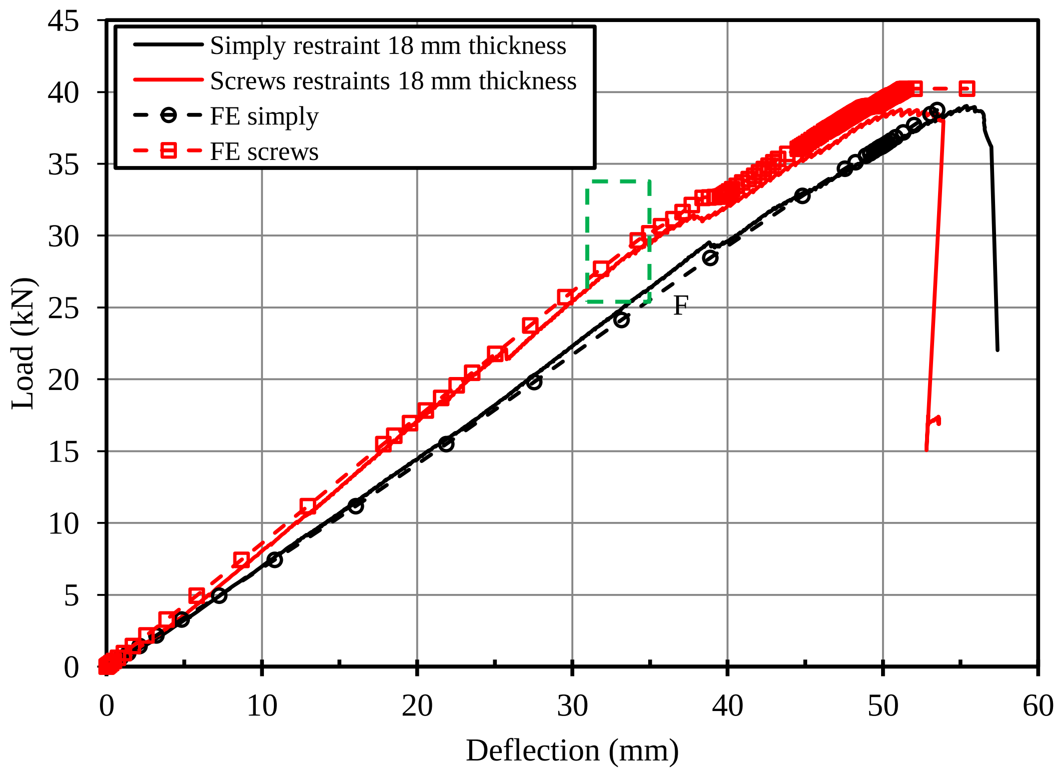

Figure 6.25 Load-deflection curve of single span 18 mm slab.

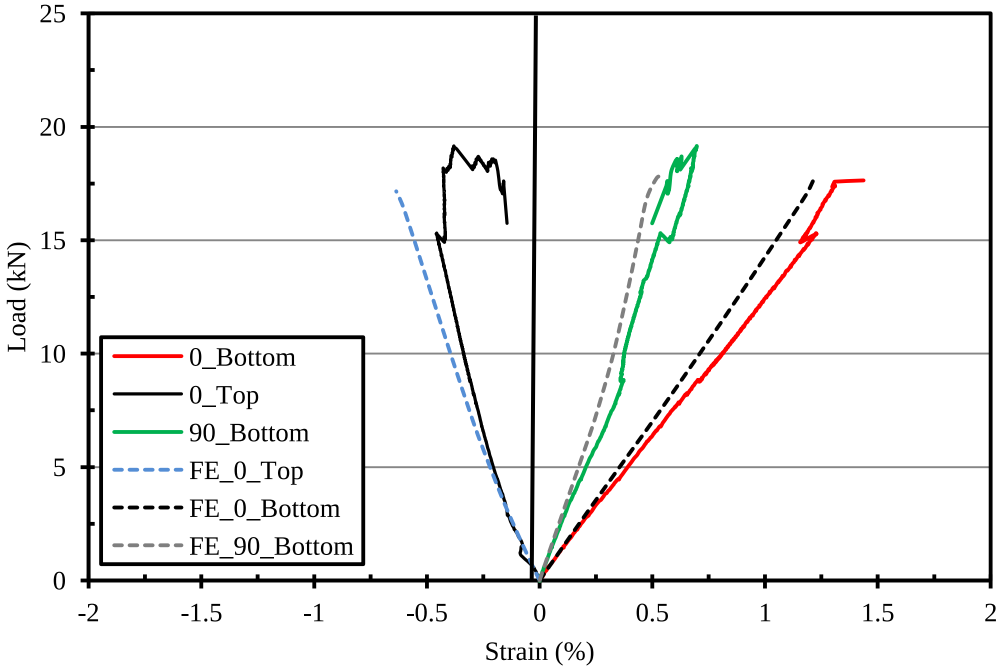

Figure 6.26 Finite element and experimental load-strain results for the 15 mm slab thickness.

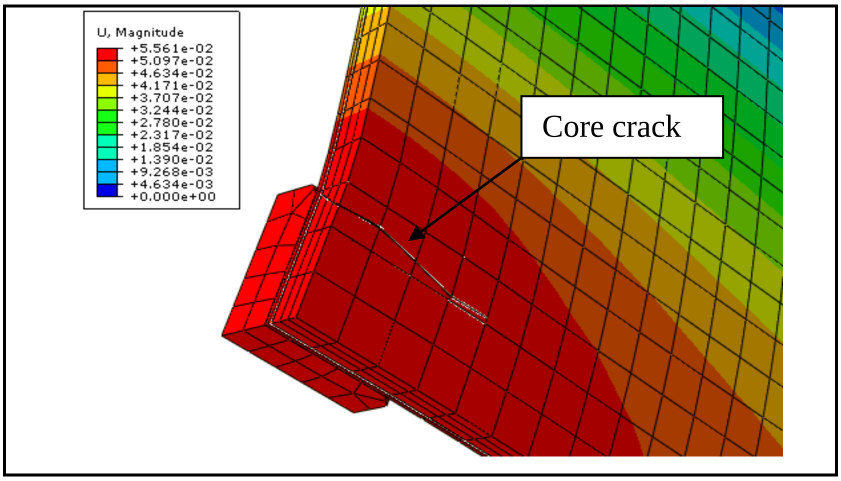

Figure 6.27 Core crack under point load.

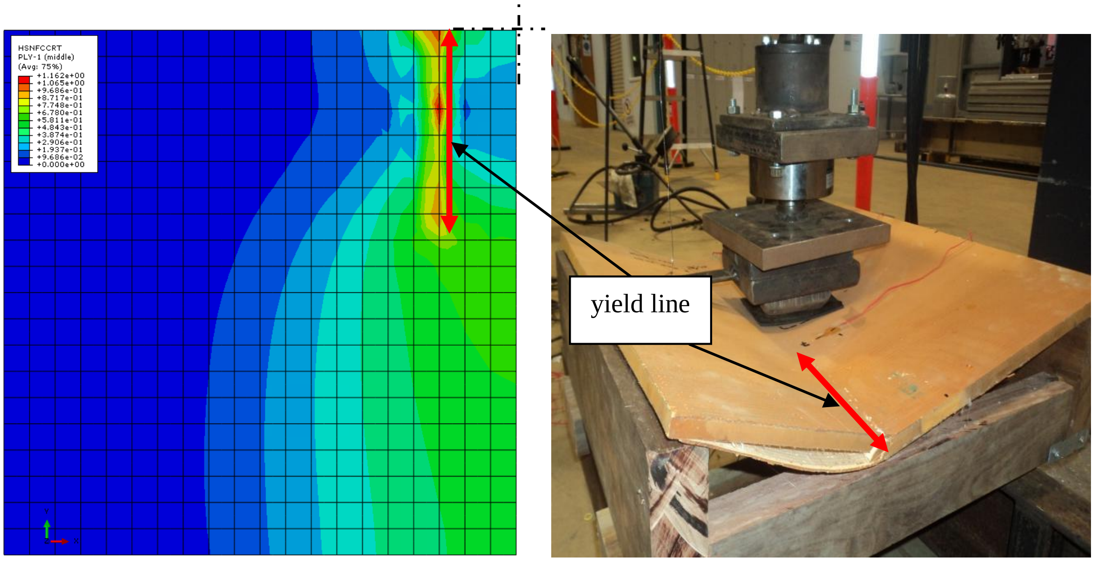

(a) FE top skin failure index (b) Top skin experimental failure

Figure 6.28 Top skin failure.

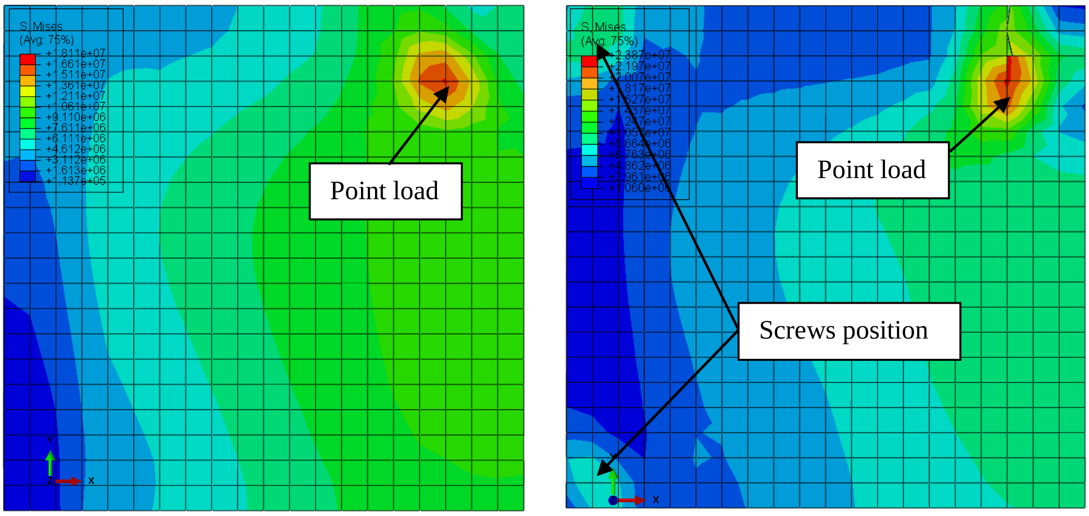

(a) Simple restraint (b) Screws restraint

Figure 6.29 Von-Mises stress distribution.

6.6.2 Two-way GFRP sandwich slab

The FEA model was used to simulate the static flexural behaviour of the two-way GFRP sandwich slab under point load. The 3D FEA model was created for the two-way slab with four edges support. A quarter of the slab was selected for the simulation due to the symmetry as shown in Figure 6.30. The materials properties, interaction properties, and load configuration are similar to the FEA model of the one-way GFRP sandwich slab. The UMAT subroutine was used for the GFRP skin modelling. The CRUSHABLE FOAM model was used for the core part. The traction-separation was used for the skin-core interaction and the Lagrange multiple for interaction between skin and the steel plate and support parts. The only difference is the support configuration. The 3D FEA model is shown in Figure 6.31. The 3D FEA model was applied to the two-way GFRP sandwich slabs to find its behaviour and understanding some of the behaviour differences. The square and rectangular slabs were analysed in simple and screws restraints. In addition, fibre orientation has been considered in the analysis with the GFRP skin plies. The GFRP skin is divided in different plies and each ply has an orientation, thickness, and material properties. The 600 x 600 mm square slab was simulated using the 3D non-linear FEA model. The results of the $0^o/90^o$ and $\pm 45^o$ fibre orientations of slabs restraint with screws are shown in Figures 6.31 and 6.31.

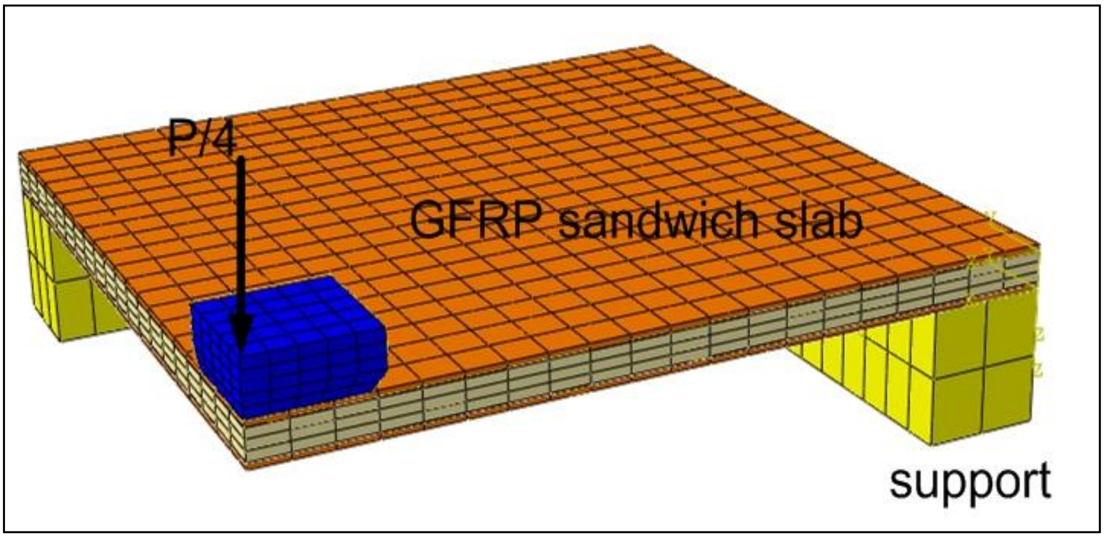

Figure 6.30 3D FEA model of two-way GFRP sandwich slab.

The results of the simple restrained rectangular slabs 600 x 900 mm and 600 x 1200 mm are shown in Figure 6.33. All experimental tests show a small drop in load between 27-30 kN. This drop is probably due to the initiation of the core cracking. The FEA element simulation shows that the core failed under the point load as shown in Figure 6.34, and this failure causes the drop in the load-deflection curves.

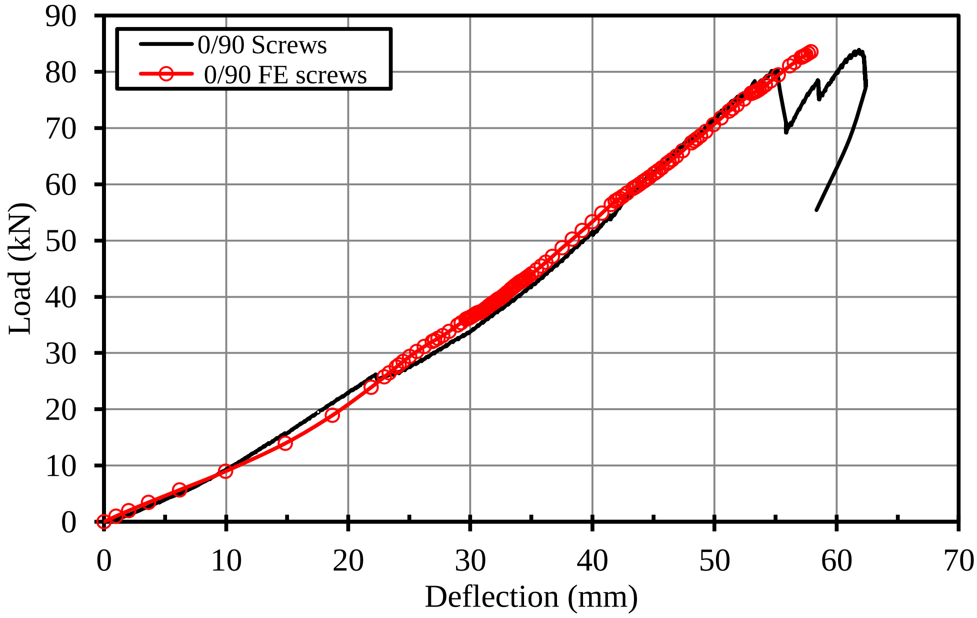

Figure 6.31 Load-deflection curve for 0°/90° two-way slab restrained by screws.

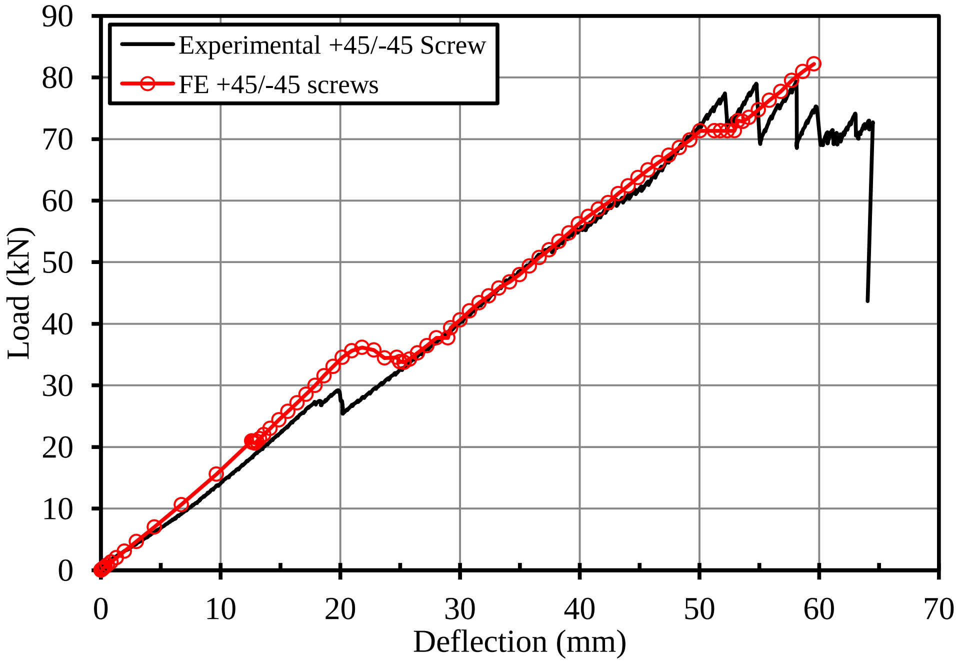

Figure 6.32 Load-deflection curve for ±45° two-way slab restrained by screws.

The 3D FEA model shows over prediction behaviour in some cases when the decrease in the load deflection happens around 30 kN, and it shows an acceptable prediction behaviour in other cases as shown in Figures 6.31-6.33. However, the FEA model predicts the final failure load with an accepted margin of accuracy. The effect of fibre orientation on the Von-Mises stress distribution through the slab is shown in Figure 6.35. It can be seen that the edges of the 0°/90° slab have small stresses compared to the diagonal stresses. In contrast, the edges of ±45^o have a high stress compare to the diagonal stress. The effect of the slab width to length aspect ratio on the Von-Mises stress distribution is shown in Figure 6.36. It can be seen that the high stress distribution follows the diagonal line of the slab in the case of the square slab. This stress distribution explains the failure pattern of the rectangular slabs as shown previously in Chapter 4. It becomes very clear that the stress distribution affects the core failure. The core fails by cracking at a distance of 300 mm from both corners of the slabs as shown in Figure 4.33(a) (Chapter 4). The stress distribution in the 600 x 1200 mm slab shows that the stresses near the short edge supports become very small compare to the stresses with mid-span of the slab. This indicates that the short edge has a very small influence on the slab with the width to length ratio (L_y/L_x) equal or greater than 2. The yield pattern is shown in Figure 6.37 for the two-way square GFRP sandwich slabs with an orientation ±45^o. It can be seen that the diagonal element suffered from the yield, and it represents the failed elements through the 3D FEA model. Full details of the experimental tests and FEA simulation results are shown in Table 6.3 for all two-way GFRP sandwich slabs.

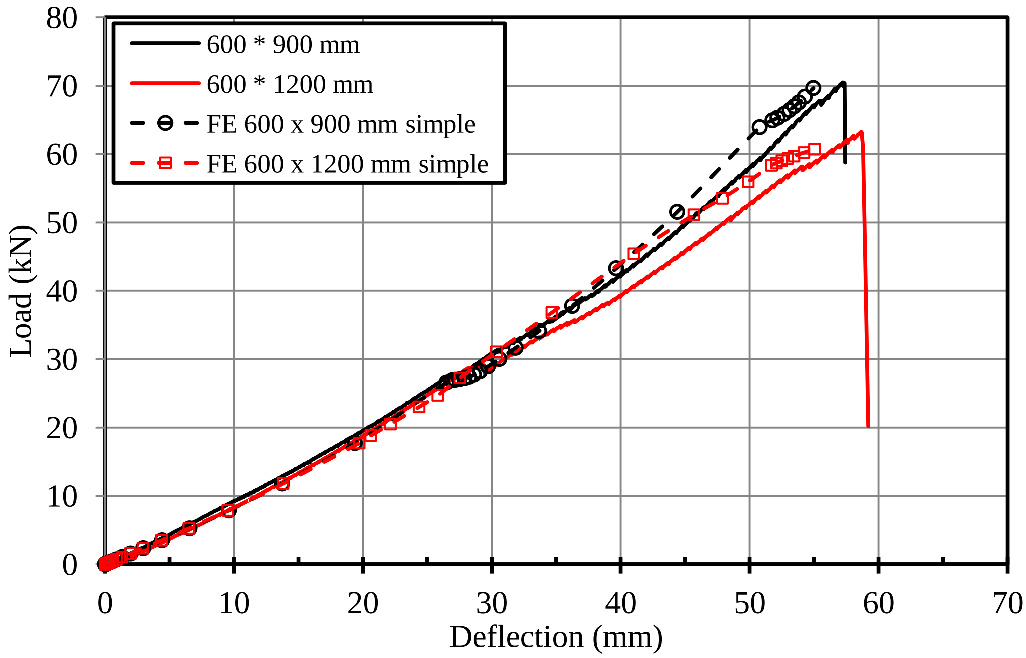

Figure 6.33 Load-deflection curves for rectangular two-way slab with simple restraint.

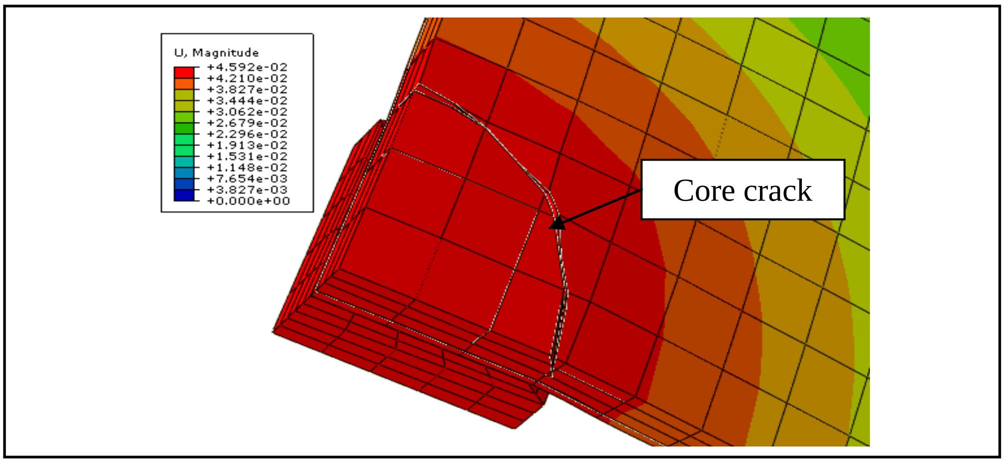

Figure 6.34 Core crack under point load.

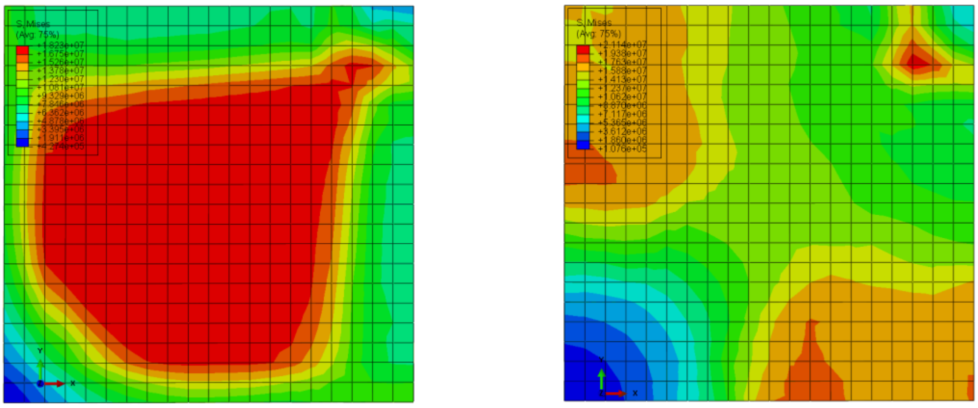

(a) 0°/90° fibre orientation. (b) ±45° fibre orientation.

Figure 6.35 Von-Mises stress distribution of 600 x 600 mm two-way slabs.

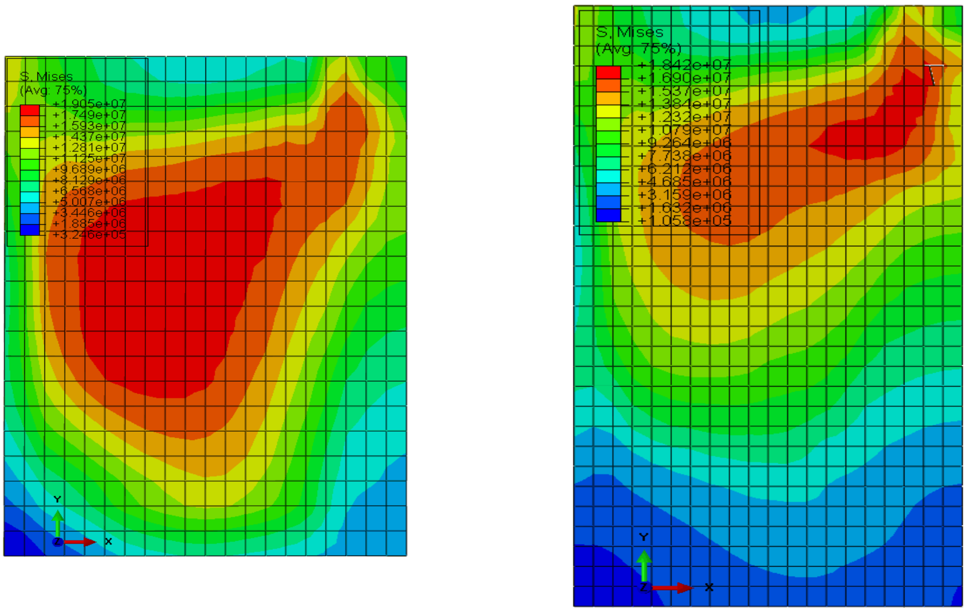

(a) 600 x 900 mm. (b) 600 x 1200 mm.

Figure 6.36 Von-Mises stress distribution in rectangular slab.

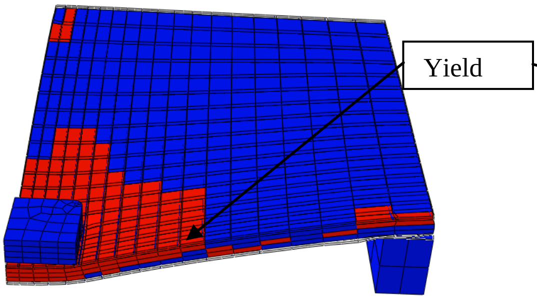

(a) FE 0°/90° screws

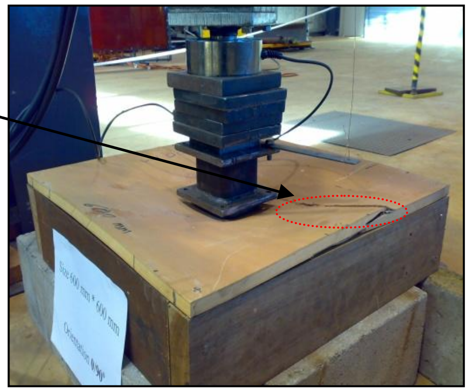

(b) Experimental 0°/90° screws

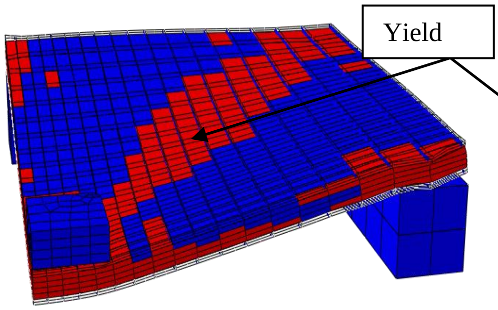

(c) FE ±45° screws

(d) Experimental ±45° screws

Figure 6.37 Yield pattern.

Table 6.4 FEA and experimental results for GFRP sandwich slabs.

Name	Size mm x mm	Support	Restraint type	Experimental failure		FE results		
				Load kN	Deflection mm	Load kN	Deflection mm	Load error %
P1	600 x 600	one-way	Simple	19.60	43.11	20.15	43.70	2.8
P2	600 x 600	one-way	Simple	38.74	54.99	38.47	55.44	-0.7
P3	600 x 600	one-way	Screws	38.32	49.94	40.23	55.41	5.0
P4	600 x 600	two-way	Simple	78.51	53.73	68.43	48.44	-12.8
P5	600 x 600	two-way	Screws	82.95	60.63	83.55	57.89	0.7
P6	600 x 600 (±45°)	two-way	Simple	77.93	57.58	74.63	45.38	-4.2
P7	600 x 600 (±45°)	two-way	Screws	77.81	57.67	80.94	58.68	4.0
P8	600 x 900	two-way	Simple	70.45	57.24	65.87	52.68	-6.5
P9	600 x 900	two-way	Screws	69.29	57.19	70.32	57.9	1.5
P10	600 x 1200	two-way	Simple	63.24	58.65	69.66	54.95	10.2
P11	600 x 1200	two-way	Screws	64.86	60.01	61.95	59.44	-4.5

6.7 Free vibration simulation of slabs

Since the same FEA model will be used for the optimum design of GFRP composite structural element, this model should be verified with the experimental dynamic behaviour. The dynamic verification considers different structural applications. The verification was done for the slabs free vibration behaviour for one-way and two-way slabs. The verification with the GFRP composite sandwich beam behaviour is discussed in Appendix-B.

A 3D FEA model was conducted to find the free vibration behaviour of the GFRP sandwich slabs. A 3D solid element type C3D20R was used to simulate the GFRP skin with plies. The solid modified phenolic core material was simulated by using a 3D element C3D8R. Timber support was simulated by using the 3D element as well. The interaction between the solid core and skins is assumed to be full with no separation allowed and the tie interaction was used in this interaction. While, the interaction between the slab and the timber support is not full, and the Lagrange multiplies model was used in the simulation (ABAQUS 2008). Separation was allowed between the GFRP sandwich slab, and the timber supports in the cases of simple restraint and screws restraint. A fastener point-to-point option in Abaqus was used to simulate the screws. A tie model interaction was used in the glue boundary restraint simulation.

The FEA analysis was done on all the experimental tests. The FEA analysis includes all the variables of boundary conditions, restraint conditions, fibre orientations and spans. A comparison of the results between the experimental and the FE analysis is shown in Figure 6.38 for support type S1 (one-way) and in Figure 6.39 for support type S2 (two-way). The FEA showed a good prediction of the GFRP sandwich slabs first natural frequency. Full FEA results are provided in Table 6.5. The second and third frequencies are included as well for comparisons. The FEA analysis provides the mode shape for natural frequency. The mode shape provides a good indication about the deformation of the existed GFRP sandwich slabs. The results of $0^o/90^o$ fibre orientation of the first mode shapes are shown in Table 6.6 S1and S2 supports.

The mode shapes of S3 and S4 supports are shown in Table 6.7. The results show that the first mode shape in the continuous span simple restraint boundary condition is same as the mode shape of single span with simple restraint in Table 6.6. Providing a mid-span support does not provide any restraint in the first mode as shown in Table 6.7. However, the mid-span support affects the first mode of the continuous slabs with the restraints S2 and S3 as shown in Table 6.7.

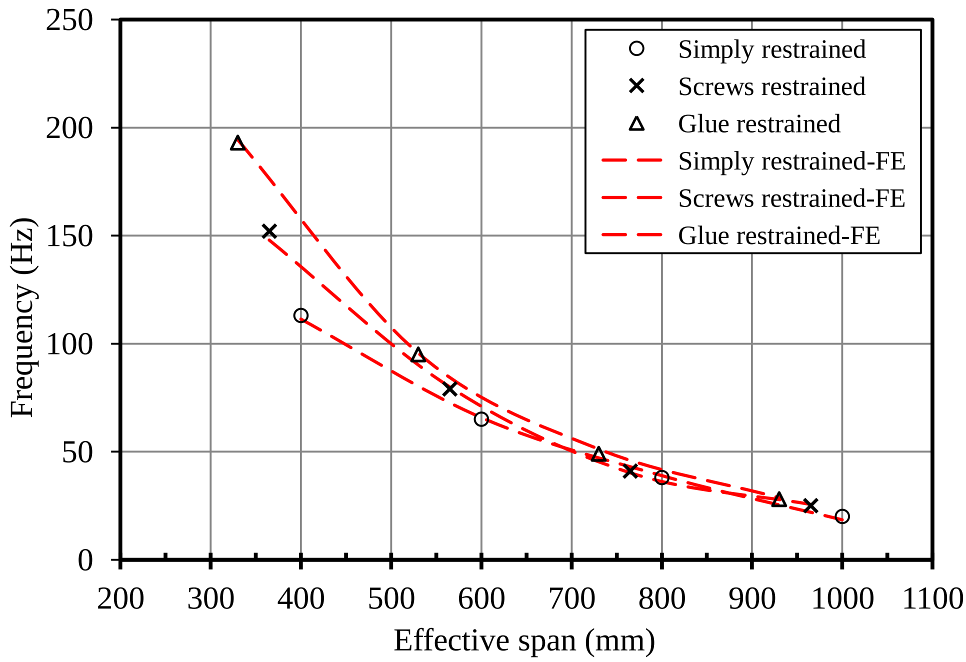

Figure 6.38 Experimental and numerical first natural frequency of S1 support.

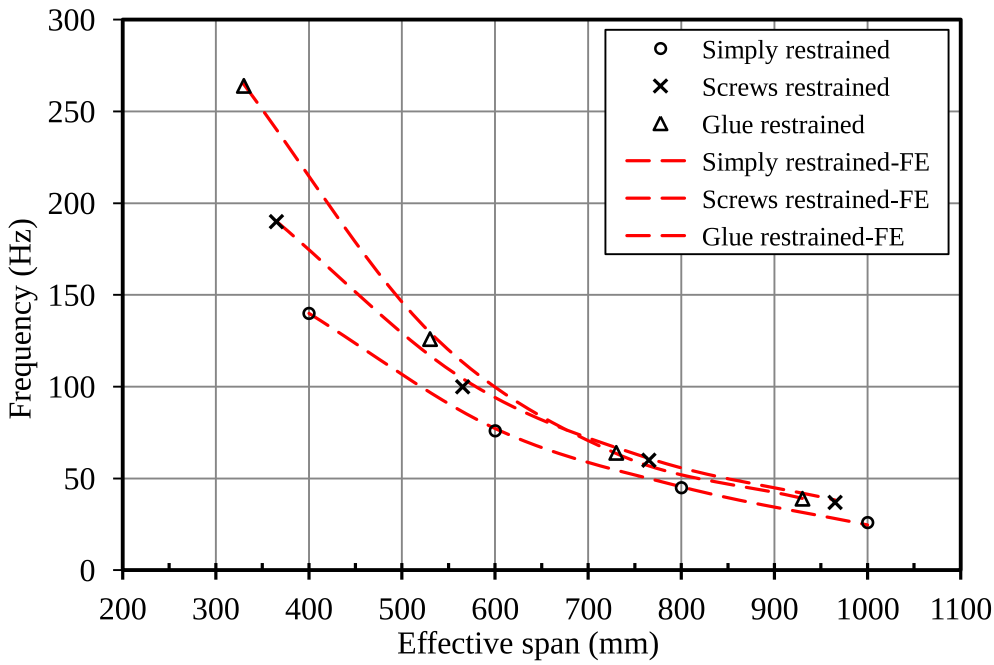

Figure 6.39 Experimental and numerical first natural frequency of S2 support.

Table 6.5 FEA free vibration simulation results.

Name	Support type	Restraint type	Skin fibre orientation	Slab size mm x mm	Experimental Hz			FEA Hz		
					f1	*f2*	*f3*	*f1*	*f2*	*f3*
T1	One-way (S1)	Simple (R1)	$0^o/90^o$	400 x 400	113	127	232	111	130	255
T2			$0^o/90^o$	600 x 600	65	82	146	65	83	166
T3			$0^o/90^o$	800 x 800	38	54	99	39	49	97
T4			$0^o/90^o$	1000 x 1000	20	32	57	18	27	59
T5			$-45^o/+45^o$	600 x 600	44	74	132	44	74	141
T6	Two-way (S2)	Simple (R1)	$0^o/90^o$	400 x 400	140	164	260	140	171	273
T7			$0^o/90^o$	600 x 600	76	104	140	77	144	146
T8			$0^o/90^o$	800 x 800	45	59	82	45	88	93
T9			$0^o/90^o$	1000 x 1000	26	40	53	25	45	53
T10			$-45^o/+45^o$	600 x 600	87	122	156	88	120	154
TS1	One-way (S1)	Screw (R2)	$0^o/90^o$	400 x 400	152	200	270	148	203	272
TS2			$0^o/90^o$	600 x 600	79	111	166	80	88	177
TS3			$0^o/90^o$	800 x 800	41	57	95	40	51	98
TS4			$0^o/90^o$	1000 x 1000	25	38	72	26	33	62
TS5			$-45^o/+45^o$	600 x 600	65	111	150	65	103	201
TS6	Two-way (S2)	Screw (R2)	$0^o/90^o$	400 x 400	190	308	384	190	319	394
TS7			$0^o/90^o$	600 x 600	100	174	220	104	204	217
TS8			$0^o/90^o$	800 x 800	60	116	136	61	133	144
TS9			$0^o/90^o$	1000 x 1000	37	84	98	38	89	94
TS10			$-45^o/+45^o$	600 x 600	118	176	262	116	172	267
TG1	One-way (S1)	Glue (R3)	$0^o/90^o$	400 x 400	193	230	380	194	226	377
TG2			$0^o/90^o$	600 x 600	95	123	210	96	114	198
TG3			$0^o/90^o$	800 x 800	49	70	124	51	64	109
TG4			$0^o/90^o$	1000 x 1000	28	41	75	29	37	66
TG5			$-45^o/+45^o$	600 x 600	77	119	170	77	110	202
TG6	Two-way (S2)	Glue (R3)	$0^o/90^o$	400 x 400	264	392	414	265	561	593
TG7			$0^o/90^o$	600 x 600	126	286	314	129	275	292
TG8			$0^o/90^o$	800 x 800	64	138	154	63	142	153
TG9			$0^o/90^o$	1000 x 1000	39	86	93	39	90	96
TG10			$-45^o/+45^o$	600 x 600	136	295	390	138	299	387
TC1	One-way continuous (S3)	Simple (R1)	$0^o/90^o$	800 x 800	38	54	103	38	48	95
TC2			$0^o/90^o$	1000 x 1000	20	32	66	20	27	59
TCS1	One-way continuous (S3)	Screw (R2)	$0^o/90^o$	800 x 800	106	123	129	121	123	127
TCS2			$0^o/90^o$	1000 x 1000	87	97	111	87	96	109
TCG1	One-way continuous (S3)	Glue (R3)	$0^o/90^o$	800 x 800	128	140	181	133	143	176
TCG2			$0^o/90^o$	1000 x 1000	109	117	144	112	118	141
TTC1	Two-way continuous (S4)	Simple (R1)	$0^o/90^o$	800 x 800	45	59	84	46	58	88
TTC2			$0^o/90^o$	1000 x 1000	26	42	54	26	47	53
TTCS1	Two-way continuous (S4)	Screw (R2)	$0^o/90^o$	800 x 800	116	124	128	116	123	127
TTCS2			$0^o/90^o$	1000 x 1000	94	120	140	96	119	143
TTCG1	Two-way continuous (S4)	Glue (R3)	$0^o/90^o$	800 x 800	152	185	207	156	197	216
TTCG2			$0^o/90^o$	1000 x 1000	96	126	138	97	124	137

Table 6.6 First mode shape of single span slabs of $0^o/90^o$ fibre orientations

Support Type	Restrained Type		
	Simple	Screws	Glue
S1	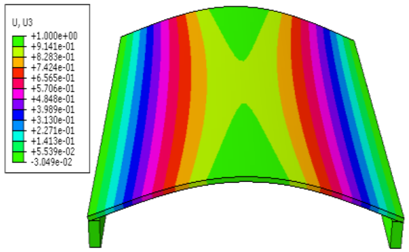		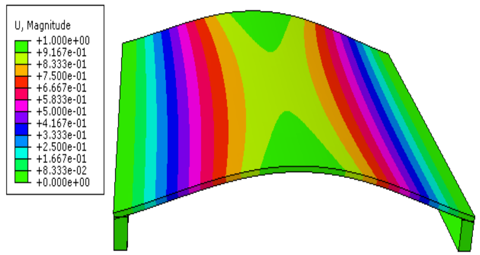
S2	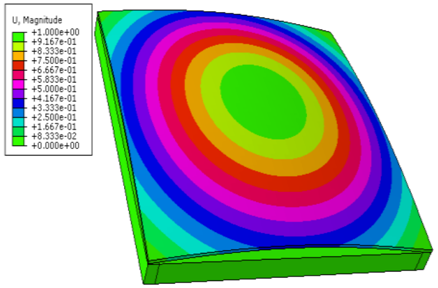	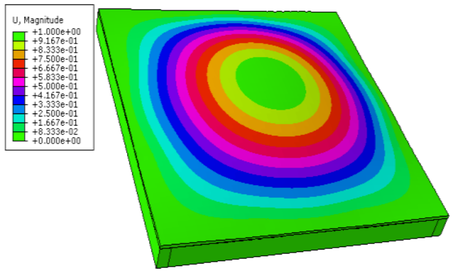	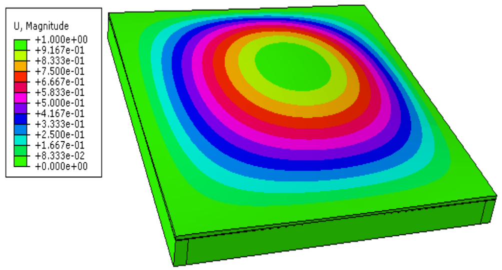

Table 6.7 First mode shape of continuous span slabs of $0^o/90^o$ fibre orientations

Support Type	Restrained Type		
	Simple	Screws	Glue
S3	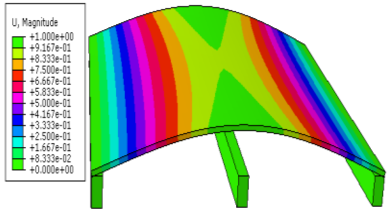	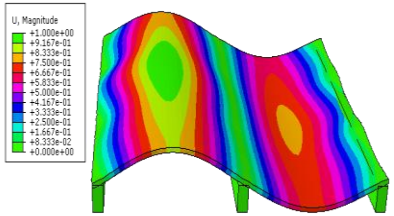	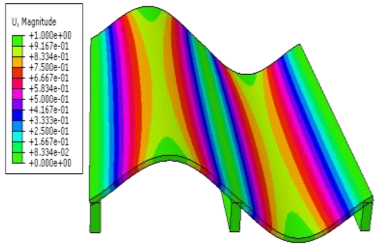
S4	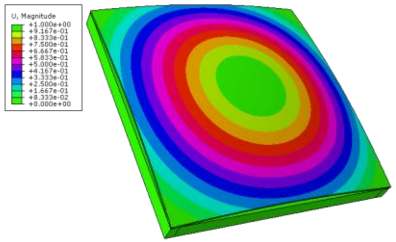	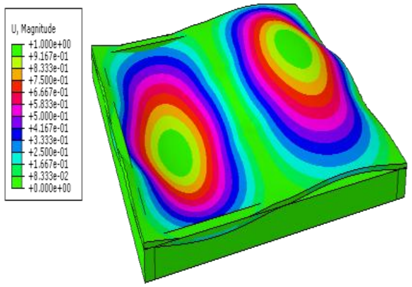	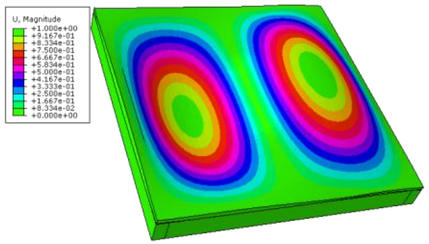

6.8 Chapter conclusions

The present chapter considers the development of a 3D FEA model and the behaviour of different materials in the GFRP sandwich slab. Verification of the FEA model with static and free vibration experimental behaviour is presented. The selection of the material models has been made according to the available existing studies on the simulation of GFRP sandwich structures.

The Hashin model showed an acceptable behaviour in the simulation of the GFRP skin material, and CRUSHABLE FOAM model showed a good prediction for modified phenolic core material behaviour. The experimental test of skin-core interaction also verified with the traction-separation numerical modelling. Mesh sensitivity analysis showed that the medium mesh size is enough to get and accurate simulation with the present FEA model. Static load behaviour has been verified with different cases for simply supported GFRP sandwich beams and slabs. The simulation included different failure modes and different geometric properties. The FEA model showed an ability to simulate core crushing, core shear and top skin failure modes with a good accuracy compare to the experimental tests. In general, the core material did not reach the plastic hardening zone in the cases when the failure is due to the core shear and top skin compression. FEA model did not show degradation in the skin-core interaction before the final failure.

The FEA simulation at failure level showed a small variation compared to the experimental values. This variation becomes clear in the final stage of failure. However, prediction of the ultimate failure load is more acceptable, and it is more important than the post failure behaviour. The non-linear FEA model can predict the strain in both tension and compression zones. The FEA showed that the drop point in slab load-deflection curve is due to the full cracking of the core part. The FEA model presents an acceptable behaviour in the free vibration simulation of the GFRP sandwich slabs. In addition, providing a mode shape helps in understanding the frequency results. Simple restraint single span and simple restraint continuous span showed same first natural frequency.

This chapter shows that the static behaviour model can be used in the free vibration simulation with an acceptable accuracy. Applying the same model gives good results in the calculation of natural frequency, especially in the first mode. The

FEA model can simulate the natural frequency of the GFRP sandwich slab with a good accuracy. The FEA model simulates different restraints and their effects on the GFRP sandwich structures. The present FEA model is used in the design of GFRP sandwich structures in the next chapter. The following chapters focus on the optimum design of GFRP sandwich structures using FE modelling and optimisation methods. The present 3D FEA model is linked to the optimisation method through the modeFRONTIER software.

Chapter 7

Optimum design of GFRP sandwich slabs and beams

7.1 Introduction

Economic and light-weight structure design is an important goal for the designer. Several studies were carried out to design FRP plates and slabs under single and multi-objective optimisation (Muc & Muc-Wierzgoń 2012; Walker & Smith 2003). Multi-objective optimisation has become the target of recent design studies, because it can optimise two or more objectives at the same time (Almeida & Awruch 2009; Alrefaei & Diabat 2009; Ashby 2000; Omkar et al. 2009). Park et al. (2009) optimised a FRP composite one-way plate made from carbon and glass fibre. GA was used to find the optimum design for the plate using single and multi-objective optimisation. An orientation of $0^o/90^o$ was used for the plies study to find the effect of the number of plies on the cost and weight design objectives. Sebaey et al. (2011) studied the stacking sequence of laminated FRP composite panels under biaxial tension and compression forces. The study indicated that the load ratio has a large influence on the stacking sequence as well as the force types in tension or compression.

Single and multi-objective optimisation techniques have been applied to the design of the fibre composite sandwich beams by a number of researchers (Ashby 2000; Farkas & Jarmari 1998; Swanson & Kim 2002). Theulen and Peijs (1991) for example, presented an optimisation of strength objective and stiffness objective of a sandwich beam. Their research concluded that the maximum bending stiffness occurred at a core to skin mass ratio of 2. Walker and Smith (2003) presented a multi-objective design optimisation of fibre composite structure coupling using FEA and genetic algorithms (GA). They found that the mass and deflection as a multi-objective could be optimised by the GA to suit the design engineer's requirements.

GFRP sandwich panels are used in fabrication of structural beams. The single GFRP sandwich beam can be designed to carry the external service load. However, the fabrication of a single sandwich beam with a big cross section depends on factory capacity and it may be impossible beyond a certain beam depth. Therefore, the glue-laminated beam made from using smaller GFRP sandwich sections is used to satisfy the design requirements. The design of the glue-laminated GFRP sandwich beam represents another aspect in the design of GFRP sandwich structures.

Free vibration is an issue of increasing importance in the design of FRP composite structures. Increasing spans and more effective use of construction materials result in lightweight structures with a high live load to dead load ratio. Consequently, many structures have become more sensitive to vibration when subjected to dynamic loads. Walking and jumping represent the internal dynamic loads sources on the slabs in buildings. In addition, there are external source of vibration such as the traffic outside the building (Hechler et al. 2008).

The novel GFRP sandwich panels have been fabricated for use in the civil structural building applications (Van-Erp 2010). The experimental investigations of the beam and slab elements were presented in Chapters 3, 4 and 5. This chapter discusses the optimum design of the novel GFRP sandwich slab and beam as structural members. The design is considered a multi-objective optimisation problem because the need to reduce cost and mass of the structure. The design constraints are deflection, frequency, and stress constraints.

7.2 Design criteria

FRP sandwich slabs and beams have been used as main structural members in civil engineering applications. A high strength to weight ratio encourages engineers to use sandwich structure to get a light-weight structure and to enhance the capability of the structures to carry more live loads. However, standard specifications and codes for FRP composite use in civil engineering are not available yet except for the British standard code for the design of FRP composite BS4994 (Bank 2006) and the

EUROCOMP design code (Clarke 1996). Optimisation of FRP slab and beam represents a good objective for the researchers to find the slab configuration of core thickness, plies thickness, and orientation angles. Generally, every structural part has to withstand the external work loading and keep its structural deflection within allowable serviceability limits. Under this simple guideline, there are few limitations such as service load, deflection limits, safety factor, and free vibration recommendations.

7.2.1 Service load

Estimating the expected service load is very important in the design of slabs and beams. Australian/New Zealand Standards AS/NZS 1170.1:2002 (2002) specifies the service load applied to floors by different values of distributed and concentrated loads. This service load is expected to apply on the floors in the domestic and industrial building as normal life activities. The current design methodology will consider this load as an applied external load. Domestic activities have a 3 kN/m^2 distributed load and 4.5 kN point load. Industrial activities have a 5 kN/m^2 distributed load and 4.5 kN point load. In addition, the dead load is also considered including the slab self-weight, finishing (0.42 kN/m^2), and partitioning (0.96 kN/m^2) (AS/NZS 2002).

7.2.2 Deflection

Deflection of the FRP slabs and beams is also an important issue in this design. EUROCOMP specifies allowable deflection limits in the applications of FRP in structural flooring systems by span/150 for walkways, span/250 for floors supporting brittle finishing, and span/400 for the floor supporting columns (Clarke 1996). These limits were recommended in order to avoid the effects of floor deformation on other connected constructions such as partitions, cladding and tiles finishing. The allowable deflection for beams is considered as span/400.

7.2.3 Safety factor

The safety factor of FRP composite designs is very important for the civil engineering designers, especially for long term behaviour. Most designers depend on experiments to evaluate the design safety factor for existing structures. Usually the safety factor is considered for the load in the ultimate limit state and considered for the materials in the serviceability limit state (Clarke 1996). The materials safety factor recommended for the short term loading is 2 and for long term loading is 4 (Gay et al. 2003). The long term safety factor is higher than the short term factor to avoid expected creep.

Quinn and Associates (1999) divided the safety factor of any composite structures to several parts, manufacturing method (f1 = 1.5), environment (f2 = 1.5), temperature (f3 = 1.1), cyclic load (f4 = 1.1), and curing procedure (f5 = 1.2). EUROCOMP (Clarke 1996) divided the FRP material partial safety factor into three parts; material strength calculation methods (k1 = 1.0 - 2.25), production processes (k2 = 1.1 - 2.7) and long term effects (k3 = 1.0 - 3.0). The overall safety factor represents the combination of all three factors. In addition, the overall safety factor should be greater than 1.5 and less than 10. Furthermore, EUROCOMP specifies the load partial factors in the ultimate limit state design as 1.35 and 1.5 for dead and live loads respectively. Hollaway and Heads (2001) use loading factors for the ultimate limit state as 1.15 and 1.5 for dead and live loads respectively. Karbhari (2000) presented a study on safety factor calculation for FRP civil engineering infrastructures. Karbhari divided the safety factor into five parts as, material property derivation (0.5-0.97), processing method (0.6-1.0), curing type (0.8-1.0), manufacturing (0.8-1.0) and ageing (0.3-0.8).

The preceding literature shows that partial safety factor of materials can have different values to calculate. Calculating the materials safety factor based on the EROCOMP procedure requires the information about how the material strength was calculated, the manufacturing process, operating temperature and loading duration. These factors for the novel GFRP sandwich slab are selected from the EUROCOMP design tables. The prosperities of this panel were found by testing and theory, which gives k1 value of 2.25. This panel is produced by automated machine and this gives k2 value of 1.1, and finally, k3 is equal to 2.5 for operating design temperature 25-50 ^{o}C and for long term loading.

7.2.4 Free vibration

Dynamic vibration in a domestic structural slab comes from the human body motion. A single body motion is classified into heel impact and jumping-off impact. Vibration induced by people affects serviceability, fatigue life of structure, and safety factor (Bachmann 1995). ISO 10137:2007 (2007) specified vibration sources into two types of sources, inside the building and outside the building. The vibration inside the building is produced by people activities, and machines. The vibration outside the building is produced by traffic and construction activities. The ISO standard mentions that the frequency range of these activities is between 1 to 80 Hz. These values are based on the worst case combination of activities vibration in the x-axis, y-axis and z-axis (ISO:10137 2007).

Free vibration caused by human activities lies between 6 to 12 Hz (Ebrahimpour & Sack 2005). Naeim (1991) found that the minimum recommended wood floor structure frequency is 12 Hz for dancing activates. Dolan et al. (1999) studied the wood floor panel under two conditions, unoccupied structure (no furniture or live loads) and occupied structure in the normal loading. Their investigation showed the minimum structure frequency should be 14 Hz and 15 Hz for occupied and unoccupied structures respectively. Hunaidi (2000) studied the effect of traffic on building vibration using trucks and buses as a source of vibration travelling in different speeds. They concluded that mid-floor vibration ranged between 20.3 to 62.9 Hz and 35 to 92.2 Hz for first and second storey floors respectively.

7.3 Genetic Algorithm optimisation method

Many methods have been used to find the optimum design of fibre composite structures in different applications as discussed in Chapter 2. Most of the optimisation methods are service with continuous design variables. Civil engineering structural design involves selection of design variables that satisfy requirements of the practical codes. In general, these variables are discrete for most practical civil engineering problems. All optimisation techniques try to find the global optimum design and avoid local optimum solution. However, the design process could be summarized in three steps: i) conceptual ii) preliminary design and iii) detailed design (Hassani & Hinton 1999). Optimisation methods are classified by depending on the concept of optimisation as follows: simultaneous mode of failure, criterion of optimality, and mathematical programming (Bhavikatti 2003). Optimisation methods help design engineers to make decisions in the design and manufacturing process. Simply, the optimisation problem for x_i variables could be described as:

$$\text{Objective function} = \begin{cases} Minimization\ f(x)_{min.} \\ Maximization\ f(x)_{max.} \end{cases} \quad 7.1$$

$$\text{Constraints} = \begin{cases} Stress\ constraints\ g(x)_{stress} \\ Deflection\ constraints\ (x)_{defl.} \\ etc. \end{cases} \quad 7.2$$

Genetic algorithm (GA) is an efficient method in the optimisation which is based on a stochastic approach and relies on a survival of the fittest in the natural process. In the last few decades, GA has been widely used for structural design optimisation due to its capability to deal with complicated and large variable problems. GA was successfully applied to the design of reinforced concrete structures (Atabay 2009; Perera & Vique 2009; Perera et al. 2009), steel structure (Cheng 2010; Prendes Gero et al. 2006), topology structure optimisation (Aguilar Madeira et al. 2005; Rahami et al. 2008) and fibre composite structures (Almeida & Awruch 2009; Falzon & Faggiani 2012; Kalantari et al. 2010).

The principle of GA depends on the concept of natural selection and natural genetics. The basic idea of the GA is to generate a group of design variables randomly within the allowable values of each variable. A basic flow chart is shown in Figure 7.1. The set of design variables represents the population of the variables for certain iteration in the calculation. The fitter design variables should be selected from the population. Then, the random process is used to produce a new generation of variables. The size of the problem for each generation remains constant. The successful generation has a higher probability with a better fitness value. The benefit of using GA is that the solution does not require the function to be continues or differentiable. The bit-string crossover is an operator for reproduction. Where, the new generation is produced by using two strings as parents and by swapping the two strings, as described in Figure 7.2. Mutation is an important procedure to get diversity of design variables as genes. In fixed-length strings, mutation can be achieved by randomly changing the value of the genes (Weise 2008). The mutation between string chromosomes may occur by either single or multi-gene mutation as shown in Figure 7.3.

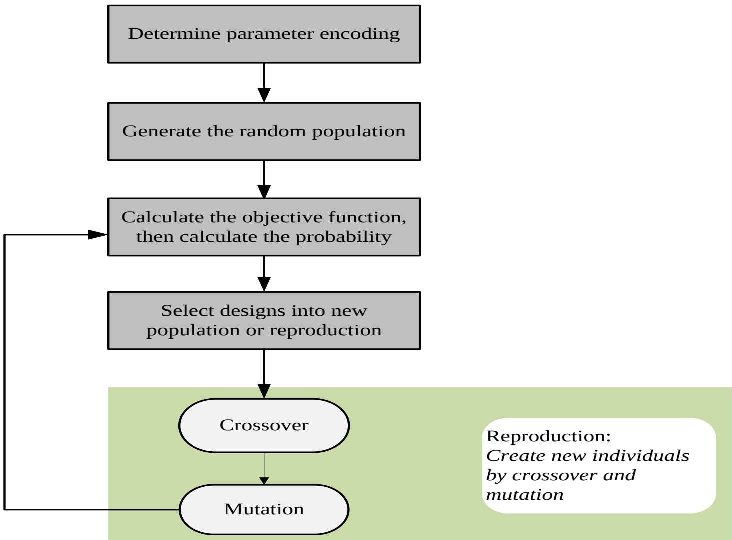

Figure 7.1 GA flow chart.

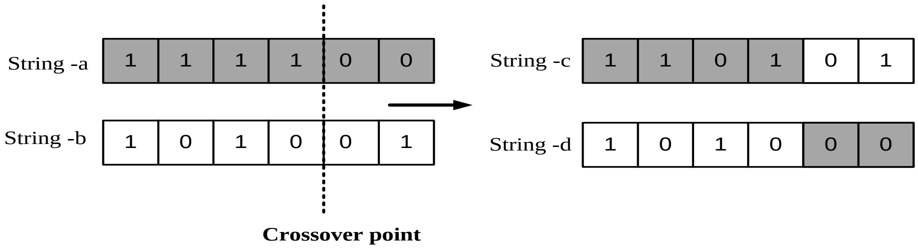

Figure 7.2 The bit-string crossover of parents a, and b to form off-strings c and d.

(a) Single-gene mutation (b) Multi-gene mutation

Figure 7.3 Mutation of string chromosomes.

The fundamental theorem of the genetic algorithm (GA) was developed by Holland as below (Burns 2002):

$$m(H,\bar{t}+1) \geq m(H,\bar{t}) * \frac{\bar{f}(H)}{\bar{f}_{avg}}\left[1 - p_c \frac{\delta(H)}{\bar{L}-1} O(H) p_m\right] \qquad 7.3$$

where *m* is the Schema number, $\bar{t}$ is the generation number, $\bar{f}(H)$ is the fitness value of Schema *H*, f_{avg} is the average fitness value, *δ(H)* is the length of Schema *H*, $\bar{L}$ is the total length of the string, *O(H)* is the order of Schema, and p_c and p_m are the probabilities of crossover and mutation respectively.

Two features can be noticed in the GA, the first is the stochastic algorithm. This means that the random procedure is essential in both selection and reproduction (Sivanandam & Deepa 2007). The second is the GA always remains all the population of solution in its memory. This allows it to recombine between different solutions to find the best one. Robustness makes the GA a great optimisation tool and is essential for the algorithm success. It gives the method the ability to deal with different type of problems without particular requirements for use of the GA.

7.3.1 Multi-objective genetic algorithm (MOGA)

The need of multi-objective optimisation has been grown since the structural engineers have put a target to get an optimal design for the structure by implementing efficient use of structural materials. In the real life, there are many objectives required for the structure design, and most of these objectives are conflicting with each other. The single objective solution might be the best for one objective and not for the others. In multi-objective optimisation, the design process happens simultaneously and the final results are considered all objectives. Finding acceptable solution of multi-objective problem needs an investigation of group of solutions. These solutions called Pareto optimal solution and there is no improvement on one objective without a significant degradation on the other functions (Sivanandam & Deepa 2007). Pareto optimality defines the frontier that can be satisfied by trade-off between objectives. Pareto frontier represents all the possible solutions for the problems. A decision maker is important for this stage to select the optimal design (Bui & Alam 2008). Mathematically, the *k* multi-objective can be expressed as a vector function $\vec{f}(x)$:

$$\vec{f}(x) = \begin{bmatrix} f_1(x) \\ f_2(x) \\ \dots \\ \dots \\ f_{\bar{k}}(x) \end{bmatrix} \quad 7.4$$

In general form:

$$min\, f_{i=1,\dots,\bar{k}}(x)|_{x\in\bar{W}} \quad 7.5$$

where $\bar{k}$ is the total number of objective functions. x is the design variable and $\bar{W}$ is the feasible solution. Figure 7.4 presents an optimisation for maximising two objective functions f_1 and f_2. The dark gray area represents the Pareto frontier for both functions and the ranges are *(X_2-X_3)* and *(X_5-X_6)*.

$$Optimal\ design\ X^* \in (X_2 \rightarrow X_3), (X_5 \rightarrow X_6) \quad 7.6$$

This range contains infinite design points. Starting from X_1 there is an increase in the value of both objectives. At X_2, the function f_2 represents the global maximum in the domain but f_2 is not the maximum. The dark gray *(X_2-X_3)* there is a decrease in the value of f_2, and an increase of f_1. This means the points at the interval *(X_2-X_3)* cannot dominate the points at the interval *(X_3-X_4)*. In the interval *(X_5-X_6)* both functions increase and at X_6 the objective f_1 represent the global maximum in the domain. In addition, the points in the interval *(X_5-X_6)* are dominated the points in the white left and right interval. Finally, the optimum design could be one of the interval points *(X_5-X_6)*.

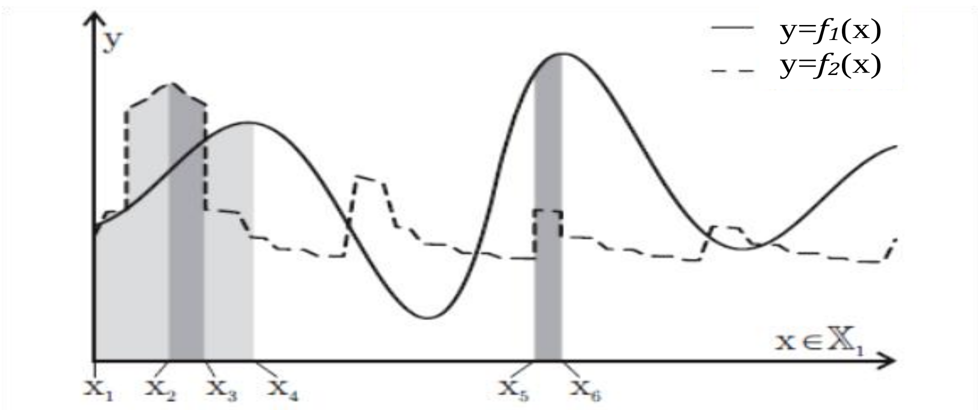

Figure 7.4 Pareto optimisation.

The idea behind Multi Criteria Decision Making (MCDM) is to help the designer select an optimum global design among a set of design variables in the Pareto frontier (Tanaka et al. 1995). In addition, the decision making helps to satisfy the multi-objective optimisation goal by identify the optimum solution among the Pareto solution set. Therefore, the decision making required to specify a preference in the selection of the optimum design among Pareto frontier set. In the multi-objective scatter chart, there are many design points in the Pareto frontier as shown in Figure 7.5. The circle shows the MCDM selection as an optimum design point (Branke et al. 2008).

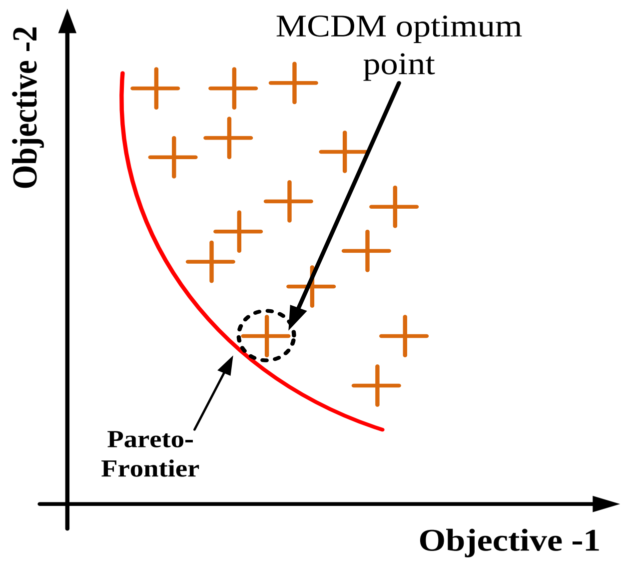

Figure 7.5 Multi criteria decision making (Avila et al. 2006).

7.3.2 Adaptive range multi-objective genetic algorithm

Multi-objective optimisation requires estimation of a large number of the objective functions. The idea of the adaptive range multi-objective genetic algorithm (ARMOGA) is to reduce the number of functions called by enhancing the search region. The ARMOGA depends on the statistics of the former data in the direction of the search (Sasaki & Obayashi 2005). The principle of ARMOGA depends on multi-objective evolutionary algorithms (MOEAs), and it consists of archiving, fitness sharing, range adaptation, and constrain-handling techniques. The difference between ARMOGA and MOEAs is shown in Figure 7.6. In this figure, the difference between the search regions shows that the ARMOGA search region is quicker than the

MOEAs search region. The ARMOGA method depends on the range adaptation of the former data to reduce the number of evaluations needed to obtain the Pareto solution. Figure 7.7 shows the three regions of the ARMOGA I, II and III in more details. Whereas, the average of the normal distribution is μ_i with the standard deviation σ_i, and the control parameters are α_r andfl_i, the description of the regions are:

Region I ($p_i \leq \mu_i - fl_i, 0 \leq r_i \leq \alpha_r$):

$$r_i = \alpha_r * r_i^{'} \quad 7.7$$

$$r_i^{'} = \int_{-\infty}^{p_{n,i}} N(0,1)(z)dz \quad 7.8$$

$$p_{n,i} = \frac{p_i-(\mu_i-fl_i)}{2\sigma_i} \quad 7.9$$

Region II ($\mu_i - fl_i < p_i < \mu_i * fl_i,\ \alpha_r < r_i < 1 - \alpha_r$):

$$r_i = (1 - 2\alpha_r) * r_i^{'} \quad 7.10$$

$$r_i^{'} = \frac{p_i-(\mu_i-fl_i)}{2fl_i} \quad 7.11$$

Region III ($\mu_i * fl_i \leq p_i, 1 - \alpha_r \leq r_i \leq 1$):

$$r_i = \alpha_r * r_i^{'} + (1 - \alpha_r) \quad 7.12$$

$$r_i^{'} = \int_{-\infty}^{p_{n,i}} N(0,1)(z)dz \quad 7.13$$

$$p_{n,i} = \frac{p_i-(\mu_i-fl_i)}{2\sigma_i} \quad 7.14$$

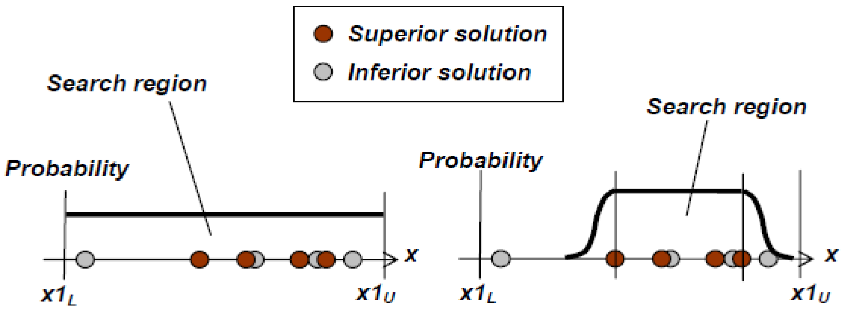

(a) MOEAs (b) ARMOGA

Figure 7.6 Range adaptive.

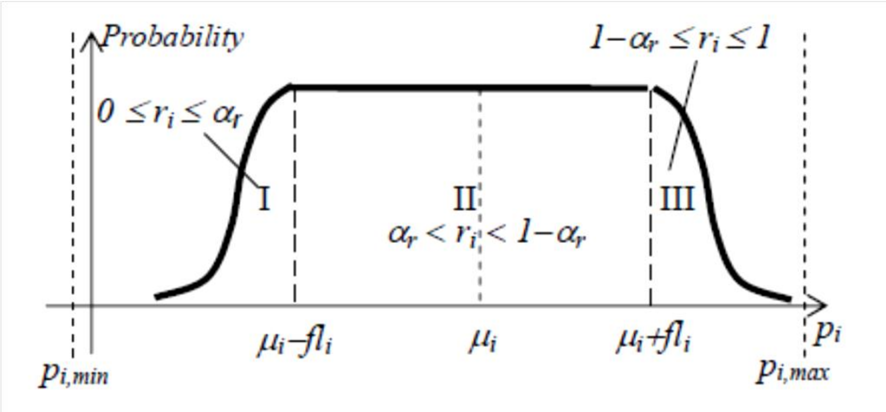

Figure 7.7 ARMOGA regions.

7.4 Interaction between FEA and optimisation method

Interaction between the FEA and ARMOGA optimisation methods was done by using a modeFRONTIER software technology. The modeFRONTIER 4.3 offers many benefits to link computer-aided engineering (CAE) to the single and multi-objective design optimisation methods. modeFRONTIER provides an environment for the designer to integrate their FEA by using different optimisation methods such as gradient-based methods, genetic algorithms, and robust design optimisation methods.

An ABAQUS file in python language should be generated and submitted to the modeFRONTIER program as shown in Figure 7.8 (a). The ABAQUS program is run by modeFRONTIER in order to generate the FEA output. Then, the output results are used in calculating of the design constraints. New design variables are then generated to satisfy the design objective functions. Running new design iteration requires inserting these variables inside the ABAQUS python file and running the FEA with the new variables. The optimisation flow chart for different slab design is shown in Figure 7.8(b).

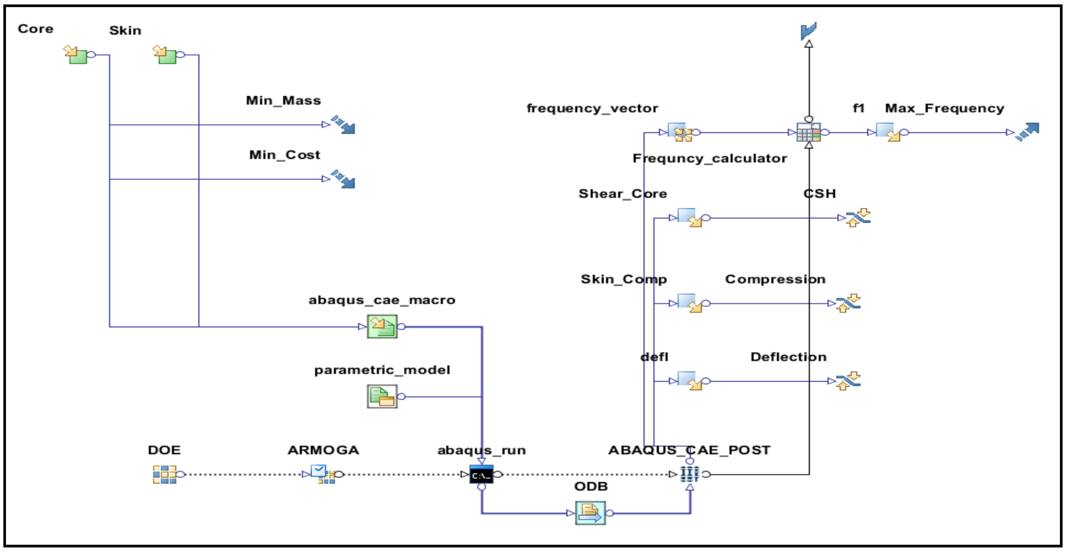

(a) Sample of flow chart used by modeFRONTIER.

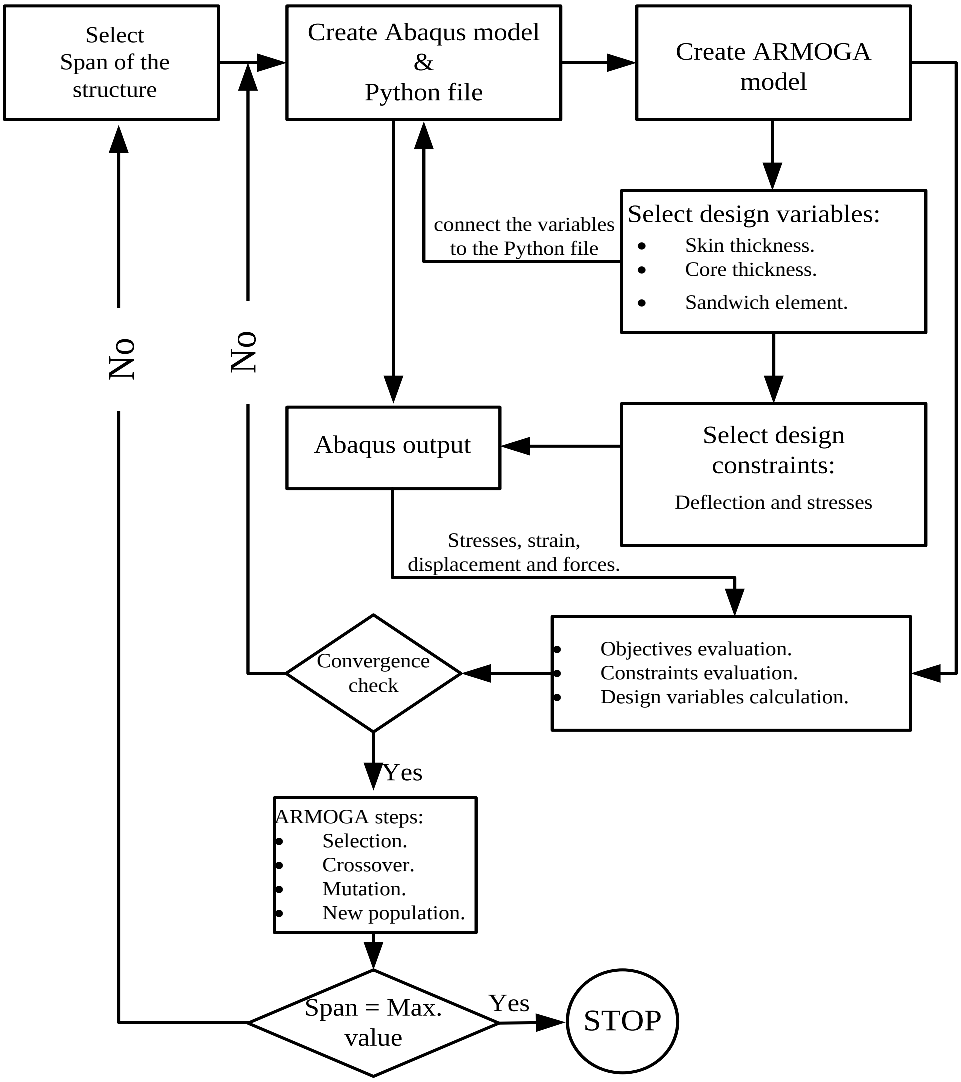

(b) Design flow diagram.

Figure 7.8 Optimisation flow charts.

7.5 Multi-objective design optimisation of GFRP sandwich slabs

The optimisation work is conducted using numerical optimisation. The numerical optimisation includes both objectives cost and mass simultaneously. Multi-objective optimisation under a combination of two types of load such as distributed load and concentrated load is complicated using analytical optimisation, and it is required the use of FEA method. In addition, the FEA method helps in simulating the materials behaviour in more accuracy. Therefore, doing numerical optimisation using FEA method has been adopted to overcome the complexity of multi-objective design for FRP structures. The same FEA model developed in Chapter 6 is used in the design optimisation. The mechanical properties of the GFRP sandwich slab for the FEA model are shown in Table 6.1 (Chapter 6). The slabs were produced by the factory with a width of 1200 mm and this width (L_y) was used as a constant through the numerical design optimisation. A summary of the design objective and constraints are presented in Table 7.1. Schematic diagram of the one-way and two-way slabs is shown in Figure 7.9. The width of the slab (L_y) is assumed fixed through the design which is equal to the original panel width.

Table 7.1 Objectives and constraints

Design criteria	Reference		Design values	
Load	AS/NZS 1170		Dead load	• Self weight. • Finishing=0.42 kN/m^2. • Partitioning=0.96 kN/m^2.
			Live load	Domestic= 3kN/m^2 + 4.5kN
				Industrial= 5 kN/m^2 + 4.5 kN
Deflection	EUROCOMP		Floor supporting brittle finishing	Span/250
Free vibration	ISO 10137 and literature.		Rang	1-80 Hz
			Human activities	Up to 15 Hz
Safety factor	Material	EUROCOMP (Clarke 1996)	= k1 x k2 x k3 = 2.25 x 1.1 x 2.5 ≈ 6.2	
	Load	EUROCOMP (Clarke 1996)	Dead load	1.35
			Live load	1.5
Stress constraints	• Skin stress (Tension and compression). • Core stress (compression and shear).			
Objectives	• Cost minimisation. • Mass minimisation.			

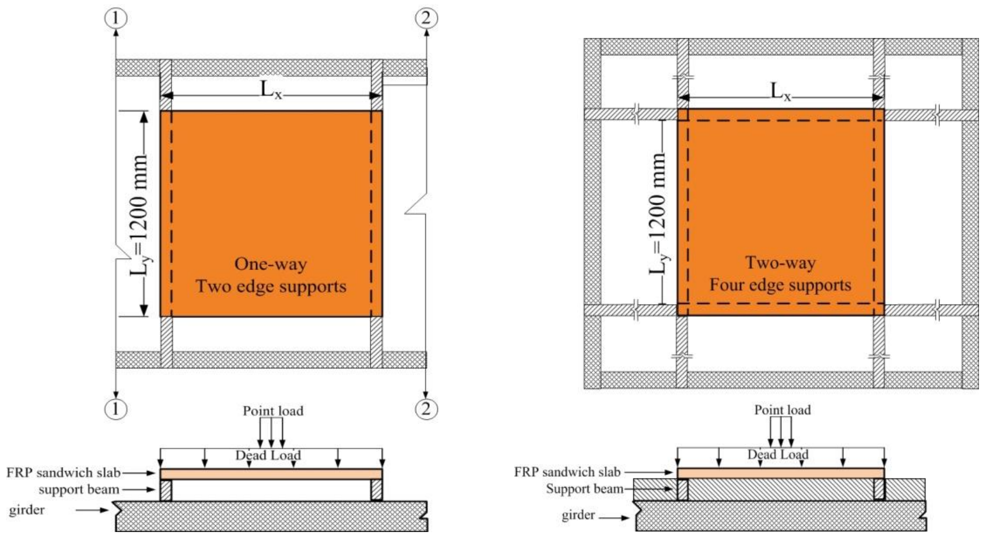

(a) One-way slab (b) Two-way slab

Figure 7.9 Schematic diagrams for slabs.

In the design of sandwich structure, both skin and core thicknesses are important. The core thickness represents the distance between the combined stiff faces. Increasing the thickness of the core will increase the moment of inertia (I) of the sandwich slab. Both core and skin thicknesses affect the mass and the cost of the slab and the design objectives are shown below:

(a) Mass minimization (M)

The first objective function is the minimization of sandwich slab mass is shown by Equations 7.15 and 7.16:

$$M = mass\ of\ skins + mass\ of\ core \tag{7.15}$$

$$M = 2\,\rho_s t\, L^2 + \rho_c\, c\, L^2 \tag{7.16}$$

where ρ_c and ρ_s are the core and skin densities.

(b) Cost minimization (C)

The cost of the material is used as a unit value, whereas the cost of the skin is assumed to be five times the cost of the core. Based on the materials prices in Australia, the relative cost of skin (C_s) to core (C_c) is equal to 5 and this value was used in the calculations (Van-Erp 2010). This assumption is based on the available estimated market prices in Australia. The cost minimisation is the second objective and it can be written as:

$$C = cost\ of\ core + cost\ of\ skins \qquad 7.17$$

$$C = 2\ t_s\, L^2\, C_s +\ c\, L^2\, C_c \qquad 7.18$$

where C_c and C_s are the core and skin cost respectively.

7.5.1 Serviceability and ultimate design constraints

Design constrains are a very important part of design optimisation. It limits the objective function and the design variables within a specific certain region. Design criteria were presented in section 7.2, and these can be converted to design constraints. There are two static design load constraints, serviceability load constraints and ultimate load constraints. The design objectives are the cost and mass of the slab as shown above in Equations 7.16 and 7.18. GFRP skin material design constraints were considered the Hashin failure index to identify the material allowable or ultimate limit. The failure index is having value of 1.0 at failure. The design constraints are then:

Case-1: **Serviceability design**

Applied load= Dead load + Live load 7.19

Design constraints:

Mid span deflection $\delta - \frac{span}{250} \leq 0$ 7.20

Fibre tensile stress $F_f^t - \frac{1}{S.F} \leq 0$ 7.21

Fibre compression stress $F_f^c - \frac{1}{S.F} \leq 0$ 7.22

Core compressive strength $\sigma_{cc} - \frac{\sigma_{core}^{ult}}{S.F} \leq 0$ 7.23

Core shear strength $\tau - \frac{\tau^{ult}}{S.F} \leq 0$ 7.24

where S.F is the safety factor. F_f^t and F_f^c are the fibre tensile and compression failure indices respectively. σ_{core} and τ are the core compression and shear stresses respectively. Subscript *ult* refers to the ultimate strength.

Case-2: **Ultimate design**

$$\text{Applied load} = 1.35 \text{ x Dead load} + 1.5 \text{ x Live load} \tag{7.25}$$

Design constraints:

Fibre tensile strength $F_f^t - 1 \leq 0$ 7.26

Fibre compressive strength $F_f^c - 1 \leq 0$ 7.27

Core compressive strength $\sigma_{core} - \sigma_{core}^{ult} \leq 0$ 7.28

Core shear strength $\tau - \tau^{ult} \leq 0$ 7.29

Cost and mass minimisation objectives were studied using the above two cases of constraints. A one-way square slab with dimensions of 1200 mm x 1200 mm was investigated here. A scatter chart comparison between the service and ultimate load designs is shown in Figure 7.10. The cost and mass of the service load design is much higher than it is for the ultimate load design. In addition, the data in the Figure 7.11 shows that total slab thickness is higher for the serviceability load design than the ultimate load design. The core to skin ratio is higher in the service design than the ultimate design. This comparison shows that the governing constraint for the design of the GFRP slab is the allowable service deflection. The ultimate load design reduces the total thickness of the slab in order to satisfy the stress failure criteria in the skin and core. Whereas, the serviceability load design increases the slab thickness to satisfy the deflection constraint.

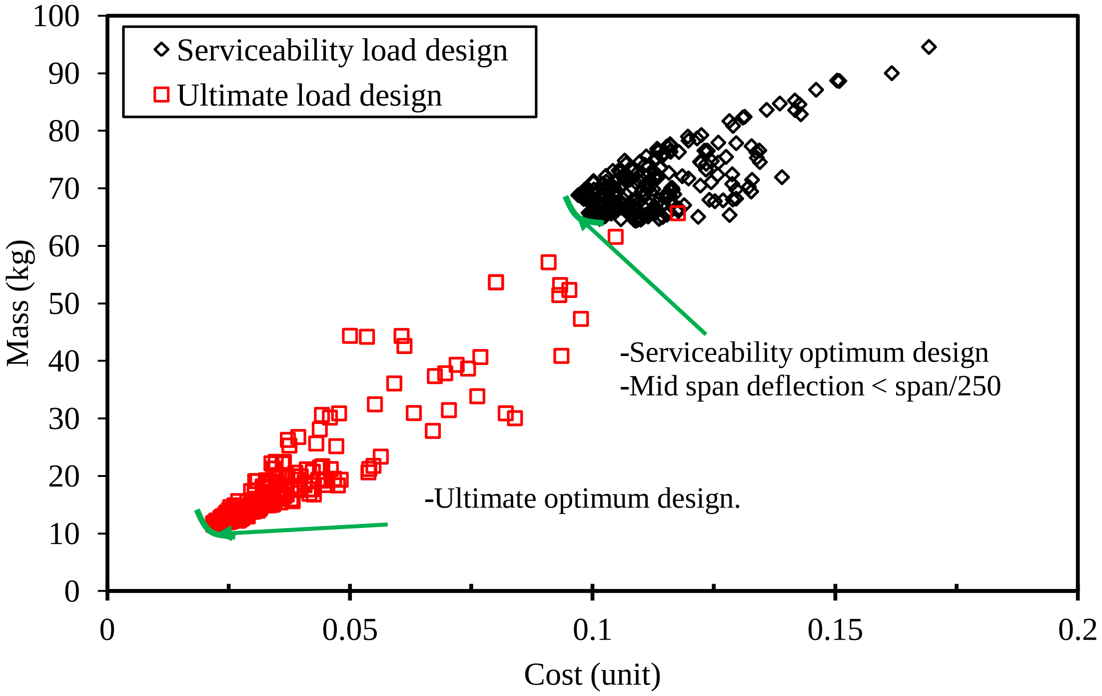

Figure 7.10 Cost and mass scatter chart for the service and ultimate load designs.

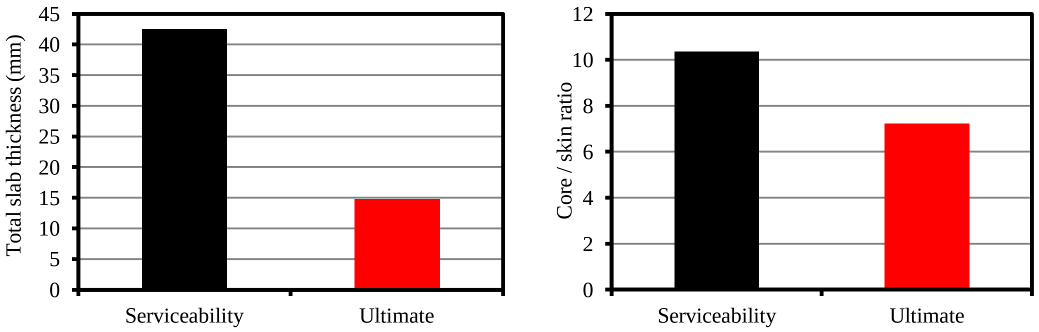

(a) Total thickness. (b) Core to skin ratio.

Figure 7.11 Design variables.

The normalized constraints of the ultimate load design with the mass of the slab are presented in Figure 7.12(a). It can be seen that not all the stress constraints control the design of the GFRP sandwich slab. Core shear and skin tension show a large influence on the design objective. By contrast, core compression and skin compression are limited up to 15% of the ultimate load failure. Serviceability design constraints are shown in Figure 7.12(b). This shows that normalized stress constraints are limited by 45% of the allowable stresses, without affecting the service design. The design appears to be controlled by the mid-span deflection. The mid-span deflection constraint has a strong influence on the design.

The FEA models for the analysis of both serviceability limit and ultimate limit design were done on one-way slab of 1200 mm x 1200 mm. Calculation of the mid-span deflection of the ultimate load design at service loading level shows that the ultimate design does not satisfy the serviceability requirement and it gives higher deflection than the serviceability limit as shown in Figure 7.13. The load factor represents the failure load divided by the serviceability load. The serviceability design is considered the mid-span deflection as a constraint and this gives the slab cross section higher than the ultimate limit slab design. Because of this, the serviceability design constraint is more applicable for this type of slab structure. The ultimate design procedure might be applicable to another type of GFRP sandwich structure when the deflection is not governing the design.

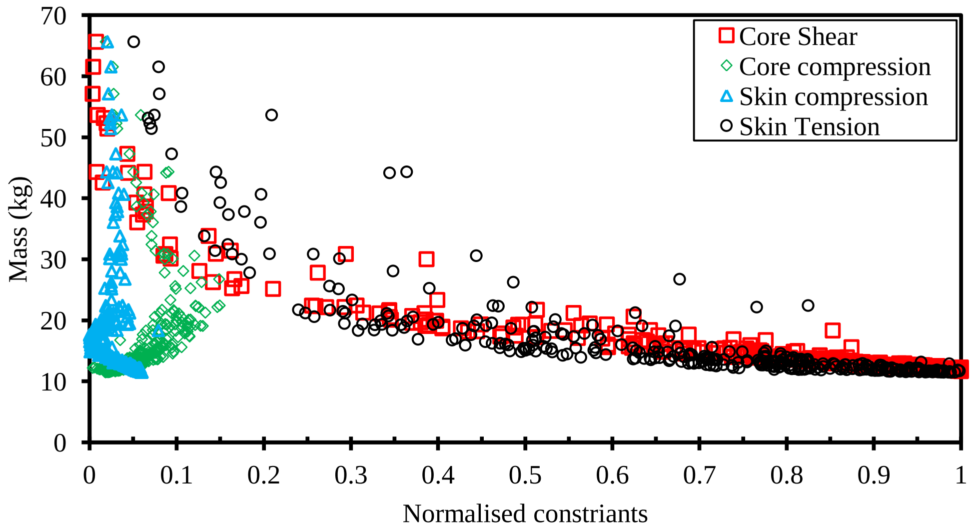

(a) Ultimate load design.

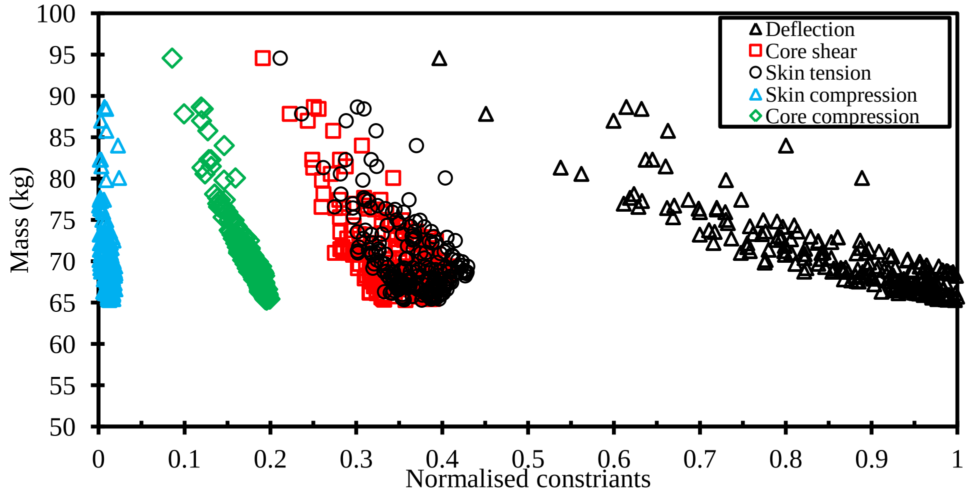

(b) Service load design.

Figure 7.12 Comparison between stress design constraints.

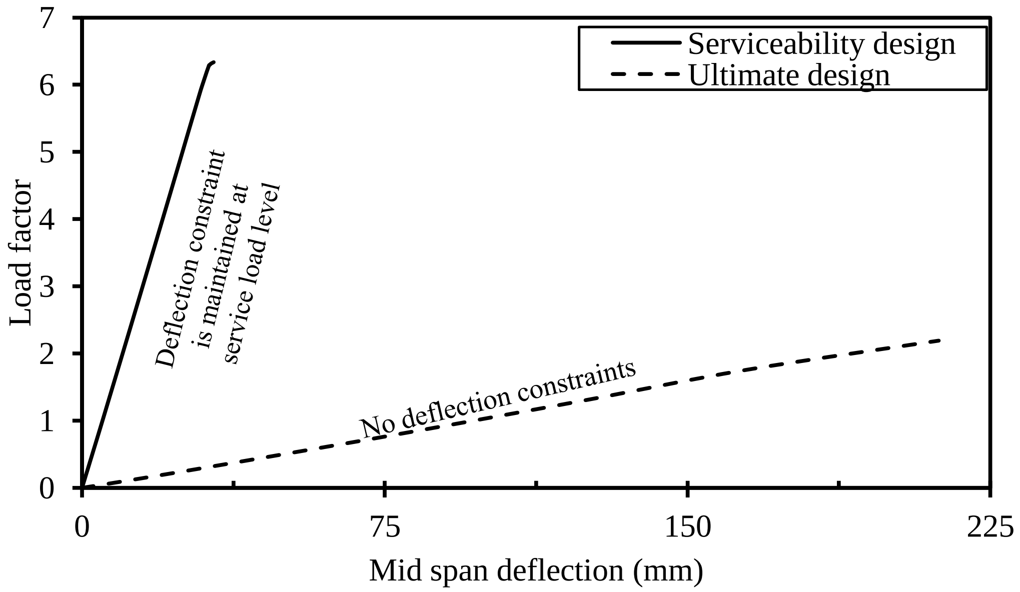

Figure 7.13 Comparison between serviceability and ultimate load design slab behaviour.

7.5.2 One-way and two-way slabs design

7.5.2.1 Fibre orientations

The GFRP sandwich slab is made of top and bottom skins and modified phenolic core material. The GFRP skin is made of few plies, and each ply should be oriented to make the slab as strong as possible. Designing the fibre orientation in the skins is an important aspect in FRP composite structures (Farshi & Herasati 2006). The present work considers the fibre orientation design of the GFRP sandwich slabs in two structural support types for one-way and two-way.

The design was based on a two plies GFRP skin as shown in Figure 7.14. The optimisation design found that the optimum fibre orientation for one-way GFRP sandwich slabs is 0^o and 90^o as shown in Figure 7.15. In one-way slabs, the strongest fibre is located in the 0^o to carry the load and transfer it to the supports. Design optimisation of two-way GFRP sandwich slabs showed that fibre orientation is sensitive to slab width to length (L_y/L_x). The width (L_y) is assumed constant and equal to 1200 mm, while the length (L_x) varies from 450 mm up to 1200 mm. In addition, the fibre orientation is symmetry for the two-way slab design and θ_1 is equal to θ_2.

Optimisation results of fibre orientation in two-way slabs are shown in Figure 7.16 for normalised stiffness, and the design results are given in Table 7.2 as well. When the L_y/L_x ratio is high the orientation angle is small and increasing the L_y/L_x ratio causes an increase in the ply orientation angle. For the two-way slabs with L_y/L_x greater than 2.0 the effect of the fibre orientation is small and $0^o/90^o$ fibre orientations is suitable.

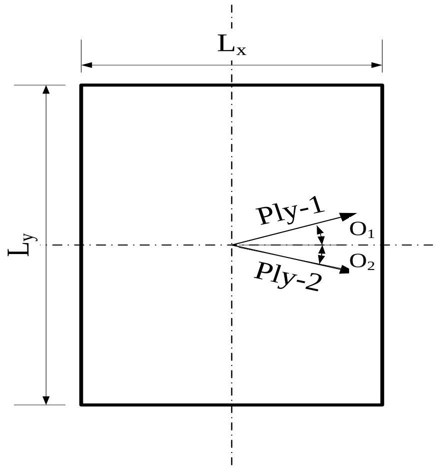

Figure 7.14 Fibre orientation in the GFRP skin.

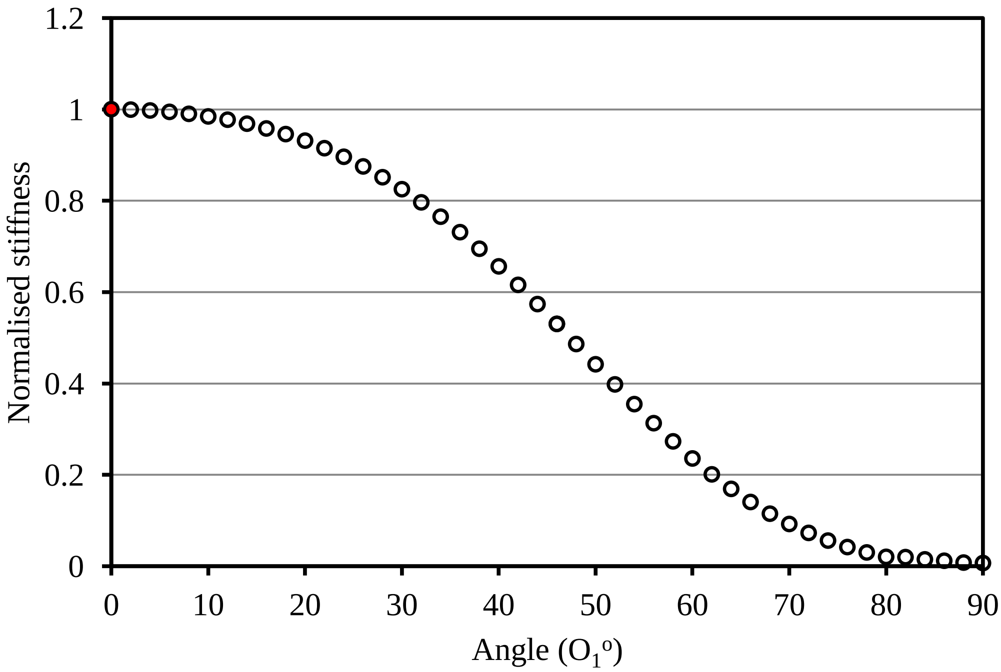

Figure 7.15 Optimum fibre orientations of square one-way slab.

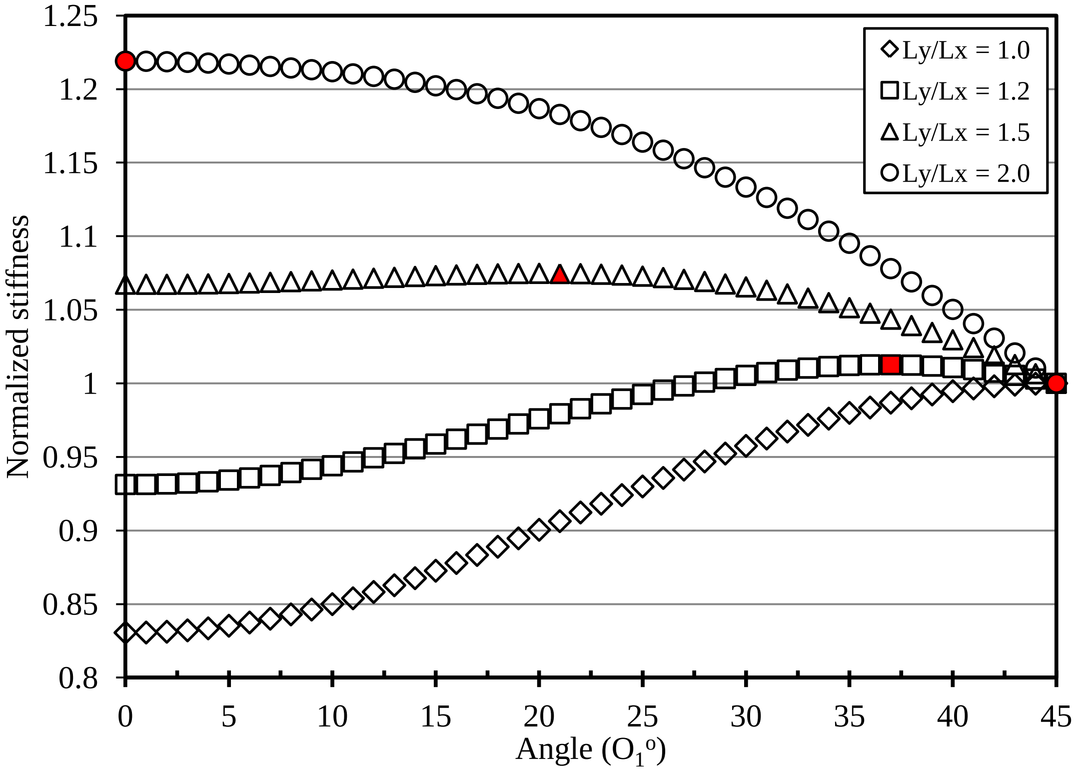

Figure 7.16 Optimum fibre orientations of two-way slab.

Table 7.2 Fibre orientation design of the GFRP skin

Slab type	L_x (mm)	L_y (mm)	L_y/L_x	Ply-1 orientation	Ply-2 orientation
One-way	450-2400	------	------	0	90
Two-way	450	1200	2.66	0	90
	600	1200	2	0	90
	800	1200	1.5	20	-20
	1000	1200	1.2	37	-37
	1200	1200	1.0	45	-45

7.5.2.2 Cost and mass objectives

In the previous section 7.5.2.1, it was shown from the that using $0^o/90^o$ ply orientations is the optimum for the one-way slab, and the optimum for two-way fibre orientation depends on the width to length (L_y/L_x) as shown in Table 7.2. In addition, it was shown in section 7.5.1 that the serviceability design is suitable for this type of slab structure when deflection is one of the design criteria. An optimisation study was conducted to design both one-way and two-way slabs under serviceability limit design constraints. The one-way slab is assumed to have a variable length (L_x) from

450 mm to 2400 mm and a constant transverse width equal to 1200 mm. The two-way slabs have a span varied in length (L_x) from 450 to 1500 mm with a constant width (L_y) of 1200 mm. These slabs were designed for the multi-objective cost and mass minimisation under serviceability design conditions. The serviceability condition had an allowable mid-span deflection of span/250. Two cases of loading conditions were studied; domestic load and industrial loading. This type of loading is a combination between point and distributed loads. The load calculation is shown below:

Domestic:

Total load = self weight + finishing + partitioning + 3 kN/m^2 + 4.5 kN

Industrial:

Total load = self weight + finishing + partitioning + 5 kN/m^2 + 4.5 kN

Scatter charts of the designs are shown in Figure 7.17 and 7.18 for the one-way and two-way slabs respectively. These graphs show the trade-off between cost and mass in GFRP sandwich slabs design. They also show how the optimum design points were selected from different Pareto-frontier regions. The MCDM was used to find the optimum design point through the Pareto-frontier set (ETESCO 2009). Optimisation results for one-way and two-way slabs are shown in Table 7.3 and Table 7.4, respectively. Cost objective and mass objective variations are shown in Figures 7.19 and 7.20 for one-way and two way designs respectively. The major point to notice from these two graphs is that the square two-way slab is lighter and less costly compared to the one-way slab for the same span length. However, the results of one-way and two-way slabs design are approximately similar when the span length (L_x) is less than 800 mm and the width to length (L_y/L_x) ratio is greater than 1.5.

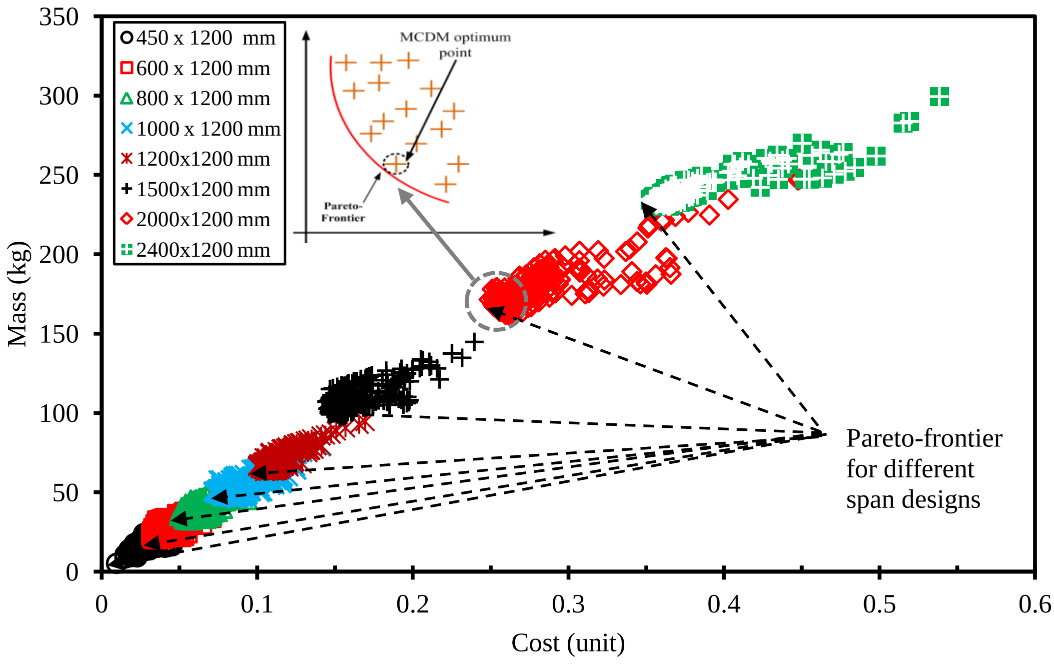

Figure 7.17 Scatter chart for different spans design of one-way slab.

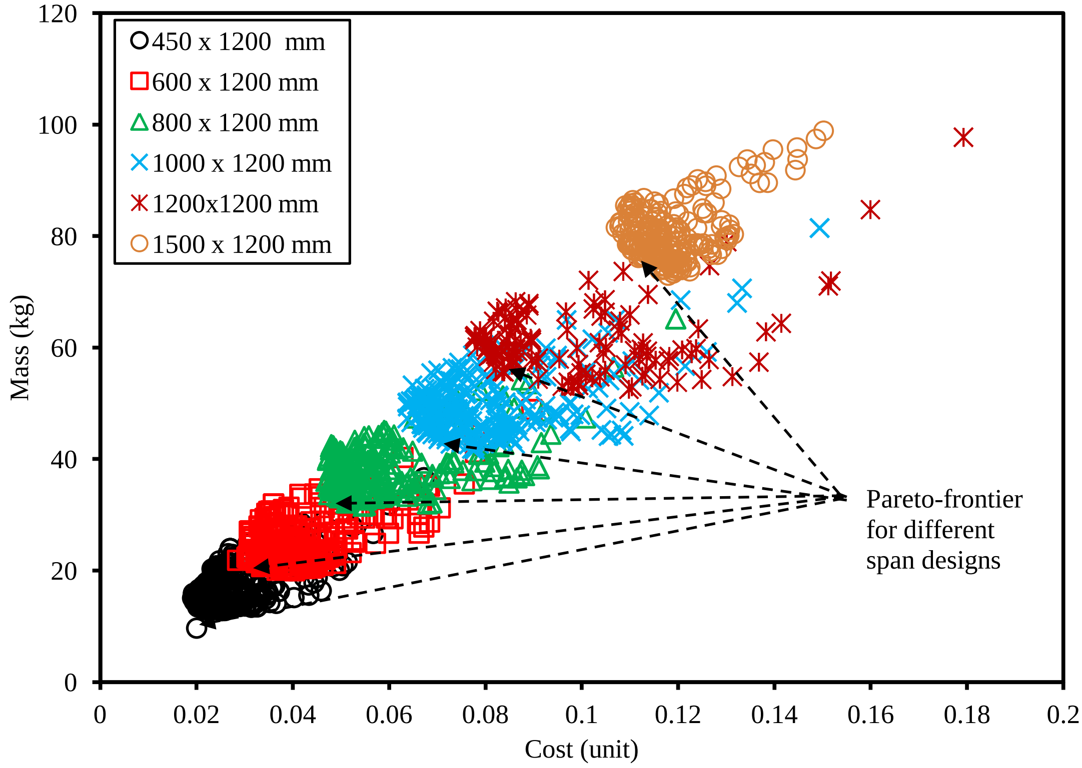

Figure 7.18 Scatter chart for different spans design of two-way slab.

Table 7.3 Cost and mass optimisation results of a one-way slab

Span (L_x) mm	Width mm	Core thickness mm	Ply-1 thickness mm	Ply-2 thickness mm	Total skin thickness mm	Cost unit	Mass kg
Load	Domestic = self weight + finishing + partitioning + 3 kN/m^2 + 4.5 kN						
450	1200	19.49	1.32	0.4	1.78	0.020	12.7
600		23.12	1.75	0.37	2.12	0.032	20.2
800		26.97	2.27	0.35	2.82	0.051	31.9
1000		31.77	2.79	0.33	3.19	0.076	47.1
1200		35.64	3.13	0.31	3.5	0.101	63.1
1500		42.79	3.83	0.3	4.09	0.151	94.7
2000		54.81	4.97	0.3	5.19	0.258	161.6
2400		65.5	5.57	0.27	5.73	0.357	228.0
Load	Industrial = self weight + finishing + partitioning + 5 kN/m^2 + 4.5 kN						
450	1200	22.69	1.43	0.4	1.83	0.022	14.5
600		25.17	1.8	0.37	2.17	0.034	21.7
800		28.99	2.25	0.35	2.6	0.053	33.7
1000		33.42	2.71	0.33	3.04	0.077	48.7
1200		38.21	3.27	0.31	3.58	0.107	67.2
1500		44.78	4.09	0.3	4.39	0.160	99.5
2000		57.34	5.37	0.3	5.67	0.274	170.2
2400		71	6	0.27	6.27	0.385	246.6

Table 7.4 Cost and mass optimisation results of a two-way slab

Span (L_x) mm	Span (L_y) mm	Core thickness mm	Ply-1 thickness mm	Ply-2 thickness mm	Total skin thickness mm	Cost unit	Mass kg
Load	Domestic = self weight + finishing + partitioning + 3 kN/m^2 + 4.5 kN						
450	1200	19.2	1.3	0.4	1.7	0.020	12.5
600		22.8	1.7	0.38	2.08	0.031	19.9
800		26.5	1.2	1.2	2.4	0.048	30.8
1000		30.8	1.28	1.28	2.56	0.068	44.0
1200		32.47	1.32	1.32	2.64	0.085	55.4
1500		33.81	1.41	1.41	2.82	0.112	72.5
Load	Industrial = self weight + finishing + partitioning + 5 kN/m^2 + 4.5 kN						
450	1200	21.74	1.4	0.4	1.8	0.021	14.0
600		24.2	1.75	0.36	2.11	0.033	21.0
800		28.1	1.25	1.25	2.5	0.051	32.6
1000		31.1	1.37	1.37	2.74	0.070	45.0
1200		33.1	1.4	1.4	2.8	0.088	57.0
1500		36.1	1.52	1.52	3.04	0.120	77.6

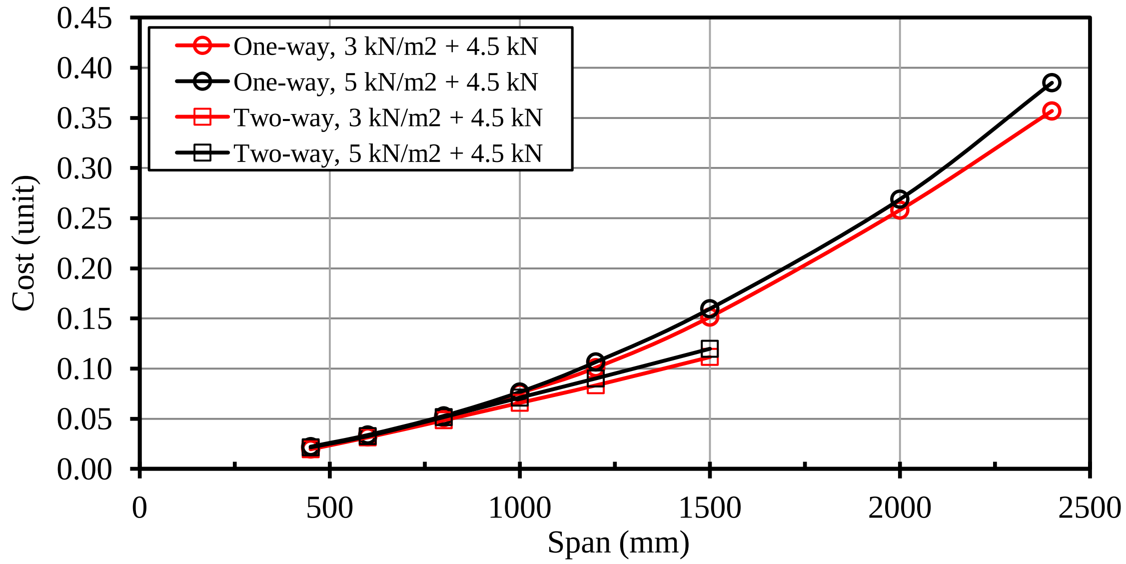

Figure 7.19 Cost objective with span.

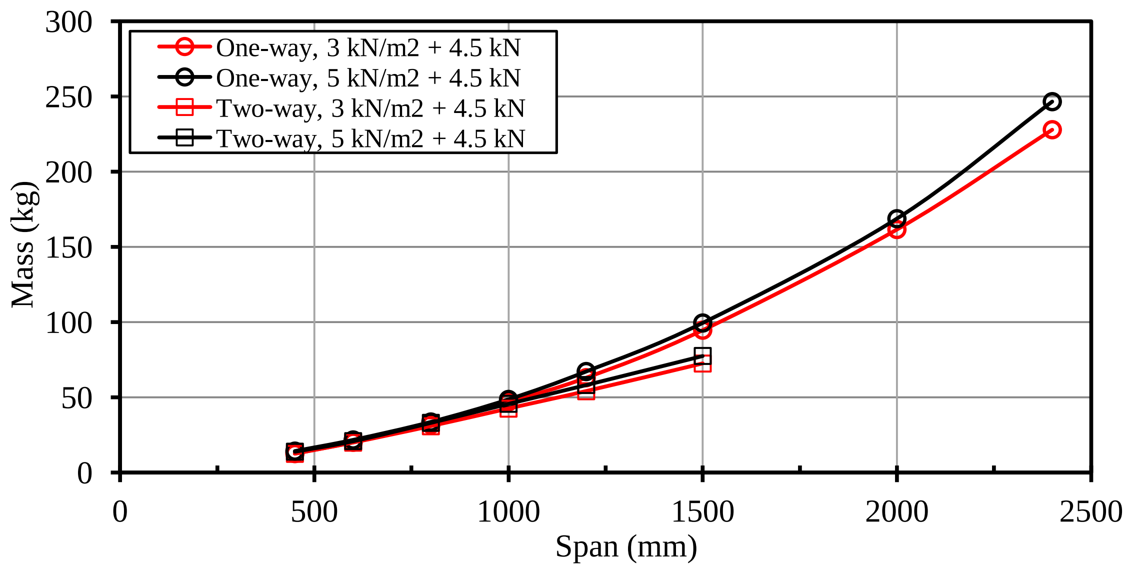

Figure 7.20 Mass objective with span.

The selection of the optimum design point from the Pareto-frontier leads to the relationship between the span and the design variables of the slab. The behaviour of core thickness and span length is shown in Figure 7.21. It shows that the behaviour is approximately linear for the one-way slab and is non-linear for the two-way slab. This is due to the effect of the two-way slab width to length ratio. Optimal skin thickness for one-way and two-way slabs is shown in Figure 7.22. Increasing the span length of GFRP sandwich slabs leads to an increase in the moment applied to the slab. In order to maintain the same service deflection, the slab design requires an increase in rigidity (*D*) of slab. Increasing the sandwich slab rigidity requires increasing core and skins thickness. In the one-way slab, the thickness of the 90^o ply is small compared to the thickness of the 0^o ply as shown in Figure 7.22. From this, it can be concluded that the design output is influenced by the span of the slab, and external load values. In addition, the distributed load effect is influenced by the slab dimensions compare to the point load which is constant. In the short span slab, the design is dominated by the point load while in the long span slab the distributed load contribution becomes more significant than the point load.

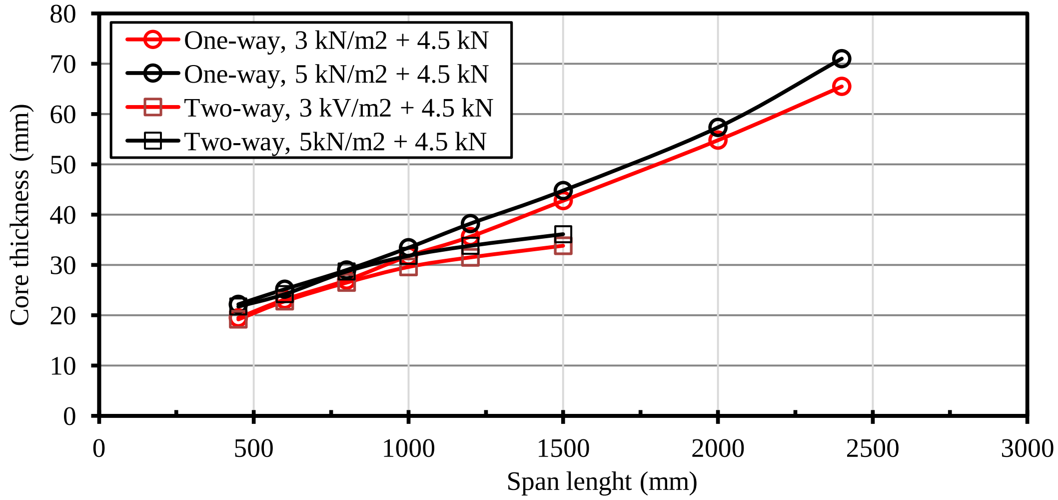

Figure 7.21 Optimum core thickness.

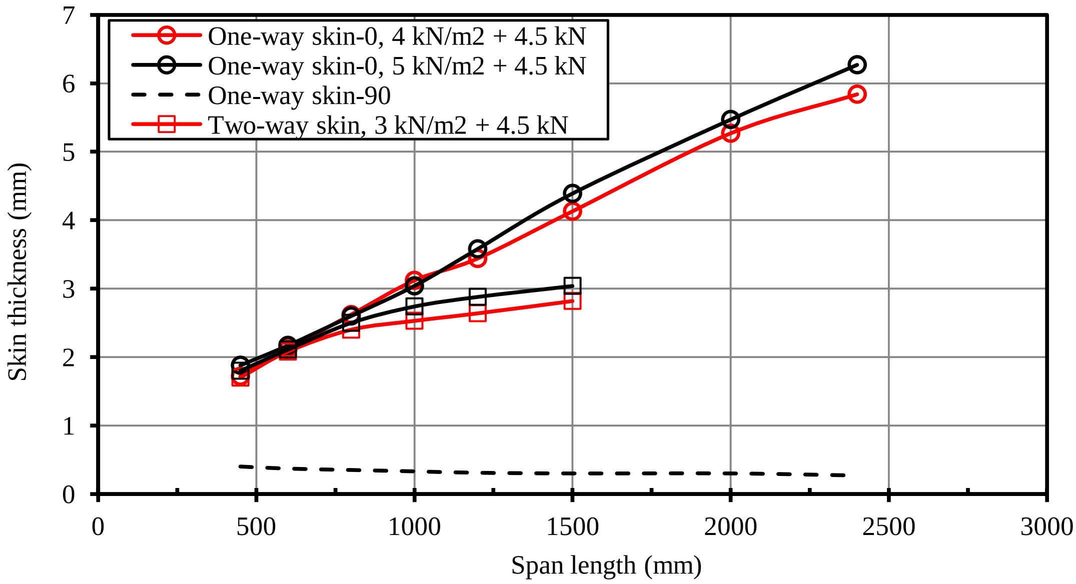

Figure 7.22 Optimum skin thickness.

Optimisation results of the multi-objective design show that the average cores to skin thickness ratios are 10.8 and 11.5 for one-way and two-way slabs respectively. In the present design, the load factor was calculated by using non-linear finite element modelling as discussed in Chapter 6. Load factors for all designs are calculated by finding the ultimate failure load. The load factor represents the failure load divided by the service load where the service load is explained in Table 7.1. The optimised slabs were analysed to find the ultimate load capacity by using the non-linear 3D FEA method. The non-linear analysis shows a failure load is 5.5 to 7 times higher than the service load as shown in Figure 7.23. Although, the optimum design maintains the same optimisation constraints for all designs, it can be seen that the failure load factor of the optimised slabs is different.

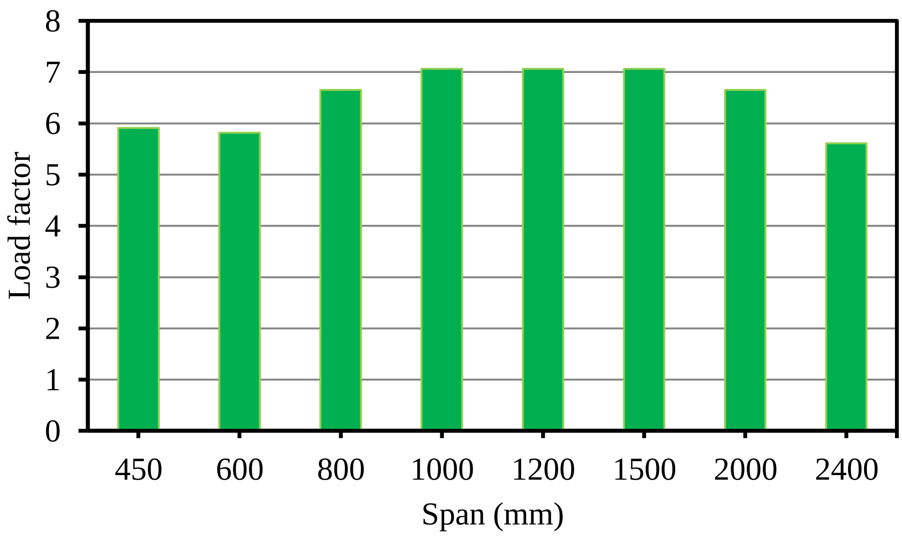

Figure 7.23 Load factor for the designed one-way slabs.

7.5.2.3 Frequency design

Vibration of the floor is a common problem in buildings due to affect of dynamic loading. Human activities and traffic are the most common sources of vibration. Human activates is an internal source of vibration, and traffic is an external source of vibration. Many occupants claim against the vibration and noise of the traffic (Hunaidi 2000). The internal vibration depends on the design of the building structure. The external vibration depends on vehicle weight, road condition, soil type, and the distance from the source of vibration. Several things can be done outside the building to reduce the traffic vibration such as road maintenance, building in-ground barriers, and keeping a safe distance from the road (Xu & Hong 2008). This study focuses on investigating internal source of free vibration.

Tables 7.3 and 7.4 give the optimisation design results for two cases of loading, domestic and industrial loading. The FEA model was presented in Chapter 6 for the free vibration of the slabs. It can also be used to find the natural frequency of the designed slabs in Tables 7.3 and 7.4. The slab is set on a rigid support and there is no deflection at the support. The analysis results are shown in Figures 7.24 for the industrial and domestic designs of the GFRP slab. The frequency of the slab is reduced by increasing of slab span length. The two-way slab shows a different frequency than the one-way slab.

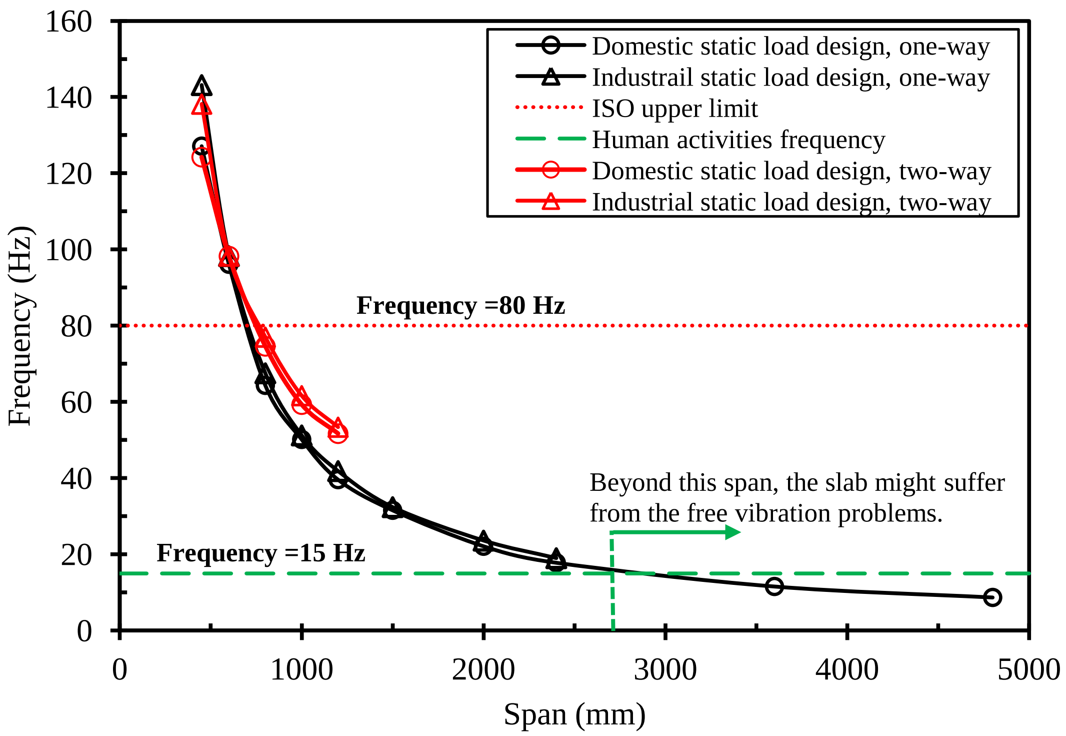

Figure 7.24 Slabs first natural frequency.

The ISO frequency for serviceability requirement is between 1-80 Hz. Investigation of the static design of the one-way slab shows that the design of one-way slab has a frequency equal to 17 Hz when the span is equal to 2400 mm, and it is greater than 15 Hz. Therefore, the static design of the sandwich slab satisfies the frequency requirements for the human activities up to 2400 mm span length. Beyond this length the natural frequency would be lower than 15 Hz as shown in Figure 7.24.

The design of the spans with a higher frequency can be met by increasing the cross-section of the slab. The analysis of the two-way slab showed that the static design of the slab has a frequency higher than 15 Hz when the slab span length is less or equal to 1200 mm. In addition, slab static design showed that both one-way and two-way slabs satisfy the higher free vibration limit of the ISO standard for spans less than 1000 mm.

The domestic slab design was selected for the frequency design. Five frequency intervals were selected for the one-way slab design, 15 Hz, 20 Hz, 30 Hz, 50 Hz and 80 Hz. The 80 Hz interval was selected for the two-way slab design. Optimisation was done using cost and mass minimisation and the frequency constraint. The results of this optimisation are shown in Figures 7.25 and 7.26. The higher frequency required higher values of the core and skin thicknesses. Furthermore, the higher frequency and higher span length required large thickness of the slab. The behaviour of core and skin thickness is non-linear with the span length compared to the static design. Finally, frequency design is important for the slab in the range of free vibration above the human activities rang (15 Hz).

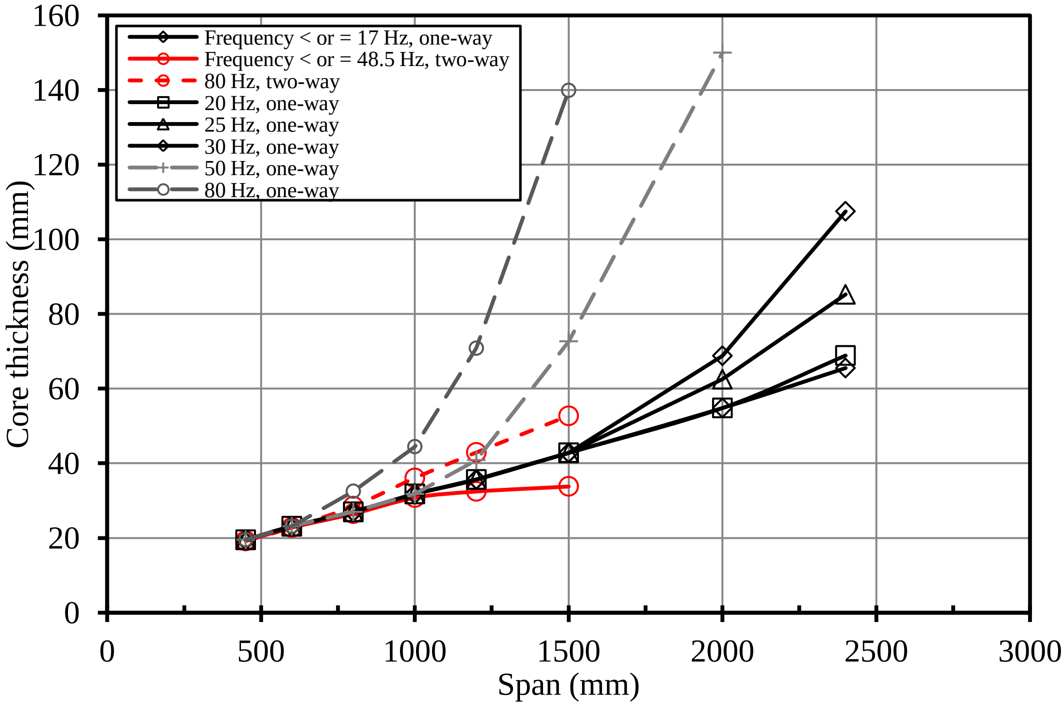

Figure 7.25 Core thicknesses with frequency for one-way and two-way slabs.

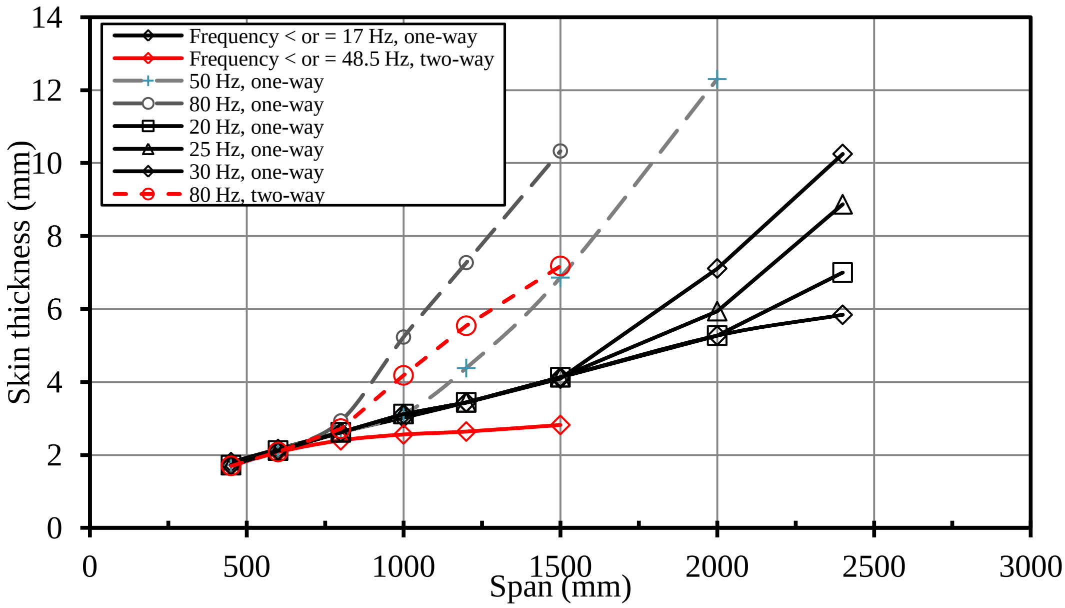

Figure 7.26 Skin thicknesses with frequency for one-way and two-way slabs.

7.6 Multi-objective design optimisation of GFRP sandwich beam

The previous studies used the sandwich beam rigidity equation to find the best core and skin thicknesses with minimum mass. The solution of the bending stiffness equation and the mass equation of the sandwich beam gave values for core and skin thicknesses (Allen 1969; Araújo et al. 2009). Froud (1980) found that the optimum bending stiffness design is located at the point where the core mass is equal to two times the skins mass. Li et al. (2011) used the same procedure to find the best ratio of the core mass to skin mass, which they found a value to be four. The difference between Froud (1980) and Li et al. (2011) finding is the approximation the sandwich beam rigidity calculations. Murthy et al. (2006) verified Froud's (1980) research findings by using experimental tests on a sandwich beam. Murthy et al. found that Froud's findings are valid for honeycomb core sandwich panels.

In this section, the numerical optimisation is done for single layer and glue-laminated GFRP sandwich beam. The numerical optimisation used the FEA with the multi-objective design optimisation for mass and cost objectives. This type of GFRP sandwich panel is produced for civil engineering applications with high strength core and good skin-core interaction. The experimental investigation conducted in the past using such GFRP sandwich panels did not show any skin wrinkling as a failure mode

(Islam & Aravinthan 2010, Manalo et al. 2010c). Therefore, this is not considered in the design optimisation.

7.6.1 Problem description

The design criteria of the slab design were presented in section 7.5. The slab is usually supported by a beam. The role of the beam is to support the slab and provides an acceptable stiffness to the structure. The beam in the structure is subjected to different forces, flexural, shear and torsion. In the design, the beam structure should be able to carry the loads transferred from the slabs. In the current design optimisation, the beam is expected to carry flexural and shear loads. The load values will be calculated based on the slab spans as shown in Figure 7.27. The optimum thickness design is used here to calculate the slab self-weight.

The applied load on the beam is a combination of the slab external load, and it's self-weight. The internal beam was selected for design optimisation as shown in Figure 7.27, and the beam is assumed to be simply supported at both ends as shown in Figure 7.28. The beam loading is calculated and shown in Table 7.5. The sandwich element is made of top skin, bottom skin, and core material. The top and bottom skins are made up of two layers of $0^o/90^o$ fibre glass plies. In the design the 0^o and 90^o plies have the same thickness as shown in Figure 7.28. The 0^o-ply carries the major forces and the 90^o-ply carries the secondary forces. The multi- objective optimisation problem is formulated as follows:

Objective 1: Mass minimisation

$$M = 2\,\rho_s t\, L\, b + \rho_c\, c\, L\, b \qquad 7.30$$

Objective 2: Cost minimisation

$$C = 2\;t_s\, L\, b\, C_s + \; c\, L\, b\, C_c \qquad 7.31$$

where b is the beam width.

The constraints of the beam design are same as the slab design constraints except the deflection constraint. The mid-span deflection of the beam is shown below:

$$\delta - \frac{span}{400} \leq 0 \qquad 7.32$$

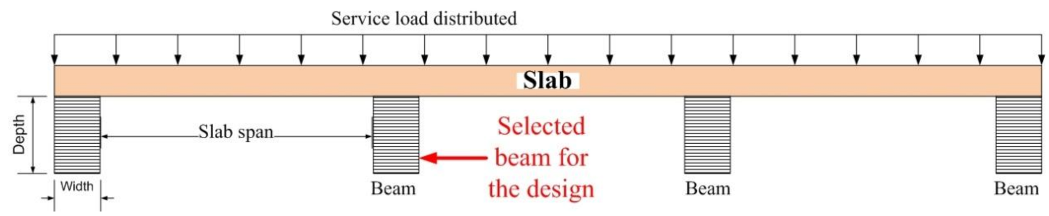

Figure 7.27 Schematic diagram of beams supporting slab.

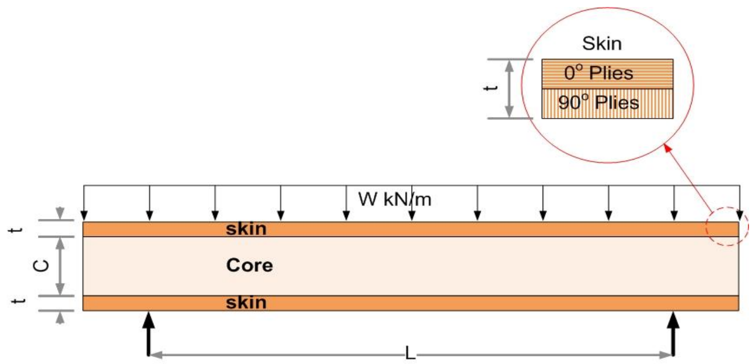

Figure 7.28 Schematic diagram of single sandwich beam.

Table 7.5 Beam loading values.

Slab span mm	Slab self weight kN/m^2	Slab distributed load kN/m^2	Beam span length mm	Beam load kN/m
450	0.26	6.4	1200, 2400, 3600, and 4800	3.0
600	0.30			4.0
800	0.34			5.4
1000	0.40			6.8
1200	0.46			8.2
1500	0.54			10.4
2000	0.70			14.2
2400	0.84			17.4

7.6.2 Single layer sandwich beam

Optimum design of a GFRP sandwich beam is important to avoid material waste and to obtain an economic product (Simoes & Negrão 2005). A number of studies have discussed the two objectives optimisation of an individual sandwich panel to optimise the cost or mass, and strength (Meidell 2009; Murthy et al. 2006; Swanson & Kim 2002). Optimisation of the bending stiffness has been studied with either the minimum mass or minimum cost to find the best values for the core and skin thicknesses for a specific bending stiffness (Froud 1980; Gibson 1984).

This work optimises the design of a GFRP sandwich simply supported beam with two objectives. The main objectives are to minimise the cost and mass of the beam. The design methodology will explore the effect of the thicknesses of the sandwich beam components at service load and the optimum core to skin ratio for the sandwich in terms of cost and mass ratios. The depth to width ratio of the beam is assumed equal to 2.5. The span of the beam is varied between 1200 mm and 4800 mm.

The search for the optimum design was conducted for different sandwich beam spans; 1200, 2400, 3600, and 4800 mm. The applied service load is calculated based on the slab span length as shown in Table 7.5. The allowable deflection at service load is equal to span/400. The required mass and cost of the beam are calculated according to the Equations 7.30 - 7.31. The cost and mass ratios of the core to skin are presented. A sample of scatter chart of the multi-objective design of the single sandwich beam is presented in Figures 7.29. These results for the load of 8.2 kN/m. It can be seen that increasing the mass has a direct effect on increasing the cost and mass of the GFRP sandwich beams. Table 7.6 shows the design results of the loads 3.0, 8.2 and 17.4 kN/m. All results of the core and skin thicknesses are shown in Figure 7.30.

Multi Criteria Decision Making (MCDM) was used in the optimisation. The MCDM chooses one reasonable design point from among a set of available ones in the Pareto-frontier. The Pareto-frontier set is the most eligible set of design points to represent the optimum design as shown in Figure 7.29. The design points for the 4 different span lengths were selected using the MCDM, and the results of the optimisation are shown in Figure 7.30. Each point has been selected from a Pareto-frontier for the specific span. The figure shows that there is a direct relation between the core thickness and skin thicknesses with the span of the beam.

For each span there is an optimum core and skin thicknesses. The cost and mass ratios were calculated for the core and skin as shown in Table 7.6. It can be seen that the average core to skin cost ratio is 1.1, and the average core to skin mass ratio is 3.68 as shown in Figure 7.31. The beam design with different loads showed same behaviour regarding to the core to skin ratio and the overall beam depth. The overall beam depth with respect to the span length and the applied load is shown in

Figure 7.32. The design optimisation showed that the overall depth of the single sandwich beam is 120 mm to 420 mm for beam spans between 1200 mm to 4800 mm. However, the experimental tests were done on a small scale samples with 15 mm and 18 mm thick panels, due to the limitation of the current manufacturing facilities. Hence, the influence of scale effects need further investigation.

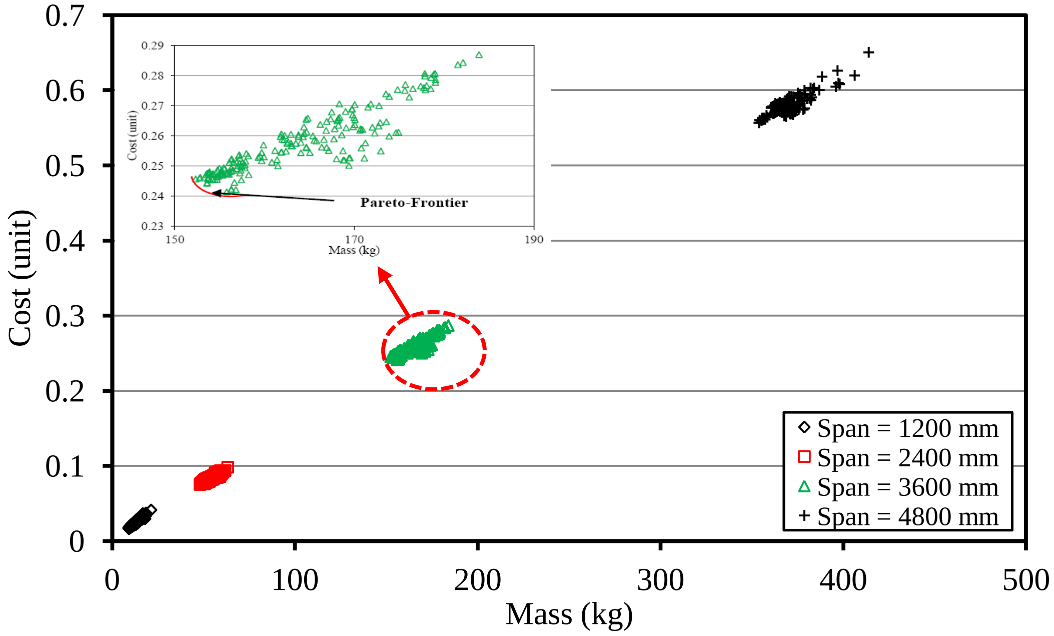

Figure 7.29 Scatter chart of mass and cost of the sandwich beams (load = 8.2 kN/m).

Table 7.6 GFRP sandwich beam cross section optimisation results.

Span mm	Thickness mm		Core/skin ratio		
	Core	GFRP skin	Thickness	Mass	Cost
Load = 3.0 kN/m					
1200	107.4	9.77	10.99	3.66	1.10
2400	147.2	13.38	11.00	3.67	1.10
3600	204.7	18.6	11.01	3.67	1.10
4800	253	23	11.00	3.67	1.10
Load = 8.2 kN/m					
1200	129.7	11.7	3.70	3.70	1.11
2400	193.8	17.6	3.67	3.67	1.10
3400	263.4	23.8	3.69	3.69	1.11
4800	317.9	28.8	3.68	3.68	1.10
Load = 17.4 kN/m					
1200	154.8	14	11.06	3.69	1.11
2400	238.6	21.6	11.05	3.68	1.10
3400	319.8	29	11.03	3.68	1.10
4800	385	35	11.00	3.67	1.10

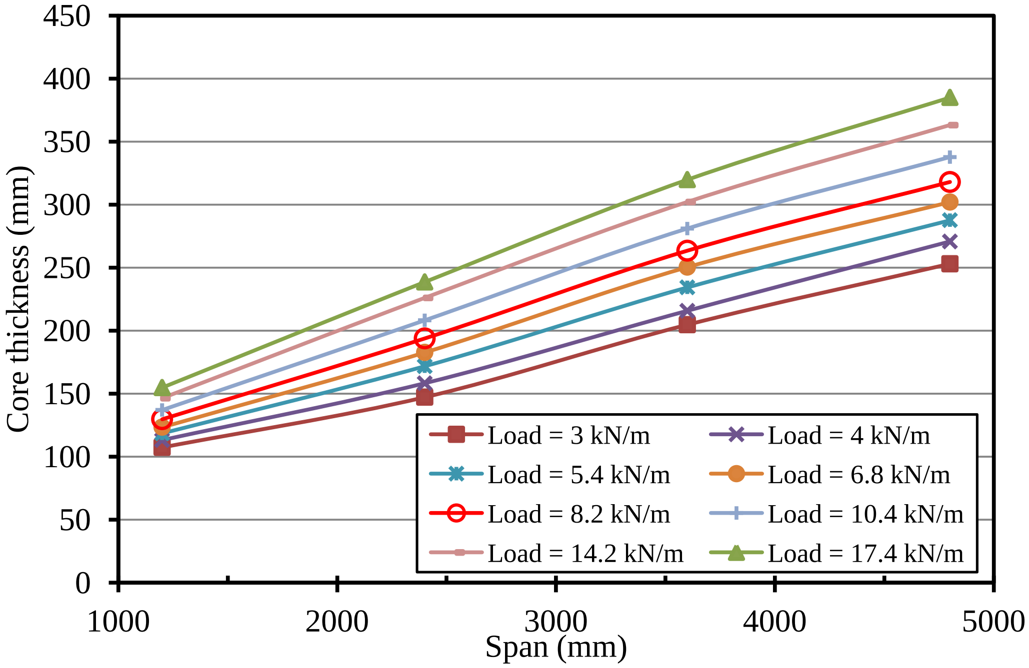

(a) Core thickness

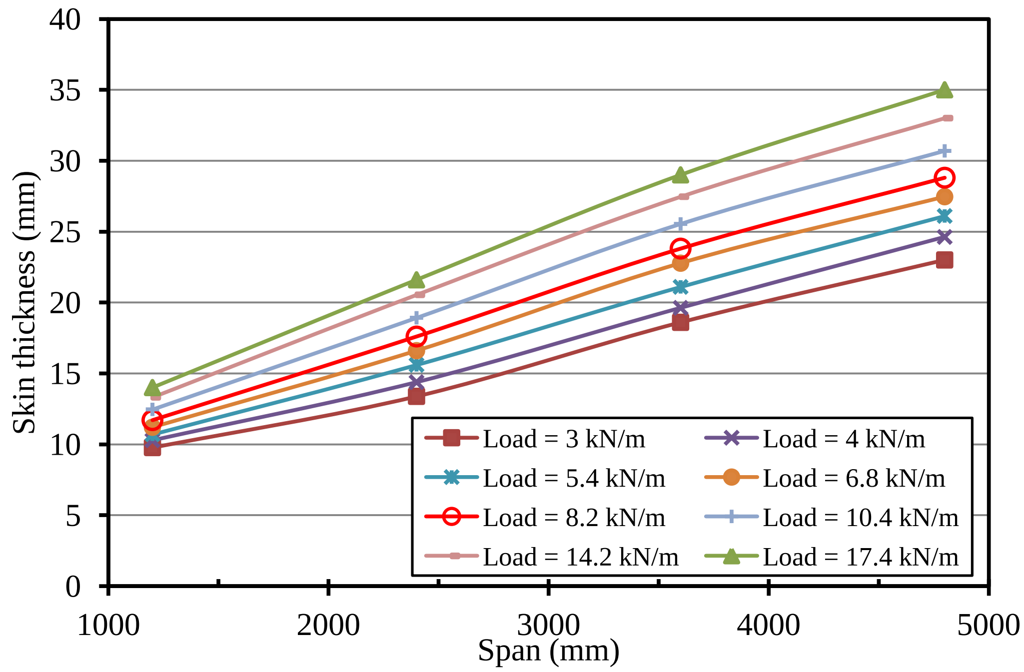

(b) Skin thickness

Figure 7.30 Optimum core and skin thicknesses.

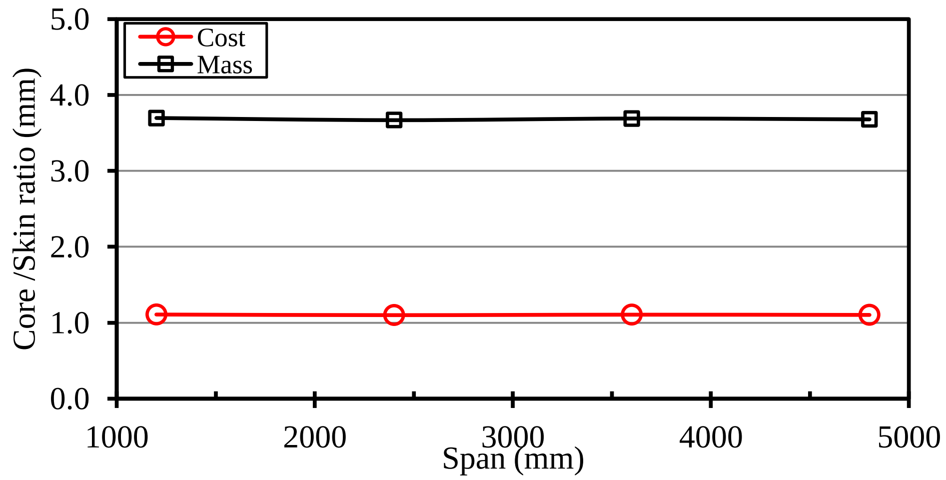

Figure 7.31 Optimum cost and mass core to skin ratios.

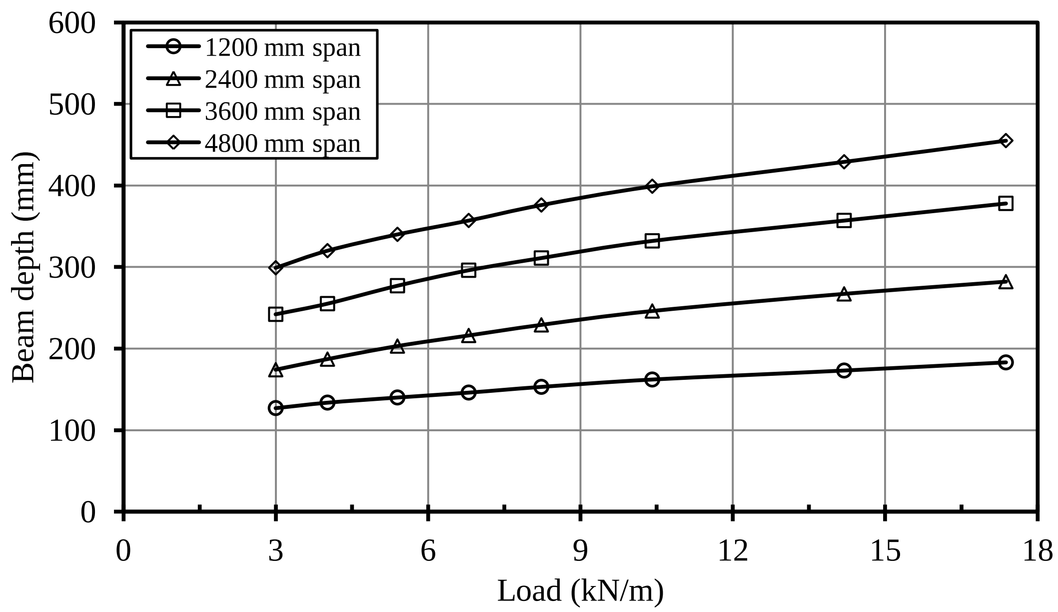

Figure 7.32 Optimum single sandwich beam depth.

7.6.3 Glue laminated sandwich beam design

Design a glue-laminated beam is needed when there is a limited facility to fabricate a single sandwich with a big cross section. The multi-objective optimisation was used to design the glue laminated GFRP sandwich beam with different loads and span lengths as shown in Table 7.5. The allowable mid-span deflection for the beam is assumed equal to span/400. The core to skin thickness ratio found for a single sandwich beam of 11.0 was used. The single sandwich beam optimum core to skin ratio was developed in the previous section 7.6.2. The glue-laminated GFRP sandwich beam design considers the variables of, total beam depth, beam width, span, applied load, and number of sandwich layers. Multi-objective optimisation was used, and the cost and mass of the beam were considered. The ARMOGA method was used to find the optimum solution. Four beam span lengths have been designed covering 1200, 2400, 3600, and 4800 mm.

The results of the single sandwich beam depth optimisation are shown in Figure 7.32. The beam depth to width constraints were added to the design, and were assumed equal to 2.5. The optimisation selects the minimum allowable width due to the low influence of the stress constraints. The total beam depth has an approximately linear relationship with the applied load as shown in Figure 7.32.

The optimisation was extended to the design of glue-laminated GFRP sandwich beams under different span lengths and loads. The glue-laminated GFRP sandwich beam design starts from two layers up to 10-layers. The design optimisation for the glue-laminated beam showed that the optimum depth of this beam is larger than the optimum depth of the single sandwich beam. A sample of the glue-laminated results is shown in Figure 7.33, for the two layered beam design. The results of the glue-laminated beam depth indicate that the beam has the same load-depth behaviour as the single sandwich beam. In addition, the behaviour seems to be approximately linear with respect to the applied load.

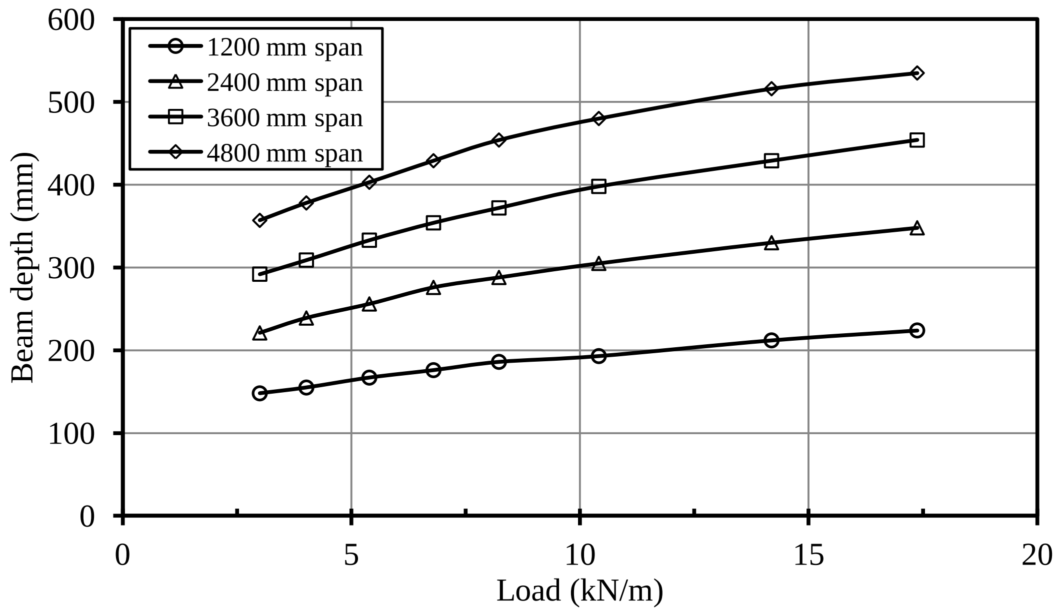

Figure 7.33 Optimum depth of two sandwich layers GFRP sandwich beam.

The behaviour of the glue-laminated beam constraints is shown in Figure 7.34. It can be seen that the stress constraints have a small effect compare to the deflection constraints. The stress constraints are limited by less than 30% of its strength. Therefore, the design seems to be controlled by the mid-span deflection. Investigation of the glue-laminated sandwich depth results shows that the number of sandwich layers affects the beam depth, especially when the number of layers is less than 6. Generally, the glue-laminated beam has a higher depth than the single sandwich beam. The beam depth was normalized with the single sandwich beam depth, and it is based on the number of sandwich layers as shown in Figure 7.35. The difference in total depth of the glue laminated sandwich beam becomes small for cross sections with more than six layers. The glue-laminated beam has a normalized depth 20-30% higher than the single sandwich beam. Optimisation was stopped for up to 10 layers because the depth variation becomes small after that number of layers. A sample of the glue laminated beam cross section design with different layers is shown in Figure 7.36. It shows the differences between different cross sections design with respect to the sandwich layers number. Finally, the single sandwich beam is more economic and lighter than the glue-laminated GFRP sandwich beam, because the former has a lower cross section than the latter.

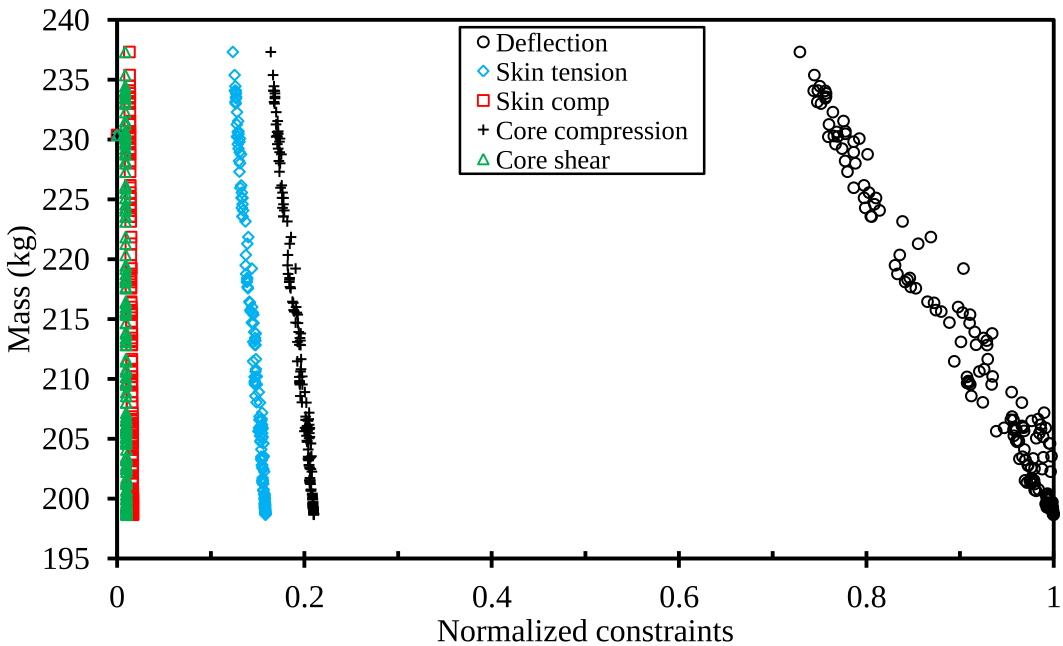

Figure 7.34 Design constraints of the glue laminated GFRP sandwich beam (4800 mm, 6-layers).

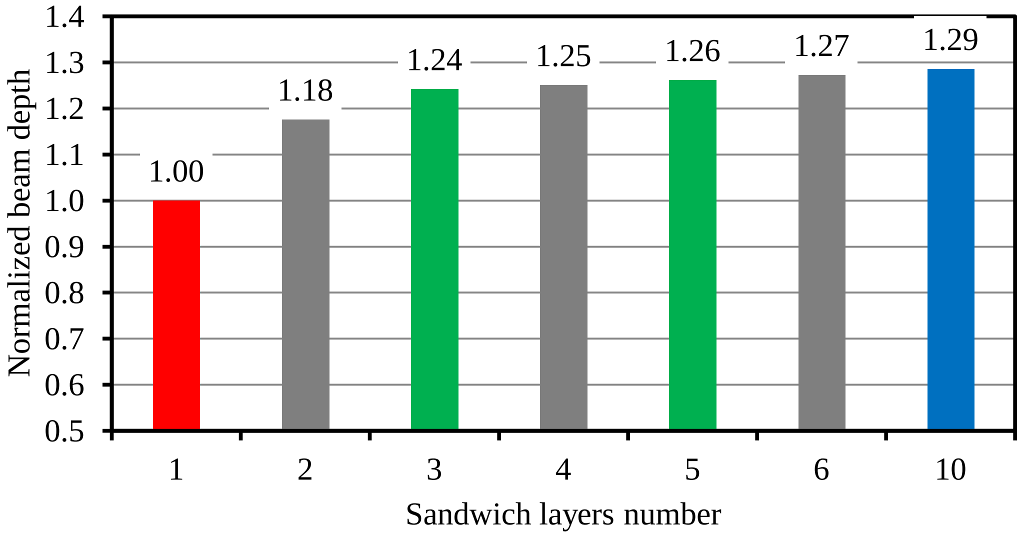

Figure 7.35 Effect of the number of sandwich layers on the optimum beam depth (4800 mm span, and 17.5 kN/m load).

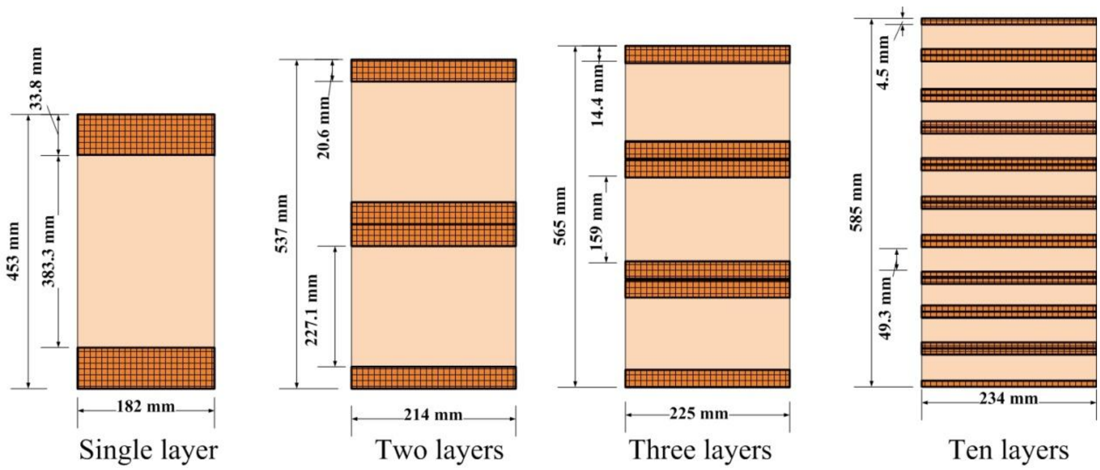

Figure 7.36 Optimum designs for the beam with 4800 mm span, and 17.5 kN/m applied load.

Sandwich beams with the different number of layers have been analysed using the FE, and the normalized stress is shown in Figure 7.37. The stress distribution is approximately same for one and two sandwich layers as shown in Figure 7.37(a). The effect of neutral GFRP skins in the even sandwich layers is small on the flexural strength. Increasing the number of sandwich layers has an impact on the stress distribution of the beam cross section. The glue laminated sandwich beam has a more homogeneous cross section stresses than the single sandwich beam as shown in Figure 7.37(b). Moreover, the glue-laminated beam has an intermediate GFRP reinforcement through the beam cross section.

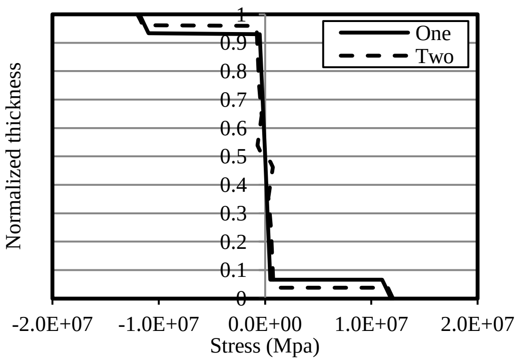

(a) Stress distribution in the one and two layers beam.

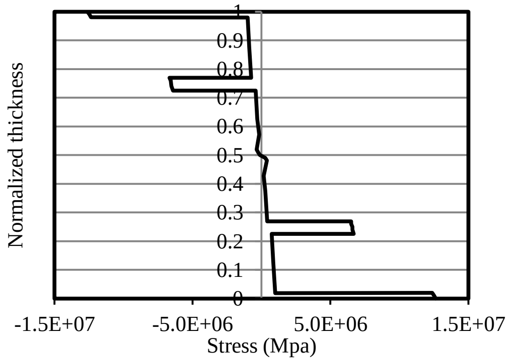

(b) Stress distribution in the 4-layers glue laminated beams.

Figure 7.37 Effect of GFRP sandwich layers on the beam section stress distribution.

In the design of beams, the applied external load and beam span can be converted into a moment. The applied moment represents the normalized value or the combination of the span and the load. All design optimisation findings are graphed against the applied moment as shown in Figure 7.38. The figure shows that the optimum beam depth has a non-linear behaviour with the applied moment. Furthermore, the glue laminated sandwich beams have a higher depth than the single sandwich beam. Trend lines are drawn for the single and two layers glue laminated GFRP sandwich beams as shown in Figure 7.38.

However, producing a single sandwich beam with a big cross section might be limited due to factory capacity. Therefore, the glue-laminated GFRP sandwich beam may be an option to fabricate a beam with a cross section greater than a single sandwich layer beam. The number of sandwich layers depends on the thickness of the single sandwich panel used to fabricate the glue-laminated beam. The design optimisation shows the relation between the beam depth and the applied moment as shown in Figure 7.38. The required glue-laminated beam depth can be found based on the applied moment. Then, the single sandwich layer can be found by the number of sandwich layers. In addition, the core and skin thicknesses for the single sandwich layer can be found by using the optimum core to skin thickness ratio of 11.0.

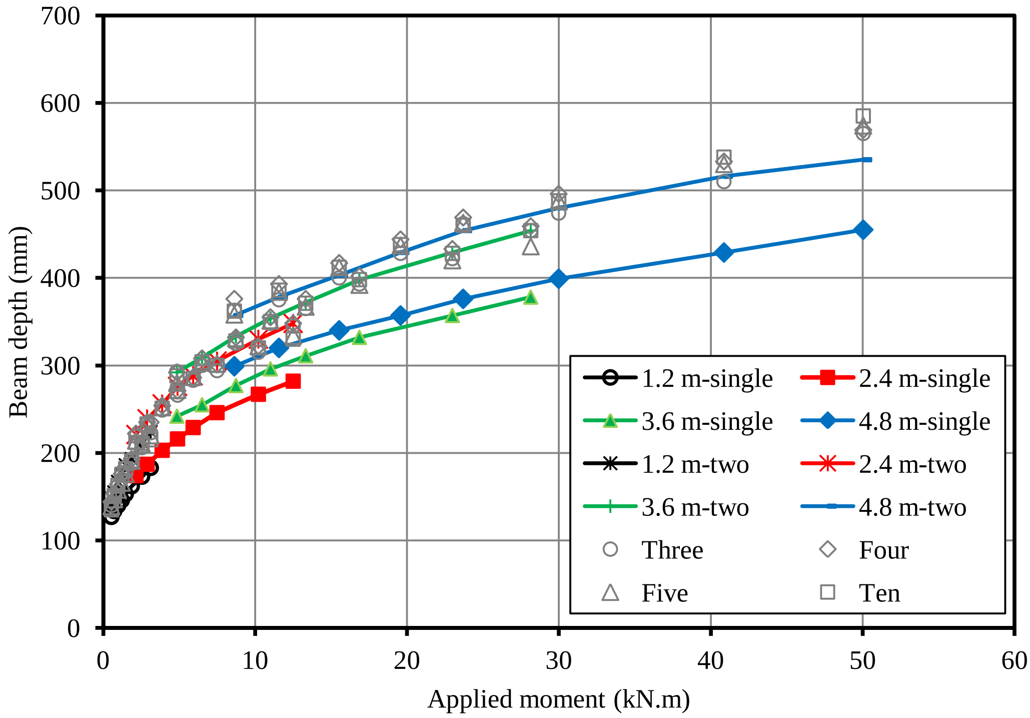

Figure 7.38 GFRP sandwich beam depth with applied moment.

7.7 Slab - beam design

The slab is usually connected to the beam, and the slab behaviour is affected by the beams behaviour. On the other hand, the design of the beam is based on the slab self-weight, and the external applied load on the slab. This chapter is discussed the design of individual slabs and beams under externally applied load conditions. The optimum design of the beams and slabs has focused on their length. Due to thesis limitations, a sample of the slab-beam structure with dimensions 4800 mm x 4800 mm was conducted in this study. The slab-beam model can be generated in different structural configurations based on its dimensions, applied loads, and geometry. Four models were generated for slab dimensions of 4800 mm x 4800 mm as shown in Figure 7.39.

Models were compared based on, cost, mass, deflection, loading capacity, and natural frequency. Although, the slabs and beams were designed under the same constraints, the slab - beam models showed different behaviours. The details of the analysis are shown in Appendix-D. The analysis showed that model-B gives the best behaviour among the one-way models. The one-way model-B and two-way model-D structures showed approximately similar analysis results. In addition, more investigation is required for the slab-beam model, including experimental work, numerical analysis, and design optimisation to have a complete idea about the design of slab-beam structure.

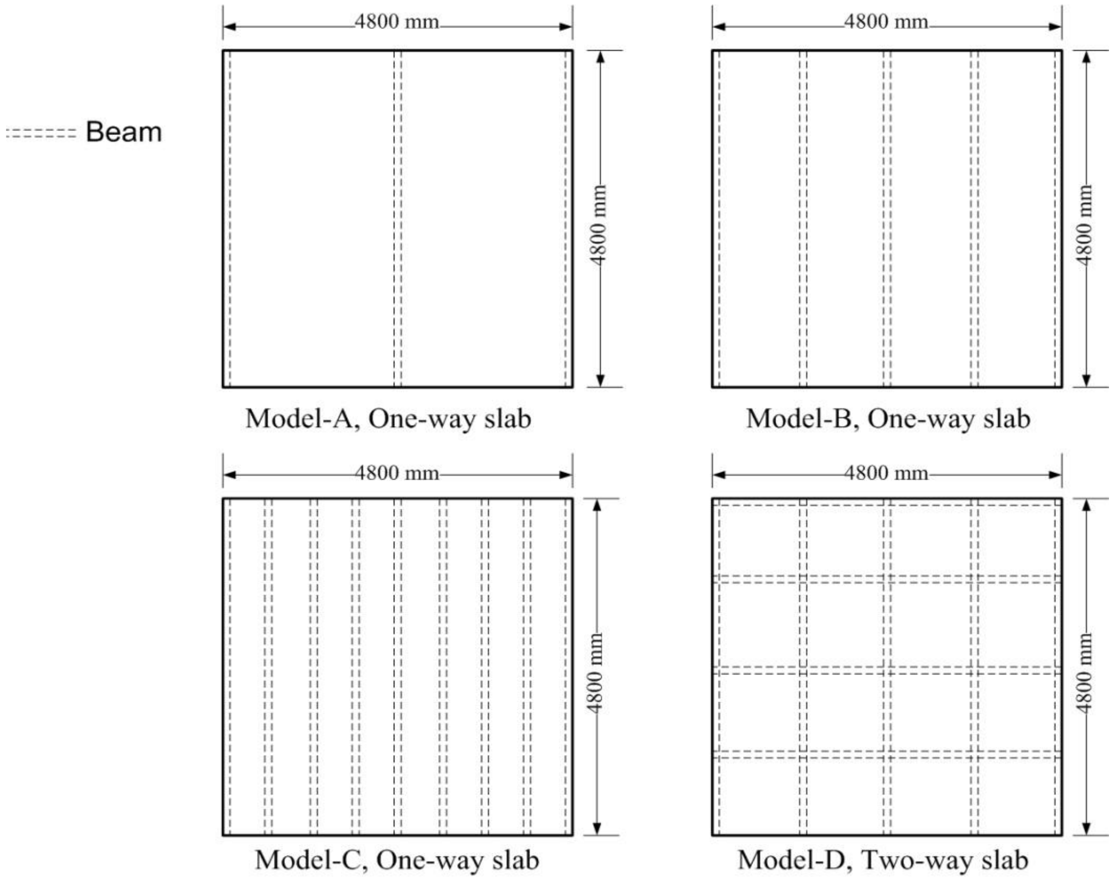

Figure 7.39 Slab-beam models.

7.8 Chapter conclusions

This chapter presents the results of multi-objective design of GFRP sandwich slabs and beams by using numerical optimisation. The slabs were designed according to the available standards and specifications for civil engineering structures. Static load and free vibration were considered using numerical multi-objective design optimisation. It was shown that the serviceability limit is more critical, and the design is controlled by mid-span deflection limits. In addition, the one-way slab and two-way slab showed approximately same results for the width to length (L_y/L_x) greater than 1.5. Optimum skin fibre orientation is $0^o/90^o$ for one-way slabs. The optimum orientation for the two-way slab depends on the width to length (L_y/L_x) and it is equal to 45^o for the square slab. Two-way slabs are lighter and more economic than the one-way slabs. The average core to skin thickness of one-way and two-way slabs multi-objective designs is 10.8 and 11.5 respectively.

The static slab design is satisfied with the human activities frequency inside buildings when the free vibration values are less than 17 Hz. However, the frequency should be considered in the slab when it is subjected to a frequency higher than the human activities rang (17 Hz) and when the one-way slab span is greater than 2400 mm. Furthermore, the static design of slab satisfies the upper limit of the ISO free vibration (80 Hz) when the span of the slab is less than 1000 mm. The GFRP slab design has a non-linear behaviour with the span variation when it is based on the frequency constraints.

Multi-objective optimisation of the beam design shows a core to skin mass ratio equal to 3.68 for the single sandwich beam cross section optimisation. In addition, it shows that the optimum core to skin thickness ratio is equal to 11.0. The optimum design indicates that both skin and core thicknesses increase with the increasing of beam span length. The depth of the glue laminated beam increases with the applied load. The single sandwich beam requires less depth than the glue-laminated beam with the same span and load. However, the effect of the number of sandwich layers on the beam depth becomes very low when the beam has more than 6-layers. A sample was given for the slab-beam model, and the results emphasise that more investigation is required on the design of slab-beam model. Finally, the multi-objective optimisation results can be used for design purposes of the GFRP sandwich slabs and beams in the specified loads and spans.

Chapter 8

Summary and conclusions

8.1 Summary

Applications of FRP composite materials in civil engineering and naval structures are growing more than ever. The objective of this research was to study the behaviour of the structures made from a novel GFRP sandwich panel, provide an acceptable FE numerical modelling, and establish an effective methodology to optimise the structural design. To achieve this target, an extensive review of the FRP structures design and optimisation methods used for designing FRP composite structures was conducted. Several beams and slabs specimens were tested under static load and free vibration excitation. An external UMAT subroutine was written and used for the FE simulation. The FE simulation included several samples of beams and slabs. The optimisation procedure considered that the optimisation method is capable of handling multiple conflicting objectives as shown in the literature. The design optimisation was conducted on both slabs and beams. The GFRP sandwich slab design considered different slab geometry and loads. The beam design considered single and glue GFRP sandwich beams.

This chapter presents summary and final conclusions for the overall thesis. The main conclusions are divided into three parts; behaviour of the GFRP sandwich structures, FEA of the GFRP sandwich structures, and design of GFRP sandwich structures. Recommendations are presented for the future work at the end of this chapter for the researchers who are interested in this field.

8.2 Main conclusions from this study

8.2.1 Behaviour of GFRP sandwich structures

This work investigated the behaviour of GFRP single and glue laminated GFRP sandwich beams. The experimental investigation was done under static four point bending test. Two geometry variables were studied and these are; span of the beam and number of cross section sandwich layers. Experimental investigations of the beams lead to the following conclusions:

- Shear span to depth ratio (a/d) is the main factor controlling the behaviour of GFRP sandwich beams under combined shear and moment forces. In addition, single sandwich beams showed higher shear and bending strength than glue laminated beams.
- Three different failure modes were observed in the experimental tests, core crushing, core shear and top skin failure. However, the GFRP sandwich beam did not show debonding as a failure mode because the skin-core interaction strength is close to the tensile and shear strengths of the core.
- The analytical equations proposed by other researchers for shear show an acceptable prediction for the specimens with an a/d less than 2 while prediction using the bending equation is better for beams with an a/d greater than 4.5.

The one-way and two-way GFRP sandwich slabs were tested with different dimensions, boundary conditions, and boundary restraint types under static load. The conclusions are as follows:

- The core to skin ratio and total slab thickness have a big effect on GFRP sandwich slab load capacity. In general, increasing the GFRP skin thickness from 1.8 mm to 3.0 mm enhances the slab load capacity to a double.
- The support system has an effect on slab behaviour. The two-way supported slab has an approximately double loading capacity compared to the one-way supported slab. The effect of screw restraints on behaviour is small. In addition, the square two-way slab with $\pm 45^o$ fibre orientation has a lower deformation than the $0^o/90^o$ orientation two-way square slab. Slab width to length (L_y/L_x) ratio affects the load carrying capacity of GFRP sandwich slab

supported on 4-sides. Slab carrying capacity decreases with the increase in L_y/L_x ratio.

- The mechanism of failure of one-way slabs is different from the failure mechanism of two-way slabs. One-way slabs failure is initiated due to core cracking and is followed by the bottom skin debonding. Two-way slabs showed a different failure mode based on skin fibre orientations and slab L_y/L_x ratio. The failure of the $0^o/90^o$ two-way slab fibre orientation is different from the $\pm45^o$ two-way slab skin orientation. The former showed a failure along the line parallel to the support and the latter showed a diagonal failure.
- Two-way square slabs showed a membrane action in the load-deflection behaviour. The slab was controlled by plate bending at initial stages of deformation and when the mid-span deflection is up to span/66. The one-way square slab did not show such behaviour.

Free vibration tests were conducted on one-way and two-way GFRP sandwich slabs with single and continuous spans. In addition, the effects of simple, screw and glue restraint types were investigated, and the conclusions are shown below:

- Two-way slabs have a higher frequency than one-way slabs. Slabs with $\pm45^o$ fibre orientation have a higher frequency than slabs with a $0^o/90^o$ fibre orientation in two-way support. However, the $\pm45^o$ fibre orientation has a lower frequency than the $0^o/90^o$ fibre orientation in one-way boundary conditions. Types of boundary restraint make a big contribution to increasing the natural frequency of the slab. Screw restrained slabs have a higher frequency than simple restrained slabs. Moreover, the glue restrained slabs have a larger frequency than the screw restrained slab.
- Continuous slabs have a higher frequency than single span slabs with the same slab size. However, they did not show any difference when the restraint is simple.

8.2.2 FE simulation and modelling of GFRP sandwich structures

The FEA model was developed and verified by experimental investigation as a requirement of the optimisation design methodology. The model was verified with the individual material and full sandwich beam and slab structures modelling. The conclusions of the FE simulation are summarised below:

- The CRUSHABLE FOAM model was used to simulate the modified phenolic core material. This model shows an acceptable prediction for the core behaviour in tension and compression.
- The 3D Hashin model was used for GFRP skin simulation. Using both the 3D Hashin model and CRUSHABLE FOAM model showed a relatively good prediction in the simulation compared to the experimental behaviour.
- Simulation of the GFRP sandwich beams shows that the FEA model can predict the behaviour of the beam with different a/d and failure modes. The same FEA model was used in the simulation of the GFRP sandwich slabs. The FEA model explains the stress distribution in the GFRP sandwich slabs, and the failure behaviour of the slabs. The FEA model also showed that the first drop in the slab load-deflection behaviour is due to the core cracking under point load.
- Most of the FEA cases showed that the core did not reach the hardening behaviour zone, especially when the structure failed by core shear or skin compression. However, the hardening part is important in the simulation of the core material behaviour when the structure exhibits core crushing failure.
- The 3D FEA model gave good results in the simulation of the free vibration of the GFRP sandwich structures. Finally, the FEA model is qualified to be used in the design optimisation of the GFRP sandwich beams and slabs.

8.2.3 Design optimisation of GFRP sandwich structures

The FEA model was linked to the optimisation method to find the optimum design of the GFRP sandwich slab. Multi-objective optimisation was conducted in the design by using the ARMOGA method. The design variables were load, dimension and boundary condition. Based on the design optimisation results the following conclusions were drawn:

- The design was controlled by the deflection constraint. However, increasing the safety factor of material strength might make the material strength constraints controlling the design.
- Multi-objective design optimisation showed the optimum core to skin thickness ratio is 10.8 and 11.5 for the one-way and two-way slabs respectively. In addition, it showed a core to skin ratio of 11.0 for single sandwich beams.
- The mass and cost multi-objective design for two-way and one-way slabs showed approximately the same results when the L_y/L_x ratio was higher than 1.5. The one-way slab had a higher designed depth than the two-way slab when the L_x/L_y ratio was less than 1.5.
- The static design satisfies the free vibration requirements for human activities up to a span length of 2400 mm. In addition, beyond this span, the free vibration had to be considered for the design requirement of GFRP sandwich slabs.
- The optimum single GFRP sandwich beam had a total depth less than the glue-laminated beam. In addition, the total depth of glue laminated beam increased with the increase in the number of sandwich layers.
- Different structures can be created using slabs and beams design optimisation results for the slab-beam model. These structures required an analysis for the cost, mass, deformation, failure load and natural frequency to select the optimum one.

8.3 Recommendations for future work

This study presents the results of an experimental investigation, FE simulation, and optimisation design information of GFRP sandwich structures. The following are some areas recommended for further study based on the findings and conclusions of this study:

- Although flexural investigation was done in the single sandwich beams and glue laminated sandwich beams, further investigations need to be considered for the behaviour under torsional loads. In addition, more investigation is required for the core crushing failure zone. The crushing zone part can be investigated using the relation between the loading value, area of the load and the skin thickness.

- The effect of distributed loads on the behaviour of GFRP sandwich slabs under the influence of geometry variations. Under distributed load, the maximum shear is located near the support and it might affect the failure behaviour of the GFRP sandwich beam.
- Experimental investigation of the combined slab-beam model behaviour can be done towards optimising the slab-beam model for different structural cases and external loading. The slab-beam model can be studied for building and bridge applications.
- An optimisation methodology can be developed to select the materials of the core and skins based on few variations in the materials design. For example, the relation between density and mechanical properties of modified phenolic core material can be studied. In addition, the design optimisation finding might be validated with the experimental investigation towards increasing the confidence of the design process.
- The impact and cyclic loading is another aspect that might affect the design of the GFRP sandwich structures. The failure mode and loading of GFRP sandwich beams and slabs can be studied under impact load condition. It is also important to investigate cyclic loading. These aspects need more attention in the next stage of research.

References

AASHTO 2008, *Guide Specifications for Design* of *PEDESTRIAN BRIDGES*, Washington.

Abachizadeh, M & Tahani, M 2009, 'An ant colony optimization approach to multi-objective optimal design of symmetric hybrid laminates for maximum fundamental frequency and minimum cost', *Structural and Multidisciplinary Optimization*, vol. 37, no. 4, pp. 367-76.

ABAQUS 2008, *Standard User's Manual*, ver 6.8-1, Hibbitt, Karlsson & Sorensen Inc.

Abro, A, Uddin, N & Vaidya, U 2007, *Design and Analysis of Thermoplastic Composite Bridge Superstructures*, University Transportation Center for Alabama, Birmingham.

Aguilar Madeira, JF, Rodrigues, H & Pina, H 2005, 'Multi-objective optimization of structures topology by genetic algorithms', *Advances in Engineering Software*, vol. 36, no. 1, pp. 21-8.

Allen, HG 1969, *Analysis and Design of Structural Sandwich Panels*, Pergamon Press Oxeford, England.

Almeida, FS & Awruch, AM 2009, 'Design optimization of composite laminated structures using genetic algorithms and finite element analysis', *Composite Structures*, vol. 88, no. 3, pp. 443-54.

Alrefaei, MH & Diabat, AH 2009, 'A simulated annealing technique for multi-objective simulation optimization', *Applied Mathematics and Computation*, vol. 215, no. 8, pp. 3029-35.

Altenbach, H 1998, 'Theories for laminated and sandwich plates', *Mechanics of Composite Materials*, vol. 34, no. 3, pp. 243-52.

António, CC & Hoffbauer, LN 2009, 'An approach for reliability-based robust design optimisation of angle-ply composites', *Composite Structures*, vol. 90, no. 1, pp. 53-9.

Araújo, A, Martins, P, Mota Soares, C, Mota Soares, C & Herskovits, J 2009, 'Damping optimization of viscoelastic laminated sandwich composite structures', *Structural and Multidisciplinary Optimization*, vol. 39, no. 6, pp. 569-79.

Aravinthan, T 2008, 'R&D on Engineering Fibre Composite- Past, Present and Future', in T Aravinthan (ed.), *Fibre Composites in Civil Infrastructure Past, Present and Future*, Toowoomba.

Aravinthan, T 2009, 'Innovative fibre composite girder for replacement of hardwood timber girder', paper presented to 7th Austroads Bridge Conference, Auckland, New Zealand.

ASCE 1984, *Structural Plastics Design Manual*, American Society of Civil Engineers, New York.

Ashby, M 2000, 'Multi-objective optimization in material design and selection', *Acta materialia*, vol. 48, no. 1, pp. 359-70.

ASTM-Standard 2006, ASTM D7250 / D7250M - 06 Standard Practice for Determining Sandwich Beam Flexural and Shear Stiffness, ASTM International, West Conshohocken, PA.

ASTM 2008, Standard D3737 - Standard Practice for Establishing Allowable Properties for Structural Glued Laminated Timber (Glulam), ASTM International, West Conshohocken, PA.

Atabay, S 2009, 'Cost optimization of three-dimensional beamless reinforced concrete shear-wall systems via genetic algorithm', *Expert Systems With Applications*, vol. 36, no. 2, Part 2, pp. 3555-61.

Australia, S 2002, Structural Design Actions, AS/NZS 1170.1:2002, Australian/New Zealand Standard.

Avila, S, Lisboa, A, Krahenbuhl, L, Carpes Jr, W, Vasconcelos, J, Saldanha, R & Takahashi, R 2006, 'Sensitivity analysis applied to decision making in multiobjective evolutionary optimization', *IEEE Transactions on Magnetics*, vol. 42, no. 4, pp. 1103-6.

Ayhan, Ö 2009, 'The effects of pilot hole, screw types and layer thickness on the withdrawal strength of screws in laminated veneer lumber', *Materials & Design*, vol. 30, no. 7, pp. 2355-8.

Bachmann, H 1995, *Vibration Problems in Structures: Practical Guidelines*, Birkhäuser.

Bank, L 2006, *Composite for Construction: Structural Design with FRP Material*, JOHN WILEY & SONS, New Jersey.

Belytschko, T & Black, T 1999, 'Elastic crack growth in finite elements with minimal remeshing', *International Journal for Numerical Methods in Engineering*, vol. 45, no. 5, pp. 601-20.

Berthelot, J-M & Sefrani, Y 2007, 'Longitudinal and transverse damping of unidirectional fibre composites', *Composite Structures*, vol. 79, no. 3, pp. 423-31.

Bhavikatti, SS 2003, *Structural Optimization Using Sequential Linear Programing*, VIKAS PUBLISHING HOUSE PVT LTD, New Delhi.

Bosia, F, Gmür, T & Botsis, J 2002, 'Deformation characteristics of composite laminates-part II: an experimental/numerical study on equivalent single-layer theories', *Composites Science and Technology*, vol. 62, no. 1, pp. 55-66.

Branke, J, Deb, K, Miettinen, K & S owi ski, R 2008, 'Multiobjective optimization: Interactive and evolutionary approaches', *Lecture Notes In Computer Science; Vol. 5252*.

Bui, L & Alam, S 2008, *Multi-Objective Optimization in Computational Intelligence: Theory and Practice*, IGI Publishing Hershey, PA, USA.

Burns, S 2002, *Recent Advances in Optimal Structural Design*, American Society of Civil Engineers(ASCE), New York.

Cardoso, B, Sousa, LG, Castro, JA & Valido, AJ 2002, 'Optimal design of laminated composite beam structures', *Structural and Multidisciplinary Optimization*, vol. 24, no. 3, pp. 205-11.

Chen, C, Harte, A & Fleck, N 2001, 'The plastic collapse of sandwich beams with a metallic foam core', *International Journal of Mechanical Sciences*, vol. 43, no. 6, pp. 1483-50.,

Cheng, J 2010, 'Optimum design of steel truss arch bridges using a hybrid genetic algorithm', *Journal of Constructional Steel Research*, vol. 66, no. 8-9, pp. 1011-7.

Cheng, L & Karbhari, VM 2006, 'New bridge systems using FRP composites and concrete: a state of the art review', *Progress in Structural Engineering and Materials*, vol. 8, no. 4, pp. 143-54.

Chiandussi, G, Fontana, R & Urbinati, F 1998, 'Design sensitivity analysis method for multidisciplinary shape optimisation problems with linear and non-linear responses', *Engineering Computations*, vol. 15, no. 2, pp. 391-417.

Choi, J, Lee, W, Park, J & Youn, B 2008, 'A study on robust design optimization of layered plate bonding process considering uncertainties', *Structural and Multidisciplinary Optimization*, vol. 35, no. 6, pp. 531-40.

Clarke, JL (ed.) 1996, *Structural Design of Polymer Composite- EUROCOMP Design Code and Handbook*, E&FN Spon, UK.

Correia, VMF, Soares, CMM & Soares, CAM 1997, 'Design sensitivity analysis and optimal design of composite structures using higher order discrete models', *Engineering Optimization*, vol. 29, no. 1, pp. 85 - 111.

Crews, K, Samali, B, Li, J, Bakoss, S & Champion, C 2004, 'Testing and assessment procedures to facilitate the management of timber bridge assets', paper presented to 3rd CECAR - Civil Engineering Conference in the Asian Region, Seoul – Korea.

Cripps, A 2002, *Fibre-Reinforced Polymer Composites in Construction*, CIRIA, London.

Cunningham, PR, White, RG & Aglietti, GS 2000, 'The effects of various design parameters on the free vibration of doubly curved composite sandwich panels', *Journal of Sound and Vibration*, vol. 230, no. 3, pp. 617-48.

Daly, A & Duckett, W 2002, 'The design and testing of an FRP composite highway deck', *TRL Journal of Research*, vol. 5, no. 3, p. 501.

Dawood, M, Taylor, E & Rizkalla, S 2010, 'Two-way bending behavior of 3-D GFRP sandwich panels with through-thickness fiber insertions', *Composite Structures*, vol. 92, no. 4, pp. 950-63.

Deshpande, V & Fleck, N 2000, 'Isotropic constitutive models for metallic foams', *Journal of the Mechanics and Physics of Solids*, vol. 48, no. 6-7, pp. 1253-83.

Dolan, J, Murray, T, Johnson, J, Runte, D & Shue, B 1999, 'Preventing annoying wood floor vibrations', *Journal of Structural Engineering*, vol. 125, p. 19.

Doltsinis, I, Kang, Z & Cheng, G 2005, 'Robust design of non-linear structures using optimization methods', *Computer Methods in Applied Mechanics and Engineering*, vol. 194, no. 12-16, pp. 1779-95.

Donadon, M, de Almeida, S, Arbelo, M & de Faria, A 2009, 'A three-dimensional ply failure model for composite structures', *International Journal of Aerospace Engineering*, vol. 2009, pp. 1-22.

Ebrahimpour, A & Sack, RL 2005, 'A review of vibration serviceability criteria for floor structures', *Computers & Structures*, vol. 83, no. 28-30, pp. 2488-94.

Erdal, O & Sonmez, FO 2005, 'Optimum design of composite laminates for maximum buckling load capacity using simulated annealing', *Composite Structures*, vol. 71, no. 1, pp. 45-52.

Ertas, AH & Sonmez, FO 2010, 'Design of fiber reinforced laminates for maximum fatigue life', *Procedia Engineering*, vol. 2, no. 1, pp. 251-6.

ETESCO 2009, *modeFRONTIER User's Manual*, vol. Version 4.1.1.

Falzon, BG & Faggiani, A 2012, 'The use of a genetic algorithm to improve the postbuckling strength of stiffened composite panels susceptible to secondary instabilities', *Composite Structures*, vol. 94, no. 3, pp. 883-95.

Fam, A & Son, J-K 2008, 'Finite element modeling of hollow and concrete-filled fiber composite tubes in flexure: Optimization of partial filling and a design method for poles', *Engineering Structures*, vol. 30, no. 10, pp. 2667-76.

Farkas, J & Jarmari, K 1998, 'Minimum material cost design of five-layer sandwich beams', *Structural Optimization*, vol. 15, pp. 215-20.

Farshi, B & Herasati, S 2006, 'Optimum weight design of fiber composite plates in flexure based on a two level strategy', *Composite Structures*, vol. 73, no. 4, pp. 495-504.

Farshi, B & Rabiei, R 2007, 'Optimum design of composite laminates for frequency constraints', *Composite Structures*, vol. 81, no. 4, pp. 587-97.

Freas, ADY & Selbo, ML 1954, *Fabrication and Design of Glued Laminated Wood Structural Members*, Washington : US Dept. of Agriculture.

Frederick, T, Wallenberger, Watson, JC & Li, H 2001, 'Glass Fibers', in DB Miracle & SL Donaldson (eds), *ASM Handbook: Composite*, vol. 21.

Froud, G 1980, 'Your sandwich order, sir (mechanical properties in bending of sandwich structures)', *Composites*, vol. 11, pp. 133-8.

Gan, LH, Ye, L & Mai, Y-W 1999, 'Design and evaluation of various section profiles for pultruded deck panels', *Composite Structures*, vol. 47, no. 1-4, pp. 719-25.

Gay, D, Hoa, S & Tsai, S 2003, *Composite Materials: Design and Applications*, CRC Pr I Llc, Florida.

Ghiasi, H, Pasini, D & Lessard, L 2009, 'Optimum stacking sequence design of composite materials Part I: Constant stiffness design', *Composite Structures*, vol. 90, no. 1, pp. 1-11.

Ghiasi, H, Fayazbakhsh, K, Pasini, D & Lessard, L 2010, 'Optimum stacking sequence design of composite materials Part II: Variable stiffness design', *Composite Structures*, vol. 93, no. 1, pp. 1-13.

Gibson, L 1984, 'Optimization of stiffness in sandwich beams with rigid foam cores', *Materials Science and Engineering*, vol. 67, no. 2, pp. 125-35.

Gibson, LJ & Ashby, MF 1999, *Cellular Solids: Structure and Properties*, Cambridge Univ Pr., Cambridge.

Gillet, A, Francescato, P & Saffre, P 2010, 'Single-and multi-objective optimization of composite structures: The influence of design variables', *Journal of Composite Materials*, vol. 44, no. 4, p. 457.

Granet, I 1973, *Strength of Materials for Engineering Technology*, Reston Pub. Co., Virginia.

Hadcock, RN 1982, 'Design and Analysis of Advanced Composite Structures', in G Lubin (ed.), *Handbook of Composites*, VAN NOSTRAND REINHOLD, New York.

Han, S, Benaroya, H & Wei, T 1999, 'Dynamics of transversely vibrating beams using four engineering theories', *Journal of Sound and Vibration*, vol. 225, no. 5, pp. 935-88.

Hasançebi, O, Çarba , S & Saka, M 2010, 'Improving the performance of simulated annealing in structural optimization', *Structural and Multidisciplinary Optimization*, vol. 41, no. 2, pp. 189-203.

Hashin, Z 1980, 'Failure criteria for unidirectional fiber composites', *Journal of Applied Mechanics*, vol. 47, no. 2, pp. 329-34.

Hashin, Z & Rotem, A 1973, 'A fatigue failure criterion for fibre reinforced materials', *Journal of Composite Materials*, vol. 7, pp. 448-64.

Hassani, B & Hinton, E 1999, *Homogenization and Structural Topology Optimization: Theory, Practice, and Software*, Springer Verlag, Berlin.

Huang, Z-M 2007, 'Failure analysis of laminated structures by FEM based on nonlinear constitutive relationship', *Composite Structures*, vol. 77, no. 3, pp. 270-9.

He, Y & Aref, AJ 2003, 'An optimization design procedure for fiber reinforced polymer web-core sandwich bridge deck systems', *Composite Structures*, vol. 60, no. 2, pp. 183-95.

Hechler, O, Feldmann, M, Heinemeyer, C & Galanti, F 2008, *Design Guide For Floor Vibrations*, Graz, Austria.

Hollaway, LC & Head, PR 2001, *Advanced polymer composites and polymers in the civil infrastructure*, Elsevier Science, Netherlands.

Hollaway, LC & Head, PR 1999, 'Composite materials and structures in civil engineering', in CH Zweben & A Kelly (eds), *Comperhensive Composite Materials*, Elsevier, Oxford, vol. 6.

Hoo Fatt, MS & Pothula, SG 2010, 'Dynamic pulse buckling of composite shells subjected to external blast', *Composite Structures*, vol. 92, no. 7, pp. 1716-27.

Hudson, CW, Carruthers, JJ & Robinson, AM 2010, 'Multiple objective optimisation of composite sandwich structures for rail vehicle floor panels', *Composite Structures*, vol. 92, no. 9, pp. 2077-82.

Hunaidi, O 2000, 'Traffic vibrations in buildings', *Construction Technology Update*, vol. 39, pp. 1-6.

Islam, MM & Aravinthan, T 2010, 'Behaviour of structural fibre composite sandwich panels under point load and uniformly distributed load', *Composite Structures*, vol. 93, no. 1, pp. 206-15.

ISO:10137 2007, Bases for Design of Structures - Serviceability of Buildings and Walkways Against Vibrations, ISO, Switzerland.

Issa, CA & Kmeid, Z 2005, 'Advanced wood engineering: glulam beams', *Construction and Building Materials*, vol. 19, no. 2, pp. 99-106.

Iyer, SL & Sen, R (eds) 1991, *Advance Composite Materials in Civil Engineering Structures*, American Society of Civil Engineering, New York.

Jeong, J, Lee, Y-H, Park, K-T & Hwang, Y-K 2007, 'Field and laboratory performance of a rectangular shaped glass fiber reinforced polymer deck', *Composite Structures*, vol. 81, no. 4, pp. 622-8.

Jiang, X, Kolstein, H & Bijlaard, FSK 2012, 'Moisture diffusion and hygrothermal aging in pultruded fibre reinforced polymer composites of bridge decks', *Materials & Design*, vol. 37, no. 1, pp. 304-12.

Johannes, M, Jakobsen, J, Thomsen, OT & Bozhevolnaya, E 2009, 'Examination of the failure of sandwich beams with core junctions subjected to in-plane tensile loading', *Composites Science and Technology*, vol. 69, no. 9, pp. 1447-57.

Kalantari, M, Nami, MR & Kadivar, MH 2010, 'Optimization of composite sandwich panel against impact using genetic algorithm', *International Journal of Impact Engineering*, vol. 37, no. 6, pp. 599-604.

Karakuzu, R, ÇalIskan, CR, Aktas, M & Içten, BM 2008, 'Failure behavior of laminated composite plates with two serial pin-loaded holes', *Composite Structures*, vol. 82, no. 2, pp. 225-34.

Karbhari, VM 2000, 'Determination of materials design values for the use of fibre-reinforced polymer composites in civil infrastructure', *Proceedings of the Institution of Mechanical Engineers, Part L: Journal of Materials Design and Applications*, vol. 214, no. 3, pp. 163-71.

Kathiravan, R & Ganguli, R 2007, 'Strength design of composite beam using gradient and particle swarm optimization', *Composite Structures*, vol. 81, no. 4, pp. 471-9.

Kaw, AK 1997, *Mechanics of Composite Materials*, CRC Press, New York.

Keller, T, de Castro, J & Schollmayer, M 2004, 'Development of adhesively bonded GFRP sandwich girders', *Journal of Composites for Construction*, vol. 8, no. 5, pp. 461-70,

Keller, T, Bai, Y & Vallée, T 2007, 'Long-term performance of a glass fiber-reinforced polymer truss bridge', *Journal of Composites for Construction*, vol. 11, pp. 99-108.

Kemp, M 2008, 'use of pultruded sections in civil infrastructure', paper presented to 20th Australasian Conference on the Mechanics of Structures of Materials (ACMSM20), Toowoomba.

Kim, H-Y, Lee, Y-H & Lee, S-Y 2011, 'Ultimate strength of a GFRP deck panel for temporary structures', *Composite Structures*, vol. 93, no. 2, pp. 528-37.

Kim, H-Y, Hwang, Y-K, Park, K-T, Lee, Y-H & Kim, S-M 2005, 'Fiber reinforced plastic deck profile for I-girder bridges', *Composite Structures*, vol. 67, no. 4, pp. 411-6.

Kim, H-Y, Park, K-T, Jeong, J, Lee, Y-H, Hwang, Y-K & Kim, D 2009, 'A pultruded GFRP deck panel for temporary structures', *Composite Structures*, vol. 91, no. 1, pp. 20-30.

Knight Jr, N 2006, *User-defined material model for progressive failure analysis*, NASA/CR-214526.

Knippers, J & Gabler, M 2006, 'New design concepts for advanced composite bridges the Friedberg bridge in Germany', paper presented to Proceedings of the IABSE Conference 2006, Budapest.

Klinkel, S, Gruttmann, F & Wagner, W 1999, 'A continuum based 3D-shell element for laminated structures', *Computers & Structures*, vol. 71, no. 1, pp. 43-62.

Knox, CE 1982, 'Fiberglass Reinforcement', in G Lubin (ed.), *Handbooks of Composites*, VAN NOSTRAND REINHOLD, New York, pp. 136-59.

Kollár, L & Springer, G 2003, *Mechanics of composite structures*, Cambridge Univ Pr., Cambridge.

Konsta-Gdoutos, M & Gdoutos, E 2005, 'The Effect of Load and Geometry on the Failure Modes of Sandwich Beams', *Applied Composite Materials*, vol. 12, no. 3, pp. 165-76.

Kovács, G, Groenwold, AA, Jármai, K & Farkas, J 2004, 'Analysis and optimum design of fibre-reinforced composite Structure', *Structural and Multidisciplinary Optimization*, vol. 28, no. 2-3, pp. 170-9.

Kumar, P, Chandrashekhara, K & Nanni, A 2004, 'Structural performance of a FRP bridge deck', *Construction and Building Materials*, vol. 18, no. 1, pp. 35-47.

Kutz, M (ed.) 2006, *Mechanical Engineers' Handbook: Materials and Mechanical Design*, Third edn, JOHN WILEY & SONS, INC, New Jersey.

Lavoie, JA 1997, 'Scaling effects on damage development, strength and stress-rupture life of laminated composite in tension', PhD thesis: Virginia Polytechnics Institute and State University.

Lee, C, Kam, T & Sun, S 2007, 'Free-vibration analysis and material constants identification of laminated composite sandwich plates', *Journal of Engineering Mechanics*, vol. 133, no. 8, pp. 874-886.

Lee, DS, Morillo, C, Bugeda, G, Oller, S & Onate, E 2012, 'Multilayered composite structure design optimisation using distributed/parallel multi-objective evolutionary algorithms', *Composite Structures*, vol. 94, no. 3, pp. 1087-96,

Lesko, JJ & Cousins, TE 2003, *EXTREN DWB Design Guide*, Strongwell Corporation, Bristol.

Li, M, Azarm, S & Aute, V 2005, *A Multi-Objective Genetic Algorithm for Robust Design Optimization*, ACM, Washington DC, USA.

Li, QM, Mines, RAW & Birch, RS 2000, 'The crush behaviour of Rohacell-51WF structural foam', *International Journal of Solids and Structures*, vol. 37, no. 43, pp. 6321-41.

Li, X, Li, G, Wang, CH & You, M 2011, 'Optimum design of composite sandwich structures subjected to combined torsion and bending loads', *Applied Composite Materials*, DOI: 10.1007/s10443-011-9204-0.

Lim, C-H, Jeon, I & Kang, K-J 2009, 'A new type of sandwich panel with periodic cellular metal cores and its mechanical performances', *Materials & Design*, vol. 30, no. 8, pp. 3082-93.

Linde, P, Pleitner, J, de Boer, H & Carmone, C 2004, 'Modelling and simulation of fiber metal laminates', paper presented to ABAQUS Users' Conference, Boston.

Lindgaard, E & Lund, E 2010, 'Nonlinear buckling optimization of composite structures', *Computer Methods in Applied Mechanics and Engineering*, vol. 199, no. 37-40, pp. 2319-30.

Liu, PF & Zheng, JY 2010, 'Recent developments on damage modeling and finite element analysis for composite laminates: A review', *Materials & Design*, vol. 31, no. 8, pp. 3825-34.

Lopez-Anido, R & Xu, H 2002, 'Structural characterization of hybrid fiber-reinforced polymer-glulam panels for bridge decks', *Journal of Composites for Construction*, vol. 6, no. 3, pp. 194-203.

Lorenzis, LD, Scialpi, V & Tegola, AL 2005, 'Analytical and experimental study on bonded-in CFRP bars in glulam timber', *Composites Part B: Engineering*, vol. 36, no. 4, pp. 279-89.

Loughlan, J & Ahmed, MN 2008, 'Multi-cell carbon fibre composite box beams subjected to torsion with variable twist', *Thin-Walled Structures*, vol. 46, no. 7-9, pp. 914-24.

Luke, S, Canning, L, Collins, S, Knudsen, E, Brown, P, Taljsten, B & Olofsson, I 2002, 'Advanced composite bridge decking system project ASSET', *Structural Engineering International*, vol. 12, no. 2, pp. 76-9.

Lund, E 2009, 'Buckling topology optimization of laminated multi-material composite shell structures', *Composite Structures*, vol. 91, no. 2, pp. 158-67.

Maimí, P, Camanho, PP, Mayugo, JA & Dávila, CG 2007, 'A continuum damage model for composite laminates: Part I - Constitutive model', *Mechanics of Materials*, vol. 39, no. 10, pp. 897-908.

Manalo, AC 2011, 'Behaviour of fibre composite sandwich structures: a case study on railway sleeper application', PhD thesis, University of Southern Queensland.

Manalo, A, Aravinthan, T, Karunasena, W & Ticoalu, A 2010a, 'A review of alternative materials for replacing existing timber sleepers', *Composite Structures*, vol. 92, no. 3, pp. 603-11.

Manalo, AC, Aravinthan, T & Karunasena, W 2010b, 'Flexural behaviour of glue-laminated fibre composite sandwich beams', *Composite Structures*, vol. 92, no. 11, pp. 2703-11.

Manalo, A, Aravinthan, T & Karunasena, W 2010c, 'In-plane shear behaviour of fibre composite sandwich beams using asymmetrical beam shear test', *Construction and Building Materials*, vol. 24, no. 10, pp. 1952-60.

Manalo, AC, Aravinthan, T, Karunasena, W & Islam, MM 2010d, 'Flexural behaviour of structural fibre composite sandwich beams in flatwise and edgewise positions', *Composite Structures*, vol. 92, no. 4, pp. 984-95.

Matthews, F 2000, *Finite Element Modelling of Composite Materials and Structures*, CRC, Florida.

Matthews, F & Camanho, P 1999, 'A progressive damage model for mechanically fastened joints in composite laminates', *Journal of Composite Materials(USA)*, vol. 33, no. 24, pp. 2248-80.

Meidell, A 2009, 'Minimum weight design of sandwich beams with honeycomb core of arbitrary density', *Composites Part B: Engineering*, vol. 40, no. 4, pp. 284-91.

Messac, A & Ismail-Yahaya, A 2002, 'Multiobjective robust design using physical programming', *Structural and Multidisciplinary Optimization*, vol. 23, no. 5, pp. 357-71.

Mines, R & Alias, A 2002, 'Numerical simulation of the progressive collapse of polymer composite sandwich beams under static loading', *Composites Part A: Applied Science and Manufacturing*, vol. 33, no. 1, pp. 11-26.

Miravete, A 1996, *Optimization of Design of Composite Structures*, WooDHEAD PUBLISHING LIMITED, Cambridge.

Mohan, K, Hon, YT, Idapalapati, S & Seow, HP 2005, 'Failure of sandwich beams consisting of alumina face sheet and aluminum foam core in bending', *Materials Science and Engineering: A*, vol. 409, no. 1-2, pp. 292-301.

Moreira, RAS & Rodrigues, JD 2010, 'Static and dynamic analysis of soft core sandwich panels with through-thickness deformation', *Composite Structures*, vol. 92, no. 2, pp. 201-15.

Mota Soares, CM, Marques Cordeiro, NM & Barbosa, JI 1995, 'A discrete model for the design sensitivity analysis of multi-layered composite shells of revolution', *Composites Engineering*, vol. 5, no. 5, pp. 533-50.

Muc, A & Muc-Wierzgoń, M 2012, 'An evolution strategy in structural optimization problems for plates and shells', *Composite Structures*, vol. 94, no. 4, pp. 1461-70.

Murphy, J 1997, 'Transverse vibration of a simply supported beam with symmetric overhang of arbitrary length', *Journal of Testing and Evaluation*, vol. 25, pp. 522-4.

Murray, T, Allen, D & Ungar, E 1997, ' *AISC/CISC Steel Design Guide Series No. 11: Floor vibrations Due To Human Activity*, American Institute of Steel Construction, Chicago.

Murthy, O, Munirudrappa, N, Srikanth, L & Rao, R 2006, 'Strength and stiffness optimization studies on honeycomb core sandwich panels', *Journal of Reinforced Plastics and Composites*, vol. 25, no. 6, p. 663.

Naeim, F & California, SCo 1991, *Design Practice to Prevent Floor Vibrations*, Steel Committee of California.

Namura, A, Yukihiro, K & Seiichi, M 2005, 'Study on the optimum size of railway sleeper for ballasted truck', *Structural Eningineering. Earthquake Engineering, JSCE*, vol. 22, no. 2, pp. 245S-55S.

Narayana Naik, G, Omkar, S, Mudigere, D & Gopalakrishnan, S 2011, 'Nature inspired optimization techniques for the design optimization of laminated composite structures using failure criteria', *Expert Systems With Applications*, vol. 38, no. 3, pp. 2489-99.

Nayomon, U & Nobuhiko, K 2003, 'Design, fabrication and erection of the pedistrian bridge in the road-park of Ikei-Tairagawa', *IHI Engineering Reveiw*, vol. 36, no. 2, pp. 35-39.

Neely, WD, Cousins, TE & Lesko, JJ 2004, 'Evaluation of in-service performance of tom's creek bridge fiber reinforced polymer superstructure', *Journal of Performance of Constructed Facilities*, vol. 18, no. 3, pp. 147-58.

Nguyen, T, Song, J & Paulino, G 2010, 'Single-loop system reliability-based design optimization using matrix-based system reliability method: theory and applications', *Journal of Mechanical Design*, vol. 132, pp. 011005:1-11.

O'Connor, JS 2008, 'GRP bridge decks and superstructures in the USA', *Reinforced Plastics*, vol. 52, no. 6, pp. 26-31.

Ochoa, O & Reddy, J 1992, *Finite Element Analysis of Composite Laminates*, Springer, Ontario.

Omkar, SN, Khandelwal, R, Ananth, TVS, Narayana Naik, G & Gopalakrishnan, S 2009, 'Quantum behaved Particle Swarm Optimization (QPSO) for multi-objective design optimization of composite structures', *Expert Systems With Applications*, vol. 36, no. 8, pp. 11312-22.

Omkar, SN, Senthilnath, J, Khandelwal, R, Narayana Naik, G & Gopalakrishnan, S 2011, 'Artificial Bee Colony (ABC) for multi-objective design optimization of composite structures', *Applied Soft Computing*, vol. 11, no. 1, pp. 489-99.

Panigrahi, SK & Pradhan, B 2009, 'Through-the-width delamination damage propagation characteristics in single-lap laminated FRP composite joints', *International Journal of Adhesion and Adhesives*, vol. 29, no. 2, pp. 114-24.

Park, CH, Saouab, A, Bréard, J, Han, WS, Vautrin, A & Lee, WI 2009, 'An integrated optimisation for the weight, the structural performance and the cost of composite structures', *Composites Science and Technology*, vol. 69, no. 7-8, pp. 1101-7,

Parsopoulos, K & Vrahatis, M 2005, 'Unified particle swarm optimization for solving constrained engineering optimization problems', *Lecture Notes in Computer Science (LNCS)*, vol. 3612, Springer.

Perera, R & Vique, J 2009, 'Strut-and-tie modelling of reinforced concrete beams using genetic algorithms optimization', *Construction and Building Materials*, vol. 23, no. 8, pp. 2914-25.

Perera, R, Vique, J, Arteaga, A & Diego, AD 2009, 'Shear capacity of reinforced concrete members strengthened in shear with FRP by using strut-and-tie models and genetic algorithms', *Composites Part B: Engineering*, vol. 40, no. 8, pp. 714-26.

Petras, A & Sutcliffe, M 1999, 'Failure mode maps for honeycomb sandwich panels', *Composite Structures*, vol. 44, no. 4, pp. 237-52.

Prendes Gero, MB, García, AB & del Coz Díaz, JJ 2006, 'Design optimization of 3D steel structures: Genetic algorithms vs. classical techniques', *Journal of Constructional Steel Research*, vol. 62, no. 12, pp. 1303-9.

Procházka, P, Dolezel, V & Lok, T 2009, 'Optimal shape design for minimum Lagrangian', *Engineering Analysis with Boundary Elements*, vol. 33, no. 4, pp. 447-55.

Pyo, S & Lee, H 2009, 'Micromechanics-based elastic-damage analysis of laminated composite structures', *International Journal of Solids and Structures*, vol. 46, no. 17, pp. 3138-49.

Quinn, JA 1999, *Composites Design Manual*, CRC Press, Liverpool.

Rahami, H, Kaveh, A & Gholipour, Y 2008, 'Sizing, geometry and topology optimization of trusses via force method and genetic algorithm', *Engineering Structures*, vol. 30, no. 9, pp. 2360-9.

Rahul, Chakraborty, D & Dutta, A 2005, 'Optimization of FRP composites against impact induced failure using island model parallel genetic algorithm', *Composites Science and Technology*, vol. 65, no. 13, pp. 2003-13.

Rao, MA, Ratnam, CH, Srinivas, J & Premkumar, A 2002, 'Optimum design of multilayer composite plates using simulated annealing', *Proceedings of the Institution of Mechanical Engineers, Part L: Journal of Materials: Design and Applications*, vol. 216, pp. 193-7.

Rao, S 2009, *Engineering Optimization: Theory and Practice*, Wiley & Sons, New Jersey.

Reddy, J 2004, *Mechanics of Laminated Composite Plates and Shells: Theory and Analysis*, CRC, London.

Rizzi, E, Papa, E & Corigliano, A 2000, 'Mechanical behavior of a syntactic foam: experiments and modeling', *International Journal of Solids and Structures*, vol. 37, no. 40, pp. 5773-94.

Rizov, VI 2006, 'Non-linear indentation behavior of foam core sandwich composite materials-A 2D approach', *Computational Materials Science*, vol. 35, no. 2, pp. 107-15.

Roy, RJ, Debaiky, AS, Borazghi, H & Benmorkrane, B 2005, 'Glass fibre reinforced polypropylene bridge deck panel design, fabrication and load testing', paper presented to 33rd Annual General Conference of The Canadian for Civil Engineering, Toronto.

Roy, T, Manikandan, P & Chakraborty, D 2010, 'Improved shell finite element for piezothermoelastic analysis of smart fiber reinforced composite structures', *Finite Elements in Analysis and Design*, vol. 46, no. 9, pp. 710-20.

Santiuste, C, Sánchez-Sáez, S & Barbero, E 2010, 'A comparison of progressive-failure criteria in the prediction of the dynamic bending failure of composite laminated beams', *Composite Structures*, vol. 92, no. 10, pp. 2406-14.

Sasaki, D & Obayashi, S 2005, 'Efficient search for trade-offs by adaptive range multi-objective genetic algorithms', *Journal of Aerospace Computing, Information, and Communication,* vol. 2, no. 1, pp. 44-64.

Swanson, SR & Kim, J 2002, 'Optimization of sandwich beams for concentrated loads', *Journal of Sandwich Structures and Materials*, vol. 4, no. 3, pp. 273-93.

Sebaey, TA, Lopes, CS, Blanco, N & Costa, J 2011, 'Ant Colony Optimization for dispersed laminated composite panels under biaxial loading', *Composite Structures,* vol. 94, no. 1, pp. 31-6.

Schniepp, TJ, Hayes, MD, Lesko, JJ & Cousins, TE 2002, 'Design manual development for the 36-inch double-web beam', paper presented to 3rd International Conference on Composites in Infrastructure (ICCI'02), San Francisco.

Simoes, LMC & Negrão, JHO 2005, 'Reliability-based optimum design of glulam cable-stayed footbridges', *Journal of Bridge Engineering*, vol. 10, no. 1, pp. 39-44.

Sivanandam, S & Deepa, S 2007, *Introduction to Genetic Algorithms*, Springer Verlag, New York.

Smith, I 2003, 'Vibrations of timber floors: serviceability aspects', paper presented to Timber engineering, Chichester.

Spearing, S, Lagace, P & McManus, H 1998, 'On the role of lengthscale in the prediction of failure of composite structures: assessment and needs', *Applied Composite Materials*, vol. 5, no. 3, pp. 139-49.

Steeves, CA & Fleck, NA 2004, 'Collapse mechanisms of sandwich beams with composite faces and a foam core, loaded in three-point bending. Part I: analytical models and minimum weight design', *International Journal of Mechanical Sciences*, vol. 46, no. 4, pp. 561-83.

Sun, C, Quinn, B, Tao, J & Oplinger, D 1996, 'Comparative evaluation of failure analysis methods for composite laminates', *Washington, DC: FAA, Office of Aviation Research, 1996.*

Suresh, S, Sujit, PB & Rao, AK 2007, 'Particle swarm optimization approach for multi-objective composite box-beam design', *Composite Structures*, vol. 81, no. 4, pp. 598-605.

Swanson, SR & Kim, J 2002, 'Optimization of sandwich beams for concentrated loads', *Journal of Sandwich Structures and Materials*, vol. 4, no. 3, p. 273-93.

Sze, KY 2002, 'Three-dimensional continuum finite element models for plate/shell analysis', *Progress in Structural Engineering and Materials*, vol. 4, no. 4, pp. 400-7.

Szilard, R 1974, *Theory and Analysis of Plates*, Prentice-Hall Englewood Cliffs, New Jersey.

Tabakov, P & Walker, M 2010, 'A technique for stiffness improvement by optimization of fiber steering in composite plates', *Applied Composite Materials*, vol. 17, no. 5, pp. 453-61.

Tagarielli, VL, Fleck, NA & Deshpande, VS 2004, 'Collapse of clamped and simply supported composite sandwich beams in three-point bending', *Composites Part B: Engineering*, vol. 35, no. 6-8, pp. 523-34.

Tanaka, M, Watanabe, H, Furukawa, Y & Tanino, T 1995, 'GA-based decision support system for multicriteria optimization', paper presented to Systems, Man and Cybernetics, 1995. Intelligent Systems for the 21st Century, IEEE International Conference, Vancouver, BC , Canada.

Theulen, J & Peijs, A 1991, 'Optimization of the bending stiffness and strength of composite sandwich panels', *Composite Structures*, vol. 17, no. 1, pp. 87-92.

Thompson, MD, Eamon, CD & Rais-Rohani, M 2006, 'Reliability-based optimization of fiber-reinforced polymer composite bridge deck panels', *Journal of Structural Engineering*, vol. 132, no. 12, pp. 1898-906.

Timoshenko, S & Woinowsky-Krieger, S 1959, *Theory of Plates and Shells*, McGraw-Hill, New York.

Triantafillou, TC 1998, 'Composites: a new possibility for the shear strengthening of concrete, masonry and wood', *Composites Science and Technology*, vol. 58, no. 8, pp. 1285-95.

Valido, AJ & Cardoso, B 2003, 'Geometrical nonlinear composite beam structures: optimal design', *Engineering Optimization*, vol. 35, no. 5, pp. 553-60.

Van-Erp, G, Cattell, C & Heldt, T 2005, 'Fibre composite structures in Australia's civil engineering market: an anatomy of innovation', *Structural Control and Health Monitoring*, vol. 7, no. 3, pp. 150-60.

Van-Erp, G, Cattell, C & Ayers, S 2006, 'A fair dinkum approach to fibre composites in civil engineering', *Construction and Building Materials*, vol. 20, no. 1-2, pp. 2-10.

Van-Erp, G 2010, 'Commercialisation of fibre composites in Australia?s civil engineering market', paper presented to 21st Australasian Conference on the Mechanics of Structures and Materials: Incorporating Sustainable Practice in Mechanics of Structures and Materials (ACMSM21), Melbourne.

Vasiliev, VV & Morozov, EV 2001, *Mechanics and Analysis of Composite Materials*, ELSEVIER, London.

Walker, M & Smith, RE 2003, 'A technique for the multiobjective optimisation of laminated composite structures using genetic algorithms and finite element analysis', *Composite Structures*, vol. 62, no. 1, pp. 123-8.

Wang, W, Guo, S, Chang, N & Yang, W 2010, 'Optimum buckling design of composite stiffened panels using ant colony algorithm', *Composite Structures*, vol. 92, no. 3, pp. 712-9.

Weise, T 2008, 'Global Optimization Algorithms–Theory and Application', *URL: http://www.* it-weise. de, *Abrufdatum*, vol. 1.

Wu, J & Burgueño, R 2006, 'An integrated approach to shape and laminate stacking sequence optimization of free-form FRP shells', *Computer Methods in Applied Mechanics and Engineering*, vol. 195, no. 33-36, pp. 4106-23.

Xiong, J, Ma, L, Wu, L, Li, M & Vaziri, A 2011, 'Mechanical behavior of sandwich panels with hollow Al-Si tubes core construction', *Materials & Design*, vol. 32, no. 2, pp. 592-7.

Xu, YL & Hong, XJ 2008, 'Stochastic modelling of traffic-induced building vibration', *Journal of Sound and Vibration*, vol. 313, no. 1-2, pp. 149-70.

Yoon, KJ, Kim, C & Park, HC 2002, 'Nonlinear flexural deflection of thermoplastic foam core sandwich beam', *Journal of Composite Materials*, vol. 36, no. 13, p. 1529.

Zi, G, Kim, BM, Hwang, YK & Lee, YH 2008, 'An experimental study on static behavior of a GFRP bridge deck filled with a polyurethane foam', *Composite Structures*, vol. 82, no. 2, pp. 257-68.

Zienkiewicz, O & Taylor, R 2005, *The finite element method for solid and structural mechanics*, Butterworth-Heinemann, Amsterdam.

Appendix A

FRP composite materials mechanical properties

A.1 Micromechanics of fibre composite

Fibre composite material is a combination of two materials fibre and resin. However, one of the solutions used in the analysis of FRP sandwich ply is an average property of ply. In this case, the lamina or ply is treated as a homogenous material with the average properties and these properties depend on the fibre to matrix fraction. This fraction could be volume or mass (Ye et al. 1995) and it is based on the rule of mixture. The analysis of fibre and matrix fraction called Micromechanical Analysis of a Lamina (Jones 1999).

A.1.1 Mass fraction

Considering the mass of fibre (m_f) and the mass of resin or matrix (m_m), the mass fraction of fibre will be (Jones 1999):

$$M_f = \frac{Mass\ of\ fibre}{Total\ mass} \tag{A.1}$$

In consequence, the matrix mass fraction:

$$M_m = \frac{Mass\ of\ matrix}{Total\ mass} \tag{A.2}$$

Note that the relation between the mass fraction of the fibre and matrix equal to:

$$M_f = 1 - M_m \tag{A.3}$$

A.1.2 Volume fraction

The volume fraction depends on the process of FRP composite production and it varies between 25% to 80% (Gay et al. 2003). The fibre volume fraction (V_f) is defined as:

$$V_f = \frac{Volume\ of\ fibre}{Total\ volume} \qquad A.4$$

Therefore, the volume fraction of matrix (V_m) is:

$$M_m = \frac{Volume\ of\ matrix}{Total\ volume} \qquad A.5$$

A.1.3 Density

The density (ρ) of any combined materials is:

$$\rho = \frac{total\ mass}{total\ volume} \qquad A.6$$

Or

$$\rho = \frac{mass\ of\ fibre + mass\ of\ matrix}{total\ volume} \qquad A.7$$

From equations A.4 - A.7, the total density is equal to:

$$\rho = \rho_f V_f + \rho_m V_m \qquad A.8$$

A.1.4 Mechanical properties

In the same procedure for the mass, volume and density characteristics, other mechanical properties can be defined as (Hyer 1999; Jones 1999):

- *Elastic modulus E_l (longitudinal direction (l) or parallel to fibre)*

  $$E_l = V_f E_f + V_m E_m \qquad A.8$$

- *Elastic modulus E_t (transfers direction (t) or perpendicular to fibre)*

  $$E_t = E_m \left[\frac{1}{(1-V_f)+\frac{E_m}{E_f}V_f}\right] \qquad A.9$$

- *Shear modulus G*

  $$G = G_m \left[\frac{1}{(1-V_f)+\frac{G_m}{G_f}V_f}\right] \qquad A.10$$

- *Poisson ratio v*

$$v = v_f V_f + v_m V_m \qquad \text{A.11}$$

A.2 GFRP sandwich panel components testing

The sandwich panel is made from E-CR glass fibre for the skin materials and modified phenolic solid core. Skins represent the top and bottom parts in the GFRP sandwich panel. The novel GFRP sandwich panel has been made with two generations. Generation one is made from ECR - glass fibre skin with 4-plies 0/90^0 orientations as shown in Figure A.1(a). The experimental test of first generation was done by Manalo et al. (2010d). The second generation of FRP sandwich panel is made of ECR-glass fibre skin with 6-plies 0^o/90^o/chopped as shown in Figure A.1(b). A burning test was done to find the fibre weight in the skin. It was found the fibre mass ratio is equal to 45.53 %. In addition, the density of the FRP skin is 1425 kg/m^3, and the density of modified core is 950 kg/m^3. All tests follow the ISO and ASTM standards to find the skin and core mechanical properties.

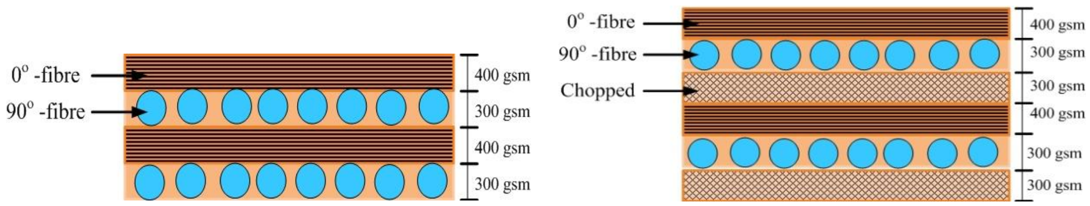

(a) 0^o/90^o (b) 0^o/90^o/chopped

Figure A.1 FRP skin configuration

A.2.1 GFRP composite skin

(a) Tension

An experimental test has been carried out to find the tensile strength of the skin in the panel generation two. The experimental test samples prepared according to ASTM D3039 as shown in Figure A.2(a). The experimental work was done by preparing ten samples of the skin. Five sample in 0^o-direction and five samples in 90^o-direction. Three of each group were tested with strain gauges and two were tested to find the ultimate failure stress. A uni-axial strain gauge type KYOWA-KFG-3-120-C1-11L1M2R was used to measure the strain. The average experimental results are shown in Table A.1 for both 0^o-direction and 90^o-direction. The stress-strain behaviour of the tensile behaviour is shown in Figure A.3. The behaviour of the skin showed an initial cracking in the matrix and the sound of the matrix cracking was heard. Then, the glass fibre carries the load up to failure, and the behaviour of the stress-strain curve is linear up to failure. The strain gauges were broken before the final failure, and the curve was extended up to the failure stress to get the expected failure strain as shown in Figure A.3. The results are shown in Table A.1

(b)Compression

GFRP sandwich panel skin tested to find its compression strength. Ten samples prepared for the test according to the ISO-14126 as shown in Figure A.2(b). Five sample with 0^o-degrees major fibre and five samples with 90^o-degrees major fibre. Three strain gages type KYOWA- KFG-3-120-C1-11L1M2R were used for the test in each fibre direction. The average results of the experimental test are shown in Table A.1.

Table A.1 Skin tensile properties

Panel type	Skin Type	Average strength MPa	Average Elastic modulus MPa	Maximum strain %	Density kg/m^3
	Tension				
18 mm	0/90^0/chopped-0^o-direction	239.7	11750	2.25	1425
	0/90^0/chopped-90^o-direction	162.9	8100	2.0	1425
15 mm	0/90^0-0^o-direction (Manalo et al. 2010d)	246.8	15380	1.6	--------
	0/90^0-90^o-direction (Manalo et al. 2010d)	208.27	12631.4	2.37	--------
	Compression				
18 mm	0/90^0/chopped-0^o-direction	194.17	12173	1.6	1425
	0/90^0/chopped-90^o-direction	124.95	10766.1	1.24	1425
15 mm	0/90^0-0^o-direction (Manalo et al. 2010d)	201.75	16102.3	1.24	--------
	0/90^0-90^o-direction (Manalo et al. 2010d)	124.23	9948	1.25	--------

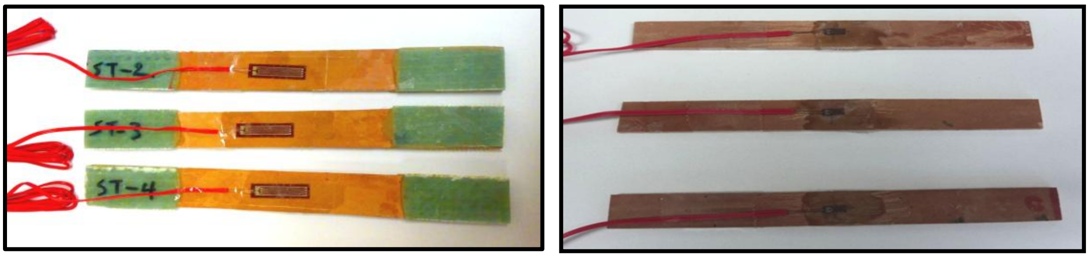

(a) Tensile (b) Compression

Figure A.2 GFRP skin samples.

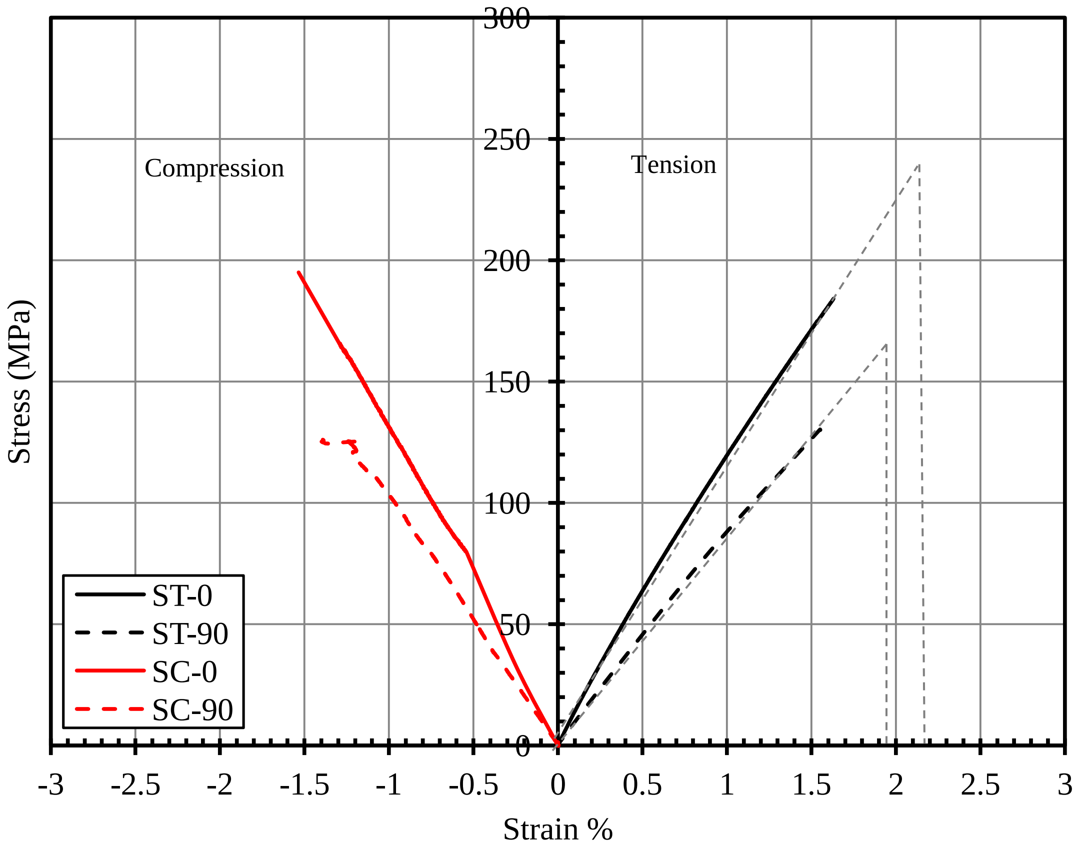

Figure A.3 Stress-strain of the GFRP skin.

A.2.2 Modified phenolic core

(a) Tension

Tensile test was done on the core materials after sanding the GFRP skins. Dog-bone samples prepared from the sandwich panel. Three samples were prepared for the tensile test according to ISO 527-2 (ISO:527-2 1993). Strain gauges type KYOWA-KFG-3-120-C1-11L1M2R was used to measure the axial strain. The modified phenolic core has an approximately linear behaviour with brittle failure as shown in Figure A.4. The average properties of the tensile behaviour are shown in Table A.2.

(b) Compression

Flat wise compression test of the sandwich panel was done according to ASTM -C 365 (ASTM-C365-94 1994). Six samples were prepared for the test. The experimental stress-strain curves are shown in Figure A.4. The behaviour of modified phenolic core material under compressing is elasto-plastic. The average compression properties are shown in Table A.2.

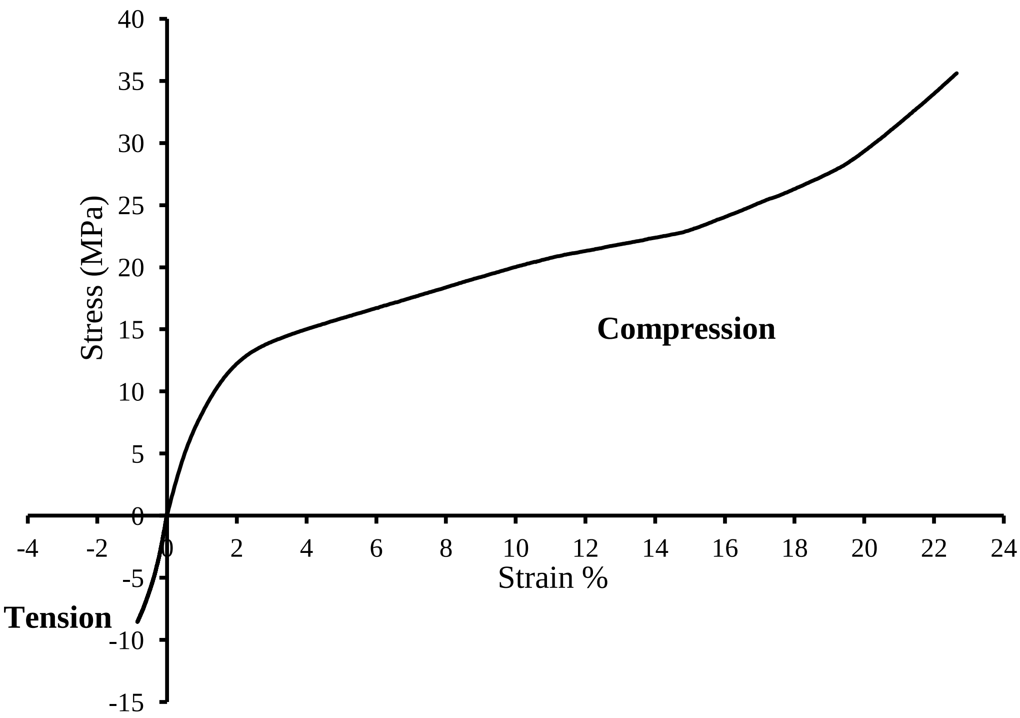

Figure A.4 Stress-strain of modified phenolic core.

(c) Shear

Core shear test was done to find the shear strength of the core materials. The shear test of the fibre composite skin and the modified phenolic core material was conducted according to the ASTM D5379/D5379M-93 standards. The experimental setup is shown in Figure A.5. Five specimens of core material of rectangular beam shape with symmetrically located V-notches at the centre were tested. The failure mode is shown in Figure A.6. The average shear strength of the modified phenolic core is shown in Table A.2.

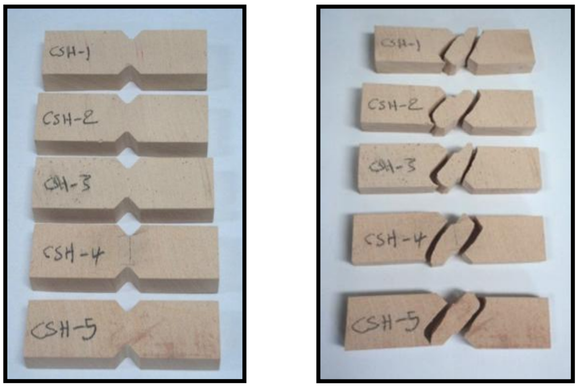

a-Before test a- After test

Figure A.5 Experimental setup

Figure A.6 Core shear specimens

(d) Flexural

Core flexural tests were done under three point bending tests as shown in Figure A.16. The core samples were prepared by sanding off the GFRP skins and cutting the core material to a specific size. The experimental setup is shown in Figure A.7. Six samples were prepared for the test as shown in Figure A.8. Strain gauges were attached to two samples. The results show that the behaviour is approximately linear. The load strain results for the samples are shown in Figure A.9. The flexural elastic modulus could be calculated from the equation:

Flexural deflection= $\delta = \frac{PL^3}{48EI}$ A.12

where, P is the load. L is the span. E is core elastic modulus and I is a moment of inertia.

The average flexural properties for the modified phenolic core samples are shown in Table A.2.

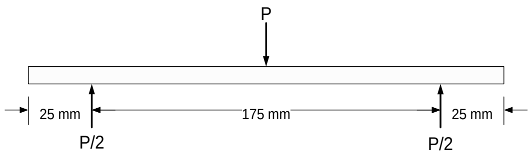

Figure A.7 Three point bending

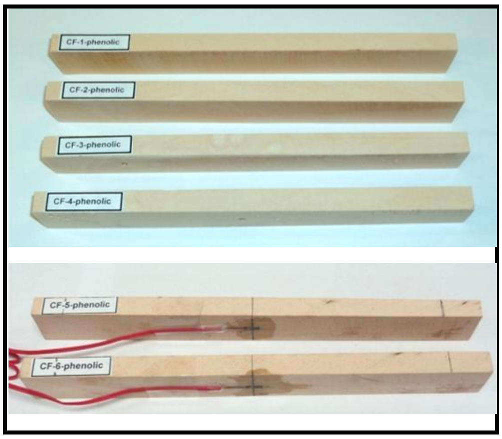

Figure A.8 Flexural samples

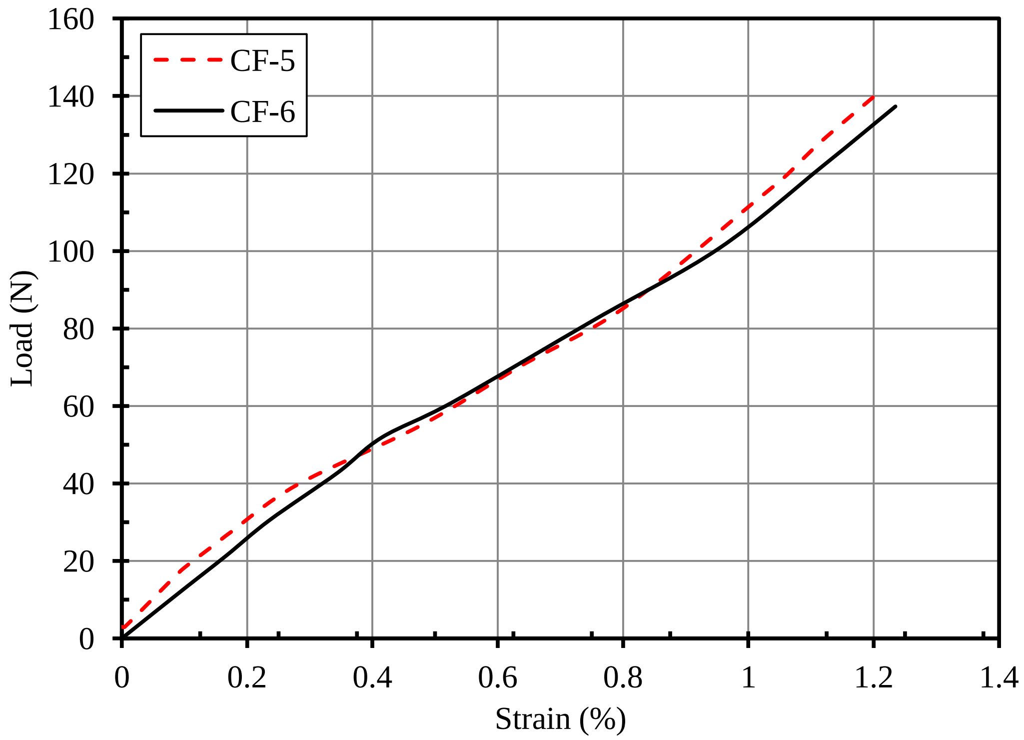

Figure A.9 Load-Strain of core flexural test.

Table A.2 Modified phenolic core mechanical properties

Test	Elastic modulus MPa	Ultimate strength MPa	Ultimate strain %
Tensile	1350.2	8.5	0.62
Compression	1201.6	35.6	22.10
Flexural	1299.3	15.9	1.20
Shear	---	8.8	---

A.2.3 Skin-core interaction

Skin - core interaction is very important in the simulation of the GFRP sandwich structure and the numerical modelling requires special attention in the representation of this interaction (Moreira & Rodrigues 2010). The present GFRP sandwich panel is fabricated in one stage and no glue was used to connect the core and the skins in the fabrication. Therefore, assessment of the skin-core interaction of this type of GFRP sandwich panel is more challenging. The International Standard ASTM C273 (ASTM-C273-61 1988) provides a standard method for testing GFRP sandwich panel to find the shear strength. However, this method did not work with the current very high shear strength panel because separation between the steel fixture and the skin happened without any failure in the GFRP sandwich panel. Therefore, we developed a new method to find out the in-plane interaction shear strength of the core–skin.

The sample was designed to determine the actual interaction between the skin and the core. The phenolic core was cut creating a cavity but leaving a specific interaction area between the skin and the core as shown in Figure A.10. The skin joint was made at the top and bottom skins by cutting the skins as shown in the Figure A.11. The skin joint helps to identify the interaction area in the top and bottom skins. The axial tension force was applied at the ends of the sample. The laser extensometer was used to measure the strain in the interaction area. The experimental test result shows a linear behaviour for the skin-core interaction and the peak in-plane stress was at 8.8 MPa with a maximum strain of 0.25% as shown in Figure A.12. A clear separation happened between the skin and the core without any particles of the core attached to the skin face. This shows that the suggested procedure is efficient in finding the interaction plane shear forces. However, it should be noted that the interaction shear stress is greater than the core tensile. We would expect that the failure in the core will happen before any failure in the interface when it is carried tension force.

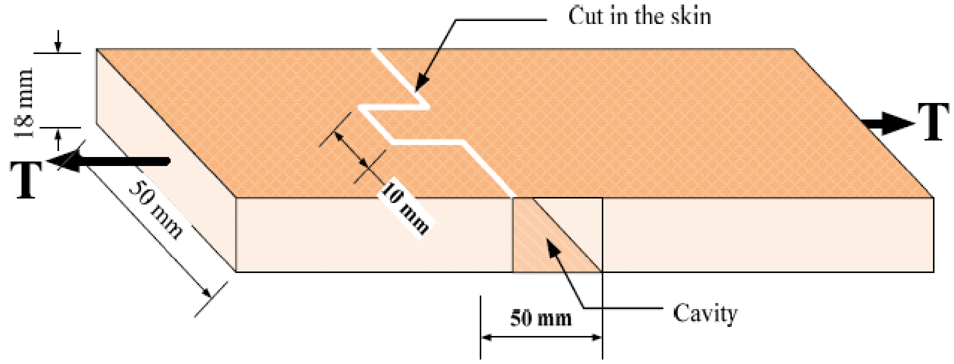

Figure A.10 Sample dimensions.

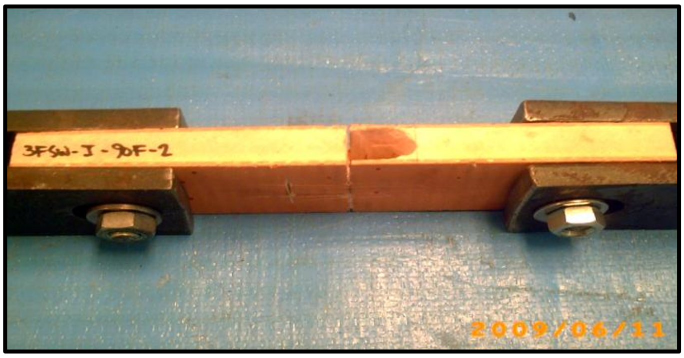

Figure A.11 Sample of skin core interaction test.

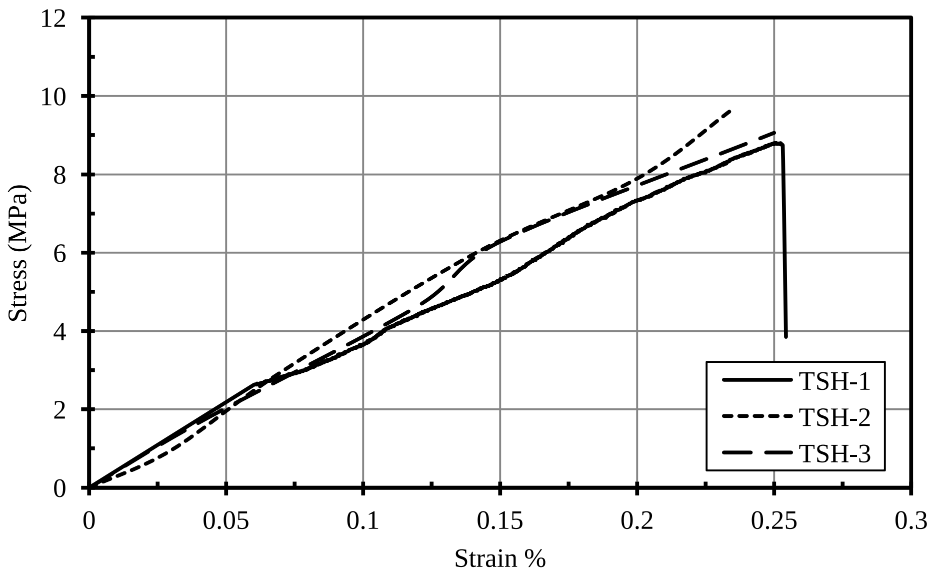

Figure A.12 Stress -strain of GFRP skin core interaction.

A.3 GFRP skin mechanical properties

The previous sections discussed the experimental tensile and compression tests of the GFRP skin. The GFRP skin is made of 6-plies $0^o/90^o$/chopped as shown in Figure A.1(b). The experimental results have indicated the overall stiffness and strength of the GFRP skin. Manalo et al. (2010) Investigated the properties of the same composite with 4-plies $0^o/90^o$ and some of the results are shown in Tables A.3 and A.4. The FE model is required an input for each plies in the skin simulation. The calculation of the ply properties is based on the micromechanics level using the rules of mixture as shown in A.1. A burning test was done on the GFRP skin sample. The burning test indicated that the mass percent of fibre in the matrix is 45.53 %. The mass percent can be converted to the volume percent as follow:

GFRP skin sample weight = 3.280 g

Fibre content in = 1.488 g

Matrix content = 1.792 g

$$t = t_f + t_m$$

$$t_f = \frac{mass}{density} = \frac{1.488}{2.6} = 0.572 \quad mm$$

$$t_m = \frac{mass}{density} = \frac{1.792}{1.2} = 1.493 \ mm$$

where, t_f and t_m are the fibre and matrix thickness respectively.

The volume ratio of the fibre in the composite is equal to:

$$V_f = \frac{0.572}{(0.572+1.493)} \times 100 = 27.77 \ \%$$

A.3.1 Ply properties

The ply mechanical strength can be found by using the equation described in section A.1. The manufacturer mechanical properties are shown in Table A.3. The fibre is manufactured by the Advatex® glass (Advantex 2012). The resin matrix properties are provided by LOC composite Pty. Ltd., Australia. The calculated ply properties are shown in Table A.4.

The mass ratio was used to calculate the $0^o/90^o$/chopped plies thicknesses. The mass of glass in the plies 0^o, 90^o, and chopped are 400, 300, and 300 gsm respectively, as shown in Figure A.1(b). The thicknesses of the GFRP skin plies were calculated and it is shown in Figure A.13.

Table A.3 Manufacturer mechanical properties

Fibre	Elastic modulus MPa	Tensile strength MPa	Elongation %	Density kg/m^3	Poisson's ratio	Shear modulus MPa
Uni-axial ECR glass	80000	3100	4.8	2620	0.25	33000
Resin	2500	62.5	2.5	1200	0.4	1600
Chopped strand mat	7800	108	1.8	----	---	

Table A.4 Plies mechanical properties

Material	Elastic modulus MPa			Poisson's ratio	Shear strength MPa	Tensile stress MPa	Compressive stress MPa
	E_{11}	E_{22}	E_{33}				
Panel thickness =15 mm							
GFRP skin ply (theoretical)	24,021.7	3,420.1	3,420.1	0.35	45.1	480.4	432.3
Phenolic core	1,154.4	…….	…….	0.3	4.25	5.95	21.3
Panel thickness =18 mm							
GFRP skin ply (theoretical)	24,021.7	3,420.1	3,420.1	0.35	45.1	480.4	432.3
Chopped fibre ply (Manufacturer)	7,500	7,500	3,420.1	0.32	45.1	105	160
Phenolic core	1350.2	……	……	0.3	8.8	8.5	24.5

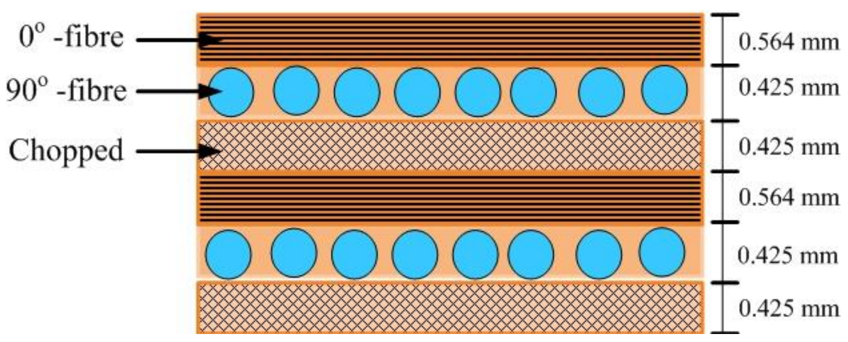

Figure A.13 Plies theoretical thicknesses.

A.3.2 GFRP skin stiffness

Based on the stacking sequence of the GFRP ski plies and the ply mechanical properties, the GFRP skin stiffness can be calculated. The classical laminate theory (CLT) can be used to find the stiffness of the laminated skin (Gay et al. 2003; Jones 1999). The E-CR chopped strand mat is assumed to have a random distribution with the properties provided by the manufacturer (Advantex 2012). The results of the CLT are shown in Table A.5. A summary of the experimental finding is shown in the Table A.5 as well. It can be seen there is a small difference between the calculated and experimental properties of GFRP skin.

Table A.5 GFRP skin stiffness

	Method	E_x MPa	E_y MPa	Tensile strength (x) MPa	Compressive strength (x) MPa	Tensile strength (y) MPa	Compressive strength (y) MPa
GFRP skin	CLT	12360	10920	247.2	218.4	222.4	196.5
GFRP skin	Experimental	11750	8100	239.7	194.1	162.9	124.95

References

Advantex 2012, *E-CR glass reinforcement* <http://composites.owenscorning.com/aboutAdvantex.aspx>.

ASTM-C273-61 1988, Standard Test Method for Shear Properties of Sandwich Core Materials, Composite Structures, ASTM International, West Conshohocken.

ASTM-C365-94 1994, Standard Test Method for Flatwise Compressive Properties of Sandwich Cores, West Conshohocken, PA, .

Gay, D, Hoa, S & Tsai, S 2003, *Composite Materials: Design and Applications*, CRC Pr I Llc, Florida.

Hyer, M 1999, 'Laminate plate and shell theory', in C Zweben & A Kelly (eds), *Comprehensive Composite Materials*, Elsevier, Oxford, vol. 6.

ISO:527-2 1993, Determination of Tensile Properties of Plastics Materials

Jones, RM 1999, *Mechanics of composite materials*, Hemisphere Pub.

Manalo, AC, Aravinthan, T, Karunasena, W & Islam, MM 2010d, 'Flexural behaviour of structural fibre composite sandwich beams in flatwise and edgewise positions', *Composite Structures*, vol. 92, no. 4, pp. 984-95,

Moreira, RAS & Rodrigues, JD 2010, 'Static and dynamic analysis of soft core sandwich panels with through-thickness deformation', *Composite Structures*, vol. 92, no. 2, pp. 201-15,

Ye, BS, Svenson, AL & Bank, LC 1995, 'Mass and volume fraction properties of pultruded glass fibre-reinforced composites', *Composites*, vol. 26, no. 10, pp. 725-31,

Appendix B

Free vibration behaviour of GFRP sandwich beams

B.1 Introduction

FRP sandwich panels have been considered by the structural engineers as a most attractive application. The FRP sandwich structures might be used in the sport stadiums, clubs, shopping centres, offices and houses. Highway bridge deck represents one of the well-known sandwich panel applications (Davalos et al. 2009; O'Connor 2008). Most current design studies are concerned in avoiding structural failure and excessive vibration problems (Ebrahimpour & Sack 2005). This Appendix presents the free vibration tests of the single and glue laminated beams.

B.2 Experimental program

B.2.1 Test specimens

The present experimental work requires preparation of sandwich beams. The single sandwich beams were prepared by simply cutting the panel into strips with 50 mm width. The glue laminated beam was adopted for this test from Manalo (2011) tests samples. The slabs prepared with different spans, boundary conditions, and fibre orientations. The GFRP sandwich beams were tested under simply supported, fixed-free, and fixed-fixed boundary conditions. The steel supports with bolts were used to hold the beams for the testing. The details of the tested beams are shown in Table B.1.

Table B.1 GFRP sandwich beam samples

Test Name	Support type	Cross section	Number of sandwiches	Dimensions mm		
				L	b	d
Beam-1	Simply-simply	Single sandwich	1	1000	50	18
Beam-2	Fixed-free	Single sandwich	1	1000	50	18
Beam-3	Fixed-fixed	Single sandwich	1	1000	50	18
Beam-4	Simply-simply	Glue laminated	8	2000	150	230

B.2.2 Test setup

In the present experimental program, the LMS Test Lab instrument and LMS SCADAS system were used to measure the natural frequency of the GFRP sandwich beams. Two channels were used in the reading one for the hammer reading and the other for the accelerometer reading. The LMS instrument was connected to the computer to transfer the data as shown in Figure B.1. The accelerometer was fixed in the mid span for the simply- simply and fixed-fixed beams, and at the free end for the fixed-free boundary conditions.

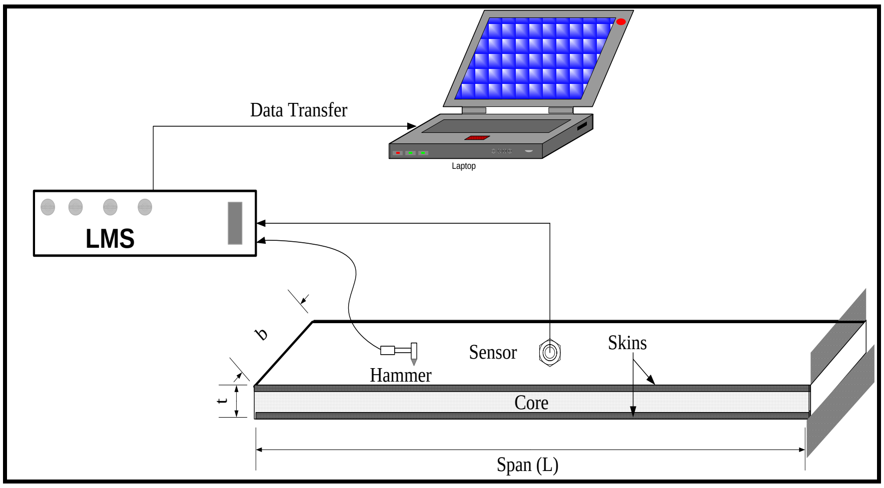

Figure B.1 Experimental setup.

B.3 Experimental tests and discussion

The experimental free vibration tests were done on the samples shown in Table B.1. The results of the four tests are shown in Figures B.2, B.3, B.4 and B.5. A summary of the test results are shown in Table B.2. The results show the effect of the boundary conditions on the first three natural frequencies. It can be seen that the cantilever beam showed a lowest natural frequency and the fixed-fixed showed a highest natural frequency. In addition, the glue laminated GFRP sandwich beam showed a 29 Hz first natural frequency.

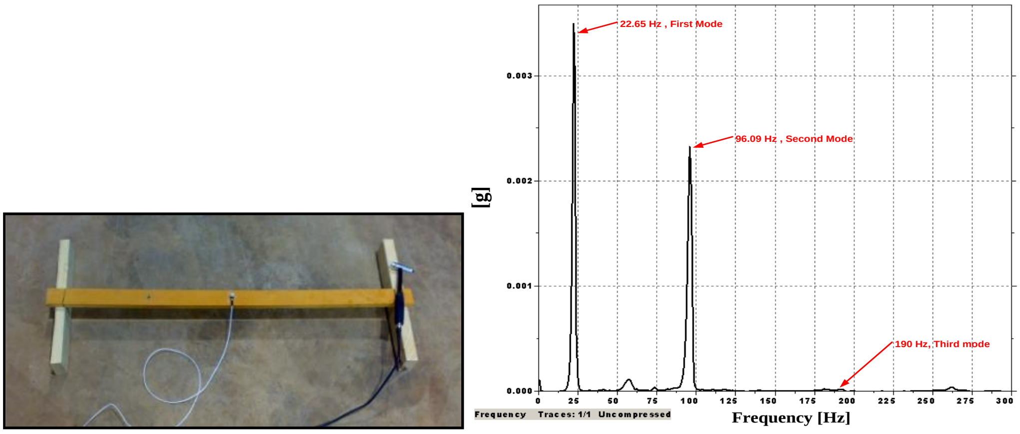

Figure B.2 Free vibration spectrum of simply supported (beam-1).

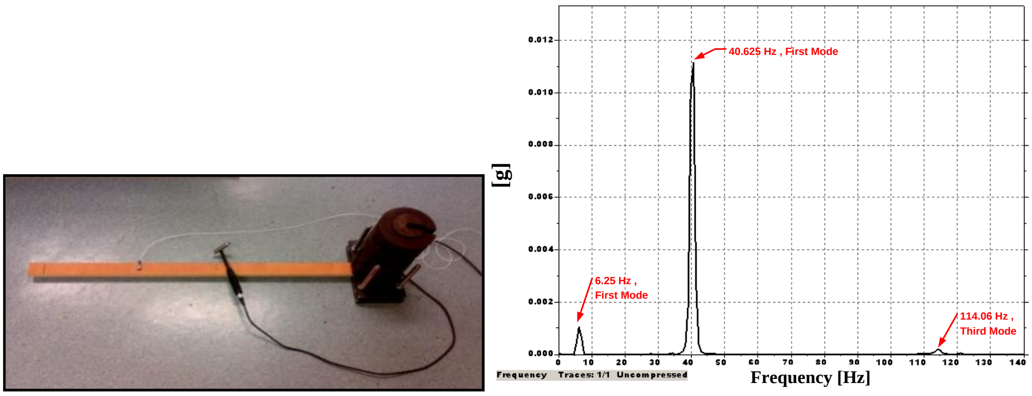

Figure B.3 Free vibration spectrum of cantilever beam (beam-2).

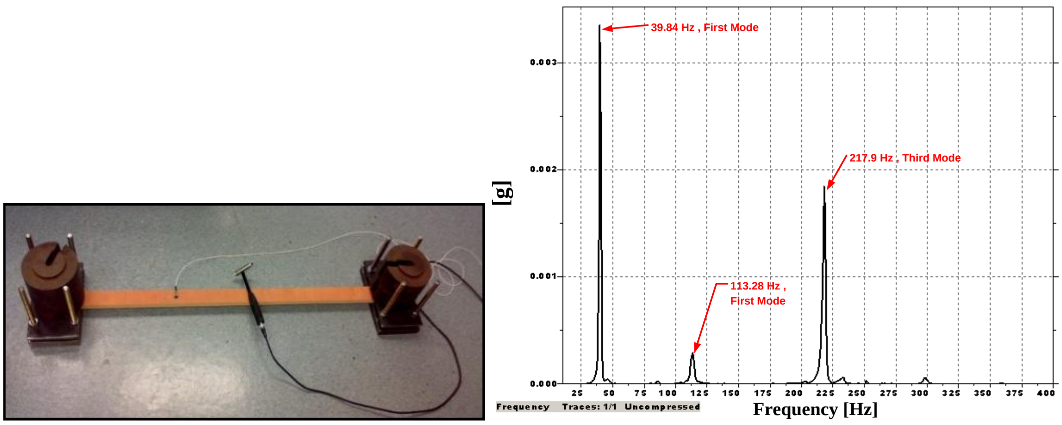

Figure B.4 Free vibration spectrum of fixed supported (beam-3).

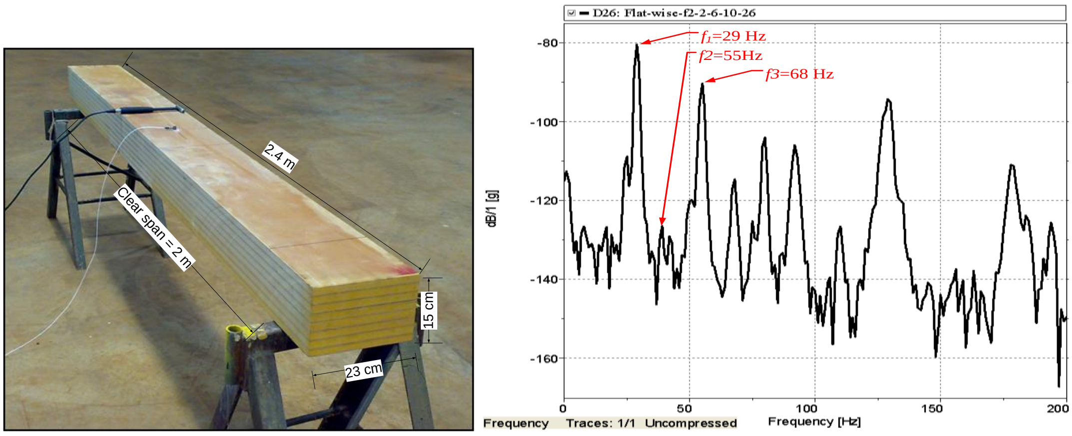

Figure B.5 Frequency spectrum of GFRP glue laminated sandwich beam (beam-4).

Table B.2 Experimental and analytical results

Test	Experimental			Analytical (equation 5.1)		
	f1 Hz	*f2 Hz*	*f3 Hz*	*f1 Hz*	*f2 Hz*	*f3 Hz*
Beam-1	22.65	86.09	190	23.57	94.13	212.21
Beam-2	6.25	40.62	114.06	7.62	47.47	132.8
Beam-3	39.84	113.28	217.9	53.47	147.41	289
Beam-4	29	55	68	22.09	44.19	66.28

The analytical values were found by using equation 5.1 (Chapter-5). The comparison between the experimental results and the analytical equation is shown in Table B.2 for single and glue laminated sandwich beam respectively. The analytical calculation of the single sandwich beam showed that the simply supported first natural frequency is very close to the experimental. The difference between the second and third natural frequency of simply supported increases compare to the experimental. The analytical results of the cantilever and fixed-fixed single sandwich beam showed a large difference compare to the experimental results. The analytical results of the glue laminated GFRP sandwich beam show a lower value than the experimental test results.

Damping is very important in the structural design. The damping properties of the structure effect on the long fatigue life of the structure. Structure with high damping might have longer life than the structure with low damping ratio. Fibre glass members usually has a low damping ratio with less than 1% (Berthelot & Sefrani 2007). A half power method was used to calculate the damping ratio of the

GFRP sandwich beam for three different boundary conditions. The damping ratio (ξ) is calculated from the equation below and the explanation of this method is shown in Figure B.6.

$$\xi = \frac{w_2 - w_1}{2w_r} \qquad \text{B.1}$$

where w_r is the resonance frequency. w_1 and w_2 are the left and right frequencies at 3dB below the resonance amplitude as shown in Figure B.6.

The damping ratio for the three different supports is calculated and shown in Table B.3. It can be seen that the cantilever beam has a lower frequency but a higher damping ratio. In contrast, the fixed-fixed beam has a higher frequency but a lower damping ratio.

The boundary condition has an obvious impact on the frequency value. However, Beam-1 and Beam-3 have a span to depth ratio greater than 20. The glue laminated sandwich beam has a span to the depth ratio equal to 8.6, and it showed a frequency equal to 29 Hz. Finally, the analytical equations required a modification to capture the right values of the GFRP sandwich beams natural frequency.

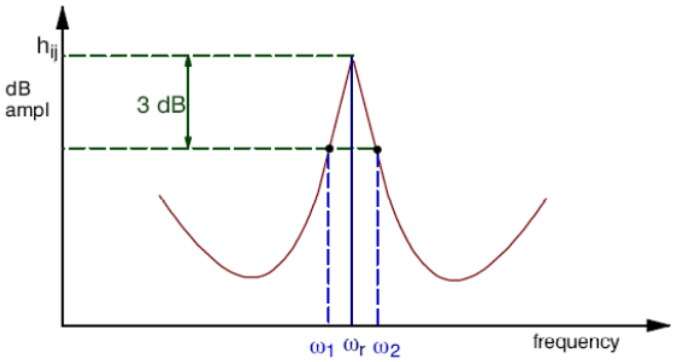

Figure B.6 Half power method for damping estimation.

Table B.3 Damping ratios

Beam support type	w_r (Hz)	w_1 (Hz)	w_2 (Hz)	Damping %
Beam-1	22.65	22.15	22.97	1.80
Beam-2	6.25	6.0	7.03	8.00
Beam-3	39.84	41.90	42.65	0.99
Beam-4	29.00	28.70	29.20	1.72

B.4 FEA simulation

A FEA simulation was formulated for analysis of the fibre composite sandwich beam. FEA methods are regarded as efficient methods to predict the natural frequency of sandwich structures. The top and bottom skins were formulated using a 3D continuum solid element type C3D20R. The core was meshed using 3D solid element type C3D8R. The FEA analysis results are shown in Table B.4, with the predicted mode shape. The results have been verified with the experimental and analytical equation for simply supported beam. The Euler-Bernoulli beam model represents one of the analytical solutions for free vibration analysis of beams (Han et al. 1999). The equation of Euler-Bernoulli beam was described in Chapter-5.

Table B.4 Free vibration results of a simply supported GFRP sandwich beam

	Frequency (Hz)			Mode Shape
	Analytical	FE	Experimental	
f_1	23.57	23.10	22.65	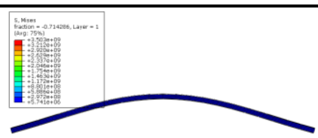
f_2	94.31	95.36	86.09	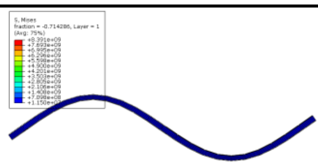
f_3	212.21	183.81	190	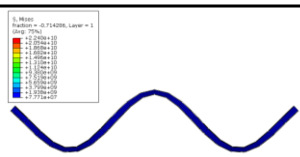

The glue-laminated GFRP sandwich beam that was tested has about 8 layers of single sandwich glued together. The full 3D FEA model was developed with dimensions of 2.4 m x 0.23 m x 0.15 m with clear span is equal to 2 m. The FEA results are shown in Table B.5, and are compared to the experimental and analytical results. The overall stiffness of a multi-layered sandwich beam could be calculated from the elastic properties of GFRP sandwich materials. Calculation of the glue-laminated stiffness is made with the assumption of no slip between sandwich layers as shown previously in Chapter-3.

The analytical solution for the GFRP glue-laminated sandwich beam natural frequency was made by using Euler-Bernoulli equation as shown in Table B.5. It can be seen that the FEA model gives a better prediction than the analytical equation, especially at the first two frequencies. Chapter-6 shows the FEA model on the slabs free vibration simulation gives an acceptable accuracy. Applying the same model gives good results in the calculation of natural frequency of the single and glue laminated GFRP sandwich beams especially in the first mode as shown in Tables B.5 and B.6.

Table B.5 Glue laminated sandwich beam natural frequency

	Frequency (Hz)			Mode Shape
	Analytical	FE	Experimental	
f_1	21.42	30.7	29	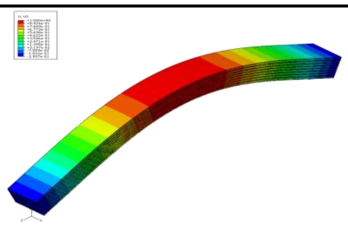
f_2	42.85	58.0	55	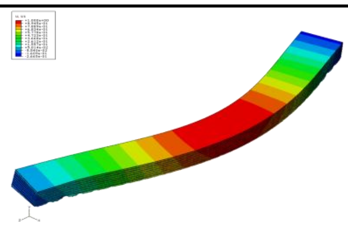
f_3	64.24	105.0	68	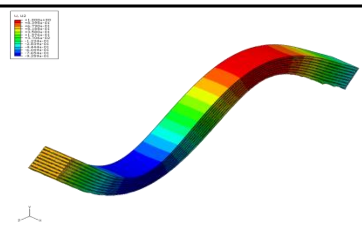

References

Berthelot, J-M & Sefrani, Y 2007, 'Longitudinal and transverse damping of unidirectional fibre composites', *Composite Structures*, vol. 79, no. 3, pp. 423-31,

Davalos, JF, Qiao, P, Ramayanam, V, Shan, L & Robinson, J 2009, 'Torsion of honeycomb FRP sandwich beams with a sinusoidal core configuration', *Composite Structures*, vol. 88, no. 1, pp. 97-111,

Ebrahimpour, A & Sack, RL 2005, 'A review of vibration serviceability criteria for floor structures', *Computers & Structures*, vol. 83, no. 28-30, pp. 2488-94,

Han, S, Benaroya, H & Wei, T 1999, 'Dynamics of transversely vibrating beams using four engineering theories', *Journal of Sound and Vibration*, vol. 225, no. 5, pp. 935-88,

O'Connor, JS 2008, 'GRP bridge decks and superstructures in the USA', *Reinforced Plastics*, vol. 52, no. 6, pp. 26-31,

Appendix C

Source code: UMAT subroutine

```
C........... UMAT FOR 3D FRP COMPOSITE FAILURE ANALYSIS............
C          BY Using HASHIN Model
C
C          WORK START:    03.12.2009
C          WORK END   :   07.02.2010
C  .... Part of a PhD research in the University of Southern Queensland (USQ)
C………………By:    ZIAD K. AWAD / 2012 ………………………………………..
C
      SUBROUTINE UMAT(STRESS,STATEV,DDSDDE,SSE,SPD,SCD,
     1  RPL,DDSDDT,DRPLDE,DRPLDT,
     2  STRAN,DSTRAN,TIME,DTIME,TEMP,DTEMP,PREDEF,DPRED,CMNAME,
     3  NDI,NSHR,NTENS,NSTATV,PROPS,NPROPS,COORDS,DROT,PNEWDT,
     4  CELENT,DFGRD0,DFGRD1,NOEL,NPT,LAYER,KSPT,KSTEP,KINC)
C
      INCLUDE 'ABA_PARAM.INC'
C
      CHARACTER*80 CMNAME
      DIMENSION STRESS(NTENS),STATEV(NSTATV),
     1  DDSDDE(NTENS,NTENS),
     2  DDSDDT(NTENS),DRPLDE(NTENS),
     3  STRAN(NTENS),DSTRAN(NTENS),TIME(2),PREDEF(1),DPRED(1),
     4  PROPS(NPROPS),COORDS(3),DROT(3,3),DFGRD0(3,3),DFGRD1(3,3)

      DIMENSION STRANT(6),TSTRANT(4)
      DIMENSION C(6,6),CDFULL(6,6)
      DIMENSION DDFDE(6), DDMDE(6), DCDDF(6,6), DCDDM(6,6)
      DIMENSION ATEMP1(6), ATEMP2(6), TDDSDDE(6,6)
      DIMENSION OLD_STRESS(6)
      DIMENSION DOLD_STRESS(6)
      PARAMETER (ZERO = 0.D0,ONE = 1.D0,TWO = 2.D0, HALF = 0.5D0)
C***************************************************************
C
C    VARIABLES TO UPDATE DDSDDE,STRESS,STATEV,SSE,SPD,SCD
C                 ------ ------ ------ --- --- ---
C    STRANT..... STRAIN AT THE END OF THE INCREMENT
C    TSTRANT.....TEMPORARY ARRAY TO HOLD THE STRAIN FOR PLANE STRESS PROBLEM
C    CFULL.......FULL 6X6 ELASTICITY MATRIX
C    CDFULL......FULL 6X6 DAMAGED ELASTICITY MATRIX
C    DDFDE....... D DF/D E
C    DDMDE....... D DM/D E
C    DCDDF....... D C/ D DF THE DERIVATIVE OF THE FULL MATRIX OVER DF
C    DCDDM........D C/ D DM THE DERIVATIVE OF THE FULL MATRIX OVER DM
C    ATEMP1,ATEMP2...TEMPORARY ARRAY USED IN JACOBIAN CALCULATION
C    TDDSDDE.....UNCONDENSED JACOBIAN MATRIX FOR PLANE STRESS PROBLEM
C    OLD_STRESS...STRESS AT THE BEGINNING OF THE INCREMENT, SAVED FOR THE ENERGY
C             COMPUTATION
C    DOLD_STRESS...STRESS AT THE BEGINNING OF THE INCREMENT,
C             IF THERE'S NO VISCOUS REGULARIZATION
C    D_STRESS...STRESS IF THERE'S NO VISCOUS REGULARIZATION, THE ABOVE IS CALCULATED
C            TO CALCULATE THE SCD, ENERGY CAUSED BY VISCOUS REGULARIZATION
C
C    STATEV(1)   damage variable dft ---- fibre tension
C    STATEV(2)   damage variable dfc ----- fibre compression
C    STATEV(3)   damage variable dmt ------ matrix tension
C    STATEV(4)   damage variable dmc ------ matrix compression
C    STATEV(5)   damage variable dmG ------ delamination
C
```

```
C
C    GET THE MATERIAL PROPERTIES---ENGINEERING CONSTANTS
C
      E11 = PROPS(1)          !YOUNG'S MODULUS IN DIRECTION 1
      E22 = PROPS(2)          !YOUNG'S MODULUS IN DIRECTION 2
      E33 = PROPS(3)          !YOUNG'S MODULUS IN DIRECTION 3
      V12 = PROPS(4)         !POISSON'S IN 12 PLANE
      V23 = PROPS(5)         !POISSON'S IN 23 PLANE
      V13 = PROPS(6)         !POISSON'S IN 31 PLANE
      G12 = PROPS(7)         !SHEAR MODULUS IN 12 PLANE
      G23 = PROPS(8)         !SHEAR MODULUS IN 12 PLANE
      G13 = PROPS(9)         !SHEAR MODULUS IN 12 PLANE
C
C    GET THE FAILURE PROPERTIES
C
      ST1 = PROPS(10)         !STRESS TENSION IN 1
      SC1 = PROPS(11)         !STRESS TENSION IN 1
      ST2 = PROPS(12)         !STRESS TENSION IN 2
      SC2 = PROPS(13)         !STRESS TENSION IN 2
      ST3 = PROPS(14)         !STRESS TENSION IN 3
      SC3 = PROPS(15)         !STRESS TENSION IN 3
      T12 = PROPS(16)         !STRESS SHEAR IN 1
      T23 = PROPS(17)         !STRESS SHEAR IN 2
      T13 = PROPS(18)         !STRESS SHEAR IN 3
C
C    CALCULATE THE STRAIN AT THE END OF THE INCREMENT
C
      DO I = 1, NTENS
        STRANT(I) = STRAN(I) + DSTRAN(I)
      END DO
c
C    ZERO THE 6X6 FULL STIFFNESS MATRIX
      DO I = 1, 6
        DO J = 1, 6
          C(I,J)=ZERO
        END DO
      END DO
C-------------------------------------------------------C
C B.3MATERAILCOMPLIANCE AND STIFFNESS MATRIX
C-------------------------------------------------------
C
      V21 = V12 * E22 / E11
      V31 = V13 * E33 / E11
      V32 = V23 * E33 / E22
C
      gg = one / ( one - V12*V21 - V23*V32 - V31*V13
     *     - two*V21*V32*V13 )
      C(1,1)= E11 * ( one - V23*V32 ) * gg
      C(1,2)= E11 * ( V21 + V31*V23 ) * gg
      C(1,3)= E11 * ( V31 + V21*V32 ) * gg
      C(2,1)= C(1,2)
      C(2,2)= E22 * ( one - V13*V31 ) * gg
      C(2,3)= E22 * ( V32 + V12*V31 ) * gg
      C(3,1)= C(1,3)
      C(3,2)= C(2,3)
      C(3,3)= E33 * ( one - V12*V21 ) * gg
      C(4,4)= G12
      C(5,5)= G13
      C(6,6)= G23
C    FULL 3D CASE
      IF(KINC.EQ.1) THEN
      DO I = 1, NTENS
          DO J = 1, NTENS
            DDSDDE(I,J)=C(I,J)
          END DO
        END DO
      END IF
C
C
C   CALCULATE STRESS FROM ELASTIC STRAINS
C
      DO 70 K1=1,NTENS
       DO 60 K2=1,NTENS
         STRESS(K2)=STRESS(K2)+DDSDDE(K2,K1)*DSTRAN(K1)
 60    CONTINUE
```

```
 70   CONTINUE
c
      DFTOLD = STATEV(1)
      DFCOLD = STATEV(2)
      DMTOLD = STATEV(3)
      DMCOLD = STATEV(4)
      DMT3OLD = STATEV(5)
C     SAVE THE OLD STRESS TO OLD_STRESS
      DO I = 1, NTENS
        OLD_STRESS(I) = STRESS(I)
      END DO
C
      CALL CheckFailureIni(ST1,SC1,ST2,SC2,ST3,SC3,T12,T23,
     1     T13,
     1     STRESS,STRANT,GFMAT,GFFIB,G12,G23,G13,
     1     CELENT,C,CDFULL,DFT,DFC,DMT,DMC,DMG,DDFDE,DDMDE,NTENS,
     2     DFTOLD,DFCOLD,DMTOLD,DMCOLD,DMT3OLD,NDI,FIBD,MATD)
C
C
C
C     UPDATE THE JACOBIAN
C
      DO I = 1, NTENS
          DO J = 1, NTENS
            DDSDDE(I,J)=CDFULL(I,J)
          END DO
        END DO
C
C     TO UPDATE THE STATE VARIABLE
C
      STATEV(1) = DFT
      STATEV(2) = DFC
      STATEV(3) = DMT
      STATEV(4) = DMC
      STATEV(5) = DMG
      STATEV(6) = RM3
      STATEV(7) = FIBD
      STATEV(8) = MATD

c     WRITE(*,*)DFT,DFC,DMT,DMC
C
C     TO COMPUTE THE ENERGY
C
      DO I = 1, NDI
        SSE = SSE + HALF * (STRESS(I) + OLD_STRESS(I)) * DSTRAN(I)
      END DO
      DO I = NDI+1, NTENS
        SSE = SSE + (STRESS(I) + OLD_STRESS(I)) * DSTRAN(I)
      END DO
C
      RETURN
      END
C***********************************************************************************
C     TO CHECK THE FAILURE INITIATION AND THE CORRESPONDING DERIVATIVE*********
C***********************************************************************************
      SUBROUTINE CheckFailureIni(ST1,SC1,ST2,SC2,ST3,SC3,T12,T23,
     1     T13,
     1     STRESS,STRANT,GFMAT,GFFIB,G12,G23,G13,
     1     CELENT,C,CDFULL,DFT,DFC,DMT,DMC,DMG,DDFDE,DDMDE,NTENS,
     2     DFTOLD,DFCOLD,DMTOLD,DMCOLD,DMT3OLD,NDI,FIBD,MATD)
C
      INCLUDE 'ABA_PARAM.INC'
      DIMENSION DDFDE(6), DDMDE(6), STRANT(6), C(6,6)
      DIMENSION DFMNDE(6), DFFNDE(6),STRESS(6),CDFULL(6,6)
      PARAMETER (ZERO = 0.D0, ONE = 1.D0, TWO = 2.D0, HALF = 0.5D0)
C**************************************************************
C*   Hashin3D: Evaluate Hashin3D failure  *
C*   criterion for fibre and matrix             *
C**************************************************************
      f1tInv = one / ST1
      f2tInv = one / ST2
      f3tInv = one / ST3
      f1cInv = one / SC1
      f2cInv = one / SC2
      f3cInv = one / SC3
```

```
      f12Inv = one / T12
      f23Inv = one / T23
      f13Inv = one / T13
C      write(*,*)st1,st2,st3,sc1,sc2,sc3,t12,t23,t13
        s11 = stress(1)
        s22 = stress(2)
        s33 = stress(3)
        s12 = stress(4)
        s23 = stress(5)
        s13 = stress(6)
c      WRITE(*,*)'END',STRESS(1),STRESS(2)
C
*     Evaluate Fiber modes
      DFT=DFTOLD
      DFC=DFCOLD
      DMT=DMTOLD
      DMC=DMCOLD
      DMG=DMT3OLD
      FIBD=0
      MATD=0
        if ( s11 .gt. zero ) then
C      -- Tensile Fibre Mode
      rft=(s11*f1tInv)**2+(s12*f12Inv)**2+(s13*f12Inv)**2
C
c      WRITE(*,*)'RFT=',rft,s11,st1
       if ( rft .ge. one ) then
       WRITE(*,*)'RFT=',rft,s11,st1
            Dmg = 1
            DFT= one
          end if
        else if ( s11 .lt. zero ) then
*     -- Compressive Fiber Mode
          rfc = (s11 * f1cInv)**2
c           WRITE(*,*)'RFC=',rfc,s11,sc1
          if ( rfc .ge. one ) then
       WRITE(*,*)'RFC=',rfc,s11,sc1
            Dmg = 1
            DFC= one
          end if
        end if
*
*     Evaluate Matrix Modes
      IF ( ( s22 + s33 ) .gt. zero ) then
C      -- Tensile Matrix mode
          rmt = ( (s22 + s33) * f2tInv )**2
     *          + ( (s23**2 + s22*s33)* f23Inv**2 )
     *          + ( s12 * f12Inv )**2
     *          + ( s13 * f12Inv )**2
c           WRITE(*,*)'RMT=',rmt
          if ( rmt .ge. one ) then
            Dmg = 1
            DMT = one
          end if
        else if ( ( s22 + s33 ) .lt. zero ) then
*     -- Compressive Matrix Mode
C
       RMC=(S22/(2*T23))**2+(((SC2/(2*T23))**2)-1)*S22/SC2+(S12/T23)**2
c           WRITE(*,*)'RMC=',rmc
          if ( rmc .ge. one ) then
            Dmg = 1
            DMC= 1.0
          end if
        end if
C---    DELAMINATION NORMAL FAILURE
       IF(S33.GT.0) THEN
       RMT3=(S33*f3tInv)**2
       END IF
       IF(S33.LT.0) THEN
       RMC3=(S33*f3cInv)**2
       END IF
C
       IF(RMT3.GE.1) THEN
       RMT3=1.0
       DMG=1
       END IF
```

```
       IF(RMC3.GE.1) THEN
       RMC3=1.0
       DMG=1
       END IF
      IF(DFT.EQ.1.OR.DFC.EQ.1) FIBD=1.0
      IF(DMT.EQ.1.OR.DMC.EQ.1.OR.DMG.EQ.1) MATD=1.0
      DO I = 1, 6
        DO J = 1, 6
          CDFULL(I,J)=C(I,J)
        END DO
      END DO
C
      IF(DMG.EQ.1.0) THEN
C
C     CALVULATE DAMAGE
C
************************************************************
*   OrthoEla3dExp: Orthotropic elasticity - 3d             *
************************************************************
*  Orthotropic elasticity, 3D case -
*
*     -- shear fraction in matrix tension and compression mode
      smt = 0.5
      smc = 0.5
*
*     -- Compute damaged stiffness
        df = one - ( one - dft ) * ( one - dfc )
*
        CDFULL(1,1)= ( one - df ) * C(1,1)
        CDFULL(2,2)= ( one - df )*(one-dmt)*(one-dmc)*C(2,2)
        CDFULL(3,3)= ( one - df )*(one-dmt)*(one-dmc)*C(3,3)
     1 * (1-RM3)
        CDFULL(1,2)= ( one - df )*(one-dmt)*(one-dmc)*C(1,2)
        CDFULL(2,3)= ( one - df )*(one-dmt)*(one-dmc)*C(2,3)
        CDFULL(1,3)= ( one - df )*(one-dmt)*(one-dmc)*C(1,3)
        CDFULL(2,1)= CDFULL(1,2)
        CDFULL(3,1)= CDFULL(1,3)
        CDFULL(3,2)= CDFULL(2,3)
        CDFULL(4,4) = ( one - df )
     *       * ( one - smt*dmt ) * ( one - smc*dmc ) * G12
        CDFULL(5,5)= ( one - df )
     *       * ( one - smt*dmt ) * ( one - smc*dmc ) * G23
        CDFULL(6,6)= ( one - df )
     *       * ( one - smt*dmt ) * ( one - smc*dmc ) * G13
      END IF
C
C     -- Stress update
C
C       IF(KINC.EQ.1) THEN
        DO I = 1, NTENS
          STRESS(I)=ZERO
          DO J = 1, NTENS
            STRESS(I)=STRESS(I)+CDFULL(I,J) * STRANT(J)
          END DO
        END DO
C       END IF
      RETURN
      END
C
```

Appendix D

Design of slab-beam structure

D.1 Introduction

Chapter 7 showed the optimum design of the GFRP sandwich slabs and beams. The design of the slabs and beams were found by using the numerical multi-objective design. The multi-objective design uses the FE method and the ARMOGA method for the optimisation solution. From the structural point view, the slab behaviour is affected by the support behaviour. Usually, the slab structure is supported by beams grid. As shown in Chapter 7, the slab design is influenced by the span of the slab. The slab span represents the distance between the beams grid. Moreover, the slab support was assumed to be rigid in the design at Chapter 7. In reality, the slab is supported by the beams and those beams have a deformation due to the load transfers from the slab. In addition, the beam load depends on the slab span or the distance between beams.

The design optimisation has been done on the slab and the beam separately. In this part, the slab and beams dimensions are chosen from the results of Chapter 7 and combined together in four different models. A theoretical analysis of the slab-beam model was done to justify the behaviour of the combined structure in terms of mass, cost, deflection, loading capacity and natural frequency.

In this appendix, the 3D FE model is developed for the four slab-beam structure candidatures. The analysis was done for different aspects between the candidatures. The comparison between the different candidatures is shown in this part.

D.2 Slab-beam model cases

The slab beam models were conducted by selecting four different structures. The structures are; A, B, C, and D as shown in Table D.1. The one-way structures (A, B, C) and two-way structures (D) are selected. The overall model dimensions are 4800 mm in length and 4800 mm in width. The slab spans were selected as a multiple of 600 mm. The standard width of the GFRP sandwich panel is 1200 mm. It can be seen that there are different spans can be generated for the slabs; 600, 1200, and 2400 mm. The main beam length is 4800 mm for A, B, and C. The transverse beams have less than 1200 mm length in the model D and the transverse beam length depend on the clear span between main beams. The details of the transfers beam are shown in model-D in Table D.1.

The slabs depth was chosen from the multi-objective optimization results in Chapter 7, it is based on the span of the slab. The beams cross section dimensions have been imported from Chapter-7 as well. All the beams and slabs dimensions are shown in Table D.1. The slab is considered to carry a uniformly distributed load (UDL). The values of the UDL is shown in Table D.1. The two-way slab (model-D) has four side supports, and the same loading of other models was applied.

Table D.1 Slab-beam models.

<table>
<tr><th colspan="2" rowspan="3">Model</th><th colspan="6">Dimensions</th><th rowspan="3">Slab distributed load</th></tr>
<tr><th colspan="3">Slab</th><th colspan="3">Beam</th></tr>
<tr><th>L mm</th><th>W mm</th><th>h mm</th><th>L mm</th><th>b mm</th><th>d mm</th></tr>
<tr><td>A</td><td>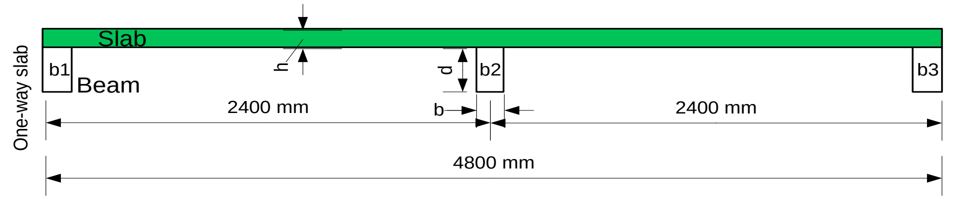
</td><td rowspan="4">4800</td><td rowspan="4">4800</td><td>85.5</td><td rowspan="4">4800</td><td>529</td><td>212</td><td rowspan="4">5 kN/m^2</td></tr>
<tr><td>B</td><td>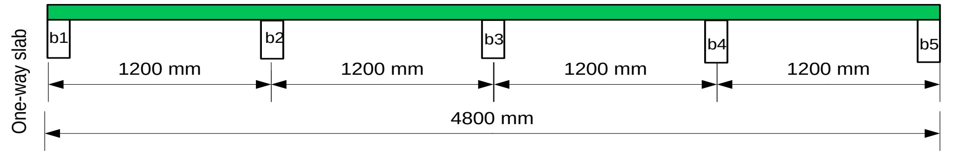
</td><td>45.3</td><td>450</td><td>180</td></tr>
<tr><td>C</td><td>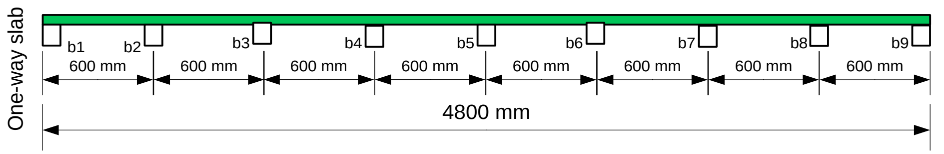
</td><td>27.3</td><td>375</td><td>150</td></tr>
<tr><td>D</td><td>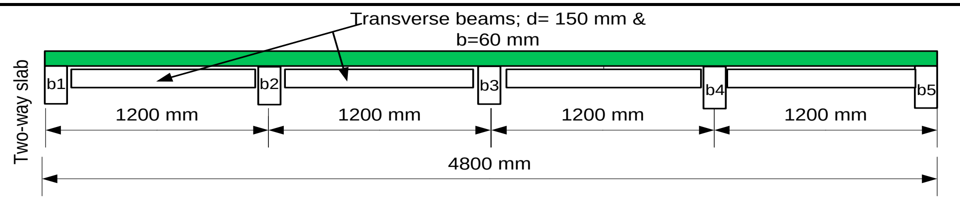
</td><td>38.7</td><td>450</td><td>150</td></tr>
</table>

D.3 Slab-beam model analysis

D.3.1 Cost and mass

The analyses of slab-beam model candidatures show different values of cost and mass. The cost and mass of the model are the total cost and total mass of the slab and the beams. Both slab and beam were designed for the multi-objective optimisation mass and cost minimisation. The slab beam model shows that the 1200 mm one-way slab model-B is the optimum from the cost and mass objectives as shown in Figure D.1. The large slab span in model-A shows the higher cost and mass than the other models. The small span slab in model-C gives a higher cost and mass than the model-B.

The comparison between the two-way slab and one-way slab structures is shown in Figure D.1. The two-way model-D shows a lower cost and mass than the one-way model-B. Therefore, the two-way design is more economic and lighter than the one-way slab model.

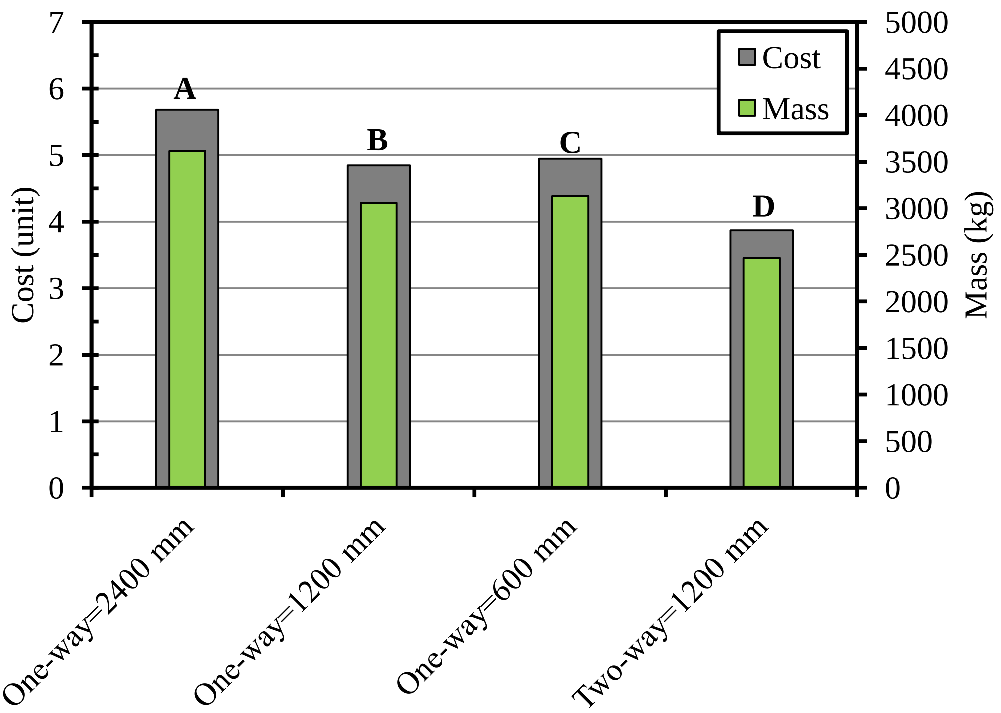

Figure D.1 Cost and mass of the slab-beam models.

D.3.2 Deflection behaviour

Deflection is the main constraint was found in the design of the slabs and the beams. Chapters 7 showed that the slab and beam GFRP sandwich structure designs are controlled by the deflection constraint. The stress constraints did not show a big contribution to the design. The 3D FE model was build for the slab-beam model-C as shown in Figure D.2. The quarter of the model was simulated due to the symmetry. In addition, the same model was built for the structures A, B, and D.

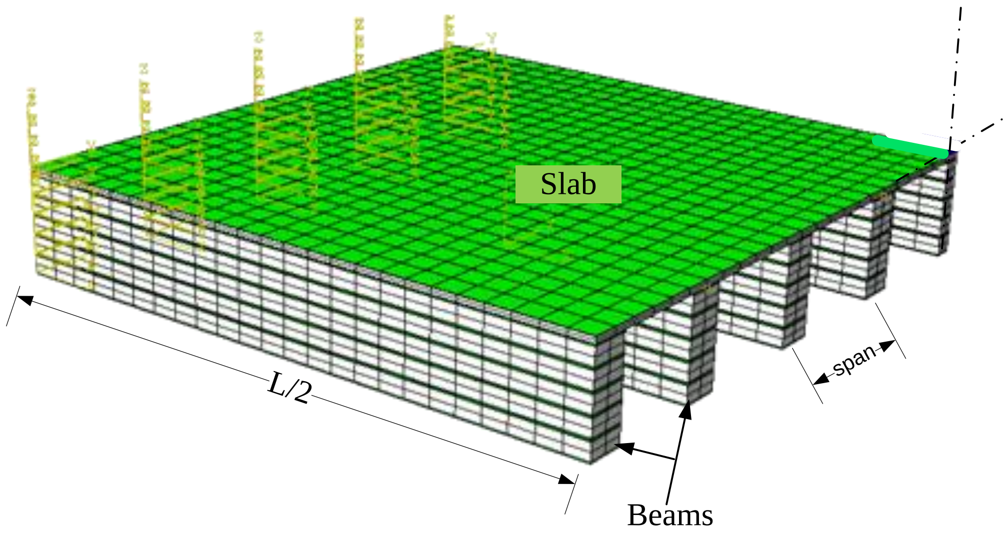

Figure D.2 3D FE for slab-beam model-C.

The FE analysis was done on the four models under UDL. The applied external loads are shown in Table D.1. The same load is applied to the four models; A, B, C, and D. The deflection of the models was measured along the centre line of the structure. The deflection for all models is shown in Figure D.3. All models show a deflection lower than the allowable limits. The slab deflection is less than L/250, and the beam deflection is less than L/400. However, it can be seen that model-A show a lowest deflection at the centre compared to the others. However, the same model shows a highest deflection than the others at the slab centre. The low deflection in the middle is due to the presence of the main beam. In addition, the highest deflection at the slab centre is due to the large span of the slab. The one-way slab model-B and two-way slab model-D have approximately the same load deflection as shown in Figure D.3. The slab-beam model-C shows a large deflection at the centre due to the effect of the point load. In conclusion, the slab-beam models-B and C show homogenous deformation compare to others. The effect of distributed load on the deflection of model-A is clear at the slab mid span. In addition, the effect of point load is obvious at the centre of the model-C structure.

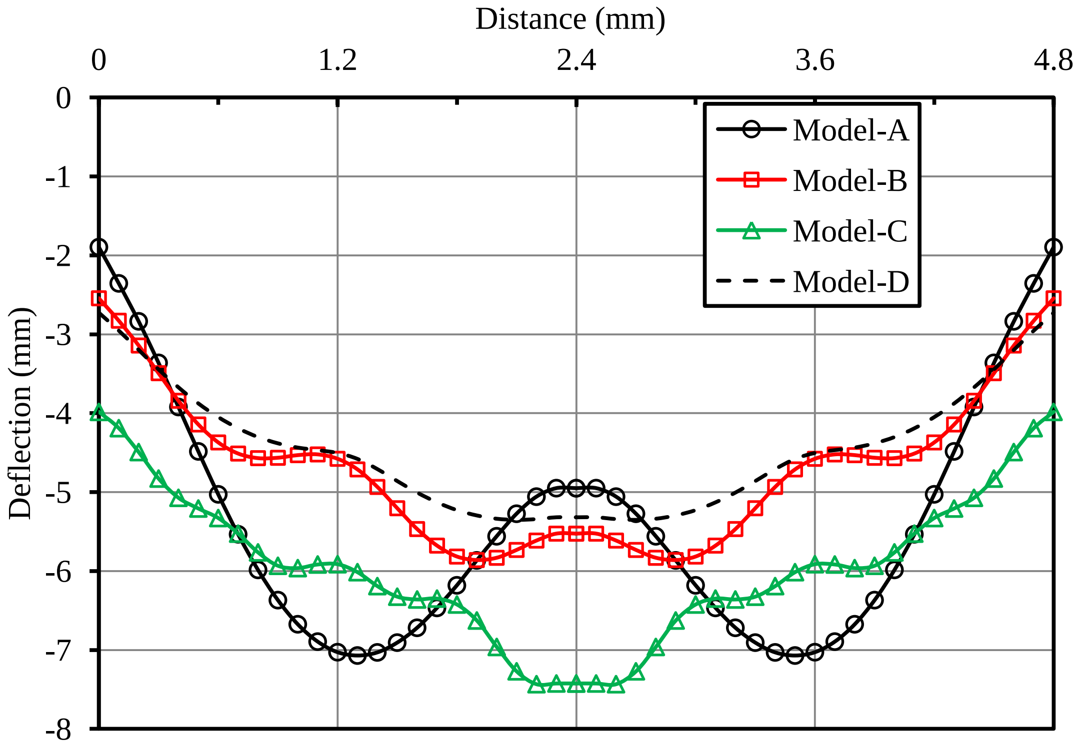

Figure D.3 Deflections of the slab-beam models at service loading.

D.3.3 Load capacity

The load capacity of the slab-beam models represents another aspect in the design evaluation. The FE model was used to analyse the slab-beam structures up to failure. The loads mentioned in Table D.1 are applied to the structure. The distributed load is applied to the whole slab.

The non-linear FE model presented in Chapter-6 is used in this part of the verification. The four models were analysed up to failure. The results of the FE analysis are shown in Figure D.4. It can be seen that all models apple to carry more than 14 times the service load (UDL and point load). The model-B shows a highest load capacity. The models-A, B, and D behave similarly in the load-deflection.

Where, the model-C showed a lower behaviour than the others. The model-C becomes more sensitive to the point load than the other models, due to the small slab span. The small slab span affects the slab thickness itself and the beam cross section.

The failure mode of the slab-beam models are shown in Figure D.5. All models show a failure flexural mode with the centre beam. There is no failure in the slab part for all models. The failure starts with the core parts at the beams due to the tension forces. The tension forces in the core developed due to the bending. Then, the core failure followed by a GFRP skin failure in the centre of the beam and in the beam supports. In the models B, C, and D, the failure happened in most beams as shown in Figure D.5 (b), (c), and (d).

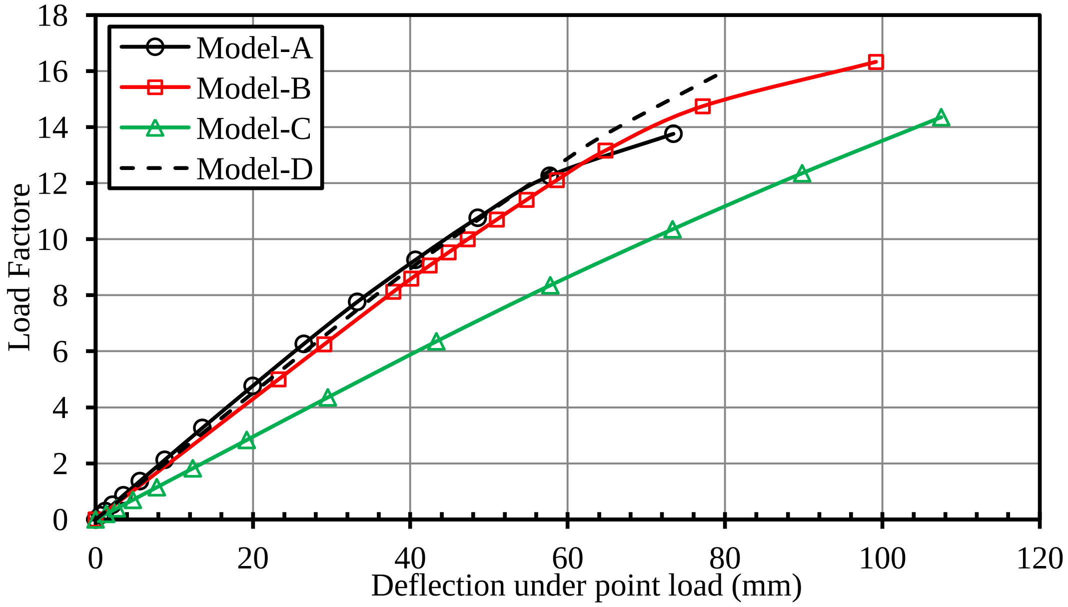

Figure D.4 Load-deflection of four models at centre.

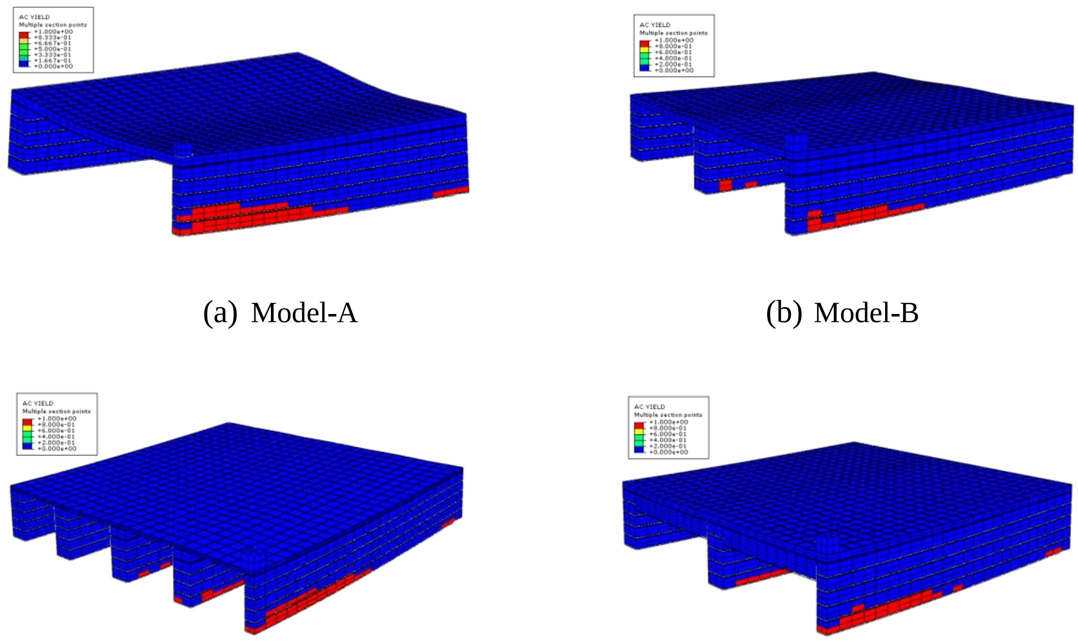

(a) Model-A (b) Model-B

(c) Model-C (d) Model-D

Figure D.5 Failure of different slab-beam models.

D.3.4 Frequency

Frequency of the structures described as one of the important points in the structural design. The frequency experimental investigations of the slabs and beams were done in Chapter-5 and Appendix B respectively. The frequency FE analysis was done in Chapter-6 and Appendix B respectively. The optimum design of the slabs under cost and mass minimisation showed that this design is satisfied the recommended minimum frequency up to 2400 mm span. The combined slab-beam model gives the real simulation to the expected structural vibration. All slab-beam models analysed with the FE model to find the natural frequency of the structure. The results of the free vibration analysis are shown in Figure D.6. The model-B shows a higher frequency than the others. The model-B represents the best design for the one-way slab-beam structures. Furthermore, the one-way model-B has a higher frequency than the two-way model-D. Three models A, B, and D show a frequency higher than 15 Hz. However, the model-C has a frequency lower than the 15 Hz, and this model could suffer from free vibration structural problems.

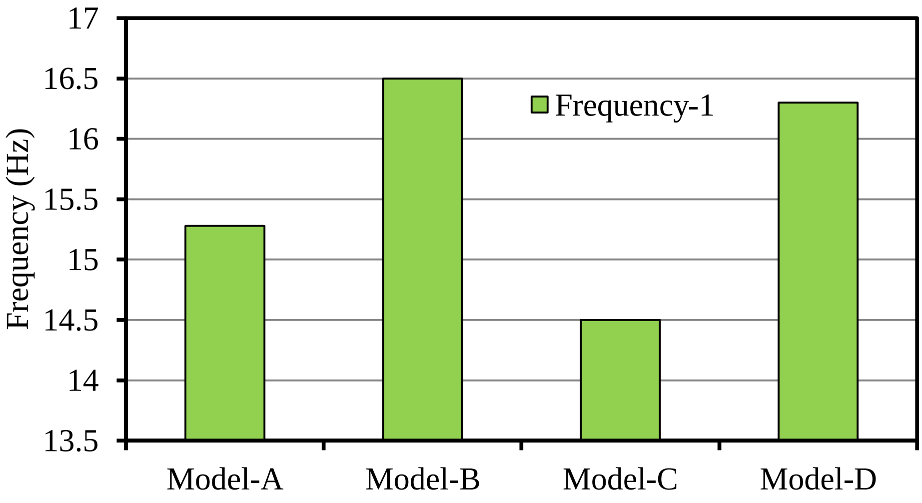

Figure D.6 First-natural frequencies of the slab-beam models.

D.4 Summary

In this appendix, different slab-beam models were created based on the optimisation design results. The comparison of the analysis results show that the models is behaving differently. In conclusion, the optimisation of slab-beam model is necessary for the structure design. In this case, a large number of model analyses are required for different sizes, and loading cases to cover a big rang of the structural configurations. In addition, optimising the slab-beam models can provide different results than optimising slab and beam separately.